Université Libre de Bruxelles

Doctoral Thesis

Study of Triple-GEM detector for the upgrade of the CMS muon spectrometer at LHC

Author:
Thierry Maerschalk

Supervisor:
Dr. Gilles De Lentdecker

“Ce qui ne tue pas rend plus fort.”

Friedrich Nietzsche

“Le ridicule ne tue pas.”

Anonyme

PhD thesis jury members:

Juan Antonio Aguilar Sánchez (ULB) (secretary)
Paul Aspell (CERN)
David Attié (CEA)
Othmane Bouhali (TAMU at Qatar)
Gilles De Lentdecker (ULB) (supervisor)
Pascal Vanlaer (ULB) (president)

Abstract

Study of Triple-GEM detector for the upgrade of the CMS muon spectrometer at LHC

by Thierry Maerschalk

This doctoral thesis is part of the upgrade of the CMS experiment at the Large Hadron Collider of CERN, the LHC. CMS, together with the ATLAS experiment, led to the discovery of the Brout-Englert-Higgs boson in 2012. But the LHC research program is not over yet. Indeed, the LHC is intended to operate even at least 20 more years. During this period, the luminosity will grow gradually up to five times its nominal value of 10^{34} cm^{-2} s^{-1} initially foreseen. This increase in luminosity requires the LHC experiments, like CMS, to upgrade their detectors as well as their data acquisition system. One of the next major CMS upgrade is the addition of a new detector layer in the forward muon spectrometer of CMS. The technology that has been chosen by the CMS collaboration for this upgrade is the Triple Gas Electron Multiplier (Triple-GEM) technology. This upgrade aims to maintain the trigger performance despite the increasing rate of particles (> 1 kHz/cm^2) and will also improve the reconstruction of muons tracks, thanks to a excellent spatial resolution (~ 250 μm). It is the study and characterization of this technology that is the subject of this thesis.

This characterization of the Triple-GEM detectors starts with a detailed study of the time resolution. This study has been performed using different Monte Carlo simulations like GARFIELD, and has demonstrated that the Triple-GEM detectors equipped with the new VFAT3 electronics (developed for this upgrade) fulfill the requirements for the CMS upgrade.

Then we have studied different detector prototypes. First, we have built two small 10×10 cm^2 prototypes and developed a test bench at the ULB laboratory. This test bench has allowed us to study another important parameter of the Triple-GEM detectors: the gain. Later, we also had the opportunity to take part in the data taking and analysis of a test beam campaign at CERN. The analysis of the data of this test beam is also presented in detail.

The last part of this work concerns the study of the spatial resolution. We have estimated the spatial resolution of the Triple-GEM detector equipped with a binary electronics by Monte Carlo simulations as well as analytically. This study has been extended to other detector technologies like the Micromegas and the silicon sensors.

Résumé

Etude de détecteur Triple-GEM en vue de la mise à niveau du spectromètre à muons de CMS au LHC

par Thierry Maerschalk

Cette thèse de doctorat s'inscrit dans le cadre de la mise à niveau de l'expérience CMS auprès du grand collisionneur de protons du CERN, le LHC. CMS, avec l'expérience ATLAS, a permis la découverte du boson de Brout-Englert-Higgs en 2012. Mais le programme de recherche du LHC n'est pas pour autant terminé. En effet, le LHC est destiné à fonctionner encore au moins 20 ans. Pendant cette période, la luminosité va croître progressivement jusqu'à atteindre environ cinq fois la valeur nominale de 10^{34} cm^{-2} s^{-1} initialement prévue et ce d'ici 2025. Cette augmentation de luminosité pousse les expériences du LHC, comme CMS, à mettre à jour les détecteurs ainsi que leurs systèmes d'acquisition de données. Une des prochaines mises à niveau majeures de CMS est l'addition d'une nouvelle couche de détection dans le spectromètre à muon vers l'avant. La technologie de détection qui a été choisie par la collaboration CMS est la technologie des Triple Gas Electron Multiplier (Triple-GEM). Cette mise à niveau a pour but de maintenir les performances du système de déclenchement et ce malgré l'augmentation de taux de particules (> 1 kHz/cm^2) et de permettre également, grâce à la très bonne résolution spatiale des Triple-GEM (~ 250 μm), l'amélioration de la reconstruction des traces de muons. C'est l'étude des caractéristiques de cette technologie qui est le sujet de cette thèse.

Cette caractérisation des détecteurs Triple-GEM commence par une étude détaillée de la résolution temporelle. Cette étude a été réalisée à l'aide de différentes simulations Monte Carlo telles que GARFIELD et a permis de montrer que les Triple-GEMs équipés de la nouvelle électronique VFAT3 (spécifiquement dévelopée pour les Triple-GEMs) remplissent les conditions pour la mise à niveau de CMS.

Nous avons ensuite étudié différents prototypes. Tout d'abord nous avons construit deux petits (10×10 cm^2) prototypes de Triple-GEM et dévelopé un banc de test au sein du laboratoire de l'ULB. Ce banc de test nous a permis d'étudier un autre paramètre important des détecteurs Triple-GEM: le gain. Au cours de cette thèse nous avons également participé à la prise de données et à l'installation de différents tests en faisceau au CERN. L'analyse des données du test en faisceaux d'octobre 2014 est aussi présentée en détail.

La dernière partie de ce travail concerne l'étude de la résolution spatiale. Nous avons estimé la résolution spatiale par simulation de Monte Carlo ainsi que de manière analytique pour des détecteurs GEM munis d'une électronique binaire. Cette étude a également été généralisée à d'autres détecteurs tels que les Micromegas ou encore les capteurs au silicium.

Acknowledgements

First, I would like to thank Gilles De Lentdecker, my supervisor during those four years of doctoral thesis, with whom I have started to work on gaseous detectors in 2009.

I would like to give a very special thank to GEM-team in Brussels, Patrizia for her energy, Erik for all the pictorial expressions, Alexandre with whom I started my physical studies, Florian my partner and emergency exit mate, Ryo for his kindness and the work on the spatial resolution, and finally Thomas for all the coffee/tea breaks.

I am grateful to all members of my thesis jury, Juan Antonio Aguilar Sánchez, Paul Aspell, David Attié, Othmane Bouhali and the president of that jury Pascal Vanlaer.

I also would like to thanks all the IIHE members for welcoming me among them and especially its director Laurent Favart and secretary Audrey Terrier.

Last but not least, I have to thanks my lovely Lili for her continuous support.

Contents

Chapter 1

Introduction

The work presented in this thesis is part of the detector development for the upgrade of the forward muon spectrometer of CMS. The upgrade of the muon end-caps of CMS consists in the addition of a new layer of detectors in the high-η region ($1.5 < |\eta| < 2.2$). The technology that has been chosen for this upgrade is the Triple-GEM detector. The GEM (Gas Electron Multiplier) is a type of gaseous ionization detectors that is capable of operating in high-rate (MHz/cm^2) environments with detection performances compatible with the CMS requirements.

This high-η region of the CMS muon spectrometer is the most challenging, where the particle rate can reach several kHz/cm^2, and it is also the less redundant since it relies only on one detector technology, the Cathode Strip Chambers. Indeed their "associate" Resistive Plate Chambers used everywhere else in the spectrometer for triggering purpose have not been installed, due to concerns regarding their rate capability.
Simulations have shown that the introduction of a new layer of GEM detector in the region, providing an extra precise hit (~ 250 μm) with a good time resolution (better than 10 ns), would improve the level one trigger muon reconstruction and momentum resolution. This would allow to maintain a low muon trigger transverse momentum threshold to keep the efficiency as high as possible in order to measure interesting physics processes featuring soft muons.
The CMS GEM Collaboration has shown during the R&D phase started in 2009 and which this work is part of, that the GEM technology is the most suitable choice for the upgrade. This led to the approval in 2015 of the so-called GE1/1 project by the CMS Collaboration and the CERN LHCC committee.

So far all the studies performed for the GE1/1 upgrade have been using the VFAT2 front-end electronics. The VFAT2 chip was used within the TOTEM experiment for the readout of GEM detectors. The requirement of GE1/1 necessitate the design of a new

ASIC, the VFAT3. Since the time resolution is a very important parameter for optimal trigger performance, we have investigated the time resolution we can expect with a CMS Triple-GEM detector read-out with the VFAT3 chip. This study has been carried-out with the state-of-the-art simulation software for gaseous detector, GARFIELD, as well as with our own simulation program, designed to be much faster and flexible. Our fast simulation program, called FastSim, has been validated with respect to several measurements obtained during beam tests at CERN and at Fermilab as well as at the ULB laboratory. This fast simulation has also been shown to be a very useful tool to also study the spatial resolution of several detector geometries including silicon detectors.

We will start this thesis, in Chapter 2, by a presentation of the current theory of particle physics: the Standard Model. Then, we will present the Large Hadron Collider (LHC), which is the current largest and most powerful particle collider ever built. To follow, we will present one of the major experiments present at the LHC: the Compact Muon Solenoid (CMS). Finally, the upgrade plan of CMS will be presented with a particular focus on the high-η upgrade.

In Chapter 3 the different physical processes that are at play within a gaseous detector will be reviewed. We will start with the general principle of detection, then we will study in detail different processes (the gas ionization, the kinetics of the electrons in the gas, etc.). Afterwards we will present different micro-pattern gaseous detectors with a particular attention to the GEM technology. Finally we will review the characteristics of the CMS Triple-GEM detectors.

Chapter 4 is devoted to the Monte Carlo simulation study of different features of the CMS Triple-GEM. First the GARFIELD simulation will be presented, followed by a detailed study of the time resolution obtained using the latter. Then, we will present the FastSim that is a simulation that has been developed during this thesis. Finally, different comparisons between the FastSim results and other Monte Carlo simulations and experimental data will be presented.

Chapter 5 is dedicated to the measurement of the performance of different Triple-GEM prototypes. First, the setup that has been built at the ULB will be presented together with two small Triple-GEM prototypes. Then the results obtained with those prototypes will be presented. Finally, we will discuss a serie of results obtained during a test beam campaign on full size Triple-GEM prototypes.

Finally, in Chapter 6, we will study in detail the spatial resolution. This study will estimate the spatial resolution analytically and by Monte Carlo simulation for a binary readout for the GEM-based detectors but also the silicon sensor and the Micromegas.

Chapter 2

Large Hadron Collider and Compact Muon Solenoid

Physicists have always tried to understand the fundamental components of matter. Nowadays it is mostly particle physics that studies the elementary constituents of matter and their interactions. The elementary particle physics has emerged with the discovery of the electron at the end of 19th century by J.J. Thomson. Since then, physicists have regularly discovered new particles and have developed new fundamental particle theories. At first, the discovery of new particles was mostly the results of experiments with cosmic rays. Those discoveries have stimulated the physicists to build high energy accelerators to produce controlled beams of particles. Those increasingly powerful accelerator have required the construction of ever larger and more complex experiments. This development has led us to the construction of the LHC, the largest and most powerful particle accelerator in the world. It has been designed for the discovery of the Higgs boson, accurate measurement of Standard Model, and search for Beyond Standard Model physics.

In this chapter we will start in section 2.1 by a brief presentation of the Standard Model of elementary particles. To follow, in section 2.2, we will present the Large Hadron Collider (LHC) and we will make an overview of the different experiments at the LHC, and the accelerators present at CERN. Finally, in section 2.3 we will present the Compact Muon Solenoid (CMS) experiment with a focus on the muon spectrometer and a presentation of the upgrades.

2.1 The Standard Model

The current theory in the field of modern particle physics is called the Standard Model (SM) and was formulated in the late 1960 by S. Glashow, S. Weinberg and A. Salam. The SM is an unification of the electroweak theory together with the quantum chromodynamics (QCD). According to the SM, matter is formed by 12 fundamental spin $\frac{1}{2}$ particles called *fermions* and their interactions are described by the exchange of characteristic gauge *bosons* (particle of integer spin) between the fermions.

2.1.1 Elementary Particles of Matter: Fermions

The 12 fermions are divided in two categories: six *leptons* and six *quarks*.

The leptons have an integer electric charge. There are three generations of charged leptons (electron e^-, muon μ^- and tau τ^-) and their associated neutrinos (ν_e, ν_μ and ν_τ) that are electrically neutral.

The quarks have a fractional electric charge:

- $+\frac{2}{3}|e|$ for the quarks up (u), charm (c) and top (t).
- $-\frac{1}{3}|e|$ for the quarks down (d), strange (s) and bottom (b).

where $|e|$ is the electric charge of the electron.
The quarks are also grouped in three generation pairs that form the hadronic matter: the first (u,d), the second (c,s) and the third (t,b) generation. In addition of their electric charge, the quarks carry also a 'color' charge.

Additionally, to each fermion is associated an anti-particle that has the same mass as the associated particle but all its quantum numbers are reversed.

2.1.2 Elementary Interactions & Gauge Bosons

In the SM, each fundamental forces has a mediator that is a gauge boson. There exist four different elementary forces:

- The electromagnetic (EM) force is carried by the photon (γ). The EM interaction applies on all charged particles. In classical physics it is described by the Maxwell equations and it is described by the Quantum ElectroDynamics (QED) theory at the quantum level.

- The weak interaction is mediated by the charged boson $W^{\pm}$ and the neutral boson Z, with masses of the order of hundred times the proton mass. Those bosons interact with all elementary particles and allow heavier fermions to decay into lighter fermions. Both the $W^{\pm}$ and the Z bosons have been discovered experimentally at CERN in 1983.
- The strong interaction is mediated by the eight massless gluons g_i and applied on all the color charged particles. Consequently it acts only on the quarks and its own gauge bosons. The strong interaction is described by the Quantum Chromo-Dynamics (QCD).
- The fourth fundamental force is the gravitation. This interaction is not included in the SM which constitutes one of its main limitations.

The strength of the different interactions, relative to the strong interaction, are reported in the table 2.1.

Strong	Electromagnetic	Weak	Gravitation
1	1/137	10^{-5}-10^{-7}	10^{-39}

TABLE 2.1: Strength of the different interactions relative to the strong interaction.

2.1.3 Scalar Boson

The last particle predicted by the SM is the scalar boson. This particle was predicted by Englert and Brout [1], Higgs [2], and Hagen, Kibble and Guralnik [3] and has been experimentally confirmed by the CMS [4] and ATLAS [5] experiments at LHC in 2012. The scalar boson is predicted in the theory by the Brout-Englert-Higgs mechanism that was introduced in order to generate the mass of the heavy bosons and the mass of the fermions.

Figure 2.1 gives a schematic representation of all the elementary particles predicted by the SM.

2.1.4 Limitations and Needs for Beyond the Standard Model

The Standard Model is currently the best model to describe most phenomena of elementary particle physics. It has been successfully tested experimentally since its formulation. However the SM can not be considered as the ultimate theory of particle interactions. Indeed, the SM has a series of limitations that are the following:

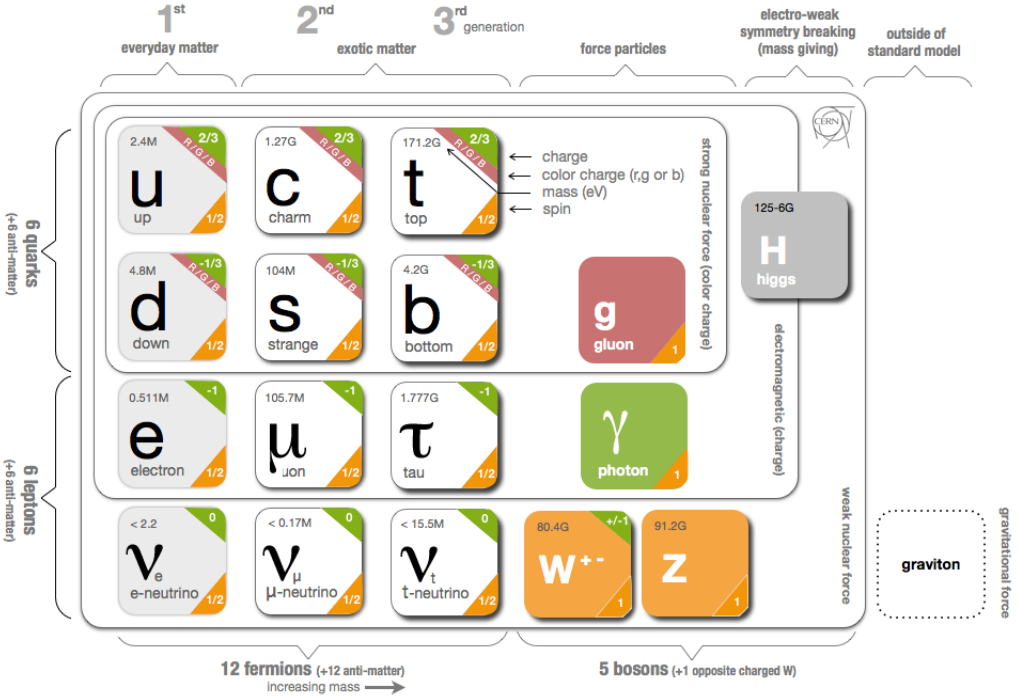

FIGURE 2.1: Schematic representation of the elementary particles predicted by the Standard Model with the addition of the hypothetical presence of the graviton that is the mediator of the gravitational force. Credits: CERN

- As already mentioned, the gravitation is not included in the SM. The current best theory to describe the gravitation is the Einstein's general theory of relativity.
- The model contains 19 free parameters (masses, mixing angle, coupling constants, etc.), that need to be measured. It is widely believed that some of these parameters should be related to each other from a mechanism that is not described by the SM.
- In the model, the neutrinos are assumed to be massless. However, experimentally we have observed that the neutrinos can oscillate from one flavor to an other and this fact implies that they have a non-zero mass.
- Today in the universe we observe a matter-antimatter asymmetry that is not explained by the SM.
- Several cosmological studies reveal strong evidence that the visible content of matter is only $\sim 5\%$ of the total matter and energy in our universe. The rest is thought to be due to the dark matter (25%) and the dark energy (70%). The SM does not provide good candidates for a dark matter particle.

All those limitations seem to require a new and presently unknown theory for the elementary particle physics. Several theories have been developed and are grouped under the name Beyond Standard Model (BSM) theory, but until this day none of these theories has been validated by the experiment.

2.2 The Large Hadron Collider

2.2.1 CERN Accelerators Overview

The CERN (Organisation Européen pour la Recherche Nucléaire - European Organization for Nuclear Research) was founded in 1954 by 12 European countries and has now 21 member states. It is a European research facility that runs the largest particle physics laboratory in the world. The CERN laboratory site is close to the Franco-Swiss border near Geneva, as shown on Figure 2.2.

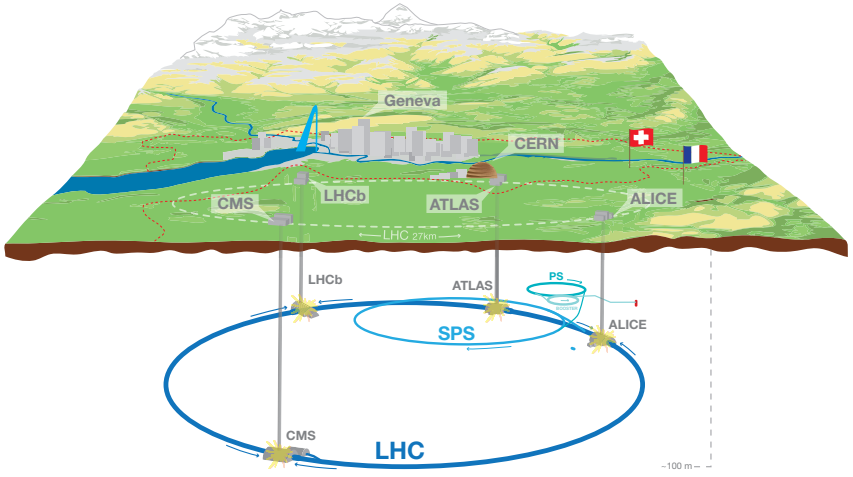

FIGURE 2.2: Overall view of the LHC and location of the four main experiments [6].

As presented on Figure 2.3, CERN operates an accelerator complex made of six accelerators and a decelerator. The succession of the six accelerators allows to gradually accelerate protons (or ions). This acceleration is done in four main steps:

- The Linear Accelerator (LINAC 2) initiates the acceleration with energies up to 50 MeV;

- The protons are injected in the Booster (PSB) and then in the Proton Synchrotron (PS). This step brings the proton's energy up to 25 GeV/c^2;
- The Super Proton Synchrotron (SPS) accelerates the protons up to 450 GeV/c^2;
- Finally, the Large Hadron Collider (LHC) accelerates the protons to their collision energy 3.5, 4 then 6.5 TeV.

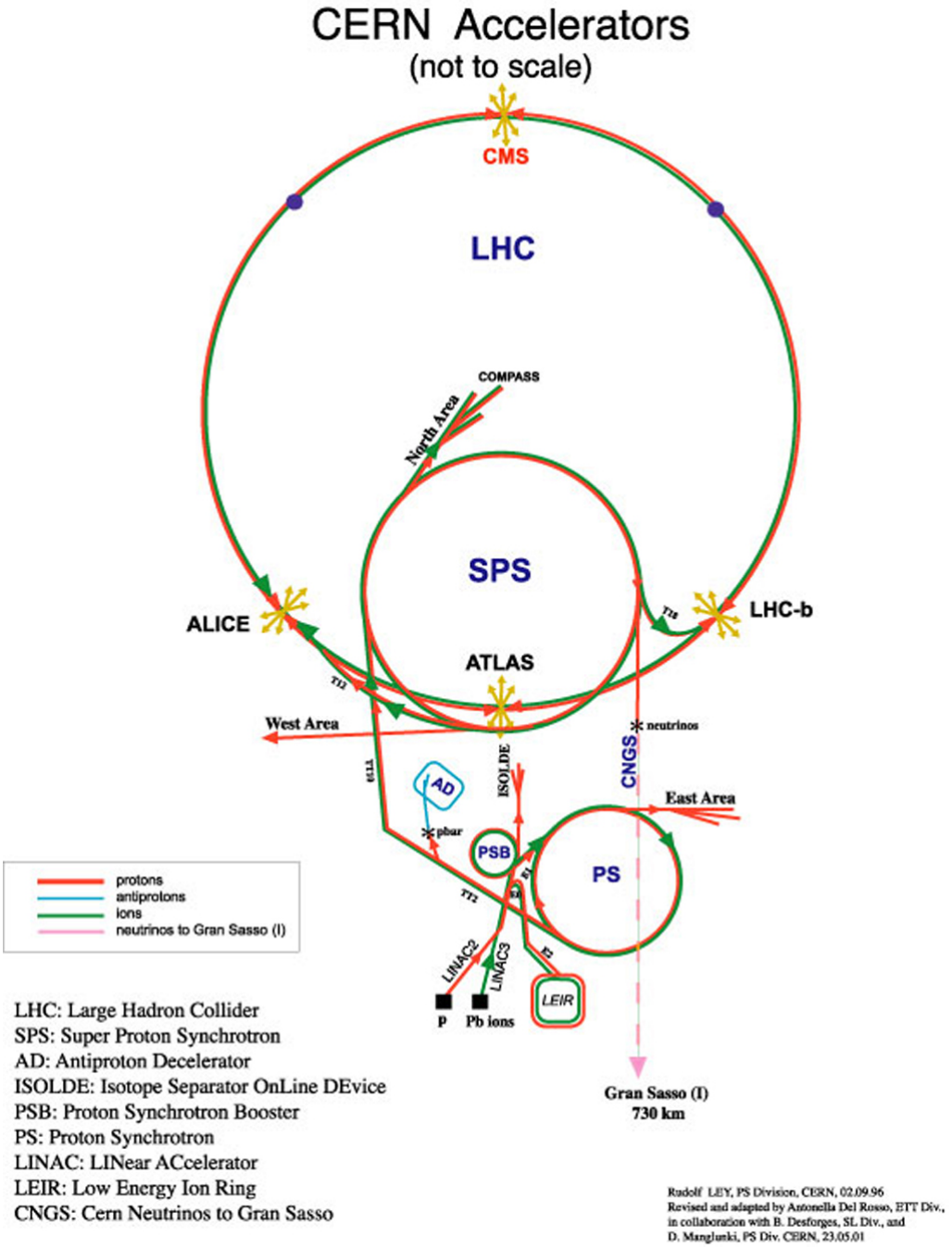

FIGURE 2.3: Overview of the accelerator complex of CERN [7].

Nowadays, the LHC is the largest and most powerful particle accelerator in the world. It consists of a 26.7 km ring built at a mean depth of 100 m underground. It has two parallel beam pipes with counter-rotating beams with four interaction regions equipped with experiments. The LHC project was approved in December 1994 by the CERN Council and it was built during the years 2000 to 2008 in the existing tunnel of the former Large Electron-Positron (LEP) collider.

2.2.2 Luminosity and Center-of-Mass Energy

At the LHC, the proton beams are accelerated simultaneously in opposite directions before colliding at one of the interaction points. The beams are made of bunches of 10^{11} protons distributed on 9 cm. We will now define two important parameters that describe the performance of LHC:

- The luminosity ($\mathcal{L}$): the number of events per second (N_{event}) generated in the collisions of a collider (like LHC) is given by:

  $$N_{event} = \mathcal{L}_{inst} \cdot \sigma_{event},$$

  where σ_{event} is the cross section of the event of interest and $\mathcal{L}_{inst}$ is the instantaneous luminosity.
  The instantaneous luminosity is a function of the number of particles per bunch n_i, the frequency of collisions f and the transverse beam profiles σ_x and σ_y [8]:

  $$\mathcal{L}_{inst} = f \frac{n_1 n_2}{4\pi\sigma_x\sigma_y}.$$

  The integrated luminosity is the amount of collected data ($\mathcal{L}_{int}$) over a time period:

  $$\mathcal{L}_{int} = \int_{t_1}^{t_2} \mathcal{L}_{inst} dt,$$

  and is generally expressed in inverse femtobarn (fb^{-1}), where a barn is equal to 10^{-24} cm^2.

- The center-of-mass energy ($\sqrt{s}$) defines the total energy available in a collision. This energy depends on the energies of the particles of the two beams E_i and their momenta p_i:

  $$\sqrt{s} = \sqrt{(E_1 + E_2)^2 - (p_1 + p_2)^2},$$

In a collider, the momentum of the two beams have the same value and the opposite direction ($p_1 = -p_2$), which means that we can write:

$$\sqrt{s} = \sqrt{(E_1 + E_2)^2}.$$

Therefore, $\sqrt{s}$ at the LHC is equal to the sum of the energies of the two opposite beams.

The nominal center-of-mass energy at the LHC is 14 TeV, and the nominal instantaneous luminosity is 10^{34} cm^{-2}s^{-1}. During the first year of operation, the LHC ran at a center-of-mass energy of 7 TeV and the total integrated luminosity was 5.1 fb^{-1}. Then the energy was increased to 4 TeV per beam (for $\sqrt{s} = 8$ TeV) until the integrated luminosity reached 19.7 fb^{-1}.

2.2.3 The LHC Experiments

There are four main experiments that are placed at the collision points of the LHC: ATLAS (A Toroidal LHC ApparatuS), CMS (Compact Muon Solenoid), LHCb (LHC beauty) and ALICE (A Large Ion Collider Experiment). Figure 2.4 shows the schematic layout of the LHC and the location of the four main experiments.

CMS and ATLAS are two general purpose experiments that study a wide range of particle physics. Those experiments were designed for the search of the Higgs boson and for the search of BSM physics. They also perform precision measurements of processes predicted in the SM. They have confirmed in 2012 the existence of the scalar boson of the SM as mention before.

Unlike the two multi-purpose experiments, LHCb and ALICE are more targeted experiments. LHCb focuses on the study of the asymmetry between the matter and the anti-matter in the Universe and ALICE is designed to study the confinement of the quarks through the quark-gluon plasma produced in heavy ions collisions.

There also exist two smaller LHC experiments that focus on forward particles: TOTEM (TOTal Elastic and diffractive cross section Measurement) and LHCf (Large Hadron Collider forward). Finally, near LHCb there is the MoEDAL (Monopole and Exotics Detector at the LHC) experiment that focuses on the search for the magnetic monopole.

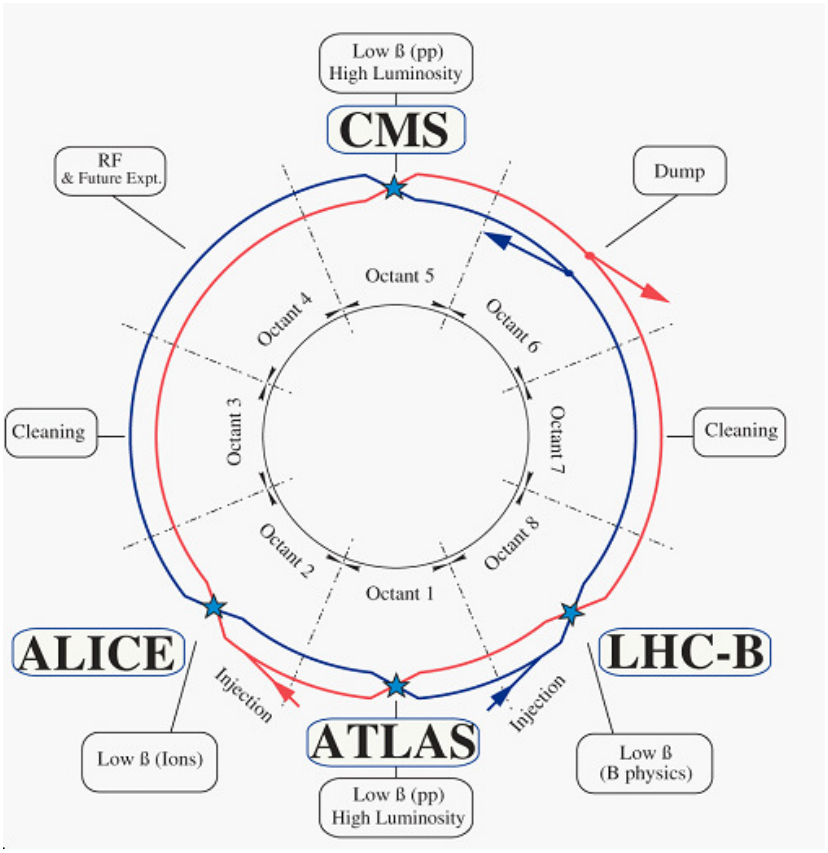

FIGURE 2.4: Layout of the LHC including the four main experiments [9].

2.2.4 Upgrade Planning

With the aging of the detectors and the evolution of different technologies, it is necessary to upgrade regularly both the accelerator systems and the experiments. Those upgrades are helpful to increase the discovery potential of the LHC experiments. The upgrade of the accelerator systems have two majors aspects: the increase of the center-of-mass energy to reach the nominal value of 14 TeV and the increase of the instantaneous luminosity. Those upgrades are planed and Figure 2.5 shows the projected LHC instantaneous and integrated luminosity as a function of the year as well as the shutdown time of the accelerator.

Between 2013 and 2014 took place the first upgrade of the LHC. This first Long Shutdown (LS1) has seen the improvement of the beam lines in order to increase the center-of-mass energy from 8 TeV to 13 TeV and soon to the nominal 14 TeV. The instantaneous luminosity has also been increased to approach the nominal value $\mathcal{L} = 10^{34}$ cm^{-2} s^{-1}, where it reached in 2012 about 7.5×10^{33} cm^{-2} s^{-1}.
The second Long Shutdown (LS2) is planned between 2019 and 2020. The goal is to increase the instantaneous luminosity up to 2×10^{34} cm^{-2} s^{-1}.

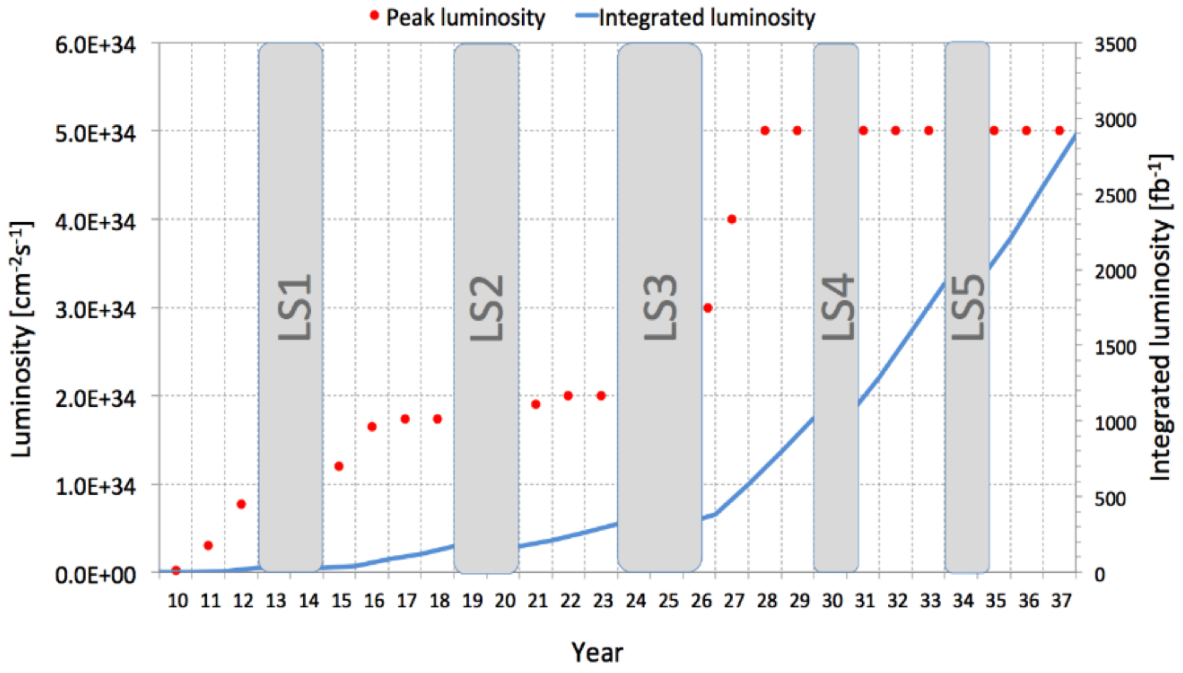

FIGURE 2.5: Projected LHC instantaneous and integrated luminosity as a function of the year and preliminary dates for Long Shutdowns (LS).

Between LS1 and LS2, there is a period of operation called Run 2 and the goal is to reach the integrated luminosity of 150 fb^{-1}. Following LS2, Run 3 will take place starting in 2021 and will continue until the LHC reaches 300 fb^{-1} that is planed for the end of 2023. The whole period, starting from November 2009 where the first collisions of the LHC took place up to the end of Run 3, is called Phase I.
Starting from LS3, planned for 2024, the next phase of LHC operation will take place. During this phase, called Phase II or High Luminosity LHC (HL-LHC), the instantaneous luminosity will be brought up to $5 - 7 \times 10^{34}$ cm^{-2} s^{-1} and integrating a total luminosity of 3000 fb^{-1}.

2.3 The Compact Muon Solenoid

The Compact Muon Solenoid (CMS) detector, shown in Figure 2.6, is one of the multi-purpose detectors operating at the LHC. The primary goal of the CMS experiment is to study proton-proton collisions at a center-of-mass energy of 14 TeV and at luminosities up to 10^{34}cm^{-2}s^{-1}.

The position of any object in CMS is described in the polar coordinate system. The origin of the system is given by the theoretical interaction point between the two proton beams. The x-axis points radially inward the center of the LHC, the y-axis points

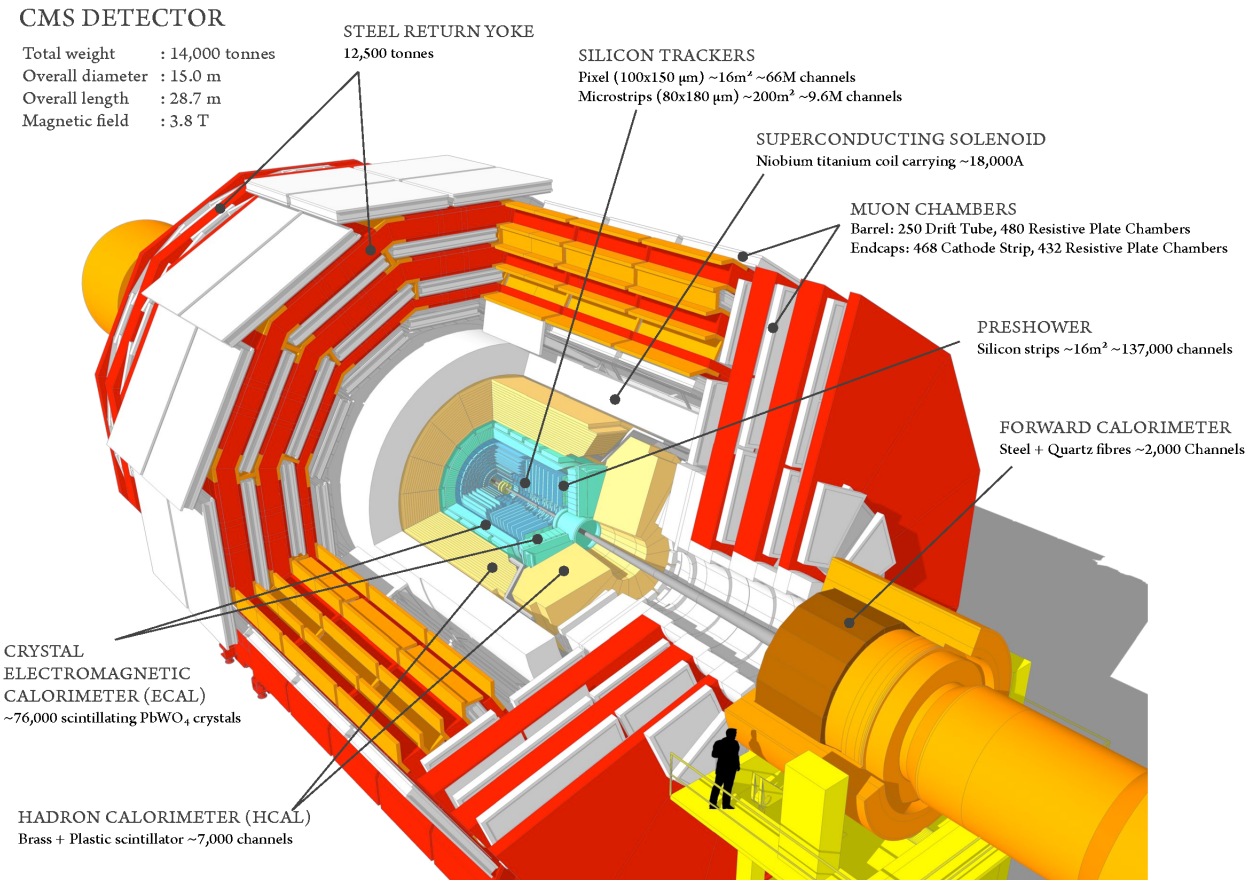

FIGURE 2.6: Cutaway view of the CMS detector [10].

vertically upward, the z-axis points along the beam direction. The azimuthal angle ϕ is measured from the x-axis in the x-y plane, the polar angle θ is measured from the z-axis and the radial coordinate in this plane is denoted by r. A variable extensively used in CMS is the so called pseudo-rapidity (η) defined as:

$$\eta = -ln\left(tan\left(\frac{\theta}{2}\right)\right)$$

2.3.1 Overview

The CMS detector is an hermetic cylinder with a length of 28.7 m, a diameter of 15 m and a total weight of 14000 t. It is divided into two regions: the central region called the barrel and the two extremities called the endcaps. The different subsystems of the CMS detector are organized in layers around the interaction point. There exist five subsystems that have a specific task and characteristic [11] for the particle detection:

- The *tracker system* is the central part of CMS and it is able to guarantee high track reconstruction efficiency and a good momentum resolution of charged particles together with the reconstruction of the primary vertices.
  The full tracker system covers a detection region up to $|\eta| = 2.5$. It is made of three layers of silicon pixel detectors in the barrel with about 66 millions of pixels and two disks of pixel modules complement those layers on each side. Then, ten layers of silicon strip sensors in the outer region and the endcaps for a total of 10 millions strips;

- The *electromagnetic calorimeter (ECAL)* is designed to detect photons and electrons with a very high energy resolution. It allows to have a good invariant mass resolution for photons pairs (1% at 100 GeV/c^2). The ECAL is an hermetic calorimeter that covers a detection region up to $|\eta| = 3$. It is made of more than 61000 $PbWO_4$ scintillating crystals in the barrel and around 15000 in the endcaps. When the photons and electrons enter the ECAL, they initiate an EM shower during which their energies are converted into light and then is collected by photo-detectors;

- The *hadronic calorimeter (HCAL)* is a complement of the ECAL which is designed to measure the hadrons jets energy. The HCAL is made of alternate brass converters and about 70000 scintillator tiles and photo-detectors that cover the detector region up to $|\eta| = 3$. Additionally, the HCAL allows the indirect detection of weakly interacting particles by measuring the missing energy;

- The *magnet* is a superconducting magnet of 6 m diameter and 12.5 m length weighting a total of 220 t, generating a magnetic field of 3.8 T. It is kept at a temperature of 4.5 K with liquid helium. The magnetic field is essential to bend the charged particles and allows the precise measurement of their momentum. The map of the magnetic field and the field lines produced by the magnet are shown on Figure 2.7;

- The *muons system* consists of three different technologies of gaseous detectors and covers the detection region up to $|\eta| = 2.4$. It plays a crucial role in the muon identification, measurement of their momentum and general triggering. A detailed description of the muon system and the different technologies is given in Section 2.3.2.

Figure 2.8 shows schematically how the various subsystems of detector contribute to the identification of the particles that pass through them.

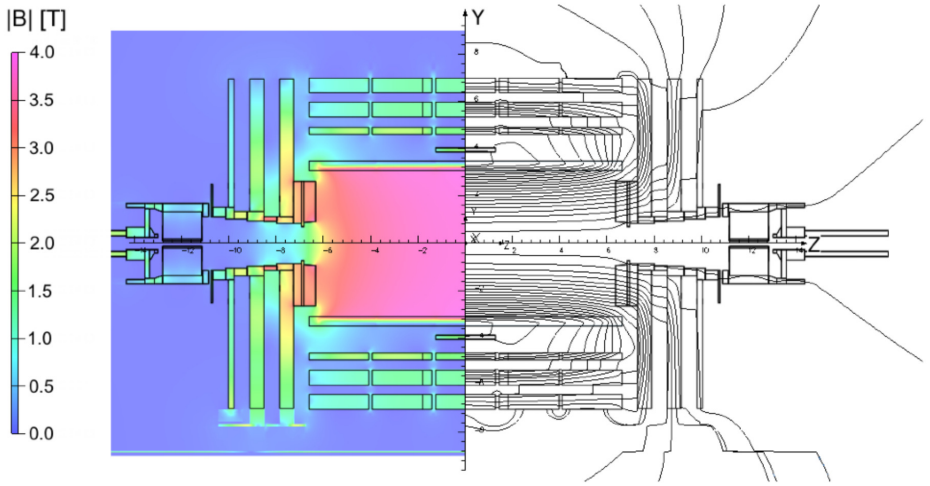

FIGURE 2.7: Map of the magnetic field (left) and field lines (right) predicted for a longitudinal section of the CMS detector by a magnetic field model at a central magnetic flux density of 3.8 T. Each field line represents a magnetic flux increment of 6 Wb [12].

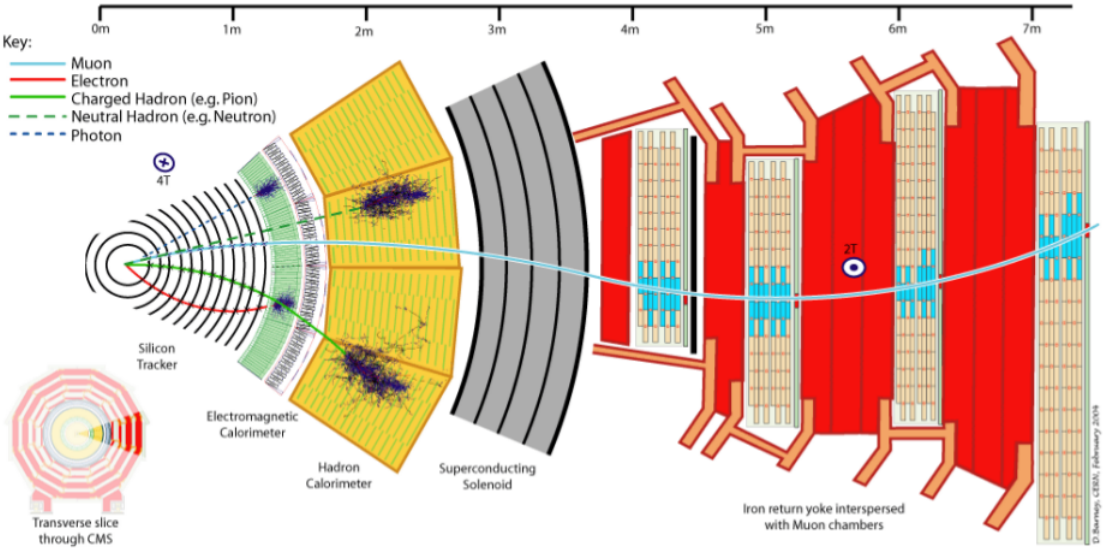

FIGURE 2.8: Schematic view of a slice of the CMS experiment showing the interaction of particles in the different detection layers.

2.3.2 Muon Spectrometer

The muon spectrometer [13] of the CMS experiment plays a crucial role since the reconstruction of muons is a powerful tool to identify interesting physics processes. Its role is to provide identification, track reconstruction and trigger of muons with momenta from GeV to a few TeV. The system is located outside of the calorimeters and the magnet and covers an area of ~ 25000 m^2. To stay relatively inexpensive and suitable for all of the CMS requirements, it is based on three technologies of gaseous detectors: the Resistive Plate Chambers (RPC), the Cathode Strip Chambers (CSC) and the Drift Tubes (DT). Figure 2.9 shows a longitudinal cross-section of a quadrant of the current CMS experiment with the details of the muon system.
The structure of the muon spectrometer is divided into two CMS regions: the barrel and the endcaps. Let's now define two important terms: The *chambers* are the basic physical modules that are independently-operating units and the *stations* are the assembly of chambers around a fixed value of r in the barrel or z in the endcap.
The barrel is divided into five wheels along the z-axis. On each wheel there are four stations. The two technologies in the barrel are the DT (the chambers 'MB' in yellow on the figure) and the RPC (the chambers 'RB' in blue on the figure).
In each endcap there are four muon stations, the two technologies are the CSC (the chambers 'ME' in green on the figure) and also the RPC (the chambers 'RE' in blue on the figure).
The stations in the endcap are labelled ME1/n-ME4/n (or RE1/n-RE3/n), where n is an integer that increases with the radial distance from the beam line.

We will now review shortly the three different technologies present in the actual muon spectrometer.

2.3.2.1 Drift Tubes

The Drift Tubes are the principal detection technology of the CMS barrel. With a total of 250 chambers (and about 200000 channels), the DTs cover the detection region up to $|\eta| = 1.2$. As shown in Figure 2.10, the 250 chambers are distributed on the five wheels of the barrel in four concentric layers that contain 60 chambers in the three first layers and 70 in the outer layer.

Figure 2.11 shows the geometry of a CMS DT detection cell and its electric field lines. The rectangular drift cell has a width of 42 mm and a height of 13 mm with at the center an anode wire of 50 μm.

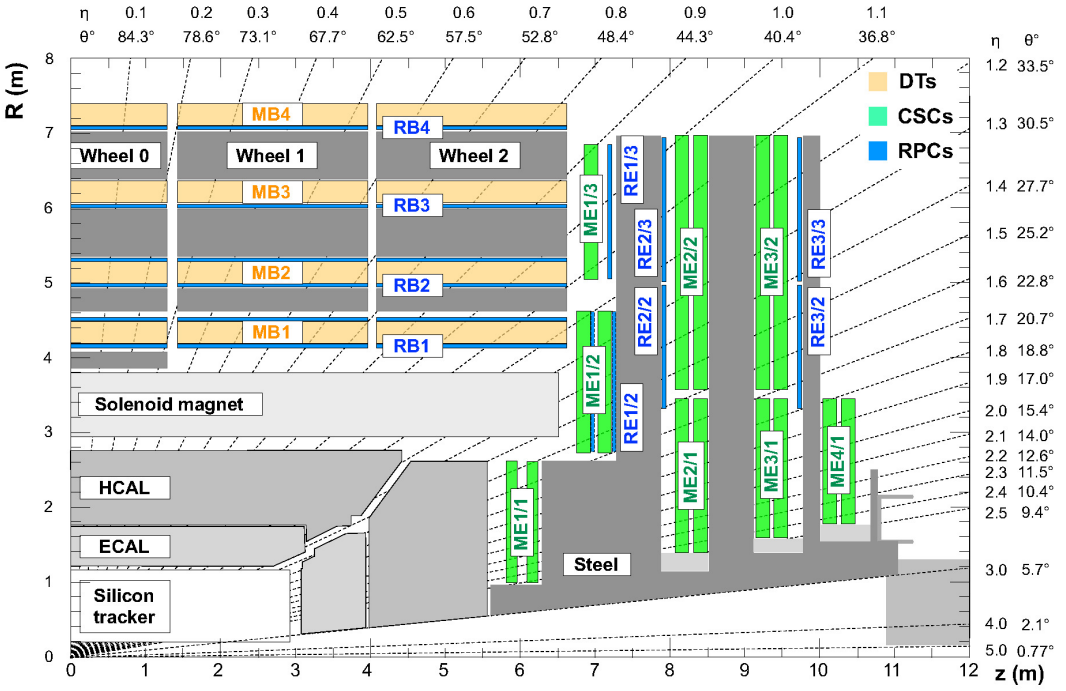

FIGURE 2.9: CMS longitudinal cross-section showing the current muon spectrometer. The Z-axis corresponds to the beam line, R correspond to the radius and the origin is the interaction point.

A CMS DT chamber is made of two super-layers (SL) of DT cells, which are made of four staggered layers of parallel cells. The major advantage of the cell structure is to protect the chambers against damage from a broken wire.

The DT chambers measure the muon coordinate in the r-ϕ plane and provides a measurement in the z direction.

The DTs are filled with a gas mixture of Ar/CO_2 (85:15) that provides a drift time of 380 ns for 21 mm and are operated at a gas gain of 10^5.

The spatial resolution of the combined layers of DTs is of the order of 100 μm, the reconstruction efficiency is higher than 95% and the time resolution is of the order of few nanoseconds.

The long drift time of the charges inside the chamber constitutes one of the main limitations of the DT technology. Indeed, the DT cannot operate at particle rates higher than several tens of Hz. In addition, in order to keep the homogeneous drift velocity, the DT have to operate in a uniform and low magnetic field. Due to those two limitations, the DTs cannot be used in the CMS endcaps where the magnetic field can go up to 3.1 T and the particle flux is between $10^2 - 10^3$ Hz/cm^2.

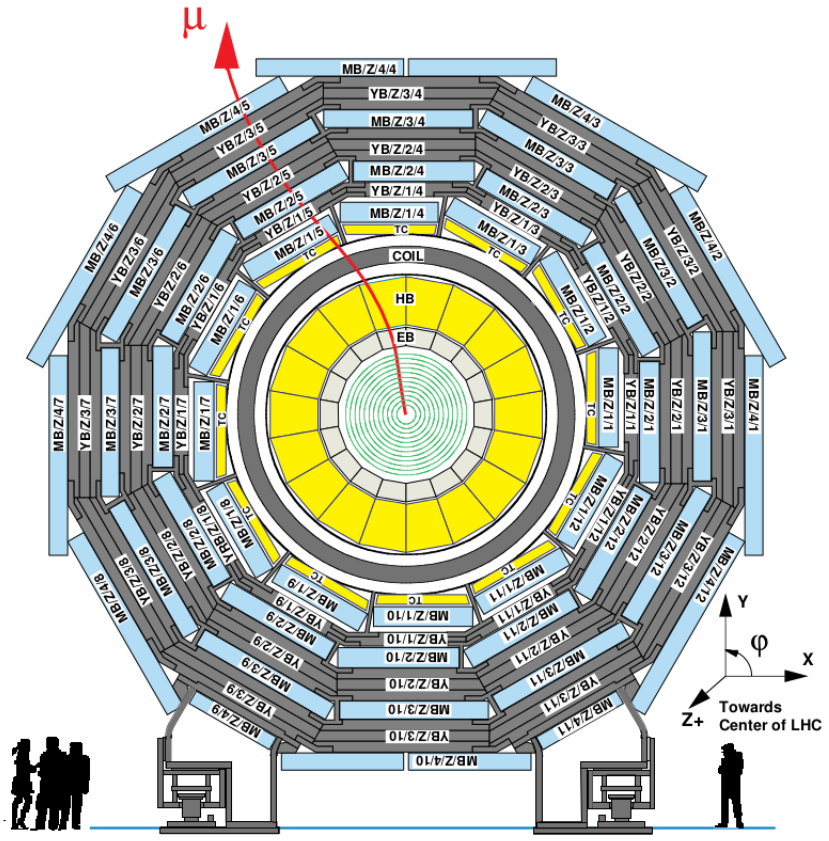

FIGURE 2.10: Transversal view of one of the five wheels of CMS [13].

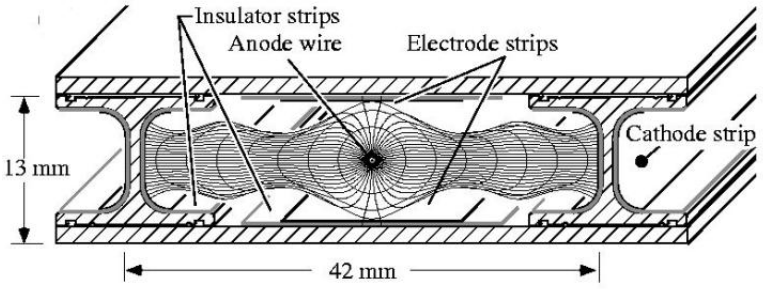

FIGURE 2.11: Schematic view of a CMS Drift Tube detection cell showing the geometry and dimension of the chamber and the electric field lines.

2.3.2.2 Cathode Strip Chamber

In the endcaps of the muon system, the Cathode Strip Chambers have the same function as the DTs. There are four stations of CSC per endcap with a total of 540 chambers that covers the pseudo-rapidity range $0.9 < |\eta| < 2.4$.
As shown on Figure 2.12, the CSC is a a multi-wire proportional chamber in which the cathode plane is segmented into strips perpendicular to the wire direction. The CMS CSC are six-plane trapezoidal chambers (of 10° in ϕ for station ME1 and 20° in ϕ for the three other stations) with a maximum length of 3.4 m and a maximum width of 1.5 m. The position of the strips in CMS is radial.

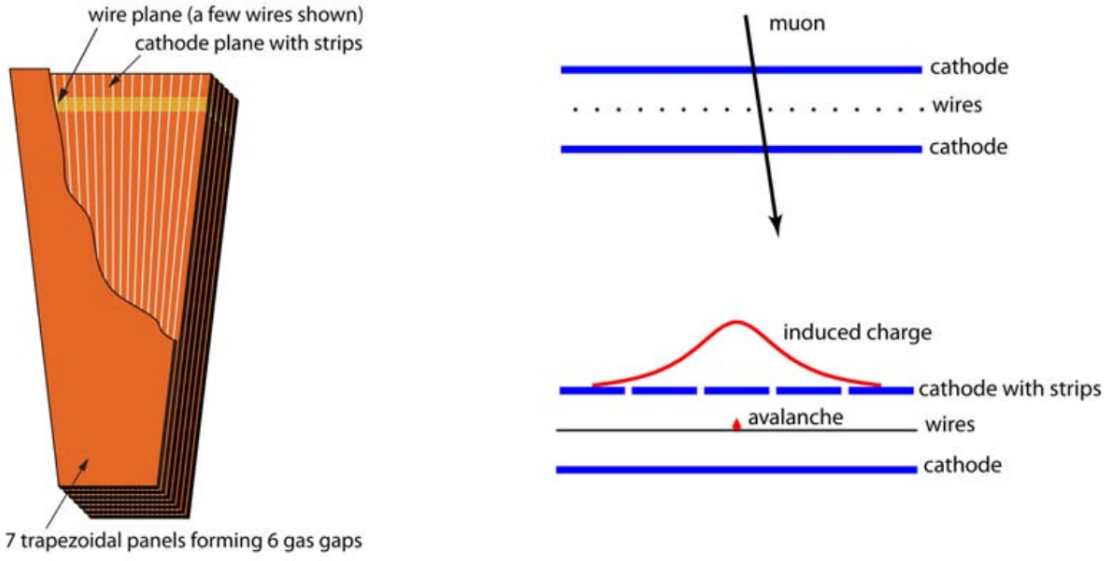

FIGURE 2.12: Schematic view of the trapezoidal shaped CMS Cathode Strip Chamber (left); Schematic representation of the induced charge on the wires and the cathode strips (right).

The CSCs are filled with a gas mixture of $Ar/CO_2/CF_4$ (40:50:10) and are operated at a gas gain of 7×10^4. The signal induced by a muon crossing the detector is read by both the wires and the cathode strips. The combination of those two signals gives a typical space resolution better than 75 μm in r-ϕ for the ME1/1 and ME1/2 chambers and better than 150 μm for the others that were the requirements of the Muon Technical Design Report (TDR) [13]. The time resolution of the CSC is 6 ns.

2.3.2.3 Resistive Plate Chamber

The Resistive Plate Chambers (RPC) are present in both the barrel and the endcaps to ensure the redundancy in the CMS muon spectrometer. In the six stations of the

barrel, there are 360 RPC chambers and in the four stations of each endcap there are 252 chambers. The RPC system covers the pseudo-rapidity range up to $|\eta| = 1.6$.
The RPC is a gaseous detector made of two parallel plates separated by a gas volume of 2 mm and covered with a 2 mm resistive Bakelite plate, as shown on Figure 2.13.

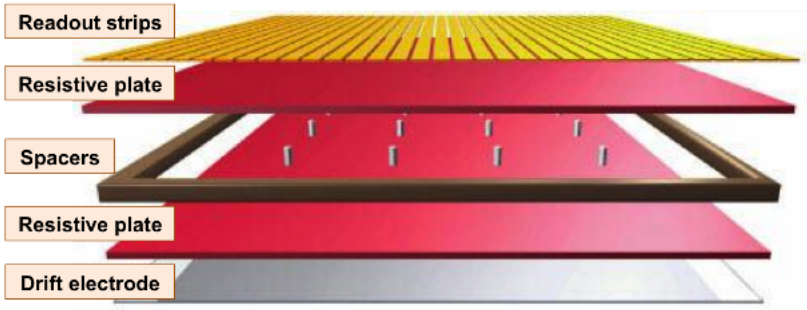

FIGURE 2.13: Schematic view of a RPC chamber.

In CMS, the RPCs are operated with a $C_2H_2F_4$/i-C_4H_{10} (95:5) gas mixture in avalanche mode. To increase the output signal, the CMS RPCs have a double gap structure with a common readout plane, as shown in Figure 2.14.

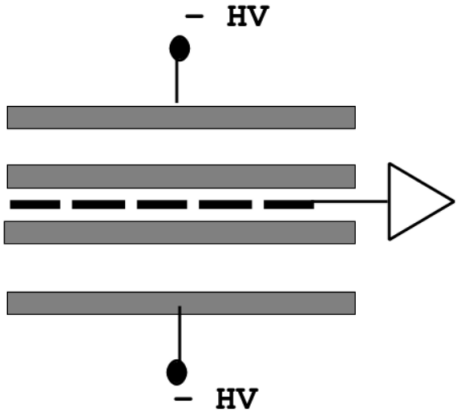

FIGURE 2.14: Layout of a double gap RPC chamber with a common readout plane.

The RPCs are particularly suitable for the BX identification and the first level triggering since they are very fast detectors and they have a time resolution of the order of 1 ns. Despite a poor spatial resolution (of the order of one centimeter), the RPC can resolve tracking ambiguities by combining their hits with the data from the DTs and the CSCs. The main limitation of the RPCs is their rate capability. Indeed, the high resistivity of the Bakelite induces charging up effects and excessive current that bring the rate capability down to below 1 kHz/cm^2. For that reason, the endcap RPCs system only covers the detection region up to $|\eta| = 1.6$, leaving the forward region ($1.6 < |\eta| < 2.4$) only equipped with CSC detectors.

2.3.3 Trigger System

The nominal bunch crossing rate of the LHC is 40 MHz which means a collision every 25 ns. When a collision occurs in CMS, the average event size is 1 MB [14]. For this reason, it is impossible to store and to reconstruct the full amount of data produced at this rate. To solve this, a trigger system selects events of interest and reduces the output rate. As shown on Figure 2.15, the CMS trigger system has a two level design.

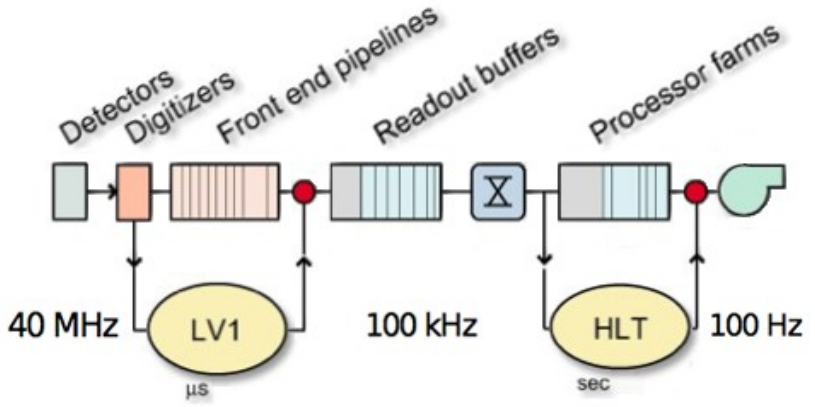

FIGURE 2.15: Structure of the trigger system of the CMS experiment.

- *Level 1* (L1): The goal of the L1 trigger is to reduce the 40 MHz rate to a maximum of 100 kHz. The selection is done at the level of the detectors by the electronics. The L1 trigger decision must be done in less than 3.2 μs that corresponds to 128 bunch crossings. As shown in Figure 2.16, the L1 combines the preliminary reconstruction from the calorimeters and from the muon system. In the L1 trigger, the tracker information is not included because it contains too many channels that would slow down the triggering process.

  When an event is accepted by the L1 trigger, the data of all the subsystems of CMS are then sent to the next trigger level.

- *High Level Trigger* (HLT): The HLT receives the data from all CMS sub-detectors with the full granularity and resolution and selects interesting physics candidates. It runs on a large processor farm and reduces the input rate from the incoming L1 at 100 kHz to several hundreds of Hz. This selection takes a few milliseconds.

After the reduction of the two trigger levels, the events are sent to the Storage Manager that stores the data on disk.

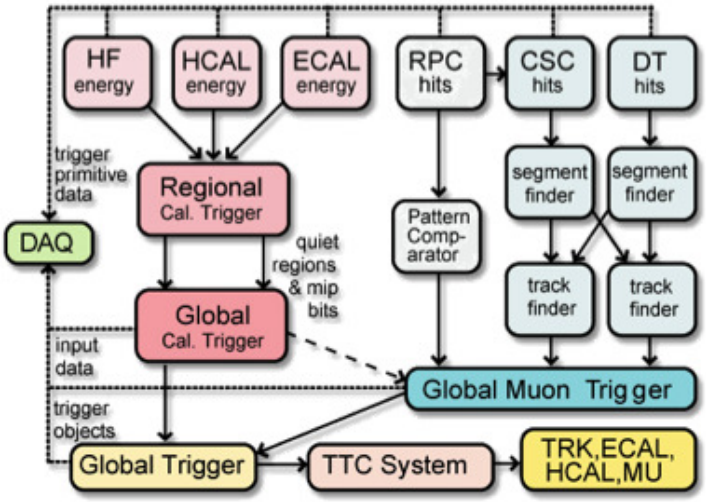

FIGURE 2.16: Overview of the current architecture of the L1 trigger system [11].

2.3.4 CMS Upgrades

Like the LHC (see Figure 2.5), the CMS experiment requires a series of upgrades in order to maintain the best performances possible for the detectors, like the efficiency and the resolution, while both the center-of-mass energy and the luminosity of the accelerator increase. The upgrade of the detector takes place during the different technical stops and Long Shutdowns of the LHC.
A first set of upgrades was planed for the Phase I and has been already completed during LS1 or will be finalized during LS2. A second set of upgrades is also planned for the Phase II of the LHC. The major Phase I upgrades [15] of the different parts of the CMS experiment are the following:

- *Tracker system*: The actual pixel detector will be replaced during LS2 in order to keep the maximum tracking efficiency at high luminosity. Indeed, the actual pixel detector was designed to operate at a maximum luminosity of 10^{34} cm^{-2} s^{-1}. The front-end electronics of this detector will also be replaced.

- *Calorimeters*: The principal upgrade of the calorimeter system is the replacement of the HCAL photo-detectors by silicon photo-multipliers that provide a better efficiency and have a better immunity to magnetic fields than the previous photo-detectors.

- *Muon system*: The main changes to the muon system are the addition of a fourth layer of CSC chambers and the extension of the RPC system. During LS1, The new CSCs have been installed at the ME4/2 station and the RPC system has been extended to cover the detection region up to $|\eta| = 1.6$.

Another major Phase I upgrade of the muon system is the introduction of GEM-based detectors. This upgrade will take place during LS2 with the installation of 2×36 GEM super-chambers in the forward end-caps of the muon system in the detection region $1.6 < |\eta| < 2.2$, as shown in Figure 2.17. The motivation for this upgrade called GE1/1 will be discussed in the next section.

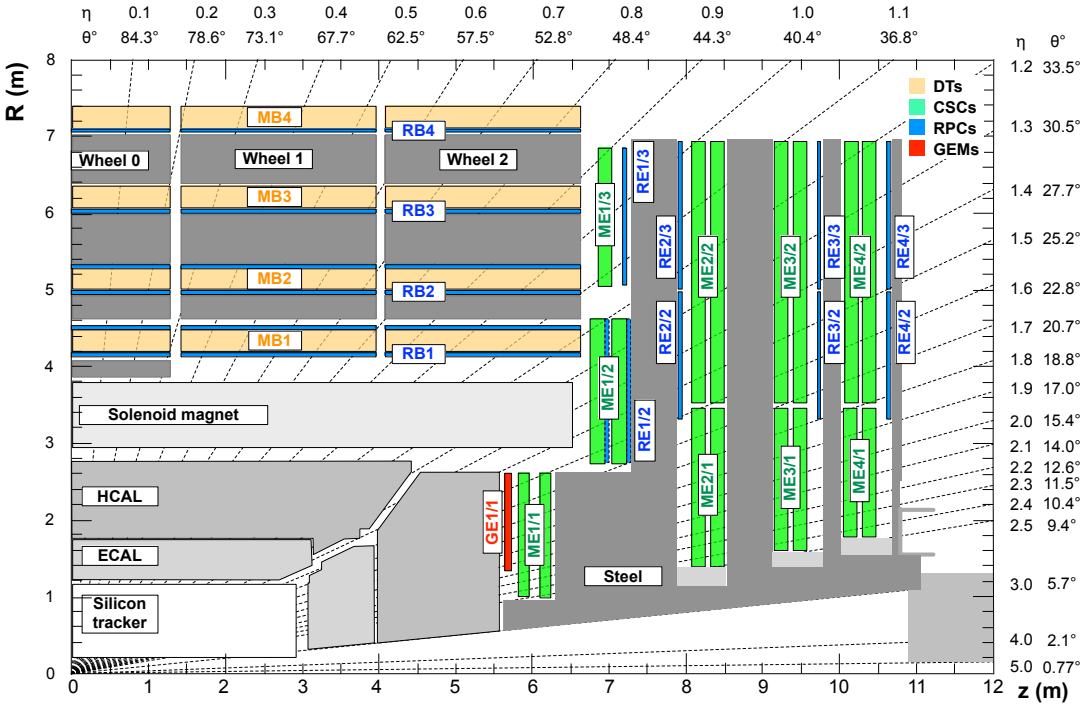

FIGURE 2.17: CMS longitudinal cross-section location with location in red of the proposed GE1/1 detector within the CMS muon system.

2.3.4.1 The CMS Muon Endcap GEM Upgrade

One of the major upgrades of the CMS muon spectrometer is the addition of a new layer of detection in the high η region. We will discuss the physics motivations of the project in this section. The characterization and performances of the Triple-GEM detectors will be presented in detail in Chapter 3.

The CMS muon spectrometer was originally designed as a redundant system that employs three detection technologies. However due to concerns about their capability to handle the high background particle rates, the RPCs, that provide redundant trigger and coarse position measurement in both barrel and endcap regions, were not implemented beyond $|\eta| > 1.6$. Nevertheless, after the LS2 shutdown, the CMS muon system must be able to sustain a physics program that maintains sensitivity for electroweak scale physics and for TeV scale searches similar to what was achieved before LS1.

The studies of the muon trigger for the Phase I upgrade [16] have shown that the L1 trigger reaches an acceptable rate for muons with a transverse momentum $P_T > 25$ GeV/c. This is no more the case after LS2 with the increase of the LHC luminosity to 2×10^{34} cm^{-2} s^{-1}. The introduction of the GEM-technology provides additional precise hits, with a good time resolution, that help to refine the stub reconstruction and improve the momentum resolution.
The improvements in the single muon trigger rate curves with the GE1/1 upgrade are shown in Figure 2.18.

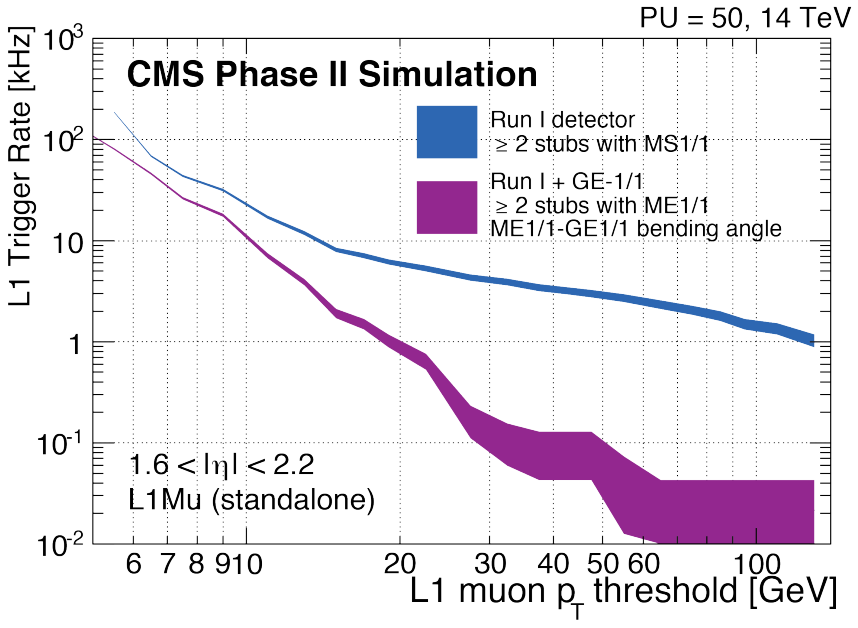

FIGURE 2.18: Level 1 muon trigger rates before and after the GE1/1 upgrade at $L = 2 \times 10^{34}$ cm^{-2} s^{-1} for constant efficiency of 94% [17].

By maintaining a low muon trigger P_T thresholds, the efficiency to measure interesting physics processes featuring soft leptons can be kept high.
As an example, let us consider the following Higgs boson decay channel: $H \to \tau^+\tau^-$. Among the various decay channels, the semileptonic $\tau\tau \to \mu\tau_h + X$ channel (where τ_h represent the hadronic decay of a τ and X is the missing transverse energy -MET-) is really important due to its relatively large branching fraction and its clean signal. These events can be triggered efficiently if the muon trigger P_T thresholds is maintained sufficiently low. As shown in Figure 2.19, simulation studies show an increase in the kinematic acceptance for $H \to \tau^+\tau^-$ signal events in this channel by as much as 35% if the muon P_T threshold is lowered from 25 to 20 GeV/c.

One of the major upgrade in view of the Phase II of the LHC, that will occur during LS3, is the deployment of the tracking trigger. This addition of the tracker in the trigger

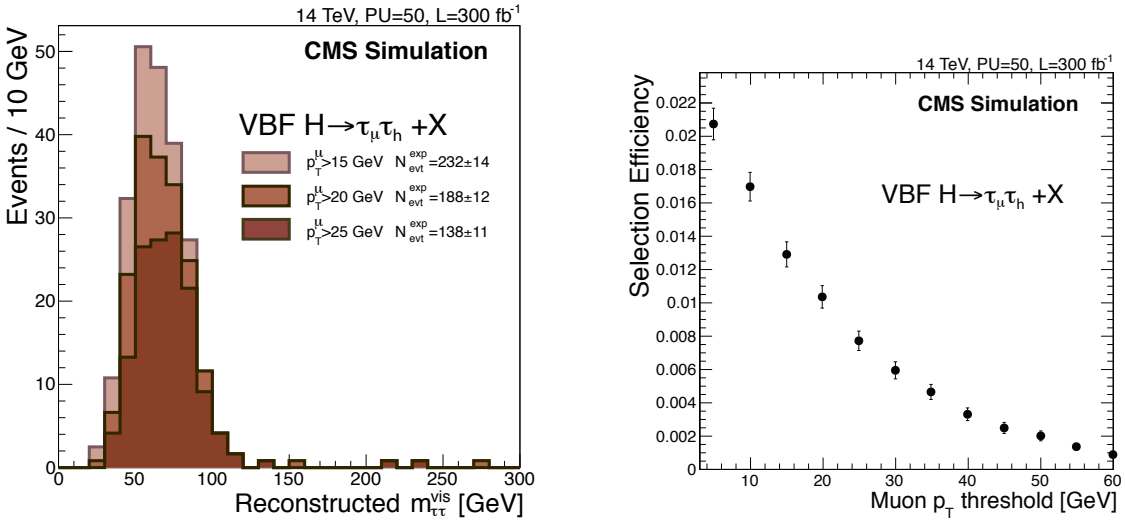

FIGURE 2.19: Distribution of the visible mass of the μ, τ_h, MET system for the selected events of the $H \to \tau\tau$ analysis with the $\mu\tau_h$ final state (left); Full $H \to \tau\tau$ analysis selection efficiency for same analysis as a function of the chosen offline muon P_T threshold (right) [17].

system of CMS will allow to match standalone muon candidates with the Tracker tracks and thus obtain an ultra-high purity and low-rate trigger targeting prompt muons. Those combined trigger objects of the track-trigger tracks and L1 standalone muon candidates (L1Mu) are referred to as L1TkMu.

Nevertheless, preserving the standalone muon triggering capabilities will continue to be a key factor for the HL-LHC. One particularly critical aspect of the standalone muon triggering is to preserve the sensitivity to scenarios of new physics predicting displaced muons.

To illustrate this, let us consider the following scenario in the context of a SUSY with hidden sectors:

$$H \to 2n_1 \to 2n_d 2\gamma_d,$$

where a SM-like Higgs boson H with mass of 125 GeV/c^2 decays into pairs of neutralinos n_1, which then decay into a stable dark sector neutralino n_d and a dark photon γ_d of mass m(γ_d) = 0.4 GeV/c^2. The light γ_d decays into a pair of collimated muons. The muons produced by the decay pointing back to the beamspot but are produced away from the beamline. Figure 2.20 shows the comparison between the performance of the L1TrkMu and the standalone muon trigger L1Mu algorithms in reconstructing at least one of the two muons with no P_T thresholds required as a function of the transverse displacement of the decay vertex from the beamspot (L$_{xy}$).

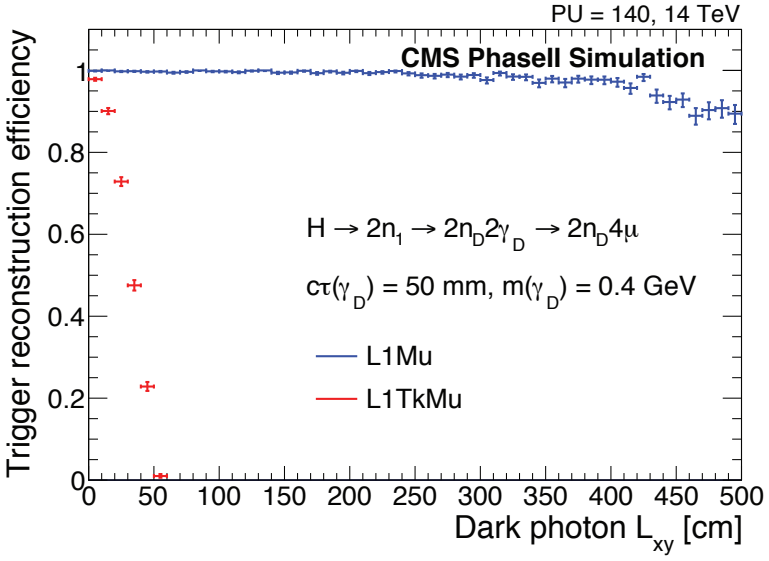

FIGURE 2.20: Comparison of the probability of reconstructing at least one muon candidate produced in the decay of a light long-lived light particle decaying to a pair of muons $\gamma_d \rightarrow \mu\mu$ as a function of the transverse displacement of the decay vertex from the beamspot (L_{xy}) for the standalone muon trigger L1Mu performance and the combined trigger objects of the track-trigger tracks and L1 standalone muon [17].

In view of the desired trigger and physics performances outlined, the set of minimum requirements on the detection performance for the upgrade of the CMS muon endcaps is shown on the table 2.2.

Properties	**CMS requirements**
Rate capability	> 10 kHz/cm^2
Single chamber efficiency (MIP)	> 97 %
Angular resolution	< 300 μrad
Single chamber time resolution	< 10 ns
Gain uniformity	< 15 %

TABLE 2.2: The minimum requirements for the upgrade of the CMS muon endcaps.

We will now briefly review the rationale for these requirements.

First, as shown in Figure 2.21, the expected hit rate within the GE1/1 acceptance is ~ 1 kHz/cm^2 at the highest η for HL-LHC running at 14 TeV and 5×10^{34} cm^{-2} s^{-1}. Taking a safety factor of ten implies a hit-rate cabability of at least 10 kHz/cm^2.

With an efficiency of 97.0% for an individual chamber, the super-chamber (that contains two chambers) will reach an efficiency above 99.9% when the signals from the two chambers are combined as a logical OR.

A precision of 300 μrad or better on the difference of the azimuthal muon positions measured in GE1/1 and ME1/1 will enable the trigger to discriminate high-P_T muons

from low-P_T muons reliably.

Both chambers making a super-chamber provide independent timing information that can also be combined with timing provided by the CSCs. This means that a time resolution of 10 ns or better for a single chamber is sufficient to reliably match GE1/1 hits to ME1/1 stubs in time when running with a 25 ns bunch crossing time at the LHC.

Finally, a uniform gain in the chamber ensure a uniform response that is necessary to ensure no geometrical trigger or reconstruction biases.

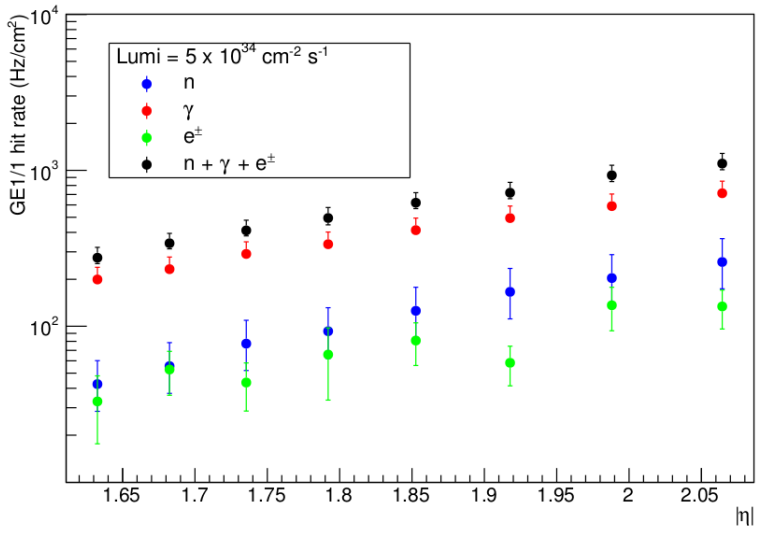

FIGURE 2.21: Hit rate of the simulated GE1/1 detector due to background particles as a function of $|\eta|$, in the harsh CMS environment corresponding to the instantaneous luminosity $\mathcal{L} = 5 \times 10^{34}$ cm^{-2} s^{-1}, typical of Phase II. The errors include statistical and systematic contributions [18].

Post LS2 Upgrades The GE1/1 upgrade is not the only proposed muon detector upgrade in the endcaps. During LS3, two new stations of GEM detectors are planed to be installed in GE2/1 and ME0. And finally, two stations of improved RPC (iRPC) detectors will be installed in RE3/1 and RE4/1. The locations of the new forward muon detectors are shown on Figure 2.22.

For GE2/1 the detectors and the electronics will be very similar that the ones that will be discussed in this thesis. However the iRPC and the detectors that will be used for ME0 may be very different. Therefore those additional upgrades will not be discussed further here.

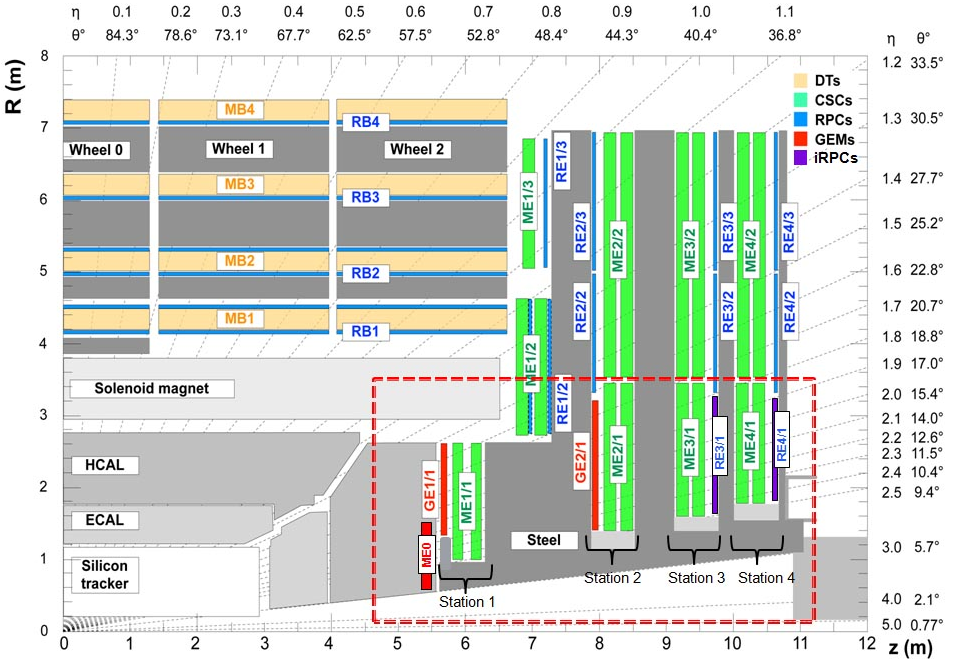

FIGURE 2.22: CMS longitudinal cross-section location with location in red of the proposed GE1/1, GE2/1 and ME0 detector and in dark blue of the improved RPC stations within the CMS muon system.

Chapter 3

Gaseous Detectors

Gaseous detectors made their appearance at the beginning of the twentieth century. At first they were mainly used for radiation detection. One of the most famous gaseous detectors is obviously the Geiger-Müller detector. The principle was invented by H. Geiger in 1913 and developed 15 years later in collaboration with W. Müller. At that time, ionization chambers and proportional chambers already existed. However, those detectors were not, or rarely, used in high energy physics. In general, the scintillator detector were the favored technology, and this is mainly due to its excellent time resolution. One has to wait for the end of the seventies and the invention of G. Charpak to see gaseous detectors playing a big role in high energy physics experiments. In 1968, G. Charpak developed his Multi-Wires Proportional Chamber (MWPC) for which he would later get the Nobel prize in 1992 for his invention. It is still on the same principle that work within the GEM detectors, introduced almost 30 years later.

In this chapter, we will discuss the physics principles that are involved to observe the passage of a charged particle through a gaseous detector. We will start by the general principle in section 3.1, then in section 3.2 and 3.3, we will see in details the ionization process and the motion of electrons and ions in the gas. To follow in section 3.4 and 3.5, we will discuss the amplification process and the choice of the gas mixture. At the end we will describe the signal formation in section 3.6. Finally in section 3.7, we will present different technologies of modern micro pattern gaseous detectors.
Most of this chapter is based on classic textbooks [8, 19, 20], other sources are specified throughout.

3.1 General Principle

To illustrate the general principle of a gaseous detector, we will briefly describe the operation of a Multi-Wire Proportional Chamber (MWPC). Such a detector is schematically shown in Figure 3.1.
A MWPC is made of wires outstretched between two parallel flat electrodes. Those two planes define the sensitive region filled with a gas mixture. Generally, the wires are connected to the ground by the electronics and the flat electrodes are at a negative tension. This geometry results in a uniform and constant electric field in the sensitive region, except in the proximity of the wires, as shown in Figure 3.1.

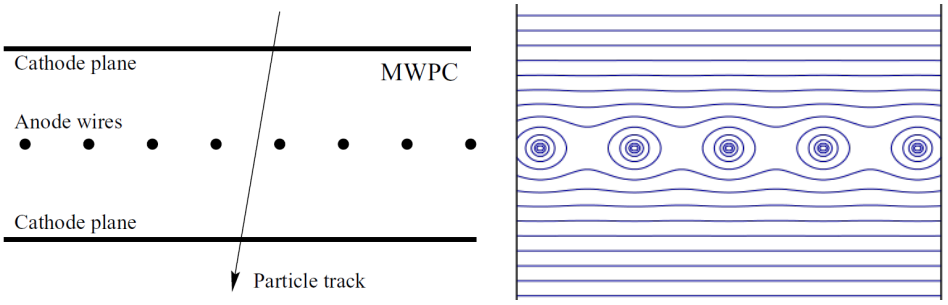

FIGURE 3.1: A schematic view of a MWPC (left) [21]; the equipotential line in a MWPC (right).

When a charged particle passes through the gas volume, it creates a primary ionization (see next section) along the track of the particle. The electric field will make the freed electrons drift to the anode wires and the ions to the cathode planes. After the amplification by avalanche around the wires, the motion of the charges will create an electric current on the electrodes. This current is the signal that will inform of the passage of a particle. This primary ionization is generally, for gaseous detector, too small to be directly detected by the electronics. In order to detect the particle, an amplification in the gas volume is thus necessary to increase the number of electrons drifting towards the electronics. This amplification process is called an avalanche (see section 3.4).

3.2 Ionization

3.2.1 Energy Loss

A relativistic charged particle going through a volume of gas, or more generally through matter, will interact with its constituents and by doing so the particle will loose some energy along its trajectory. The particle can interact in several ways. Depending on

its type, the particle can interact through weak interaction, strong interaction, or electromagnetic interaction. In the gaseous detector, the dominating interaction is the electromagnetic interaction.

There are several electromagnetic interactions possible, as the Cherenkov radiation, bremsstrahlung,... But the dominant one in our case is the Coulomb interaction. This interaction will excite and/or ionize gas molecules.

The energy loss by unit length of a relativistic charged particle is described by the Bethe-Bloch equation :

$$-\left\langle \frac{dE}{dx} \right\rangle = Kz^2 \frac{Z}{A} \frac{1}{\beta^2} \left[\frac{1}{2} \ln \frac{2m_e c^2 \beta^2 \gamma^2 T_{max}}{I^2} - \beta^2 - \frac{\delta(\beta\gamma)}{2} \right] \tag{3.1}$$

$$K = 4\pi N_a r_e^2 m_e c^2$$

where T_{max} is the maximum kinetic energy given to a free electron during a collision,z the charge of incident particle, m_e the electron mass, β is the velocity of the particle divided by the speed of light ($\beta = v/c$), γ is the Lorentz factor ($\gamma = (1-\beta)^{-1/2}$), I is the mean excitation energy, A and Z are respectively the mass number and the atomic number of the material, N_a the Avogadro number and r_e the classical radius of the electron defined as $r_e \equiv e^2/\pi\epsilon_0 m_e c^2$ (e is the electron's charge and ϵ_0 is the vacuum permettivity).

The Bethe-Bloch function is shown in Figure 3.2 for different materials. We can see that the energy loss does not depend on the mass of the particle, but only on the speed and charge of the particle.

At low energy ($\beta < 1.0$) we can observe a quick decrease in the energy loss when β increases, this is due to the term in $1/\beta^2$. The decrease continues until it reaches a minimum at $3 \leqslant \beta\gamma \leqslant 4$.
At relativistic energies ($\beta \simeq 1$, $\gamma \gg 1$), the energy loss, dominated by the term in $\ln\gamma$, increases logarithmically; this is the relativistic rise. This rise will continue until a constant value called the Fermi plateau.
The slowdown of the relativistic rise is due to the term $\delta(\beta\gamma)$ (called Fermi's density correction). This effect appears when the particle has an ultra-relativistic velocity. Indeed, at those velocities a temporary polarization of the atoms of the medium will create a screening of the electric field along the trajectory and will lower the interaction rate between those atoms and the incident particle.

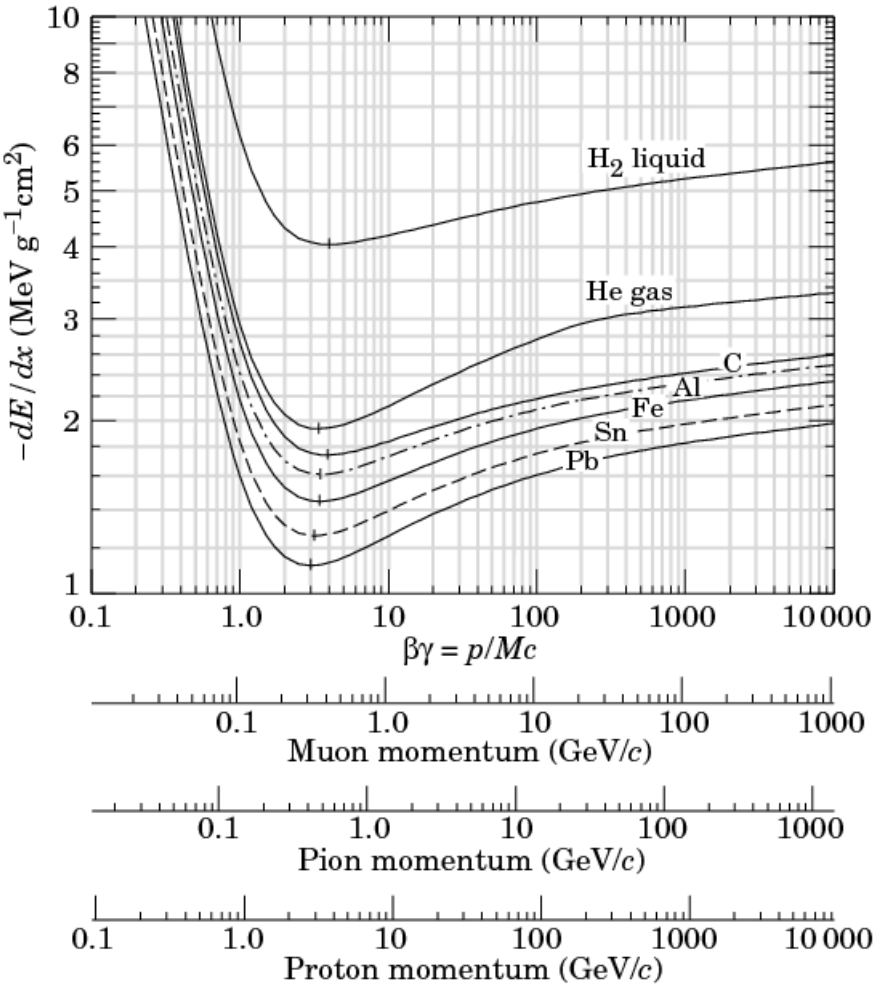

FIGURE 3.2: Average energy loss per unit length as a function of the momentum of various particles in liquid hydrogen, helium gas, carbon, aluminum, iron, tin and lead.

3.2.2 Primary and Total Ionization

The incoming particle will, as we will see, create electrons and ions pairs all along the trajectory by electromagnetic interaction. This mechanism is called primary ionization. If the resulting released electrons have an energy larger than the ionization potential of the medium, they will also ionize other molecules of the gas. This is called secondary ionization. The sum of both primary and secondary ionizations is called total ionization.

In fact, only a fraction of the energy lost by the incident particle is used for the ionization. If we define W the mean energy loss needed to create a ion-electron pair, we can write a relation giving the average total number of produced pairs along the trajectory $\langle N \rangle$:

$$W \langle N \rangle = L \left\langle \frac{dE}{dx} \right\rangle \tag{3.2}$$

Where L is the trajectory length. The energy needed to create a pair depends on the gas mixture and is experimentally determined.
Starting from this relationship, we can easily express the average number of pairs created per unit length (n_T):

$$n_T = \frac{\langle dE/dx \rangle}{W}$$

In most of the gaseous detectors, we use a gas mixture. In this case, the total number of electrons is obtained by summing the mean number of produced electrons in every gas of the mixture, weighted by the gas percentage P_i in the mixture :

$$n_T = \sum_{i=1}^{n} \left\langle \frac{dE}{dx} \right\rangle_i \frac{P_i}{W_i} \tag{3.3}$$

where the index i represents a gas among n. Note that in the case of gas mixtures, n_T is typically underestimated. Indeed in a compound the elements are not independent and the de-excitation of an atom can lead to a delayed ionization of an other atom. The values of W_i , dE/dx and n_T for different gases are shown in the table 3.1, those values are the mean values obtained experimentally.

	W_i (eV)	dE/dx (MeV/g cm^2)	n_T (e^-/cm)
He	41	1.94	7.8
Ne	36	1.68	39
Ar	26	1.47	94
Kr	24	1.32	192
Xe	22	1.23	307
CO_2	33	1.62	91
CH_4	28	2.21	53
C_4H_{10}	23	1.86	195

TABLE 3.1: Values of W_i, dE/dx and n_T for different gases [22].

3.2.3 Collisions

When a charged particle crosses a gas volume it collides with a large number of gas molecules, but only a few of these collisions actually produce ionization. The probability distribution that will follow this ionization will therefore be a Poisson distribution.
If we have a mean value of n primary electrons over a certain distance, the probability to create k primary electrons is given by:

$$P(k) = \frac{n^k}{k!} e^{-n}$$

With this expression, we can compute the probability that the incident particle does not ionize the gas, i.e. the particle can not be detected. Therefore, the minimum inefficiency of a perfect detector is given by :

$$P(k = 0) = e^{-n}$$

i.e. the probability that there are no primary ionization when passing through the gas volume.
With this expression, we can compute the minimum inefficiency for a real case. The distribution shown in Figure 3.3 gives the number of clusters of electrons produced by a 15 GeV muon in 3 mm of Ar/CO_2 (70:30). The mean value of this distribution gives

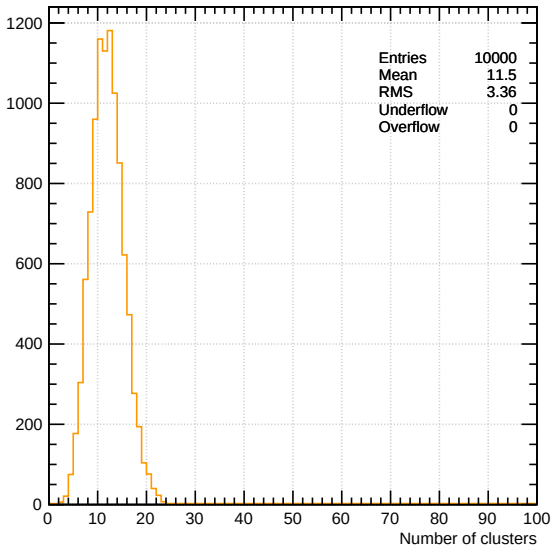

FIGURE 3.3: Distribution of the number of clusters of electrons produced by a 15 GeV muon in 3 mm of Ar/CO_2 (70:30) produced by GARFIELD.

the number of collisions leading to ionization. The minimum inefficiency is equal to :

$$P(k = 0) = e^{-11.5} \simeq 0.001\%$$

Another way to describe the ionization in a gaseous detector is to define the probability distribution of the number of electrons released directly or indirectly with each primary encounter. This distribution is called the ionization cluster-size distribution. It has been carefully studied experimentally and the results are described elsewhere [23]. Figure 3.4 shows the ionization cluster-size distribution for argon. The last bin of this distribution is the probability to have twenty or more electrons in one cluster.

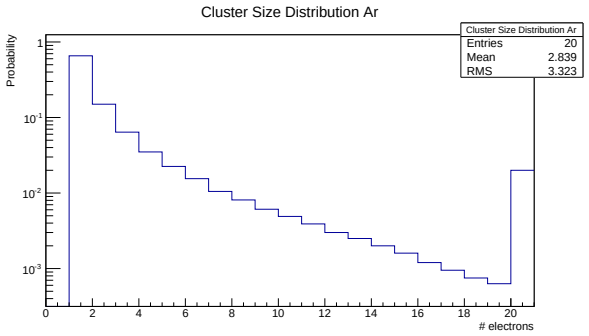

FIGURE 3.4: Ionization cluster-size distribution for argon.

3.2.4 Multiple Scattering

In addition to the inelastic collisions with atomic electrons, charged particles traversing the medium will also go through elastic Coulomb interactions with nuclei. After a number of successive small deviations, the particle will emerge at an angle θ compared to the initial direction of the particle. The distribution of the scattering angle projected in a plane parallel to the direction of the incident particle is a Gaussian with a standard deviation given by :

$$\theta_0 = \frac{13.6MeV}{\beta cp} z \sqrt{\frac{x}{X_0}} \left[1 + 0.038 \ln \left(\frac{x}{X_0} \right) \right]$$

where β, p and z are respectively the speed, momentum and charge of the incident particle while x and X_0 are respectively the thickness and the radiation length of the material. The radiation length is the characteristic thickness of matter traversed for an electron to loose all but $1/e$ of its energy by bremsstrahlung or a high-energy photon by e^+e^- pair production.

3.3 Electron and Ion Drift Velocity in Gas

The performance of a gaseous detector depends on the drift and diffusion of electrons and ions in the gas. The drift velocity determines the time of collection of ionization and therefore the speed of the detector response. Diffusion is responsible for the widening of the distribution of the charge in the gas, which affects the determination of the position of the incident particle. Before discussing the choice of the gas mixture and its influences on the performance of the detector, we will introduce some theoretical principles.

3.3.1 Gas Kinetics without External Fields

In a gas, in the absence of external field, the dynamics of the gas molecules and the ions and free electrons in the gas in equilibrium is described by gas kinetics.
This theory states that the gas particles are subjected to thermal agitation. This agitation provides a certain kinetic energy. The distribution of kinetic energy in a gas is given by the Maxwell distribution [24] :

$$P(E)dE = N\frac{2}{\sqrt{\pi}\left(k_B T\right)^{3/2}}\sqrt{E}\exp\left(-\frac{E}{k_B T}\right)dE$$

where T is the absolute temperature, N the number of molecules in the gas, and k_B the Boltzmann constant. From this distribution, the velocity distribution can be easily computed :

$$P(v)dv = N\left(\frac{2}{\pi}\right)^{1/2}\left(\frac{m}{k_B T}\right)^{3/2}v^2\exp\left(-\frac{mv^2}{2k_B T}\right)dv$$

The average energy of a gas molecule under normal conditions depends only on the temperature and is 3/2 $k_B T$ (0.04 eV) at 293 K. This energy corresponds to an average speed :

$$v = \sqrt{\frac{3k_B T}{m}} \tag{3.4}$$

where m is the particle mass.
As a consequence the electrons move much more rapidly than the ions. According to Eq. 3.4, the speed of electrons and ions is 10 cm/μs and 10^{-2} cm/μs respectively.

Thus, in the absence of any other effect, a charge distribution, initially located at a point, diffuses over time by multiple collisions and following a Gaussian:

$$\frac{dN}{N} = \frac{1}{\sqrt{4\pi Dt}}\exp\left(-\frac{x^2}{4Dt}\right)dx$$

where dN/N is the fraction of charge at a distance between x and $x+dx$ from the initial point at time t; D is the diffusion coefficient. The diffusion coefficient is proportional to the average velocity v, it decreases with the mass of the particles.
For a one-dimensional distribution, the standard deviation is given by:

$$\sigma_x = \sqrt{2Dt} \tag{3.5}$$

It is easy to generalize this expression to the case of diffusion in a volume. In this case the standard deviation is given by :

$$\sigma = \sqrt{6Dt}$$

3.3.2 Drift and Diffusion in the Presence of External Fields: Macroscopic Model

When a uniform electric field is applied, the electrons and the ions will be accelerated along the field lines. This acceleration is interrupted by collisions with the gas molecules that quickly limit the maximum velocity of the electrons and ions.

The motion of a charged particle (electron or ion) in a gas under the effect of an electric field $\vec{E}$ and a magnetic field $\vec{B}$, can be described by the equation of motion with friction [25], the friction being caused here by the collisions between the particle and the gas molecules. It is then possible to define the drift velocity ($\vec{v}_d$) as the average speed of all the charged particles. After a sufficiently long time, the friction force that increases with the drift velocity will compensate the electromagnetic force, resulting in a constant drift velocity. In the absence of magnetic field, the drift velocity is then expressed as:

$$\vec{v}_d = \frac{q}{m}\tau\vec{E} \tag{3.6}$$

where q and m are respectively the charge and mass of the particle, $\vec{E}$ the electric field and τ the time of mean free path, i.e. the average time between two collisions.
By defining the mobility of a charge in a gas as $\mu \equiv (q/m)\tau$, the Eq. 3.6 can be written as :

$$\vec{v}_d = \mu\vec{E}$$

Thus the mobility describes the differences in velocity that exist for different types of particles in a same electric field. Mobility depends on the particle charge, mass, and the gas type in which it drifts (since τ depends on gas).
In the case of a mixture of n gas, ion mobility in this gas mixture is given by the Blanc's law [26] :

$$\frac{1}{\mu} = \sum_{i=1}^{n} \frac{c_i}{\mu_i}$$

where c_i is the gas concentration i and μ_i the mobility of the ion in the pure gas.

Note also that if a magnetic field is applied parallel to the electric field, neither the drift velocity nor the direction of drift are affected by the presence of the magnetic field. This is not the case for diffusion, as we shall see later.

3.3.3 Drift and Diffusion in the Presence of External Fields: Microscopic Model

As we saw in section 3.3.1, when no external field is applied, a free electron (or ion) in the gas has a kinetic energy equal to $3/2k_BT$ and instant drift velocity randomly oriented. Under the effect of an electric field, the electrons and ions are accelerated along the field lines and their average kinetic energy increases:

$$\epsilon = \frac{1}{2}mv^2 = \epsilon_E + \frac{3}{2}k_BT$$

where ϵ_E is the mean energy gained due to the electric field. With field values typically used in gas detectors, above a few hundred V/cm, ϵ_E amounts to a few electron-volts. Therefore the contribution of thermal energy, $\sim 0.04\ eV$, can be neglected.

At each collision, the charged particle loses an average fraction $\lambda(\epsilon)$ of its energy ϵ_E. Therefore there is a balance between the energy received from the electric field and the energy lost by collision. This allows to express the drift velocity as follows :

$$\vec{v}_d = \frac{q\vec{E}}{mN\sigma(\epsilon)}\sqrt{\frac{\lambda(\epsilon)}{2}}$$

where $\sigma(\epsilon)$ is the collision cross section, and N the molecular density. $\sigma(\epsilon)$ and $\lambda(\epsilon)$ are functions of the kinetic energy ϵ or the characteristic energy $\epsilon_k \equiv \frac{2}{3}\epsilon$, we must observe their evolution with the electric field to understand the behavior of the drift velocity.
This is what is shown in Figure 3.5 and 3.6 respectively showing the characteristic energy as a function of the electric field and σ and λ as a function of the kinetic energy for argon and methane.

In pure argon, ϵ_k increases slowly from $\sim$ 3 to 10 eV for electric fields from 100 to 2000 V/cm. In this energy range, it is observed in Figure 3.6 that the cross section is close to the minimum and is equal to $10^{-15}cm^2$ and that the lost fraction of the energy is constant and very small, close to 10^{-5}. This small value is explained by the fact that in noble gases such as argon, below an excitation threshold of typically several electron volts, collisions can only be elastic. Therefore the drift velocity will be small.
On the other hand, in a poly-atomic gas, such as CO_2, methane, isobutane, etc., many

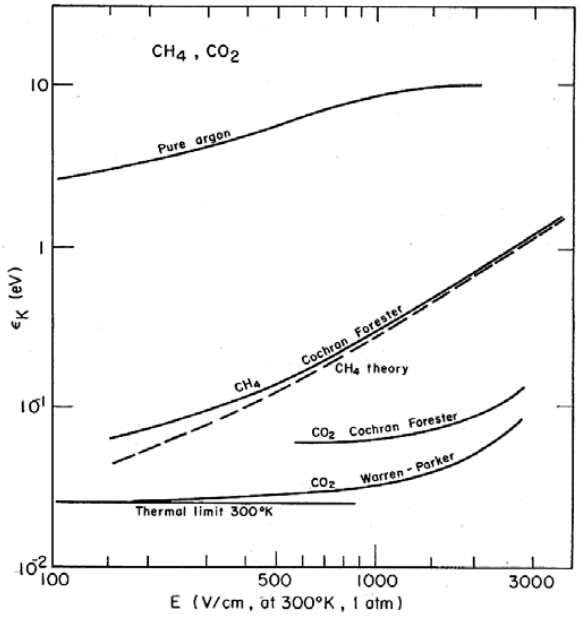

FIGURE 3.5: Characteristic energy ϵ_k function of the external field [27].

states of rotation and vibration can be excited in the collisions, which lowers the excitation threshold to a few tenths or hundredths of electron volts (0.03 eV for the CH_4 molecule). Thus the values of λ are much larger (see Figure 3.6 for CH_4) compared to argon. Therefore, adding even a small amount of poly-atomic gas (e.i. CO_2) to a noble gas changes drastically the drift velocity as shown in Figure 3.7. Regarding the diffusion, one can show that the standard deviation in the x direction (see Eq. 3.5) can be expressed in terms of the average energy of the particles ϵ, and their mobility μ :

$$\sigma_i^2 = 2\frac{2\epsilon\mu}{3q}t \tag{3.7}$$

where $\frac{2\epsilon\mu}{3q}$ can be identified to the diffusion coefficient D from Eq. 3.5. Note that the time during which the charges are drifting from a distance L is equal to $t = \frac{L}{\mu E}$, which allows writing Eq. 3.7 as :

$$\sigma_i = D'\sqrt{L} \tag{3.8}$$

where D' is the diffusion coefficient which is equal to :

$$D' = \sqrt{\frac{2D}{\mu E}} = \sqrt{\frac{4\epsilon}{3qE}} \tag{3.9}$$

Thus, the standard deviation of the charge distribution is proportional to the square root of the drift distance.

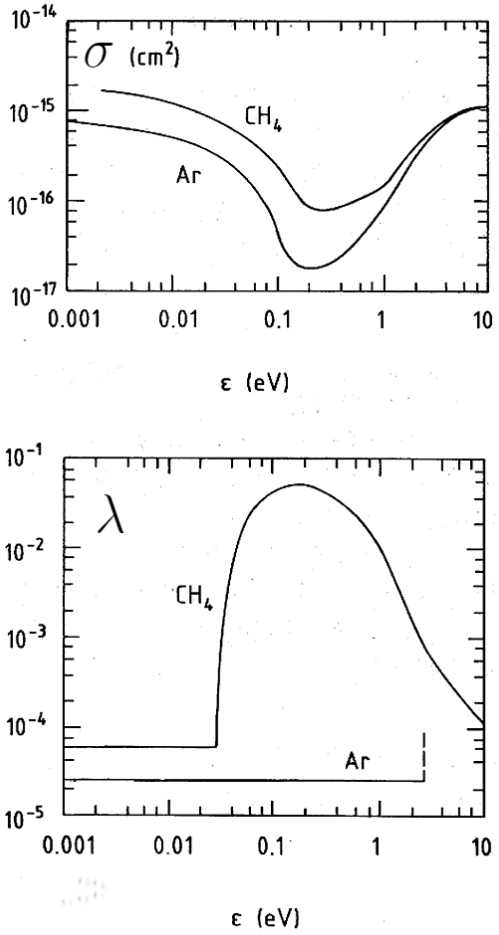

FIGURE 3.6: Cross section σ and fraction of the energy lost by collisions λ function of the kinetic energy for argon and methane.

When a magnetic field is applied, the electrons follow a helicoidal path in the direction of the magnetic field, while drifting in the direction of the electric field. One can show [24] that in this case the diffusion is reduced by a factor $\frac{1}{1+\omega^2\tau^2}$ where $\omega \equiv (qB)/m$ is the cyclotron frequency.
For example, the transverse diffusion decreases as the magnetic field increases for the Ar/CO_2 (70:30) gas mixture as can be seen in Figure 3.8.

3.4 Amplification

When an electron moves in the gas with enough energy, it may cause ionizing collisions (see section 3.2). Consequently, if the electric field exceeds a few kilovolts per centimeter, electrons can gain sufficient energy between collisions to produce excitation or ionization of the gas molecules, creating additional electron-ion pairs. The produced electrons will

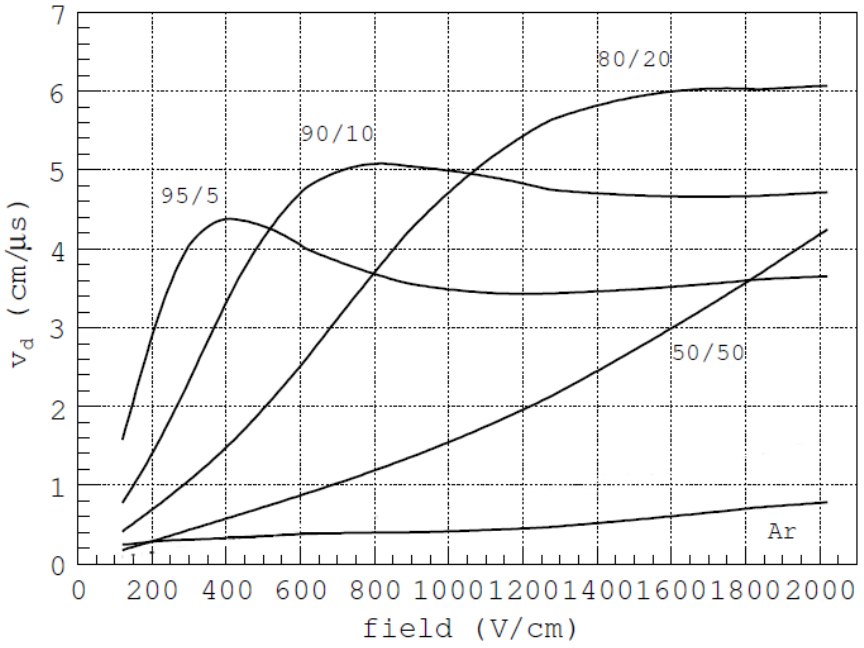

FIGURE 3.7: Electron drift velocity versus electric field for various Ar/CO_2 mixtures computed by simulation [24].

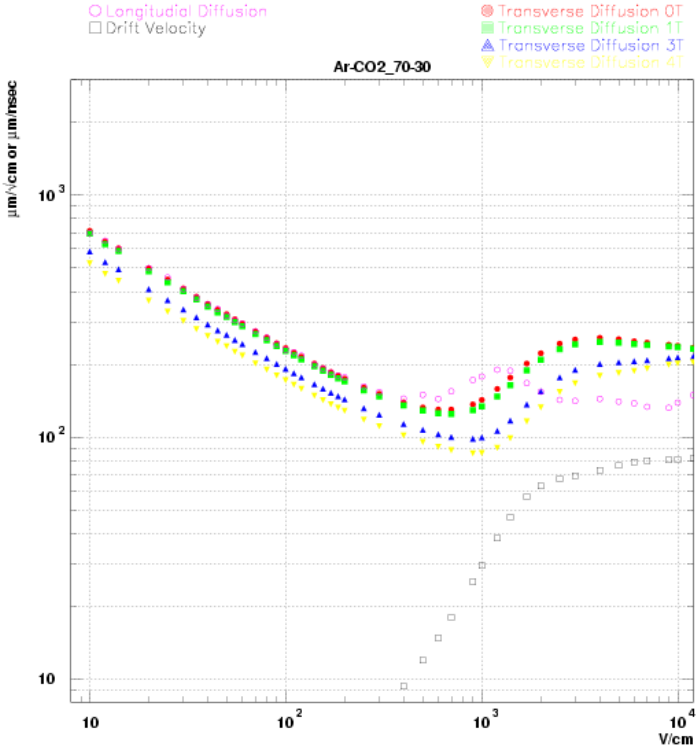

FIGURE 3.8: Longitudinal diffusion and drift velocity according to the electric field and transverse diffusion according to the electric field for different magnetic fields for Ar/CO_2 (70:30) gas mixture [28].

in turn be accelerated and therefore be able to further ionize the gas. This multiplication process is called the avalanche. We will now describe this process in a more formal way. We can define the free mean path of ionization of the electrons, i.e. the average distance an electron must travel before undergoing an ionizing collision with a gas molecule. This distance will depend on the effective ionization cross section $\sigma(\epsilon)$, which itself depends on the energy (ϵ) it takes to create a pair. The distance also depends on the density of the number of molecules in the gas (n). This leads to the following expression for the mean free path of ionization :

$$\lambda(\epsilon) = (n\sigma(\epsilon))^{-1}$$

The inverse of this distance represents the number of electron-ion pairs produced per unit length. This number is called the Townsend coefficient ($\alpha(\epsilon) = \frac{1}{\lambda(\epsilon)}$) [29].
Now that we have defined this coefficient, we must express the increase in the number of electrons in an avalanche.
In the case of a constant electric field, an electron will ionize a gas molecule after an average travel of α^{-1}, there is therefore, at that time, two electrons and one ion. The two electrons, after a mean path again equal to α^{-1}, will ionize two gas molecules (on average). And the process will repeat. On a distance dx we have an increased number of electrons equal to n times the coefficient of Townsend :

$$\frac{dn}{dx} = n\alpha$$

If we integrate this relationship, it gives us the number of electrons produced in an avalanche after a distance x :

$$n = n_0 e^{\alpha x}$$

where n_0 is the number of electrons at the start of the avalanche.
We can now define the gain as :

$$G(\Delta x) = \frac{n}{n_0} = e^{\alpha \Delta x} \tag{3.10}$$

which describes the multiplication factor of the avalanche.
The avalanche, which is a set of electrons and ions, will take the form of a drop, as shown in Figure 3.9. Indeed the difference in drift velocity between electron and ion (which is of the order of 10^3) will result in an accumulation of electrons at the front of the avalanche, while the ions will be distributed all along the avalanche forming a tail.
A priori, given the description of the gain, nothing limits the multiplication. However there is of course a limit to the gain. Indeed, the size of the avalanche will increase

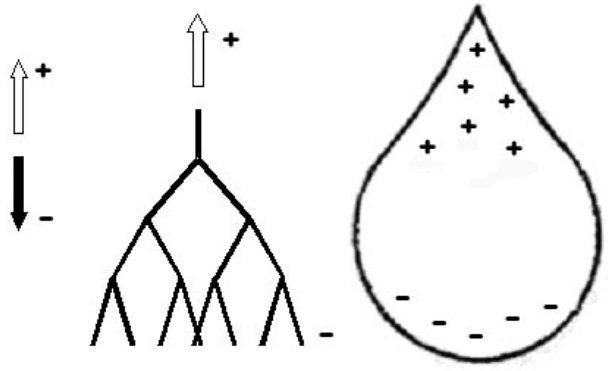

FIGURE 3.9: Diagram of the development of the avalanche.

with the distance. The electric field produced by the space charge will therefore also grow to locally cancel the external electric field. This effect will result in electron/ions recombination which will emit ultraviolet photons in an isotropic direction in the detector. These photons can also ionize the gas molecules which will create new avalanches. All these avalanches can be combined with each other and connect the electrodes by a conducting plasma, which will produce a discharge, which may damage the electrodes. An empirical limit of maximum number of charges in an avalanche was determined by Raether [29] and correspond to :

$$\alpha s \sim 20$$

where s is the characteristic dimension of the avalanche. This limit corresponds to a gain of the order of 10^8.

3.5 Gas Mixture

The choice of the gas mixture that we use in a gaseous detector is something quite complicated and depends on the expected performance of the detector. The important parameters to be taken into account in the choice of the gas mixture for the application studied in this thesis are: the electrons and ions drift velocities, the gain and the ability to absorb ultraviolet photons (and thus minimize the discharge).
The choice of argon is quite conventional, because the primary ionization for minimum ionizing particles is high enough (of the order of 100 e^-/cm see table 3.1). And compared to other noble gas (like xenon and krypton), argon is inexpensive.
It happens frequently that we should operate at a high gain, i.e. with a high electric

field, which increases the risk of discharges. To increase the electric field while avoiding discharges, a poly-atomic gas must be added. Indeed, poly-atomic gases have the property to have a lot of degrees of freedom (rotation, vibration ...). They can therefore absorb ultraviolet photons produced in the avalanche, and thus avoid the discharges. This type of gas is called a *quencher*. Gases generally used as quenchers are CO_2, CH_4 or isobutane.

3.6 Induced Signal

The signal that is observed on the electrode is not due to the collection of the charges themselves. Indeed, the collection time is too short to create a detectable current on the electrode. The signal that is recorded by the electrode, is actually the current induced by the displacement of the charges moving close to it.
To understand the observed signal, we will begin by studying the case of a moving charge close to a non-segmented electrode, we will then look at the same case but for a segmented electrode. Finally, we will end this section by calculating the signal currents induced by a moving charge close to n electrodes.

3.6.1 Non-Segmented Electrode

If we have a charge q at a distance Z_0 from a grounded electrode, we can compute the charge distribution on the electrode by the method of images [30]. To do this, a virtual charge $-q$ is placed on the other side of the electrode. The sum of the potentials of the two charges gives the total potential. From this potential, the electric field and the charge distribution on the electrode become :

$$\begin{aligned} E_z(x,y) &= -\frac{qZ_0}{2\pi(x^2+y^2+Z_0^2)^{3/2}} \\ E_x &= E_y = 0 \\ \sigma(x,y) &= \epsilon_0 E_z(x,y) \end{aligned}$$

With the charge distribution we can compute the total charge induced on the electrode. This charge is $-q$ that is the image charge.
If you change the initial position of the charge, this will change the distribution of charge, but not the induced charge. There will be no current induced by the movement of a charge close to a non-segmented electrode, as shown in Figure 3.10.

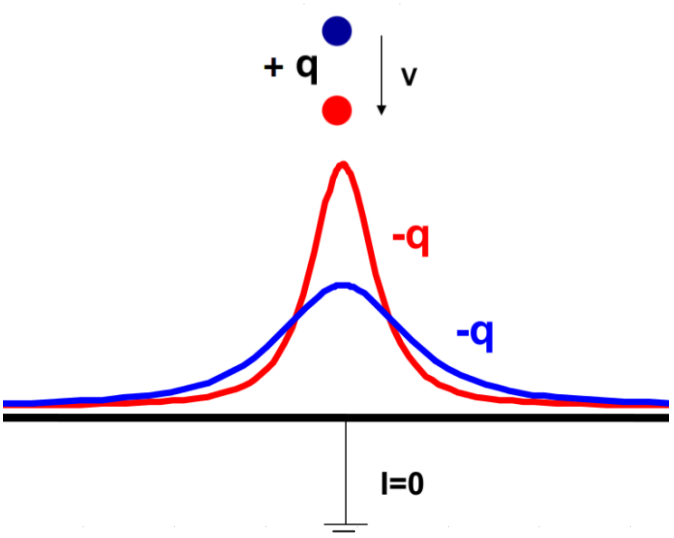

FIGURE 3.10: Diagram of the distribution of charge on a non-segmented electrode.

3.6.2 Segmented Electrode

We will now look at what happens if we segment the electrode in N parts of width W. When the charge q moves, the charge distribution on the electrode portions will now vary, which will produce a current, as shown in Figure 3.11.
To compute the induced charge at time t on the i^{th} segment, the charge distribution must be integrated on this portion:

$$\begin{aligned} Q_i\left(Z_0(t)\right) &= \int_{-\infty}^{\infty}\int_{-W/2}^{W/2}\sigma(x,y)\,\mathrm{d}x\mathrm{d}y \\ &= -\frac{2q}{\pi}\arctan\left(\frac{W}{2Z_0(t)}\right) \end{aligned}$$

where $Z_0(t)$ is the position of the charge function of its speed ($Z_0(t) = Z_0 + vt$).
In order to get the current induced on the segment considered the time derivative of the charge must be computed. The current induced by the movement of a charge q on the i^{th} segment will be given by the following expression :

$$\frac{dQ_i}{dt} = I_i(t) = \frac{4qW}{\pi(4Z_0(t)^2 + W^2)}v$$

3.6.3 Induced Currents

We will now consider the signal that will be induced by the movement of a charge on a set of electrodes. All electrodes are interconnected and are connected to the ground

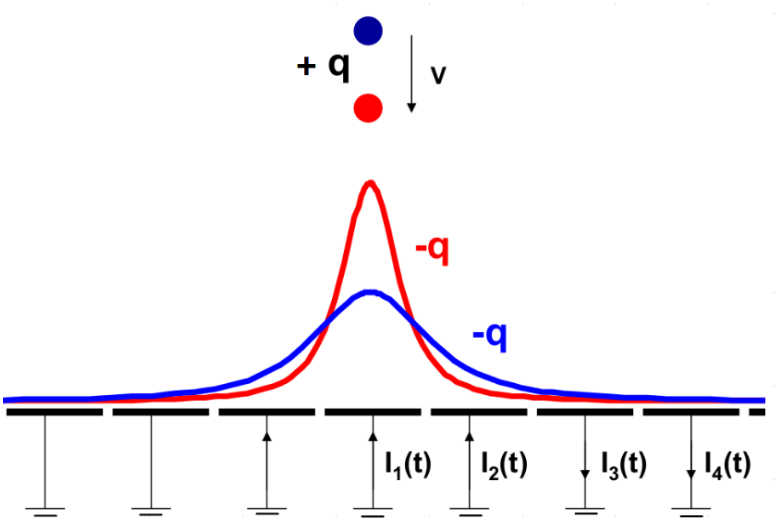

FIGURE 3.11: Diagram of the distribution of charge on a segmented electrode.

with a certain impedance. Considering a set of n grounded electrodes, and the induced current on the electrode i by a moving charge q will be noted $I_i(t)$. This configuration is, in fact, the practical problem that must be solved in the case of a gaseous detector with multiple electrodes.
To compute the induced current, we have to use two theorems.

The first is the Green's reciprocity. This theorem states that having n potentials V_i for $i = 1, ..., n$ due to n charges Q_i, and n other potentials $\hat{V}_i$ due to another charge distribution $\hat{Q}_i$ then :

$$\sum_{i=1}^{n} Q_i \hat{V}_i = \sum_{i=1}^{n} \hat{Q}_i V_i$$

The second is the Shockley–Ramo theorem. This theorem states that to compute the current I_i induced by the movement of a charge q, on grounded electrode i among n, it is enough to compute the resulting current on the electrode when it is maintained at the potential V_0 (in the absence of the charge q and all other electrodes being maintained at the ground potential).
At any point it therefore results in a potential V_i and an electric field $\vec{E}_i$.
We can define what is called the normalized potential, as well as the normalized field (respectively V_w and $\vec{E}_w$) as :

$$V_w \equiv \frac{V_i}{V_0}$$

$$\vec{E}_w \equiv \frac{\vec{E}_i}{V_0}$$

Using these two definitions, and both theorems, it is easy to show that the induced current on the electrode i is of the form :

$$I_i = -q\vec{E}_w.\vec{v} \tag{3.11}$$

In practice, the computation of the induced current on the electrode i requires :
- computing the electric field in the detector, created by all the electrodes at their operating potential;
- computing the normalized field ($\vec{E}_w$);
- computing the position and the drift velocity of the charge q.

The fields and potentials are usually computed using commercial programs [31]. The movement of the charge q can be computed knowing the drift velocity and the intensity of the electric field in the gaseous detector.

3.7 Micro Pattern Gaseous Detectors (MPGD)

The increasing constraints in particle physics experiments have led researchers to develop new technologies. It is in the late eighties that the new generation of gaseous detectors is born, with the invention of the Micro-Strip Gas Chamber (MSGC). The MSGC is the first gaseous detector using micro-strip anodes instead of wires to provide the gas amplification. After its introduction in 1988 [32], several alternatives have been introduced: namely, the Micromegas in 1995 and the Gas Electron Multiplier in 1996. In the following we will describe in details these detectors emphasizing their advantages and drawbacks.

3.7.1 Micro-Strip Gas Chamber (MSGC)

The MSGC are made of a plane of metal strips etched by photo-lithography. Several millimeters above this plane is placed a cathode plane drift. The space between this electrode and the strips plane is filled with gas; it is the sensitive region of the detector. The Figure 3.12 represents a section of a MSGC detector.
On the substrate, the metal strips consist of an alternate succession of anodes and cathodes separated by a few tens of microns. Typically, the anodes are very narrow, between 5 and 10 μm, while the cathodes are wider, of the order of 100 μm. The pitch between the anodes is typically 200 μm.

Applying a potential difference of a few kilovolts between the drift plane and the detection plane, provides an electric field nearly uniform of a hundred volts per centimeter

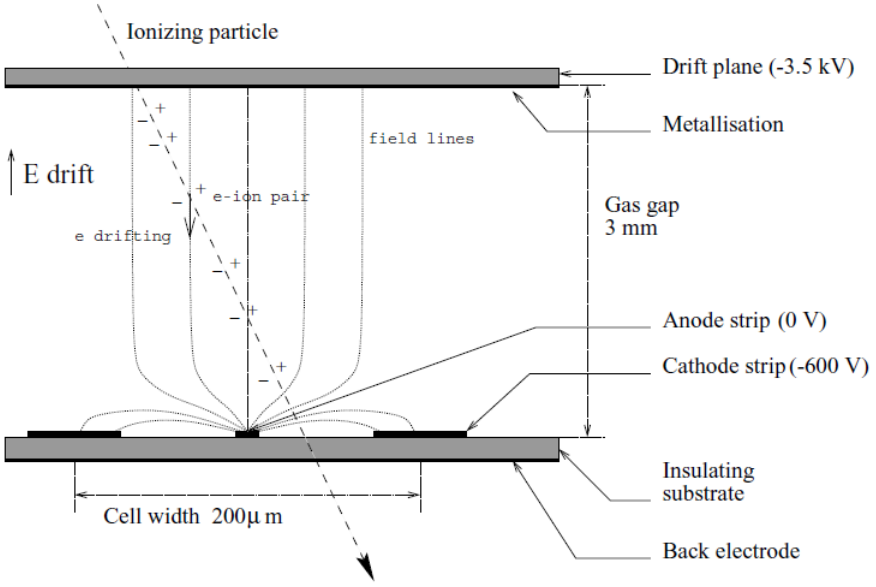

FIGURE 3.12: Diagram of the operating principle of an MSGC.

in the volume defined between the two planes, except close to the detection plane (see Figure 3.13). The charges produced by ionization (see section 3.2) drift following the field lines.

The avalanche is produced near the metal strips, where the field is no longer uniform and increases to a few tens of kilovolts per centimeter. The field lines produced by the electrode configuration will focus the primary electrons toward the anode strips, while the ions produced in the avalanche are mainly collected by the cathode strips.

With this geometry and the intense fields, the ion collection is done within a few μs by the adjacent cathodes, about one thousand times faster than in the MWPC.

A major advantage of the MSGC compared to the MWPC is the high granularity. Indeed, the photo-lithography allows high accuracy (of the order of 0.1 μm) in the placement of anodes and cathodes, which leads to a good spatial resolution (up to 30 μm as shown in ref.[33]).

3.7.2 Micromegas

The Micromegas (Micro Mesh Gaseous Structure) have been introduced in 1995 by I. Giomataris et al.[34]. Unlike MSGC, the Micromegas detector plane consists only of anodes.

Above the anode plane is placed a grid which acts as a cathode. This grid is maintained at about one hundred microns above the anode plane with cylindrical pillars of $\sim$ 300 μm in diameter. A voltage, of the order of $-500\ V$, is applied to the grid and the anode

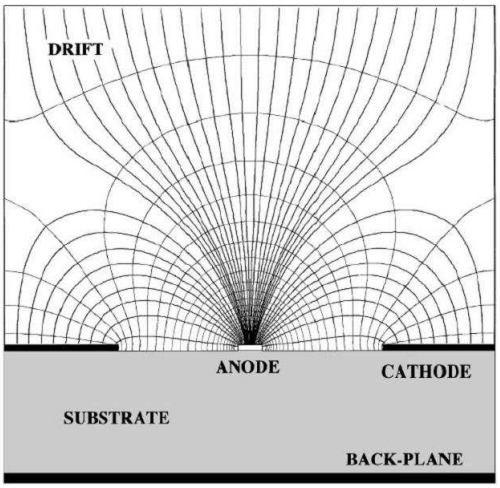

FIGURE 3.13: Diagram and line of electric field of an MSGC.

plane is grounded via the readout electronics to create an electric field of the order of 50 kV/cm. The space defined is the amplification gap.
A few millimeters above the grid is the drift electrode which defines the sensitive volume of the detector, also called drift gap.

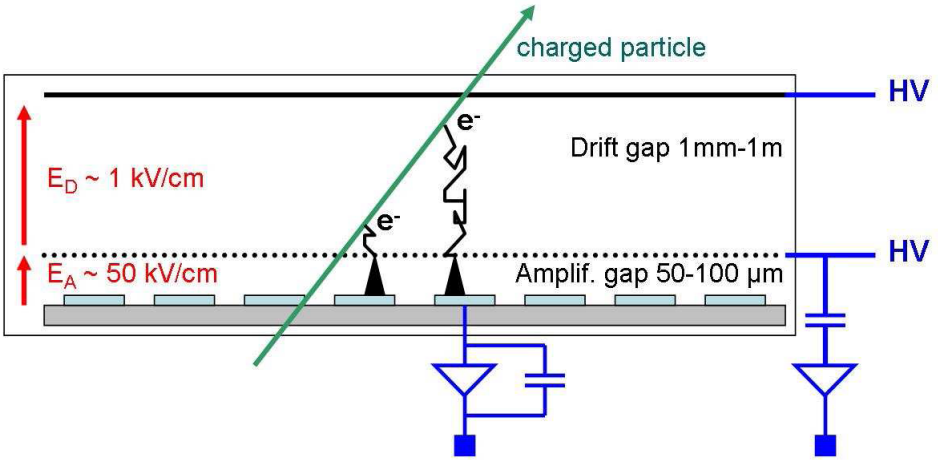

FIGURE 3.14: Operating diagram of the Micromegas.

When a charged particle passes through the sensitive volume of the detector, it deposits the ionization energy along its path. The charges produced drift in this sensitive area along the field line whose configuration is shown in Figure 3.15. The electric field is relatively small, of the order of 1 kV/cm in the sensitive volume. This field is constant, which implies a constant drift of the charges until the neighborhood of the grid.

The electrons are then caught in the holes of the grid and go in the amplification area where there is a constant field around 50 times more intense than in the drift gap. This

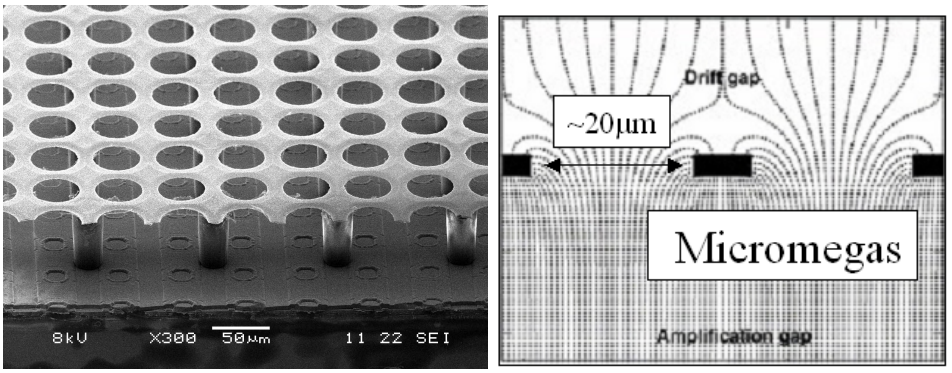

FIGURE 3.15: SEM image of a Micromegas structure (Left) [35]. The electric field lines around the Micromegas grid (Right).

very high field is responsible for the avalanche process that occurs over the entire anode-cathode distance (of 100 μm) and not only close to the anodes, as in the case of the MSGC.

The electrons quickly reach the anodes while the positive ions, slower, drift in the opposite direction and are collected at the micro-grid.
The electric field is high and constant throughout the entire amplification gap, these ions are therefore quickly evacuated. In Micromegas, less than 30% of the signal is induced by the electrons within 5 ns and 70% of the signal is created by ions in 40 ns [36].

3.7.3 Gas Electron Multiplier

The Gas Electron Multiplier (GEM) was introduced in 1996 by F. Sauli [37].
The GEM foil consists of a kapton foil of few tens of microns thick with 5 μm copper cladding surfaces on both sides. Those foils are pierced with a high density of micro-holes (50 to 100 holes per cm^2). The most common technique used to produce those holes is photo-lithography. Two different techniques of photo-lithography exist to produce GEM foils: Double-Mask and Single-Mask. The Figure 3.16 shows the schematic comparison of both procedures. By applying a potential difference between the two foils of copper, a few hundred volts, it produces an electric field of the order of 50 kV/cm in the center of the holes. Figure 3.17 left shows a GEM foil produced by Double-Mask technique and its dimensions and Figure 3.17 right shows the electric field lines in the neighborhood of the holes.
A GEM-based detector is made of a gas volume, defined between a cathode plane and an anode plane, split in two with a GEM foil. An electric field is applied in the gas volumes. The volume between the cathode plane and the GEM foil is the sensitive volume (often called the drift gap) where the primary ionization takes place. The ionization electrons

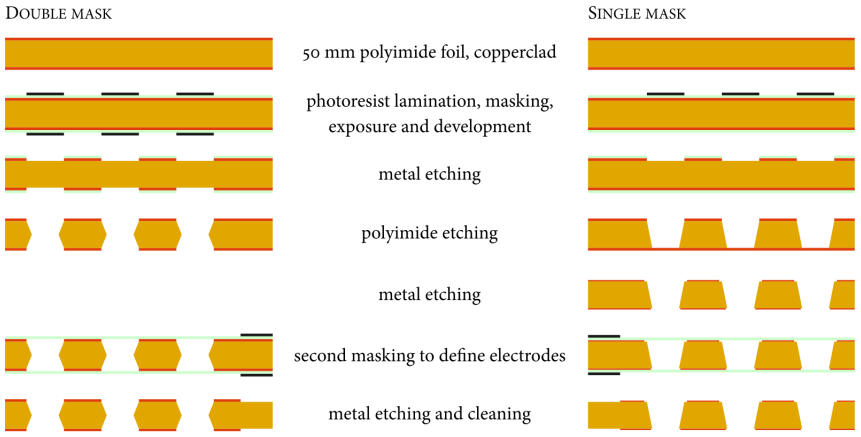

FIGURE 3.16: Schematic comparison of procedures for fabrication of a double-mask (left) and a single-mask GEM(right) [38].

drift to the GEM foil and are accelerated in the holes, causing a first multiplication. Afterward in the volume defined between the GEM foil and the anode plane, that is generally called the induction gap, the electron cloud produced in the foil will induce a signal to the anode plane. The anode plane is usually composed of readout strips directly connected to a front-end electronics.

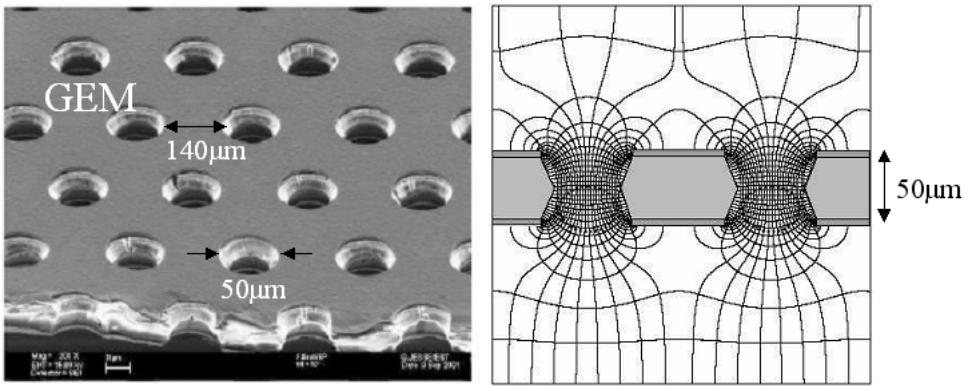

FIGURE 3.17: A SEM picture of a GEM foil with its dimensions (left); electric field lines close to the GEM holes (right).

However given the limited gain of a few hundred [39] that can provide a GEM foil, two or three GEM foils are usually stacked in the same volume of gas. The detector is then called a Double- or Triple-GEM. Figure 3.18 shows the operating diagram of a Triple-GEM.

Figure 3.19 shows the effective gain, that will be properly defined on page 55, for different multiple GEM detectors. We can directly see that a multiple-GEM can reach an effective gain of several thousands.

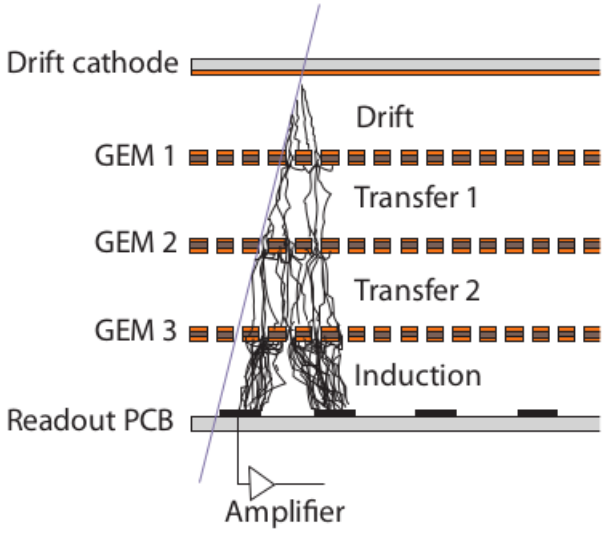

FIGURE 3.18: Operating diagram of a Triple-GEM.

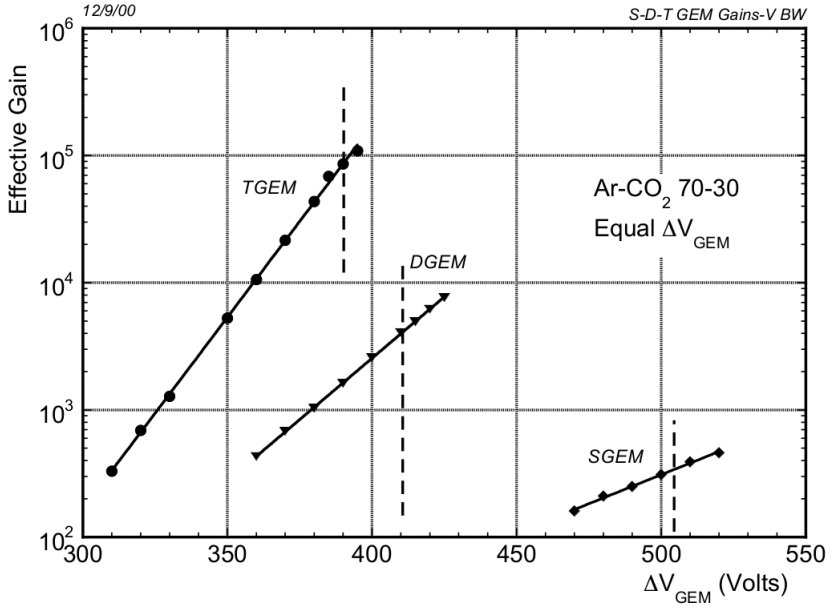

FIGURE 3.19: Effective gain (full curves) and discharge limits on exposure to alpha particles (dashed lines) of multiple GEM detectors [40].

One of the main benefit of the GEM compared to other gaseous detectors is the high rate capability, up to 10^6 mm^{-2}s^{-1} as shown in Figure 3.20.

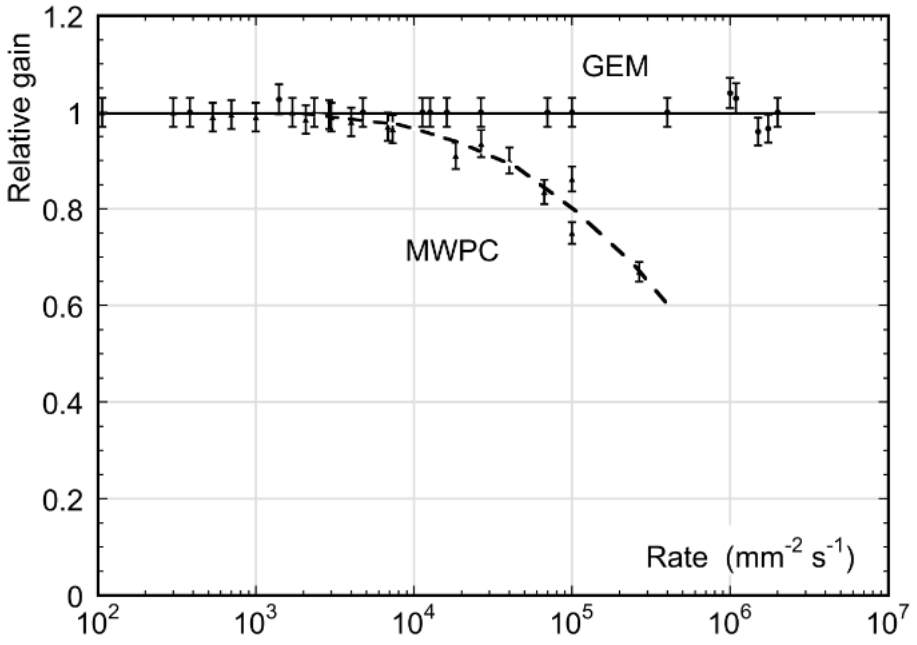

FIGURE 3.20: Normalized gas gain as a function of particle rate for MWPC and GEM [41].

Configuration of the CMS Triple-GEM In the context of the upgrade of the forward muon spectrometer of CMS, different geometries of Triple-GEM have been considered. The final detectors have a trapezoidal shape with an active area of $990 \times (220 - 445)$ mm^2.

Over the years, the CMS GEM collaboration has performed a large R&D effort during which the GEM technology has evolved and different parameters such as the electric fields in the gaps, have been studied and optimized. We report in the following the major results.

In 2010, various Triple-GEM prototypes have been studied during several test beam campaigns [42]. Two gas mixtures have been considered for operating the Triple-GEM detectors: Ar/CO_2 (70:30) and $Ar/CO_2/CF_4$ (45:15:40). Different gaps configurations were also considered.

The efficiency measured for the different gas mixtures and gap configurations are reported on Figure 3.21. In each case, the efficiency reaches the plateau at 98 % for a gain of $\sim$ 8000. One can remarks that the efficiency plateau is very long, up to a gain of $\sim$ 30000.

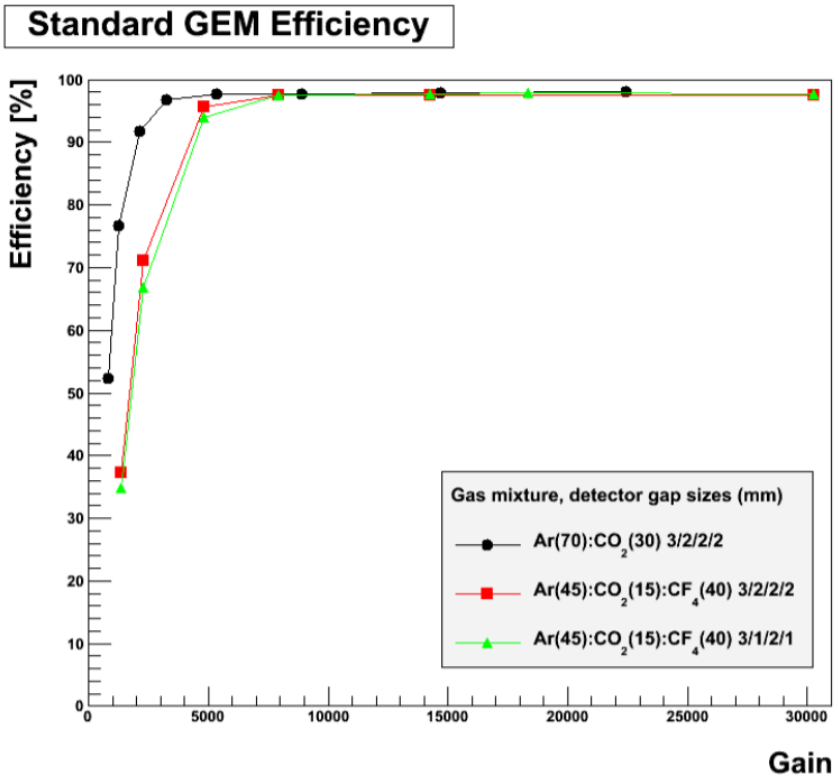

FIGURE 3.21: Triple-GEM detector efficiency for different gas mixtures and gap size configurations as a function of the gain [42].

The time resolution has been also studied during those test beams. The results are shown in Figure 3.22. The use of $Ar/CO_2/CF_4$ (45:15:40) gives a time resolution better than 5 ns for an electric field of the drift gap higher than 2 kV/cm against 8 to 10 ns in the Ar/CO_2 (70:30) gas mixture. Eventually, the gap configuration of 3:1:2:1 mm has been chosen.
A more detailed summary of the studies of the diverse prototypes can be found in ref.[43] and ref.[17].

The detector readout board is divided into eight η-partitions with 3×128 strips and the strip pitch varies from 0.6 mm (short side) to 1.2 mm (long side).
To power the different parts of the detector, the collaboration has opted to use a voltage divider made of a ceramic plate. The best working point of the detector has been calculated and is set to be at 4000 V which corresponds to a current of 800 μA through the divider. At that point, the electric fields of the four gaps are 3/3.5/3.5/5 kV/cm and the voltage applied to the three different GEM foils are 450/440/420 V, which ensure the best time resolution and a good efficiency.
For further discussions, this configuration will be called the 'standard' configuration.

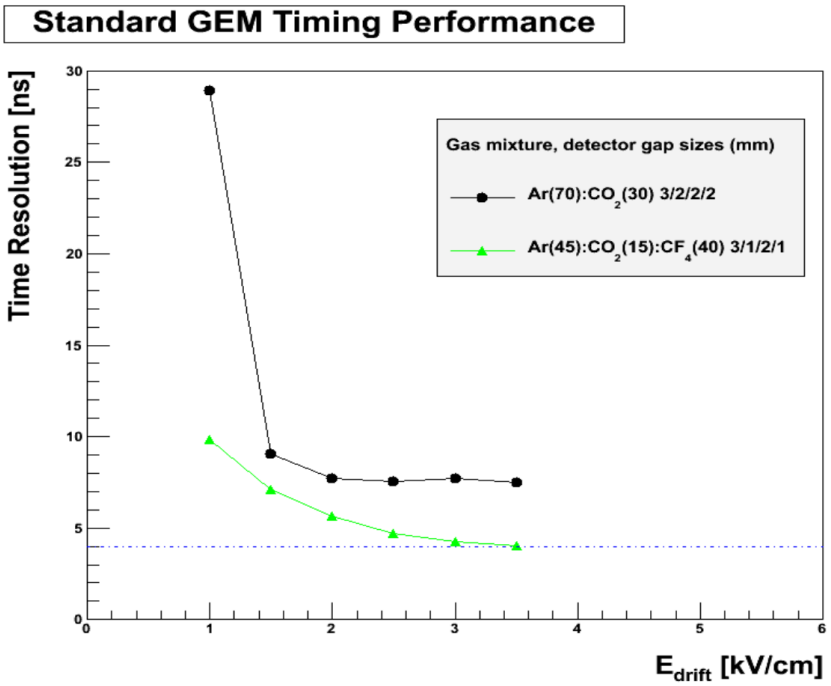

FIGURE 3.22: RMS of the time distribution as a function of the electric field in the drift gap with a fixed induction field of 5 kV/cm [43].

Gain in the Triple-GEM Detector As presented in the section 3.4, the gain in a gaseous detector is defined as the ratio of the number of electrons produced in the avalanche and the number of primary electrons n_0 (Eq. 3.10). This definition expresses an absolute gain that is quite difficult to measure in a real detector like the GEM.
Indeed, in the case of the Triple-GEM detectors, several processes can lead to the loss of electrons. The electrons can be captured on one of the copper foils or on the kapton of the GEM foils.
These losses are referred to the so-called transparency. The transparency of a GEM foil is defined as the probability that an electron which enters into a GEM hole exits that hole. The transparency depends on several parameters as the gas mixture, the voltage applied to the GEM, etc.
For this reason, the effective gain G_{eff} of a Triple-GEM detector is defined as:

$$G_{eff} = \frac{n_{eff}}{n_0},$$

where n_{eff} is the number of electrons inducing a signal to the anode plane.

The measurement of the CMS Triple-GEM gain will be discussed in detail in this work in section 5.1.3.

Full-Size GE1/1 Prototypes During the five years of R&D for the CMS Triple-GEM, several generations of GE1/1 prototypes were built and tested. Figure 3.23 shows the five generation of detectors that were developed between 2010 and 2014 and that we will review shortly.

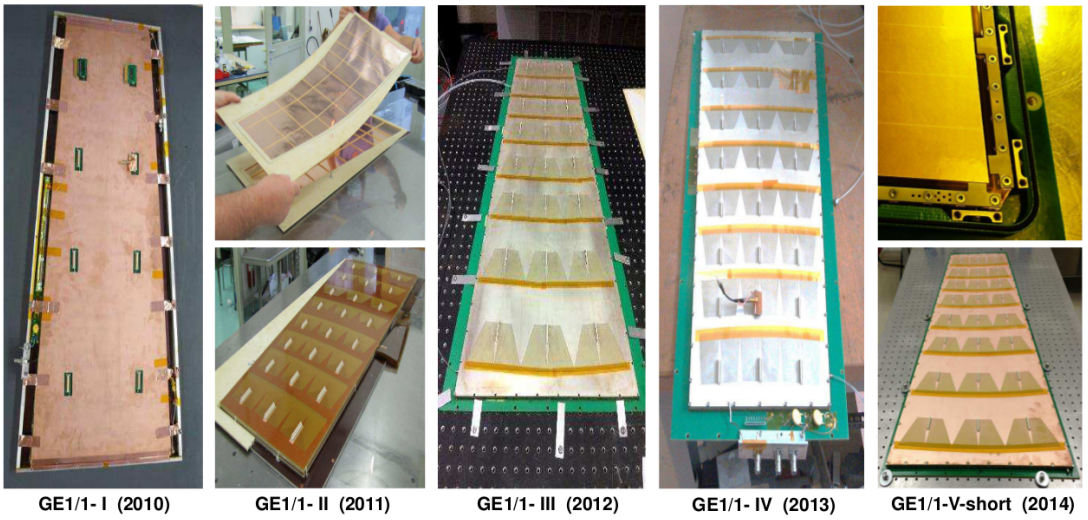

FIGURE 3.23: Five generations of GE1/1 prototypes chambers constructed and tested by the CMS GEM collaboration in 2010-2014 [17].

Each generation of prototype has been developed based on the experience of the previous generation.

GE1/1-I

In 2010 the CMS GEM collaboration has built the first large-area GEM detector. The detector is 0.5 m^2, the foils were produced with the single-mask method and the gap configuration was 3:2:2:2 mm.

GE1/1-II

In 2011 the gap configuration was changed to 3:1:2:1 mm and the segmentation of the detector was increased to 3×8 sectors (against 2×8 sectors for the previous generation).

GE1/1-III

In 2012 a new stretching and assembly technique has allowed the collaboration to mount the GEM foils of the prototype without gluing. The outer detector frame was made of several pieces and was still glued to the drift board. The third generation was the first to be powered by a custom made ceramic HV divider.

GE1/1-IV

The fourth generation that was built in 2013 is the first with a complete mechanical

assembly. One of the main benefit of not using any glue is the time it takes to build a chamber, indeed the detector can be assembled in a few hours. Unfortunately to avoid non-uniformity in the gap size, the different GEM foils had to be pre-bent. This pre-bending technique works in principle but is very time consuming.

GE1/1-V

The fifth generation of prototype, that was produced in 2014, features a re-designed stretching apparatus that is now totally inside the gas volume as shown in Figure 3.24.

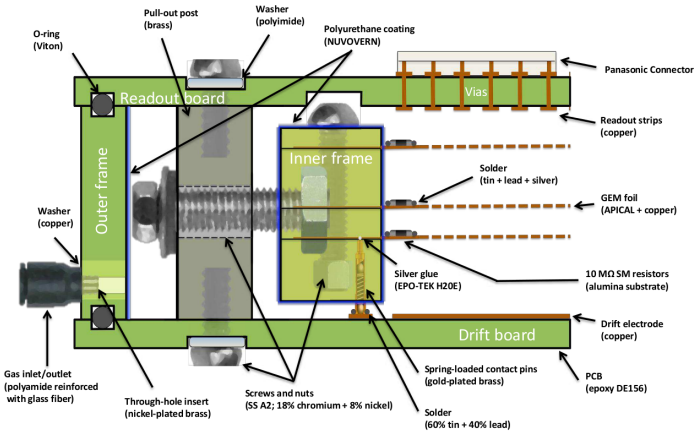

FIGURE 3.24: Cross section through inner and outer chamber frames and GEM foils of the GE1/1-V showing the stretching apparatus [17].

Chapter 4

Triple-GEM Detector Simulations

Together with the experimental study of new detectors, it is also important to study their performance with the help of Monte Carlo simulations. This helps to understand the measurements and also serves to optimize the detector parameters like its geometry or the operating voltages.

In this chapter we will present the study of several characterizing parameters (time resolution, detector efficiency) of the CMS Triple-GEM detectors using various Monte Carlo simulation programs. In section 4.1, we will introduce the GARFIELD framework. GARFIELD is used as a benchmark to compute the time resolution of the CMS Triple-GEM detector in section 4.2. Then we will describe in section 4.3 a fast and parameterized simulation of the Triple-GEM detectors that we have developed. The results obtained with this fast simulation are compared with the GARFIELD results. Finally, in section 4.4, we will present an hybrid simulation combining GARFIELD and the fast simulation.

4.1 GARFIELD

GARFIELD [44] is a multi-function computer program which has been developed to simulate gaseous detectors in two- or three-dimensions. It is interfaced with programs such as Heed [45] and Magboltz [46]. The main steps of a GARFIELD simulation can be summarized as follow:

Electric Field Maps

GARFIELD needs the electric field map of the detector to be simulated. For many two-dimensional models of chambers the exact fields are known (i.e. the drift chamber), but this is not the case for three-dimensional detector models. To

handle this problem, GARFIELD is interfaced with finite element programs like ANSYS [47] or neBEM [48].

In our case the detector structure and electric field have been simulated using the ANSYS program.

Primary Ionization

Primary ionization is either predefined by giving the position, energy and velocity direction of the primary electrons or by doing a realistic simulation of a charged particle passing through the detector using Heed. This program computes the energy loss of fast charged particles in gases.

Transport

After the primary ionization, GARFIELD needs to compute the electron transport in the gas mixture under the influence of electric and magnetic fields. The transport properties are described by the Boltzmann transport equation [49]. The solution to this equation is computed using the Magboltz program that is interfaced with GARFIELD.

During the drift each primary electron will collide with the gas molecules. GARFIELD computes the time between two collisions with a method called the *null event method* [50].

At each collision, the energy of the electron is computed and a process is applied to this electron. The process is chosen randomly with a probability distribution given by the cross section table at the given energy and for the given gas mixture. The cross sections of the different processes are shown in Figure 4.1 for Ar, CO_2 and CF_4.

Each process leads to a different result: an elastic collision will diffuse the incident electron, an ionization will produced a new electron, etc.

Between each collision the generated signal of every particle is computed on the electrodes. This induced signal is given by equation 3.11 and the procedure presented in section 3.6.3.

4.2 Time Resolution Studies

In this section we report on the study of the time resolution that can be achieved with the CMS Triple-GEM detectors. One of the objectives of the CMS GE1/1 detector upgrade is to improve the muon trigger efficiency. Therefore the time resolution of the detector has to be well understood in order to ensure the correct LHC bunch crossing identification associated to the recorded muon.

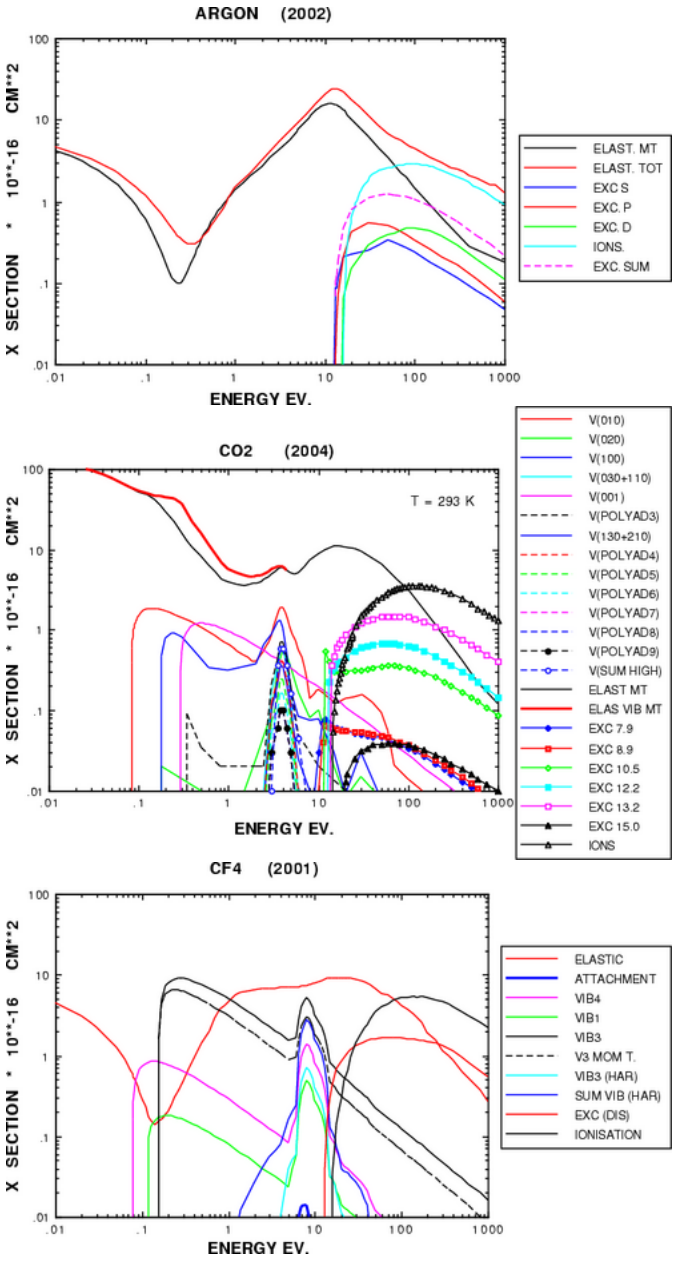

FIGURE 4.1: Cross sections of the different processes for Ar, CO_2 and CF_4 [51].

In CMS, these detectors will be read out by the new VFAT3 chips being currently designed. Hence the study of the time resolution of the CMS Triple-GEM detector has been performed with simulations. We have used the GARFIELD software to understand the detector response and signal shape. The time resolution of the detector has been evaluated for two methods that could be implemented in the VFAT3 electronics [17] [52]: the Time-Over-Threshold (TOT) and the Constant Fraction Discriminator (CFD).

This section is structured as follows: in subsection 4.2.1 the signal formation inside Triple-GEM detectors is reviewed while in subsection 4.2.2 the VFAT3 electronics is described. The time resolution is studied in subsection 4.2.3.

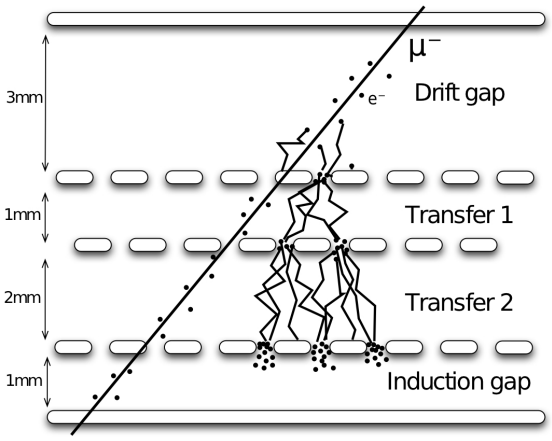

FIGURE 4.2: Sketch of the gap configuration of a CMS Triple-GEM detector.

4.2.1 Signal Formation

In a Triple-GEM detector the signal recorded on the anode strips is induced exclusively by the drift of the electrons extracted from the third GEM foil, facing the anode plane. When a charged particle crosses the detector, as shown in Figure 4.2, the primary ionization occurs all along the particle path. The primary electrons released in the Drift gap are amplified through the three successive GEM foils, while primary electrons released in Transfer 1 gap are amplified twice, etc. Both processes, the ionization and the amplification, are prone to statistical fluctuations, resulting in large variations of the induced anode current. Figure 4.3 shows three typical anode signals, namely the induced current recorded as a function of time, simulated with GARFIELD with the gas mixture $Ar/CO_2/CF_4$ (45:15:40). The geometry used for all the simulations presented in this chapter is shown in Figure 4.2 (3 mm for the Drift gap, 1 mm for Transfer 1, 2 mm for Transfer 2 and 1 mm for the Induction gap). The electric field for the Drift gap and both Transfer gaps is 3 kV/cm and the electric field for the Induction gap is equal to 5 kV/cm. The voltage applied to the three GEM foils is 400 V.
To better understand the signals shown in Figure 4.3 and 4.4, it is worth reminding that in the $Ar/CO_2/CF_4$ (45:15:40) gas mixture, the drift velocity (v_{drift}) is $\sim$ 0.1 mm/ns for an electric field above 3 kV/cm as shown in Figure 4.5. We can therefore identify the contribution of the primary ionization to the signal from the different gas gaps of the detector. The respective contributions are indicated by vertical dashed lines in Figure 4.4.

Between 0 and 10 ns after the passage of the muon, the signal induced by the electrons produced in the Induction gap is seen, between 10 and 30 ns the signal induced by the electrons released in the Transfer 2 gap and amplified only by the third GEM is observed. Between 30 and 40 ns the signal given by the electrons released in the Transfer 1 gap

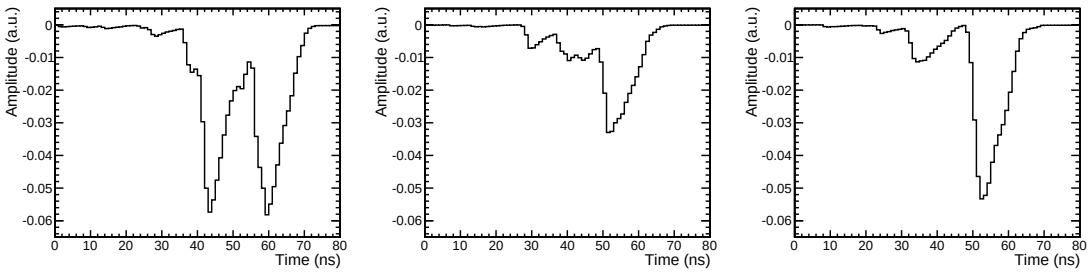

FIGURE 4.3: Three different induced signals simulated by GARFIELD for a gas mixture of $Ar/CO_2/CF_4$ - 45:15:40.

and amplified by the second and third GEMs is seen. Finally between 40 and 70 ns the signal induced by the electrons coming from the Drift gap and fully amplified by the three GEM foils is observed.

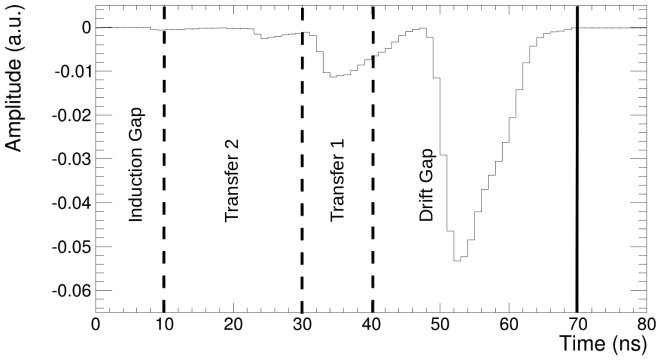

FIGURE 4.4: Induced signal simulated by GARFIELD for a gas mixture of $Ar/CO_2/CF_4$ (45:15:40).

Comparing the signals of Figure 4.3 and 4.4, we can notice large variations in the amplitude of the peaks within same regions (Induction, Transfer 1/2, Drift). These variations are due to the statistical fluctuations of both processes, namely the ionization and the amplification. On the first induced signal of Figure 4.3, we can notice two peaks between 40 and 70 ns, those peaks come from two different clusters of electrons created in the Drift gap but spatially separated by ~ 2 mm. In some extreme cases, the amplitude of the part of the signal induced by electrons coming from the Transfer 1 gap can be the highest of the signal.

4.2.2 The Readout Electronics

The front-end electronics foreseen for the CMS Triple-GEM is the VFAT3. The VFAT3 is an ASIC containing a total of 128 channels of charge sensitive preamplifiers and of associated shapers. This chip will run at the LHC frequency of 40 MHz, getting a

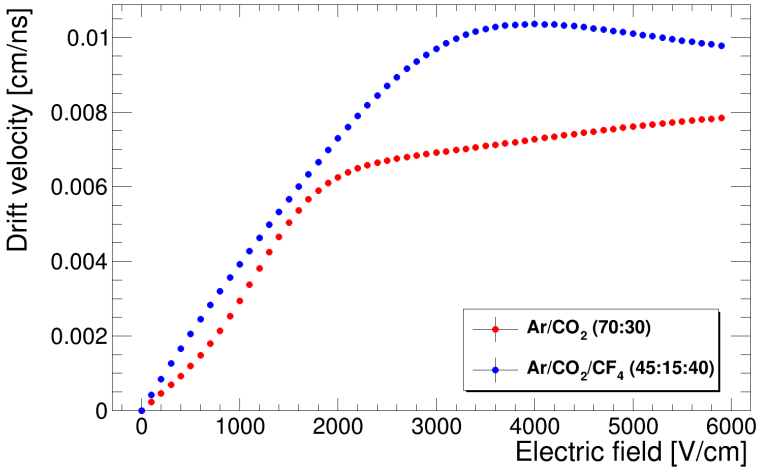

FIGURE 4.5: Evolution of the drift velocity as a function of the electric field for the Ar/CO_2 (70:30) and $Ar/CO_2/CF_4$ (45:15:40) gas mixtures simulated by GARFIELD.

clock of 320 MHz through the E-Ports [53] that handle all communication with the off-detector electronics (see Figure 4.6). The analog front-end preamplifiers and shapers are programmable to offer a large flexibility. One of the programmable parameters relevant for this study is the peaking time.
Several parameters, such as the time resolution or the detector efficiency were simulated to estimate the performances of the CMS Triple-GEM detectors. The simulations were done by convoluting the induced anode current given by GARFIELD (see section 4.2.1) with the following VFAT3 transfer function:

$$F(t) = \left(\frac{t}{\tau}\right)^n \cdot \exp\left(\frac{-n \cdot t}{\tau}\right) \tag{4.1}$$

where t is the time, τ the peaking time and n the filter order.
The convolution is discrete and uses the binning of the GARFIELD signal, that is 1 ns. The study has been performed with two possible VFAT3 designs:

- first VFAT3 ("VFAT3_ n2") design has a filter of order 2 and the possible peaking times are 20 ns, 50 ns, 100 ns, 250 ns or 500 ns.
- The second design ("VFAT3_ n3") has a filter of order 3 and possible peaking times are 25 ns, 50 ns, 75 ns, 100 ns or 200 ns.

4.2.3 Time Resolution

To unambiguously identify the LHC bunch crossing a detected particle was created in, the CMS Triple-GEM detectors must provide a time resolution better than 10 ns [17].

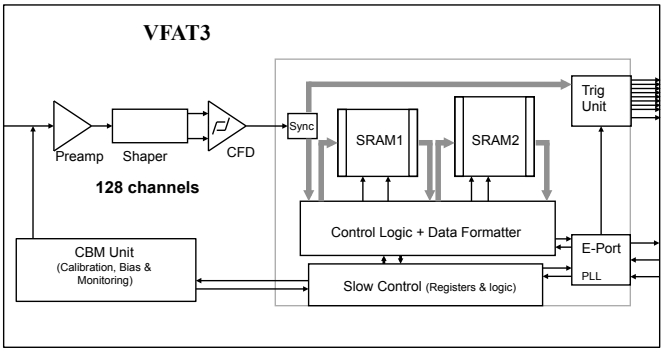

FIGURE 4.6: VFAT3 block diagram.

Assuming that the signal shape does not change with the signal amplitude, a simple threshold discriminator will induce a time walk effect [19] degrading the time resolution: two signals with the same arrival time will not necessarily cross the electronics threshold at the same time. A signal with a small amplitude will cross the threshold later than a signal with a larger amplitude. Therefore the time resolution has been studied with two methods that are not affected by this effect: the Time Over Threshold (TOT) and the Constant Fraction Discriminator (CFD). The objective of this study is to determine the best method and peaking time, optimizing the time resolution as well as the latency (the time it takes to the method to return the time tag), another important parameter for the CMS level-1 trigger. Both methods have been tested with both VFAT3 designs and several peaking times.

Time Over Threshold The concept of the Time Over Threshold (TOT) method is to compare the time when the signal is above the electronics threshold against a theoretical time stored in a Look Up Table (LUT). This LUT gives the information about t_1 the time when the signal crosses the threshold for the first time (see Figure 4.7).

To build the LUT, an arbitrary signal produced by GARFIELD is convoluted with the VFAT3 shaper transfer function and is then normalized. This normalized signal is multiplied, increasing the peak amplitude by small steps to span the entire dynamic range of the electronics. For each amplitude level the TOT is computed with a clock cycle of 1 ns and written in a LUT with the associated t_1. The size of the LUT for both VFAT designs is summarized in the tables 4.1 and 4.2. To estimate the time resolution of a signal simulated with GARFIELD, we compare the time t_1, when the signal actually crosses the threshold, and the corresponding time t_{LUT} provided by the LUT according to the counted time over threshold. The TOT is measured with a clock cycle of 3 ns. In Figure 4.8 the difference $t_1 - t_{LUT}$ is plotted for the case of a peaking time of 100

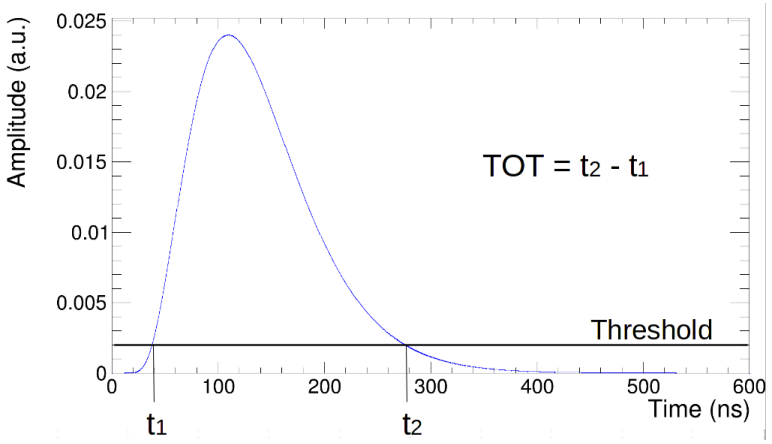

FIGURE 4.7: A Triple-GEM signal after the convolution with the VFAT3 transfer function (see Eq. 4.1). The threshold defines two times, the instant at which the rising signal crosses the threshold (t_1) and the instant at which the falling signal returns below the threshold value (t_2).

Peaking time (ns)	Entry
20	43
50	88
100	153
250	407
500	753

TABLE 4.1: Number of entries in the LUT for VFAT_ n2 design.

Peaking time (ns)	Entry
25	44
50	77
75	112
100	144
200	282

TABLE 4.2: Number of entries in the LUT for VFAT_ n3 design.

ns and for the VFAT_ n3 design; a Gaussian is fitted on the distribution. From the fit results the sigma is considered as the time resolution.

The latency of the TOT method is provided by the time t_2 the signal takes to fall below the threshold, see Figure 4.7. Indeed, it is only at that moment that the TOT can be compared with the LUT. The time to get the result from the LUT corresponds to one clock cycle.

Constant Fraction Discriminator The CFD method consists in generating a bipolar signal from the output of the shaper. This bipolar signal has the property to have

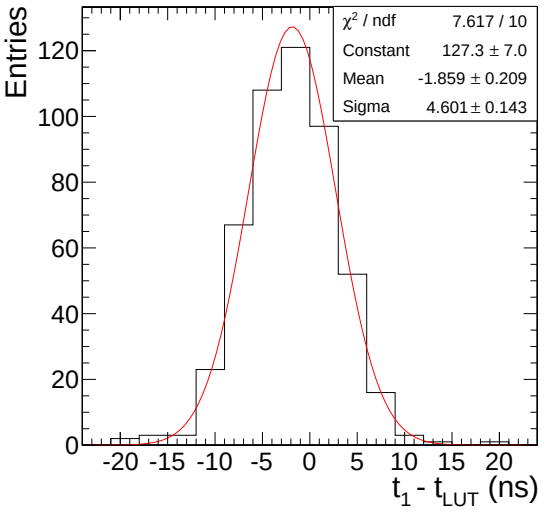

FIGURE 4.8: Time resolution distribution computed with the TOT method for a peaking time of 100 ns for the VFAT_ n3.

its zero crossing point occurring at the same time for every amplitude.

The bipolar signal is obtained as follows: a first copy of the original signal is delayed by a time t_{delay} with respect to the original signal. The delay corresponds to the difference between the time when the signal is at its maximum t_{max} and the time when the output signal has an amplitude equal to its maximum amplitude divided by a constant k: $t_{delay} = t_{max} - t_k$ as shown in Figure 4.9. The second signal is a copy of the original signal multiplied by $-1/k$.

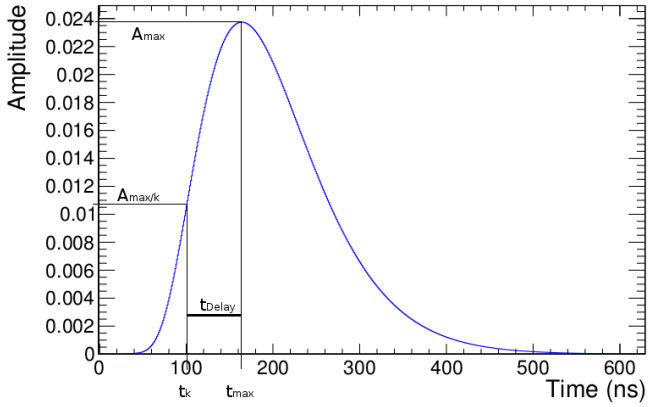

FIGURE 4.9: A Triple-GEM signal after the convolution with the VFAT3 transfer function. The delay time t_{delay} applied in the CFD construction is the difference between the time t_{max} when the signal amplitude is the maximum (A_{max}) and the time t_k when the signal amplitude is at maximum divided by the constant k ($A_{max/k}$).

Finally, the bipolar signal is the sum of those two signals. Figure 4.10 shows the Triple-GEM signal after the convolution with the VFAT3 transfer function, the two constructed

signals and the bipolar signal used in the CFD method.

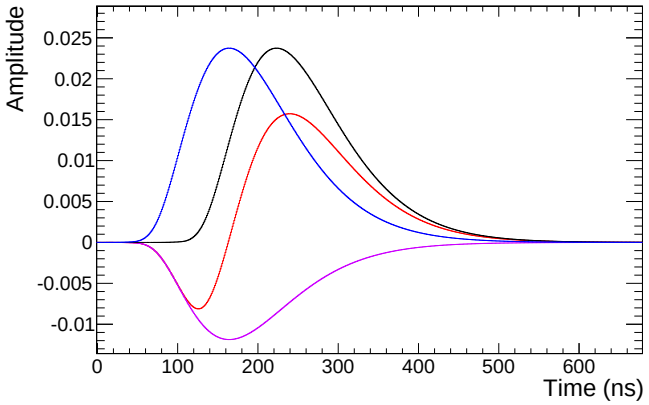

FIGURE 4.10: The blue curve is the Triple-GEM signal after the VFAT3 convolution, the black curve represents the delayed signal, the violet is the signal multiplied by $-\frac{1}{k}$, and the red signal corresponds to the sum of the black and violet curves.

The construction described above has the feature to have the zero crossing (at a time t_0) of the bipolar signal and maximum of the output of the shaper occurring at the same time. This property can be used if the t_{max} of our signal is known. To estimate the t_{max}, the mean of the t_{max} distribution of 500 simulated signals as shown in Figure 4.11 is taken.

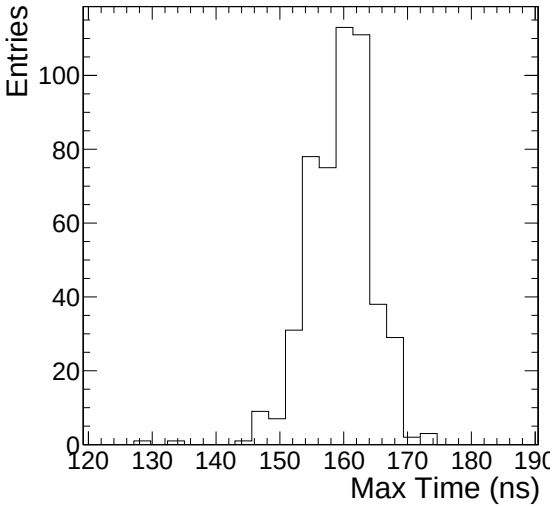

FIGURE 4.11: t_{max} distribution for VFAT_n3 with a peaking time of 100 ns.

To compute the time resolution using the CFD method, the zero crossing of 500 simulated signals is compared with respect to the estimated t_{max}. Finally, a Gaussian is fitted on the distribution, as shown in Figure 4.12. Taking into account the fit parameters, the sigma is assumed to be the time resolution.

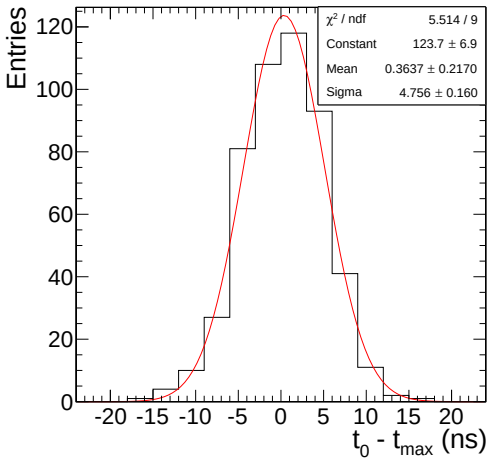

FIGURE 4.12: Time resolution distribution computed with the CFD method for a peaking time of 100 ns for the VFAT_ n3.

Finally, in order to estimate the latency using the CFD method, the mean value of the t_{max} distribution with the information related to the zero crossing is used.

Triple-GEM Configuration in GARFIELD The configuration and parameters used for these GARFIELD simulations are not the 'standard' ones that will be applied in CMS. One of the reasons is that this analysis is anterior to the GE1/1 TDR and since then our knowledge about the performance of the long CMS Triple-GEM detector has significantly improved.
The gap geometry used in these simulations is 3:1:2:1 mm, the electric fields for the different gaps are 3/3/3/5 kV/cm, the voltage applied to the GEM foils 400 V and the gas mixture is $Ar/CO_2/CF_4$ (45:15:40). The energy of the muons is 1.5 GeV.

Results The TOT and CFD methods were applied to 5 different peaking times for both VFAT3 designs. For each peaking time, 500 events simulated by GARFIELD are used.
Figure 4.13(a) and Figure 4.13(b) show, for both methods and both VFAT3 designs respectively, the time resolution as a function of the VFAT3 peaking time. We can see that the time resolution is better than 5 ns for a peaking time longer than 50 ns. This result confirms the very good time resolution of the CMS Triple-GEM detector measured during the test beam with $Ar/CO_2/CF_4$ (45:15:40) gas mixture [42] (see section 3.7.3).

Figure 4.14(a) and Figure 4.14(b) report the latency for both methods and both designs respectively.

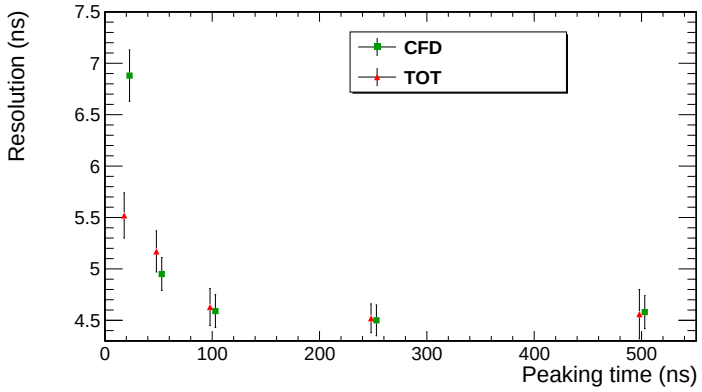

(a) VFAT_ n2

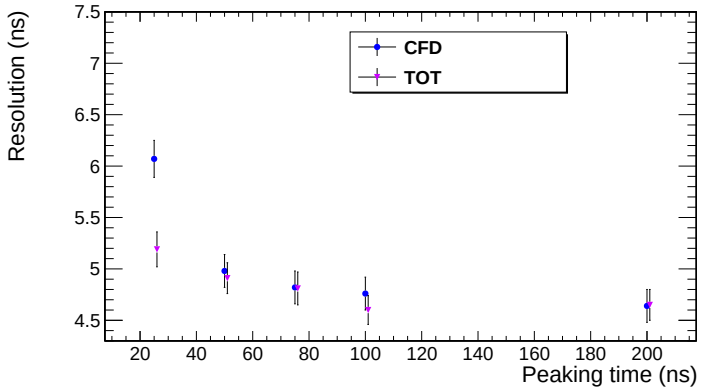

(b) VFAT_ n3

FIGURE 4.13: Time resolution for both TOT and CFD methods as a function of the peaking time, for the VFAT_ n2 (fig. 4.13(a)) and VFAT_ n3 (fig. 4.13(b)), and for a gas mixture of $Ar/CO_2/CF_4$ - 45:15:40.

By construction the CFD method is faster than the TOT and the fact that the VFAT3 output signal (Eq. 4.1) is asymmetric explains why the difference between the latency of both methods increases with the peaking time. For instance, the latency of the CFD method for a peaking time of 50 ns is of the order of 100 ns against 250 ns for the TOT method and this for both designs.

All the results are summarized in the tables reported in Appendix A.

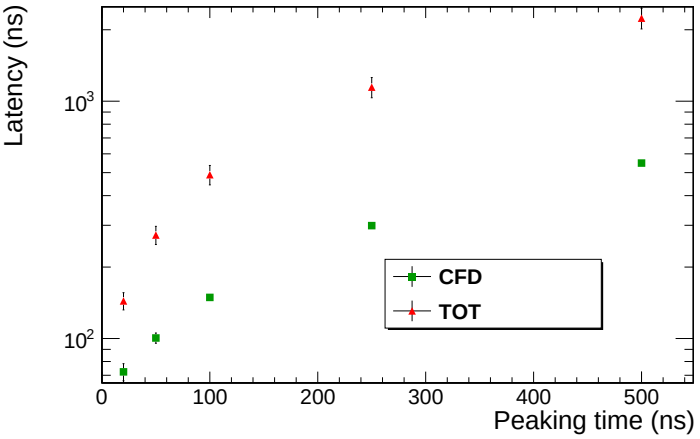

(a) VFAT_ n2

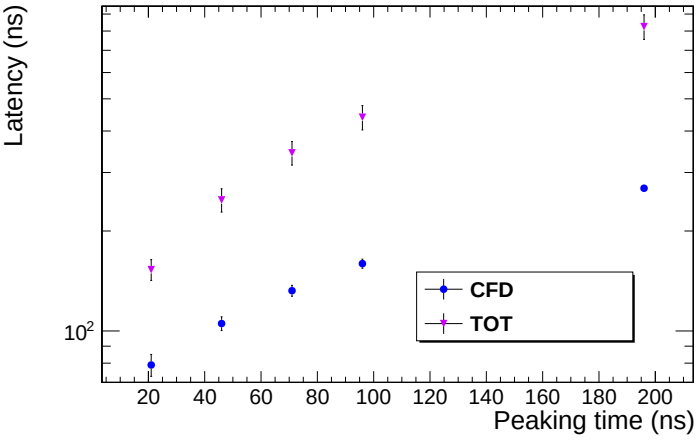

(b) VFAT_ n3

FIGURE 4.14: Latency for both TOT and CFD method as a function of the peaking time of the VFAT_ n2 (fig. 4.14(a)) and VFAT_ n3 (fig. 4.14(b)), and for a gas mixture of $Ar/CO_2/CF_4$ - 45:15:40.

4.2.4 Contribution to the Time Resolution

In this section various processes that can contribute to the time resolution observed in the previous section will be presented. The goal is to explain the expected time resolution and to identify the main contributions to the time fluctuation. Multiple processes contribute to the time resolution, some are related to the detector technology, others to the read-out electronics. The processes under consideration are the following:

- the fluctuation due to the sampling of the electronics clock (σ_{clk});
- the fluctuation in the position of the primary ionization clusters ($\sigma_{clusters}$);
- the fluctuation due to the longitudinal diffusion ($\sigma_{diff.L.}$);
- all other fluctuations (ie. gain fluctuation, ionization clusters size, etc) (σ_{other}).

Each of these contributions will be reviewed in detail now. The parameters considered for this part of the study are the 'standard' parameters used in the CMS GEM upgrade.

Electronics clock

The VFAT3 chip works at the frequency of 40 MHz derived from a clock running at 320 MHz received through the E-port (see section 4.2.2). This allows to adjust the phase of the 40 MHz clock used to 'sample' the VFAT3 comparator by steps of 3.125 ns. Therefore, according to the uniform distribution, for every event the uncertainty on the time the signal passes the comparator threshold within a clock cycle is given by:

$$\sigma_{clk} = \frac{3.125}{\sqrt{12}} = 0.9\ ns$$

Primary ionization clusters

As seen in section 4.2.1, the primary ionization may occur all along the particle path and the primary electrons are therefore released in the different gaps in clusters. The following hypothesis is assumed: the three GEM amplifications are needed to have a signal detected by the electronics. With this hypothesis, the first cluster of electrons to be detected is the cluster closest to the first GEM foil in the drift gap. The contribution to the time resolution is therefore the uncertainty on the position of this cluster. The distribution of the distance between the closest cluster and the first GEM foil depends on the number of clusters in the drift gap. In other words, it depends on the gas mixture.

A reasonable hypothesis is to assume that the clusters of electrons are uniformly distributed in the drift gap. Figure 4.15 shows the evolution of the distribution of the distance between the first GEM foil and its closest cluster as a function of the number of clusters.

As shown in Figure 4.16, in the case of $Ar/CO_2/CF_4$ (45:15:40), a minimum ionizing particle releases on average $\sim$ 15 clusters over 3 mm of gas according to GARFIELD. Figure 4.17 shows the distribution of the distance between the first GEM foil and its closest cluster for a number of clusters taken randomly following a Poisson distribution with a mean value equal to 15. The RMS of this distribution is equal to 0.22 mm.

Another effect that affects the time fluctuation due to the primary electron clusters is the transparency of the GEM foil. As presented in section 3.7.3, the transparency of a GEM foil is defined as the probability that an electron which enters into a GEM hole exits that hole. The transparency depends on the gas mixture, the voltage applied to the GEM (ΔV_{GEM}) and both the electric fields above ($|E_{above}|$) and below ($|E_{below}|$) the GEM foil.

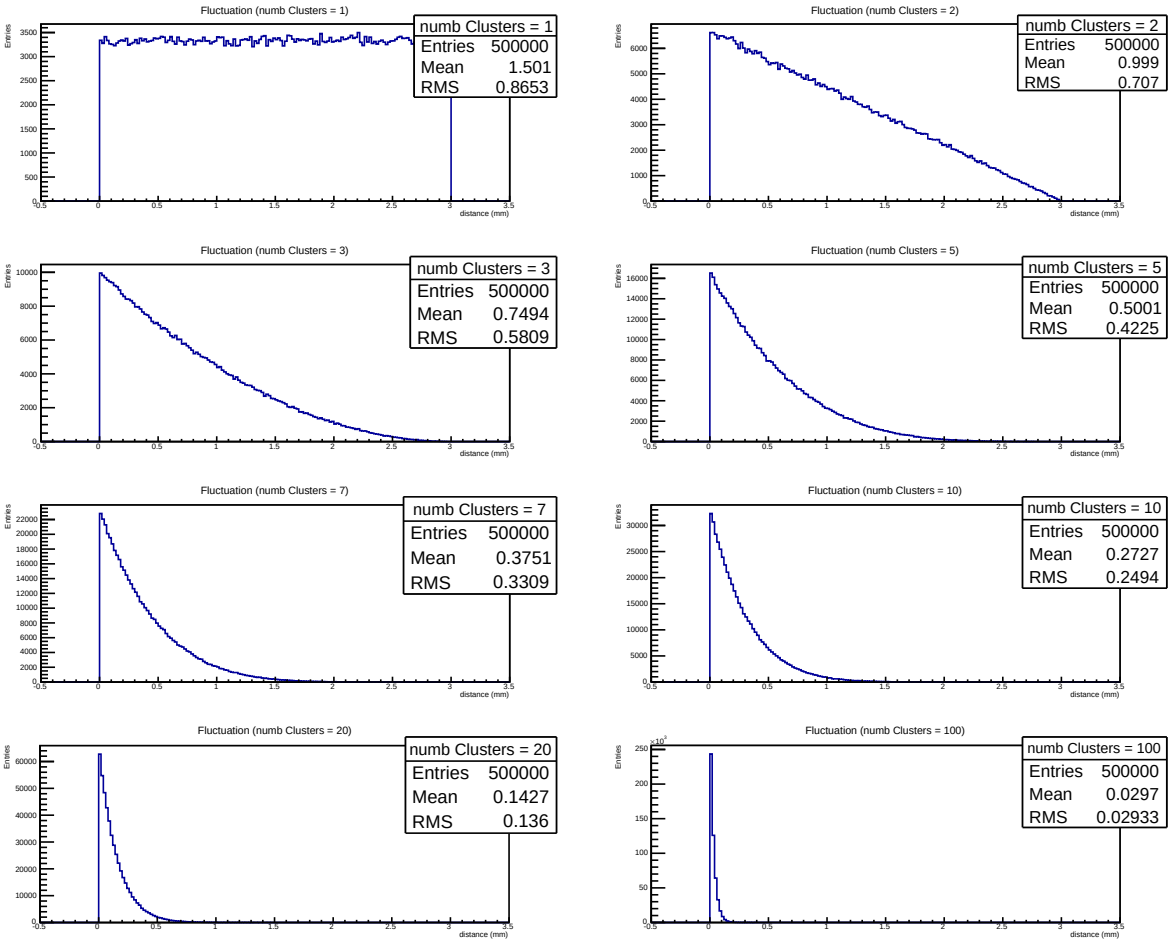

FIGURE 4.15: Evolution of the distribution of the distance between the closest cluster and the first GEM foil binned by cluster multiplicity.

As shown in Figure 4.18, in the $Ar/CO_2/CF_4$ (45:15:40) gas mixture and for the 'standard' condition of the first GEM foil ($\Delta V_{GEM} = 450$ V, $|E_{above}| = 3$ kV/cm and $|E_{below}| = 3.5$ kV/cm), the transparency is equal to 84.5%. This means that in 15.5% of the cases the primary cluster closest to the GEM foil will not create an avalanche and will not contribute to the signal. Therefore it is the next cluster which may be the first to contribute to the signal. Figure 4.19 shows the distributions of the three next clusters closest to the first GEM foil. The distribution of the distance of the first primary cluster contributing to the signal, shown in Figure 4.20, is therefore the weighted sum of the distributions shown in Figure 4.19 and the distribution shown in Figure 4.17, weighted by the probability of each cluster to be the first to contribute to the signal. The probability for the first cluster is equal to the transparency (0.845), the probability for the second cluster is the transparency times the probability that the first cluster did not contribute ($0.845 \times 0.155 = 0.131$), etc.

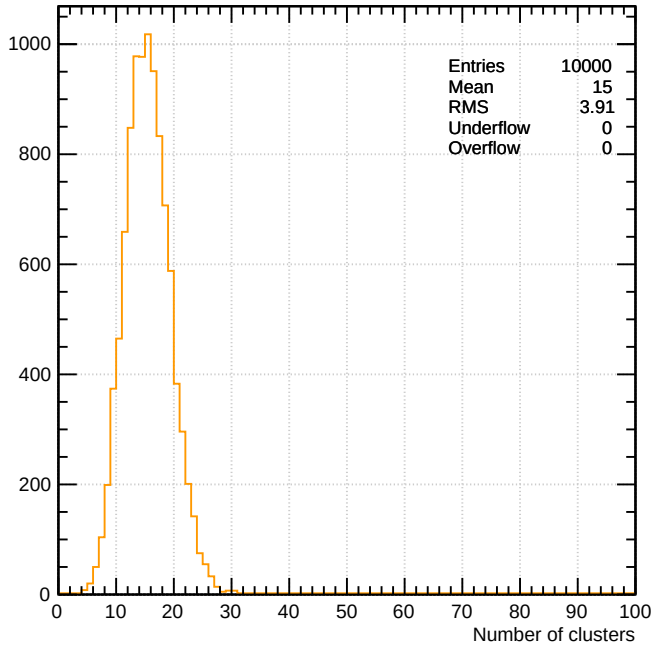

FIGURE 4.16: Number of electron clusters in 3 mm of $Ar/CO_2/CF_4$ (45:15:40) gas mixture produced by a muon of 15 GeV simulated by GARFIELD.

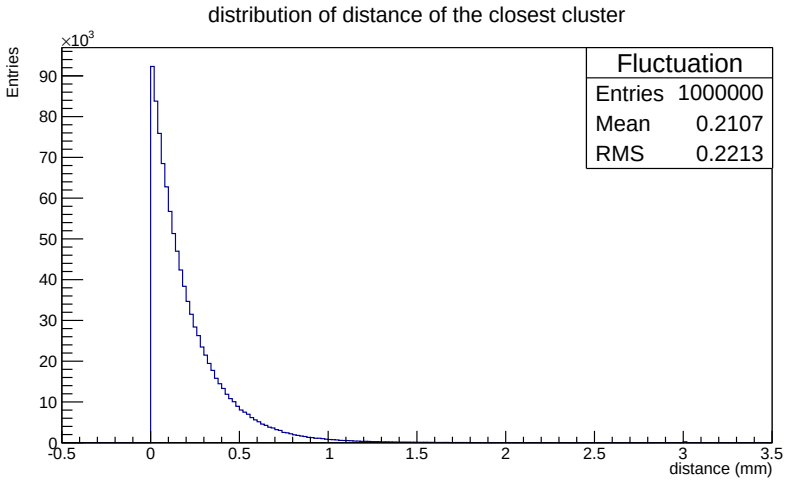

FIGURE 4.17: Distribution of the distance between the first GEM foil and its closest cluster for the $Ar/CO_2/CF_4$ (45:15:40) gas mixture and 3 mm drift gap.

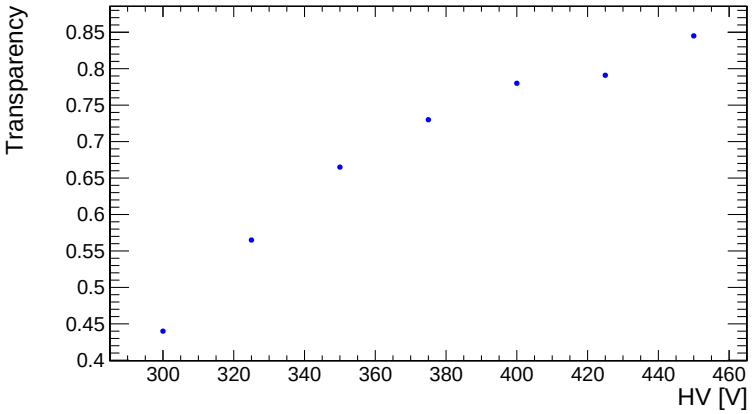

FIGURE 4.18: Transparency as a function of the voltage applied to the GEM foil for $Ar/CO_2/CF_4$ (45:15:40) with drift field of 3 kV/cm and a transfer 1 field of 3.5 kV/cm, simulated with GARFIELD.

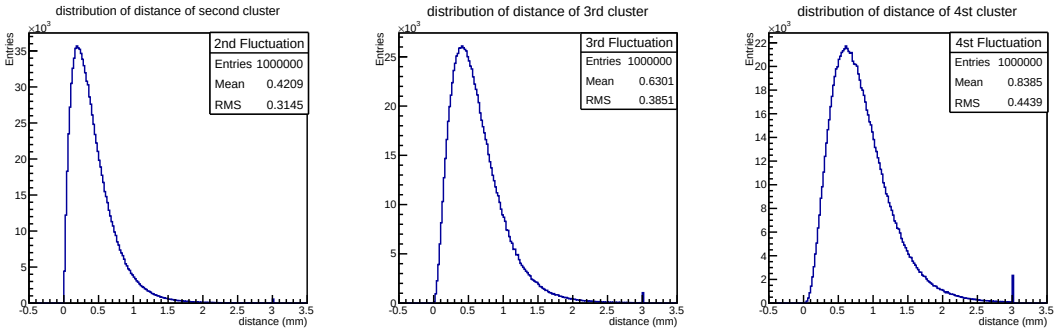

FIGURE 4.19: Distribution of the distance between the second, third and fourth closest clusters respectively and the first GEM foil for the $Ar/CO_2/CF_4$ (45:15:40) gas mixture. The last bin of those distributions are the case when the cluster does not exist (i.e. if only one cluster is produced).

One can note that those distributions are describe by the order statistics distributions [54].

The RMS of the distribution of the distance of the first primary cluster contributing to the signal and the first GEM foil ($\sigma_{position}$), shown in Figure 4.20, is equal to 0.26 mm, to be compared to the value of 0.22 mm if the transparency is not taken into account as shown in Figure 4.17.
This result leads to a fluctuation in time equal to:

$$\sigma_{clusters} = \sigma_{position} \cdot v_{drift}^{-1} = 0.26 \times 10.3 \simeq 2.7\ ns$$

Note that in this work we have neglected the effect due to the fluctuations on the number of electrons per ionization cluster, which is assumed to be small, as well as

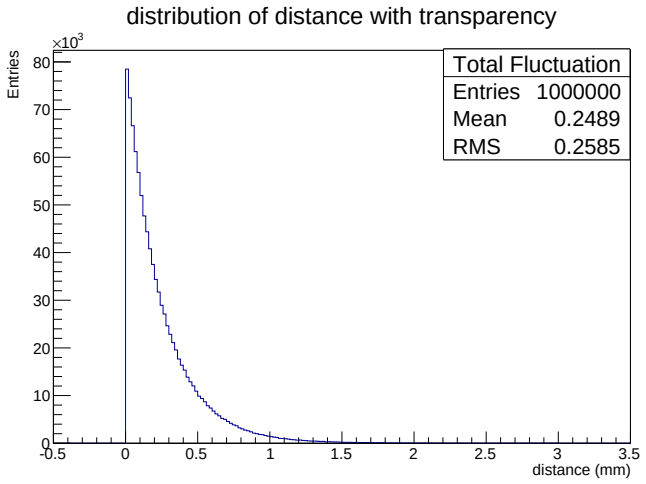

FIGURE 4.20: Distribution of the distance between the first cluster to pass and the first GEM foil for the $Ar/CO_2/CF_4$ (45:15:40) gas mixture.

the fluctuations due to a possible primary electron cluster released in the Transfer 1 gap to provide a signal passing the threshold.

Longitudinal diffusion

The electrons produced in the detector are going to diffuse during their drift towards the anode. The diffusion can be expressed in two terms: the longitudinal and the transverse diffusion. In the present case, the transverse diffusion will not affect the time resolution. However, due to the longitudinal diffusion, the drift time of the electrons may fluctuate. The contribution to the time resolution due to the longitudinal diffusion is equal to:

$$\begin{aligned}\sigma_{diff.L.} &= \left(C_d \cdot \sqrt{L} \cdot v_{drift}^{-1}\right)_{tr} + \left(C_d \cdot \sqrt{L} \cdot v_{drift}^{-1}\right)_{drift} \\ &= 0.025\ \sqrt{mm} \times \sqrt{3\ mm} \times 9.8\ ns/mm + 0.026\ \sqrt{mm} \times \sqrt{0.25\ mm} \times 10.3\ ns/mm \\ &= 0.42 + 0.13 \simeq 0.6\ ns\end{aligned}$$

where C_d is the longitudinal diffusion coefficient, which depends, as the drift velocity, on the electric field which is not the same in the drift and in the transfer regions. L is the drift distance between the closest cluster to the first GEM foil and the induction gap. In our geometry this distance is the mean value of the distribution shown in Figure 4.20 plus the 3 mm between the foil and the induction gap.

Other

There are additional contributions not taken into account: fluctuations on the time of flight of the incoming particle, ionization cluster size, gain fluctuation,

Contributions	**Ar/CO_2** (70:30)	**Ar/CO_2/CF_4** (45:15:40)
Primary clusters	4.5 ns	2.7 ns
Longit. diff.	1.5 ns	0.6 ns

TABLE 4.3: Contributions on the time resolution for the primary clusters of electrons and for the longitudinal diffusion for both gas mixtures.

electronics threshold, electronics noise, etc. Those fluctuations are difficult to compute and are not estimated in this work.

Ar/CO_2 (70:30)

The same computation can be done for other gas mixtures.

In the case of Ar/CO_2 (70:30), the contribution due to the primary ionization clusters is the following:

$$\sigma_{clusters} = \sigma_{position} \cdot v_{drift}^{-1} = 0.31 \times 14.5 \simeq 4.5\ ns,$$

and the contribution due to the longitudinal diffusion:

$$\begin{aligned}\sigma_{diff.L.} &= \left(C_d \cdot \sqrt{L} \cdot v_{drift}^{-1}\right)_{tr} + \left(C_d \cdot \sqrt{L} \cdot v_{drift}^{-1}\right)_{drift} \\ &= 0.045\ \sqrt{mm} \times \sqrt{3\ mm} \times 14.1\ ns/mm + 0.045\ \sqrt{mm} \times \sqrt{0.31\ mm} \times 14.5\ ns/mm \\ &= 1.10 + 0.36 = 1.46\ ns\end{aligned}$$

The comparison of those contributions between both gas mixtures is summarized in the table 4.3.

The discrepancies between both gas mixtures can be explained by the differences in the parameters of those gas mixtures. The longitudinal diffusion is higher in the Ar/CO_2 (70:30) gas mixture: the difference is around 0.006 $\sqrt{cm}$ when the electric field is higher than 3 kV/cm. The number of primary ionization clusters in this mixture is lower than in the Ar/CO_2/CF_4 (45:15:40) gas mixture: 4.9/1 mm on average for Ar/CO_2/CF_4 (45:15:40) against 3.8/1 mm for Ar/CO_2 (70:30). Finally, the main difference between those two gas mixtures is the drift velocity that is higher by $\sim 25\%$ at $E \geqslant 3$ kV/cm with the addition of CF_4 (as shown in Figure 4.5).

Summary of the fluctuations

The time resolution estimated with the GARFIELD simulation is around 4.5 ns for Ar/CO_2/CF_4 (45:15:40) as shown in Figure 4.13. The main contribution to the time resolution is the fluctuation due to the primary ionization clusters and in particular the position of the first cluster contributing to the signal. It has been shown that this fluctuation amounts to 2.7 ns without taking into account the

fluctuation of the number of electrons in each cluster. With this observation, this contribution to the time resolution is assumed to be the most important.
The comparison between both gas mixtures has been done and shows that the $Ar/CO_2/CF_4$ (45:15:40) gas mixture gives a better time resolution.
The difference in terms of time resolution between the two gas mixtures will be studied by simulations and the results will be detailed in section 4.3.7.

4.3 FastSim

As described in section 4.1 GARFIELD computes at each collision with a gas molecule the probability for attachment, ionization and inelastic collisions. This provides an accurate simulation of the electron drift in the gas, but it is also very time consuming when we want to simulate avalanche with high gains. This is even more true for detectors where the avalanche occurs at large distance ($\sim$ 1mm) from the anode. Therefore we have developed a dedicated parameterized simulation called FastSim in the framework of the GE1/1 upgrade project.
The goal of this simulation is to provide a fast simulation of the Triple-GEM detector fully parameterized using the input of GARFIELD. The purpose is to be able to produce, quickly and easily, signals for different configurations, like gap geometry, strip pitch, gas, etc.
One of the main advantages of the FastSim is the simulation time. Depending on the geometry (i.e. the number of strips), the full GARFIELD simulation of the signal induced on the anodes by a muon in a CMS Triple-GEM detector can take several hours. The time it takes to simulate a similar signal with the FastSim is of the order of the second.
The structure of this section is the following: a global overview of the simulation will be given, then the different classes of our simulation will be reviewed in detail. Finally, some results will be compared to a full GARFIELD simulation and to experimental data as well.

4.3.1 Structure of the simulation

The FastSim is implemented in C++ interfaced with ROOT [55] and is composed of five classes: *Geometry*, *Electrons*, *Track*, *Gain*, and *Electronics*.
The simulation uses those classes to produce a two-dimensional simulation of a Triple-GEM detector (Figure 4.21) and to compute the electronics signal according to different configurations.
Firstly, the simulation creates a detector configuration by fixing the geometry and the

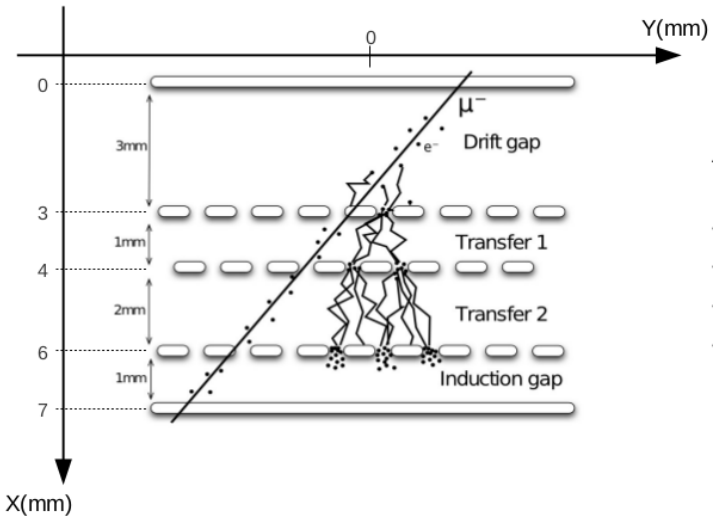

FIGURE 4.21: Coordinate system of the FastSim.

gas properties.
Secondly a muon track is created in this geometry, producing primary electrons along its path. The drift of the primary electrons towards the anode plane, their diffusion as well as their multiplication inside the gas are parameterized.
Next, the electrons arriving above the readout strip induce a signal.
Finally, the induced signal is convoluted with the electronics transfer function and the track reconstruction is performed.

4.3.2 Geometry

The *Geometry* class defines the detector geometry and the gas properties.

Detector Geometry Configuration The geometry configuration of the detector in the FastSim is defined by six attributes: the X positions of the three GEM foils, the X position of the anode plane, the read-out strip pitch and the number of strips. All the positions are defined by the distance to the cathode plane that is the origin coordinate of the X axis as shown in Figure 4.21. The configuration used to simulate the Triple-GEM for the GE1/1 upgrade project is the following: the first GEM foil is placed at 3 mm away from the cathode plane, the second foil is placed at 4 mm, the third at 6 mm and the anode plane at 7 mm.

The strip pitch can be varied between 0.6 and 1.2 mm. The number of strips is fixed to 128 that corresponds to one sector of the Triple-GEM read by the VFAT3 ASIC.

Gas Properties The gas properties are defined by three parameters: the drift velocity, the longitudinal and transverse diffusion coefficients. Those parameters, that depend on the gas mixture and the electric field, have been obtained from Magboltz [46]. Figure 4.5 shows the evolution of the drift velocity as a function of the electric field for the two gas mixtures foreseen in the CMS GEM project ($Ar/CO_2/CF_4$ (45:15:40) and Ar/CO_2 (70:30)). Figure 4.22 and 4.23 show respectively the evolution of the longitudinal diffusion coefficient and the evolution of the transverse diffusion coefficient for both gas mixtures as a function of the electric field. In a Triple-GEM detector there are

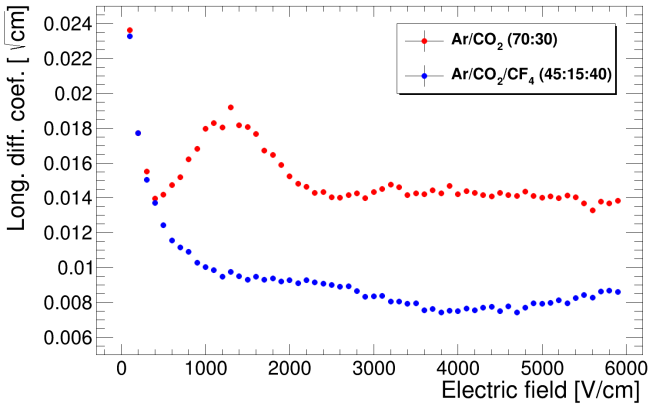

FIGURE 4.22: Evolution of the longitudinal diffusion coefficient as a function of the electric field for the Ar/CO_2 (70:30) and $Ar/CO_2/CF_4$ (45:15:40) gas mixtures simulated by GARFIELD and Magboltz.

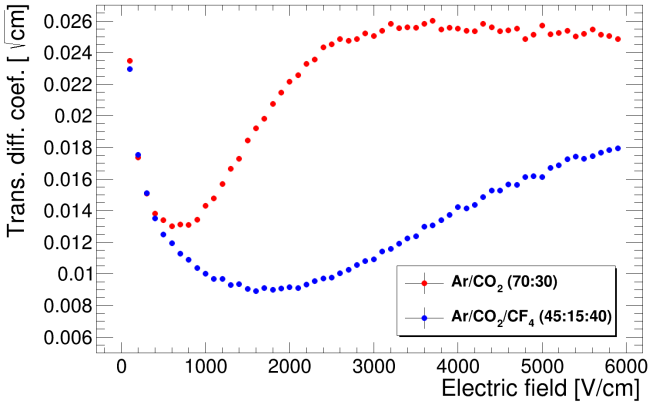

FIGURE 4.23: Evolution of the transverse diffusion coefficient as a function of the electric field for the Ar/CO_2 (70:30) and $Ar/CO_2/CF_4$ (45:15:40) gas mixtures simulated by GARFIELD and Magboltz.

four different gas gaps (as shown in Figure 4.21) and consequently four different electric fields.

To power all the elements of the detector (GEMs and cathode), the CMS GEM collaboration has decided to use a ceramic high-voltage divider [43]. Figure 4.24 shows the

schema of the ceramic high-voltage divider. The electric field inside a gap i ($|E_i|$) is

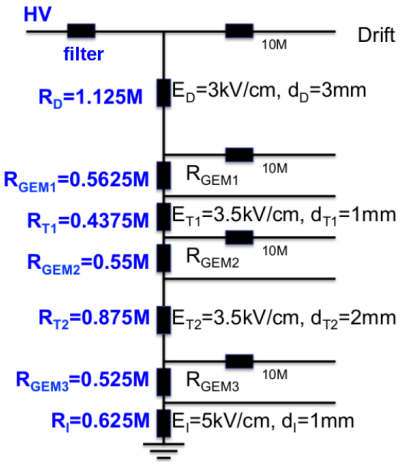

FIGURE 4.24: Ceramic high-voltage divider schema.

computed as follow:

$$|E_i| = \frac{I_{div} \cdot R_i}{D_i}, \tag{4.2}$$

where I_{div} is the divider current, R_i is the resistor of the gap and D_i the size of the gap. Before running the FastSim, for each current a configuration file is created with the three gas parameters for the four different gas gaps. The electric field in each gap is computed using the equation 4.2 and the parameters are taken from the linear interpolation between the two closest points computed with Magboltz.

4.3.3 Muon Track

In the FastSim, a muon track is defined by the primary electron clusters released in the gas volume along a straight line. The track incident angle ϕ is defined from the vertical axis (X) to the strip plane.
First the incident track perpendicular to the anode plane ($\phi = 0°$) will be described, then the non-perpendicular case will be discussed.
The perpendicular track is defined by a number of electron clusters uniformly distributed in the geometry (between 0 and 7mm along the X axis) at a Y coordinate Y_0. The number of clusters is taken randomly following a Poisson distribution. The distribution of the number of electron clusters created by a muon has been studied with GARFIELD for the two gas mixtures and are shown in Figure 4.25 and 4.26.

Each cluster has a certain number of electrons. The ionization cluster size distribution is the probability distribution of the number of electrons ionized directly or indirectly

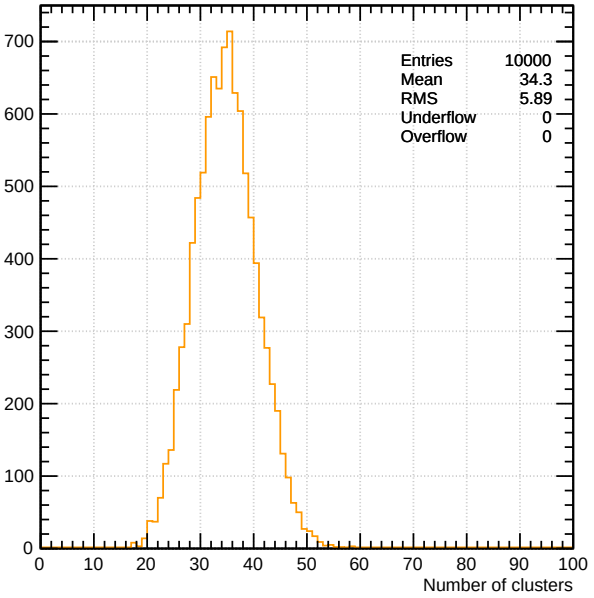

FIGURE 4.25: Number of electron clusters in 7 mm of $Ar/CO_2/CF_4$ (45:15:40) gas mixture produced by a muon of 15 GeV simulated by GARFIELD.

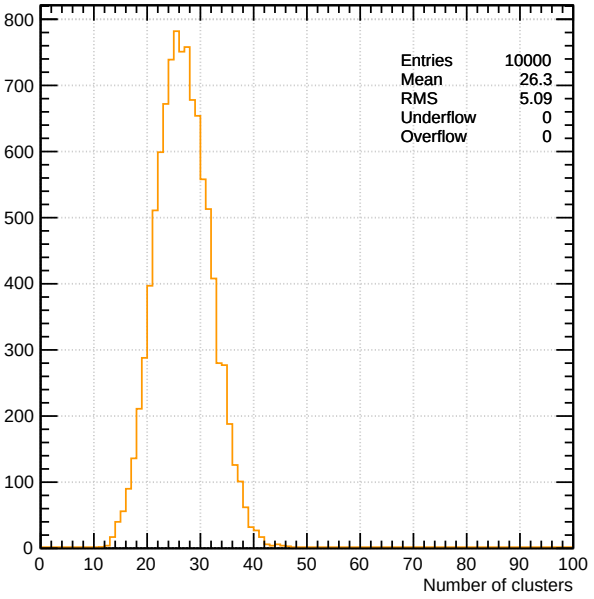

FIGURE 4.26: Number of electron clusters in 7 mm of Ar/CO_2 (70:30) gas mixture produced by a muon of 15 GeV simulated by GARFIELD.

by each primary encounter. It has been carefully studied experimentally for argon and carbon dioxide and the results are described elsewhere [20], while in the case of tetrafluoromethane (CF_4) it has been simulated with GARFIELD. Figure 4.27 shows the ionization cluster size distribution for the three gases. The last bin of those distributions is the probability to have twenty or more electrons in one cluster, which is necessary for the probability normalization.

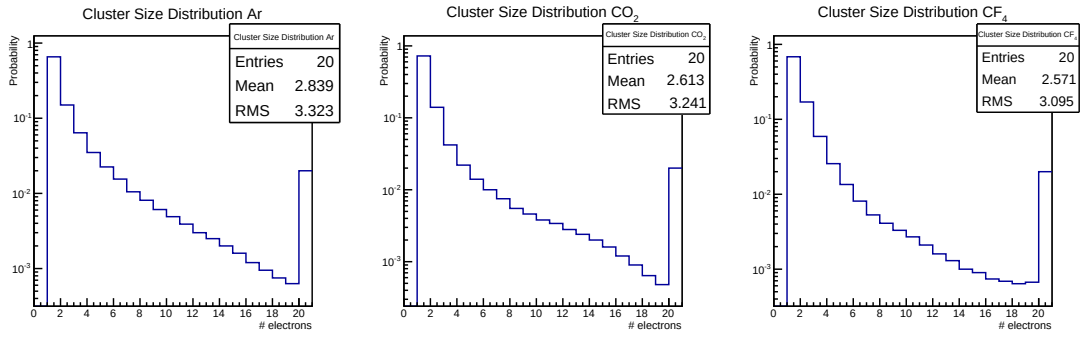

FIGURE 4.27: Ionization cluster size distribution for argon, carbon dioxide and tetrafluoromethane.

For each cluster, the number of electrons is drawn randomly from the ionization cluster size distribution corresponding to one of the gas. The gas is chosen with a probability equal to its percentage in the mixture.

For non-perpendicular tracks, the electron clusters are uniformly distributed in the geometry according to $Y = Y_0 + \tan\phi\, X$. By definition, an inclined track will create more clusters due to the longer trajectory in the gas volume. The number of clusters is computed in the same way as the straight track and then multiplied by $\dfrac{1}{\cos\phi}$.

Figure 4.28 shows an example of a perpendicular 15 GeV muon track simulated by the FastSim, in other terms the distribution of primary electrons as a function of the distance in the triple-GEM detector. In this case, 25 clusters have been created, and the number of electrons per cluster lies between 1 and 10. In total 57 primary electrons have been produced by this track.

4.3.4 Electrons

In the FastSim, an electron is represented by a class with four attributes: the position in X and Y, the time and the geometry of the detector. When an electron is created by the muon track, the X and Y coordinates are set to the position of the cluster (see previous section) and the time is set to zero. Afterward each electron will drift to the anode plane.

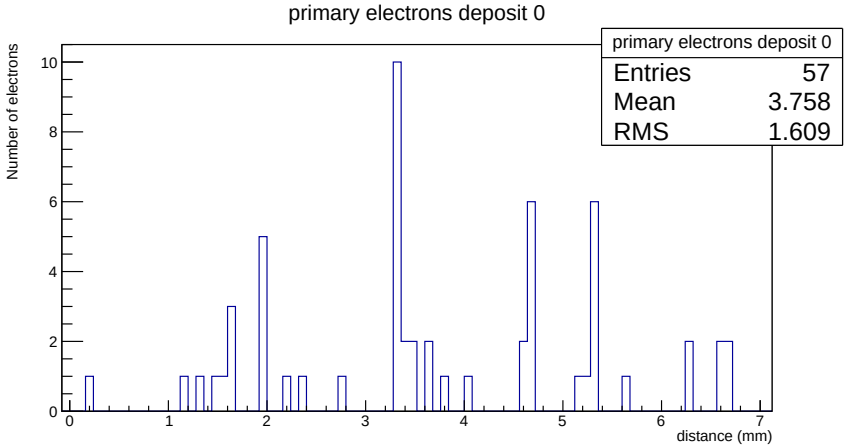

FIGURE 4.28: Cluster sizes along a perpendicular muon track of 15 GeV in Ar/CO_2 (70:30) gas mixture.

The algorithm for the drift and the diffusion of the electrons is based on the equations presented in section 3.3:

1. Starting with a state of the electron: $e^- = (X_i, Y_i, t_i)$, the distance D between X_i and the position of next GEM foil (X_{GEM_i}) or the anode plane (X_{strips}) is computed.

2. The standard deviation of the transverse diffusion is computed with:

$$\sigma_d = C_{transverse} \cdot \sqrt{D},$$

   where $C_{transverse}$ is the transverse diffusion coefficient.

3. The new Y position (Y_{i+1}) of the electron is randomly chosen according to a Gaussian with a mean of Y_i and a sigma of σ_d.

4. The X position of the electron is updated to the position of the GEM foil or the anode plane.

5. The new time (t_{i+1}) is computed as follow:

$$t_{i+1} = t_i + D \cdot (v_{drift})^{-1} + \overline{\sigma_{time}},$$

   where $\overline{\sigma_{time}}$ is a random number taken from a Gaussian distribution with a mean value of zero and the following σ_{time}:

$$\sigma_{time} = C_{longitudinal} \cdot \sqrt{D} \cdot (v_{drift})^{-1},$$

where $C_{longitudinal}$ is the longitudinal diffusion coefficient and v_{drift} the drift velocity.

The new state of the electron is updated to: $e^- = (X_{i+1}, Y_{i+1}, t_{i+1})$.
This algorithm runs until the X position reaches X_{strips}.

4.3.5 Gas Gain

During the drift in the gas volume the electrons will undergo an amplification at $X_i = X_{GEM_i}$, the position of the three GEM foils. This amplification is computed with the *Gain* class.
The *Gain* class will add new electrons to the existing collection of electrons. The state of those electrons is the same as the state of the original electron initiating the amplification, that is $e^-_{new} = e^- = (X_i, Y_i, t_i)$ where $X_i = X_{GEM_i}$.
The gain of each GEM foil is based on GARFIELD simulation. The effective gain depends on the gas mixture, the voltage applied to the GEM (ΔV_{GEM}) and both the fields above ($|E_{above}|$) and below ($|E_{below}|$) the GEM foil.
The Figures 4.29, 4.30 and 4.31 show the effective gain as a function of the voltage applied to the foil for three different configurations of the electric field. The three configurations are the typical configuration for the three GEM foils in the CMS Triple-GEM detector. As explained in section 4.3.2, for each current the voltage applied to the GEM foil via the divider can be computed.

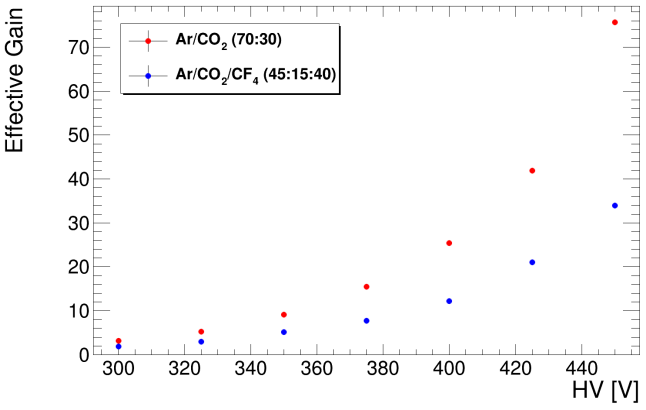

FIGURE 4.29: Effective gain as a function of the voltage for GEM 1 ($|E_{above}| = 3$ kV/cm ; $|E_{below}| = 3.5$ kV/cm) simulated by GARFIELD.

It has been shown [20] that gain fluctuations in proportional counters follow the Polya distribution:

$$P(x) = \frac{\alpha}{\mu} \cdot \frac{1}{(\alpha - 1)!} \cdot \left(\frac{\alpha \cdot x}{\mu}\right)^{\alpha - 1} \cdot \exp\left(\frac{-\alpha \cdot x}{\mu}\right),$$

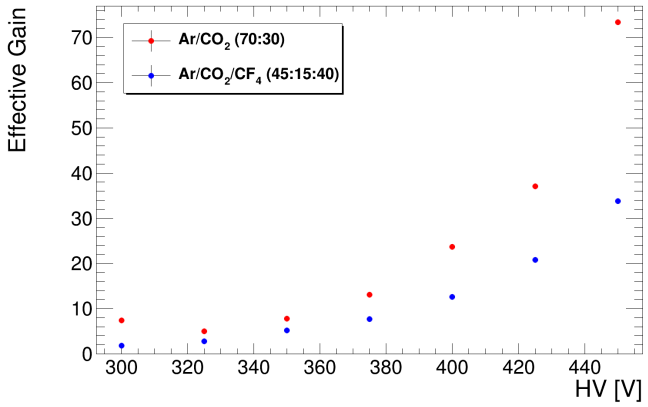

FIGURE 4.30: Effective gain as a function of the voltage for GEM 2 ($|E_{above}|$ = 3.5 kV/cm ; $|E_{below}|$ = 3.5 kV/cm) simulated by GARFIELD.

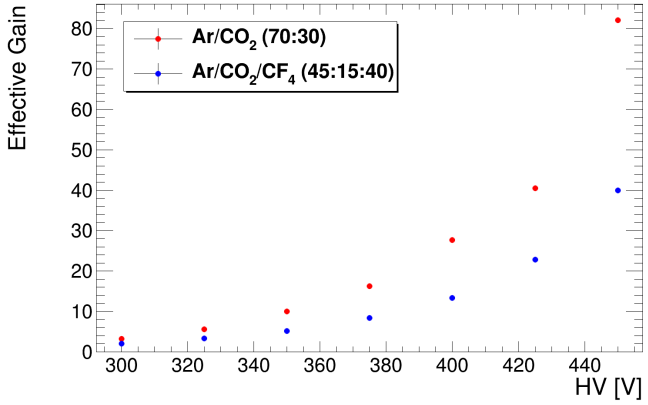

FIGURE 4.31: Effective gain as a function of the voltage for GEM 3 ($|E_{above}|$ = 3.5 kV/cm ; $|E_{below}|$ = 5 kV/cm) simulated by GARFIELD.

where μ is the mean of the distribution and α is called the Polya parameter.
It has been shown [56] that the Polya parameter is of the order of unity for argon gas mixtures. The Polya distribution becomes an exponential if $\alpha = 1$. Therefore the number of electrons created during an avalanche in the FastSim is a random number taken from an exponential distribution with a mean value given by the effective gain computed with GARFIELD.

Since the effective gain is the ratio of the number of electrons inducing a signal and the number of primary electrons, most of the processes that affect the number of electrons inducing a signal (like the attachment, the Penning effect, the transparency) are indirectly included in the FastSim where we used the effective gain provided by GARFIELD. However, as explained in section 4.2.4, the shape of the signal affects the time resolution. For this reason the transparency has also been implemented separately in the simulation. In this case, instead of lowering the global gain of the detector the transparency removes

a certain number of electrons before each GEM foil. The probability for an electron to be removed is equal to '1− transparency'.
This method can be activated in the simulation if the study requires the shape of the signal and not the average gain, as the time resolution study.

4.3.6 Electronics

The *Electronics* class computes the raw induced signal, performs the convolution with the electronics transfer function to obtain the shaped signal, records the number of hit-strips and reconstructs the position of the muon with two different algorithms. The position reconstruction is done by simulating a binary or an analog readout. These steps are described in detail in the following.

Induction of the Raw Signal In the FastSim, the electrons start to induce a current on the anodes just after the third GEM foil, when they enter the induction gap, since the GEM foils screen the electric charge before that point. The induced current is therefore very close to the one recorded in a parallel plate geometry.
In the FastSim the induced current is computed on an infinite anode plane. As presented in section 3.6.3 the current is given by equation 3.11. In the case of two parallel electrodes, the electric current ($I(t)$) induced by a charge q becomes:

$$I(t) = -q \cdot v_{drift} \cdot \frac{1}{D(t)}, \tag{4.3}$$

where v_{drift} is the drift velocity of the charge and $D(t)$ the distance between the charge and the strip at time t.
According to Eq. 4.3, the time of induction t_{ind} is:

$$t_{ind} = \frac{D_{ind}}{v_{drift}},$$

where D_{ind} is the distance of induction of the charge. In the simulation this distance is equal to the size of the induction gap for every electrons except the primary electrons created directly in the induction gap. For those electrons the distance of induction is the distance between their position of creation and the position of the anode plane.
In the FastSim the induced signal consists in a histogram with a binning of 1 ns. Each electron fills n bins of the histogram with n equal to t_{ind} starting with the bin equal to the time when the electron exits the third GEM foil and enters the induction gap. Each bin is filled with $\frac{1}{D(t)}$ so that this algorithm can give an induced current in arbitrary units (since q and v_{drift} are constant in the gap).
Figure 4.32 shows such an induced signal created with the FastSim.

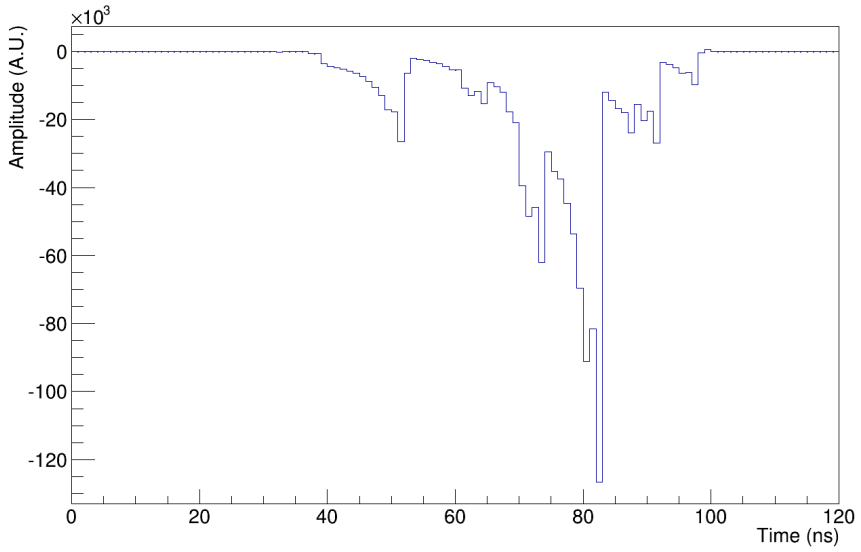

FIGURE 4.32: Induced signal for a perpendicular 15 GeV muon in Ar/CO_2 (70:30) gas mixture.

The shape of the signals computed with the FastSim is comparable to the shape found with the GARFIELD simulation (as shown in Figure 4.3).
The choice to compute the induced current on an infinite anode plane instead of separate strips and to use arbitrary units is led by the fact that the shape of the signal is only used for the time resolution analysis. Indeed, the efficiency and the spatial reconstruction use the charge collected by the strips but not the shape of the signal. The charge collected by each strip is computed separately in the FastSim. This choice has been made to keep the FastSim computations 'simple'. We will see in section 4.4.3 that the anode segmentation has a little impact on the time resolution.

Front-End Shaper The front-end electronics foreseen for the CMS Triple-GEM is the VFAT3 as explained in section 4.2.2.
The two possible VFAT3 designs are implemented in the FastSim. The simulation of this electronics is done by convoluting the induced anode current with the VFAT3 transfer function (Eq. 4.1). The convolution is discrete and uses the binning of the raw signal (1 ns).

Strips and Spatial Reconstruction In the FastSim, the spatial reconstruction is done for two algorithms. Those algorithms represent two cases of read-out electronics: the analog (where the charge is recorded) and the binary (where the recording is done only if the charge is above the threshold).
Given the detector geometry and the large size of the strips with respect to the electron transverse diffusion, a strip is considered as hit by an electron when its final Y position

is within the range $[\frac{-pitch}{2}, \frac{pitch}{2}]$ around the center of the strip. Therefore it is easy to represent the anode plane by an histogram where each bin represents one strip of width equal to the strip pitch. Each electron drifting into the induction gap will create an entry in the bin corresponding to the strip it hits. When the histogram is filled, the electronics threshold is applied. The threshold of the VFAT3 is programmable and is expressed in VFAT unit (VU) [42]. The VFAT unit can be expressed in the number of electrons[1]:

$$1VU = 0.08fC = 500e^{-}$$

For each bin, the number of electrons is compared with the threshold expressed in number of electrons.

In the case of the binary read-out, if the number of electrons is below the threshold, the output is set to zero. If the number of electrons is above the threshold, the output is set to one.

In the case of the analog read-out, if the number of electrons is below the threshold, the output is also set to zero. If the number of electron is above the threshold, the output is set to the number of electrons. This output gives the information of the charge.

Binary Read-out For a binary read-out chip, all adjacent strips with a collected charge above a given threshold are considered. The reconstructed position of the charged particle track with the binary read-out (Y_{bin}) is the geometrical center of those strips:

$$Y_{bin} = \frac{1}{N} \sum y_i,$$

where N is the number of hit strips and y_i is the middle position of the strip i.

Center of Gravity The position reconstructed with the CoG method (Y_{CoG}) is computed using the following formula:

$$Y_{CoG} = \frac{1}{q_{tot}} \sum q_i y_i,$$

where q_{tot} is the total number of electrons, i is the strip number, q_i is the number of electrons on that strip.

4.3.7 Results

Time Resolution The time resolution has been studied with the FastSim signals. The goal is to compare the results obtained with the FastSim signals with the time resolution obtained with the GARFIELD simulation study presented in section 4.2.

[1] Since the VFAT3 chip was still under design while performing this analysis, these numbers are based on the VFAT2 design.

The CFD method has been chosen for this comparison since it is the algorithm that will be implemented in the VFAT3 electronics [57].
The CFD method has been applied to the convoluted signals (with the VFAT_n3 design) for the five different peaking times (20, 50, 75, 100 and 200 ns).
To compare the resolution obtained with both simulation signals, the parameters used in the FastSim have been chosen to be the same as the one used in the GARFIELD simulation:

- the geometry of the gaps is 3:1:2:1 mm;
- the electric fields for the different gaps are 3/3/3/5 kV/cm;
- the voltage applied to the GEM foils is 400 V;
- the gas mixture is $Ar/CO_2/CF_4$ (45:15:40);
- the muon energy is set to 1.5 GeV.

For further discussions, this set of parameters will be called 'non-standard' parameters with respect to the 'standard' parameters defined in section 3.7.3.
At 1.5 GeV 12 primary clusters of electrons are created on average in 3 mm of $Ar/CO_2/CF_4$ (45:15:40) against 15 for a muon of 15 GeV. As explained in section 4.2.4, the number of primary clusters of electrons affect the time resolution. The number of primary clusters in the FastSim has been also changed for this comparison.
Figure 4.33 shows the time resolutions for both simulations as a function of the peaking time of the VFAT3 electronics. With the FastSim, the time resolution has been computed with and without the transparency.

The time resolution appears to be over-estimated with the FastSim when the transparency is disabled. Indeed, the values of the resolution show a discrepancy of 5 to 12% between the FastSim without transparency and GARFIELD. When the transparency is activated, the time resolution is degrading slightly as expected (see section 4.2.4) and is getting closer to the GARFIELD results except for the 25 ns peaking time. The discrepancy for the other peaking times is less than 7%.
It is important to note that despite the simplification of the FastSim compared to the GARFIELD simulation, the results of the FastSim are very satisfying: in absolute values, the differences are smaller than 0.5 ns.
Figure 4.34 and 4.35 show the time resolution as a function of the VFAT_n3 peaking time for the 'standard' and 'non-standard' simulation parameters obtained by the FastSim, respectively without and with the simulation of the transparency.

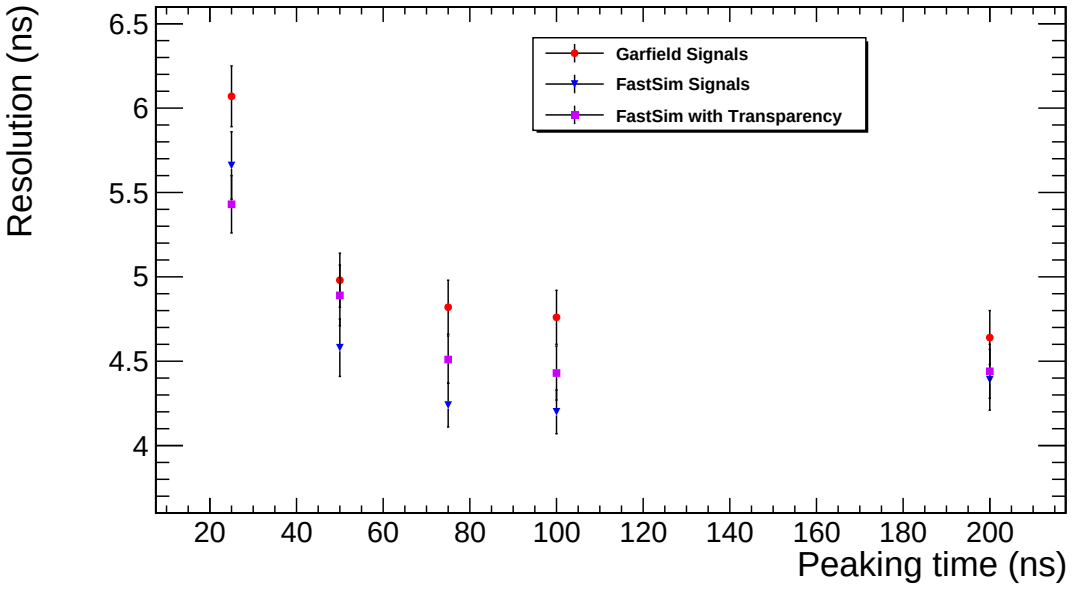

FIGURE 4.33: Time resolution computed with the CFD method for both the GARFIELD simulation and the FastSim as a function of the VFAT_ n3 peaking time for a gas mixture of $Ar/CO_2/CF_4$ (45:15:40).

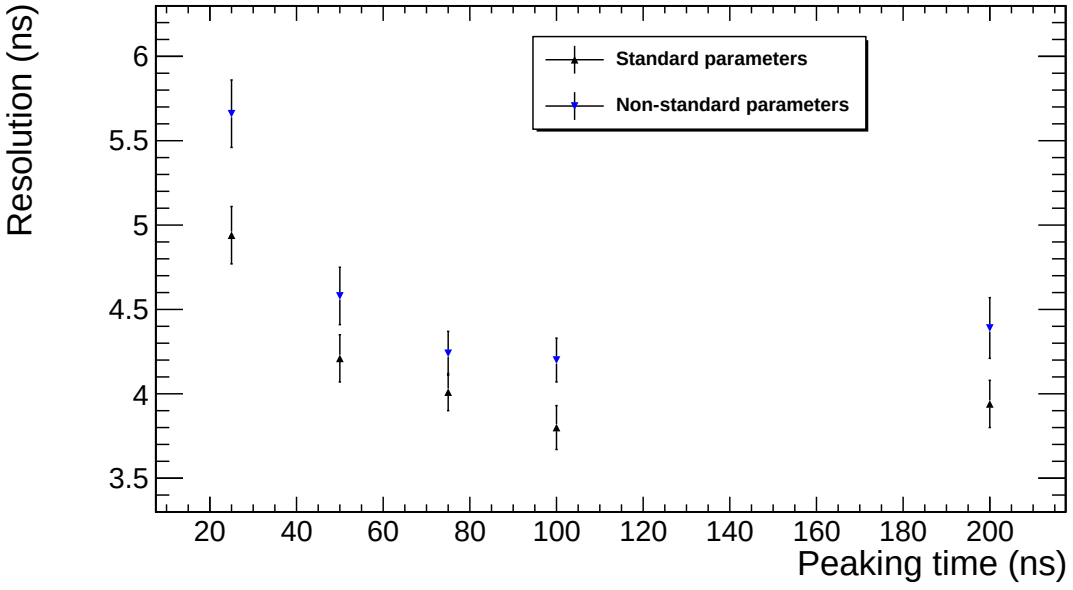

FIGURE 4.34: Time resolution computed with the CFD method for the FastSim without transparency as a function of the VFAT_ n3 peaking time for a gas mixture of $Ar/CO_2/CF_4$ (45:15:40) for the 'non-standard' parameters and the 'standard' parameters.

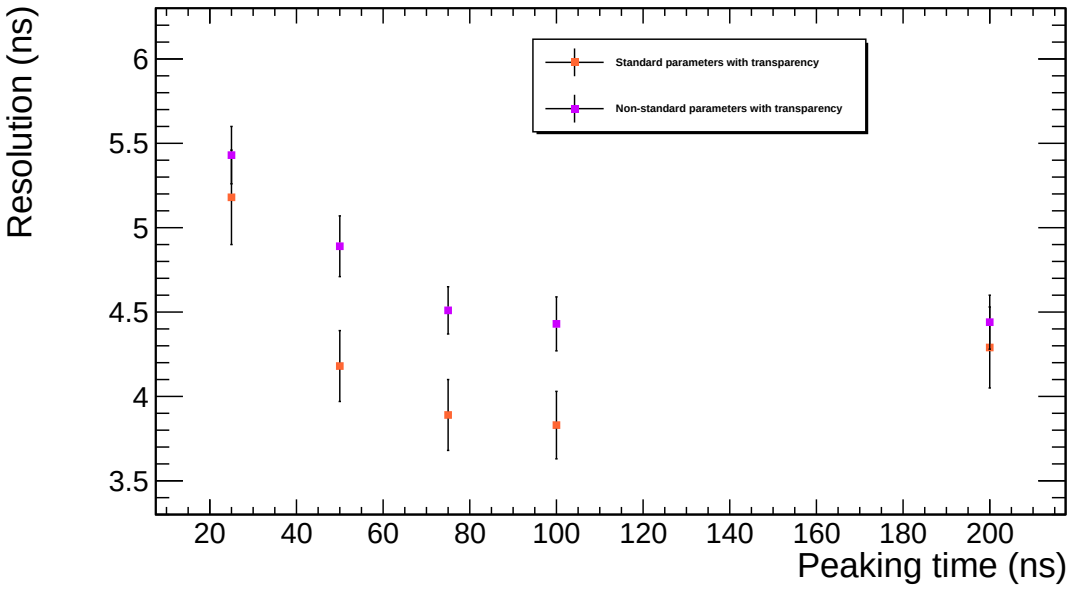

FIGURE 4.35: Time resolution computed with the CFD methods for the FastSim with transparency as a function of the VFAT_n3 peaking time for a gas mixture of $Ar/CO_2/CF_4$ (45:15:40) for the 'non-standard' parameters and the 'standard' parameters.

Those results show that the time resolution improve when we use the 'standard' parameters which have been optimised for that purpose [42]. This is now easily understandable since several of the processes that contribute to the time fluctuation are affected by the parameters of the simulation: the number of primary electron clusters, the electric fields which affect the drift velocity and, finally the voltage applied to the GEM foils which affect the transparency.

Finally, the time resolution has been computed with the FastSim for Ar/CO_2 (70:30). The Figure 4.36 shows the time resolution obtained with the FastSim for 3550 V at the voltage divider instead of 4000 V for $Ar/CO_2/CF_4$ (45:15:40). The voltage is put at a lower value since the gain in Ar/CO_2 (70:30) is higher than for the $Ar/CO_2/CF_4$ (45:15:40) gas mixture.

The time resolution is equal to 6.73 ns. This results confirm that the CMS Triple-GEM detector can provide a time resolution better than 10 ns for both gas mixtures.
All the time resolution results are summarized in the tables reported in Appendix A.
It is important to note that the FastSim reproduces very well the measurements shown in Figure 3.22. Although the configurations of the fields and of the gaps (as well as the electronics) that are not exactly the same, the measurements have shown that the best time resolution of 4 ns is achieved with $Ar/CO_2/CF_4$ (45:15:40) while it reaches at best 7 ns for Ar/CO_2 (70:30).

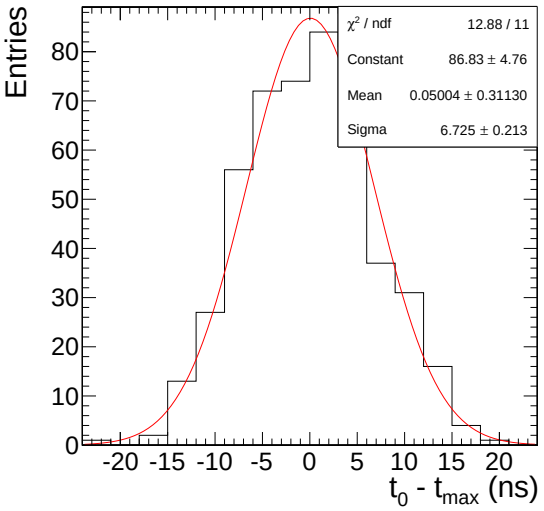

FIGURE 4.36: Time resolution computed with the CFD methods for the FastSim with transparency for the VFAT_ n3 design at a peaking time of 100 ns for a gas mixture of Ar/CO_2 (70:30) for 3550 V at the voltage divider.

Efficiency To further validate the FastSim, we have studied the detector efficiency. This is possible in the context of the upgrade of the CMS muon endcap system, where the performance of large-area GEM detector prototypes have been widely studied. For instance one full-size GE1/1 prototype of 1 m long has been assembled by the Florida Tech group and tested at Fermilab. The results of the beam test done at Fermilab are described in ref.[58].

During this test beam, the detector was operated with Ar/CO_2 (70:30) gas mixture and the APV25 readout electronics [59]. The Florida Tech group has emulated the behavior of the binary output of the VFAT3 chip with an offline reconstruction from the analog APV25 readout. The detector efficiency has been calculated with three different thresholds: 0.8 fC, 0.98 fC and 1.2 fC.

To compare those results with the FastSim, three efficiency curves have been produced with parameters chosen to be as close as possible to the beam test conditions.

The main difference with the parameters described in section 4.3 is the ceramic divider. The values of the different resistors were not the same and consequently the various electric fields have different values. The values of the resistances are shown in the table 4.4.

Figure 4.37 shows the three efficiency curves from the Fermilab test beam and the three efficiency curves computed with the FastSim as a function of the divider current.

The efficiency points found with the FastSim have been fitted with a Sigmoid function ($f(x) = \frac{a}{1+\exp(b\cdot(x+c))}$) and the confidence belts of 68 and 95% are represented in yellow. A shift of 20 μA can be seen between the data and the simulation, but the shape seems

R_D	1 MΩ
R_{GEM1}	0.55 MΩ
R_{T1}	0.5 MΩ
R_{GEM2}	0.5 MΩ
R_{T2}	1 MΩ
R_{GEM3}	0.45 MΩ
R_I	0.5 MΩ

TABLE 4.4: Values of the resistances of the ceramic divider used during the beam test done at Fermilab.

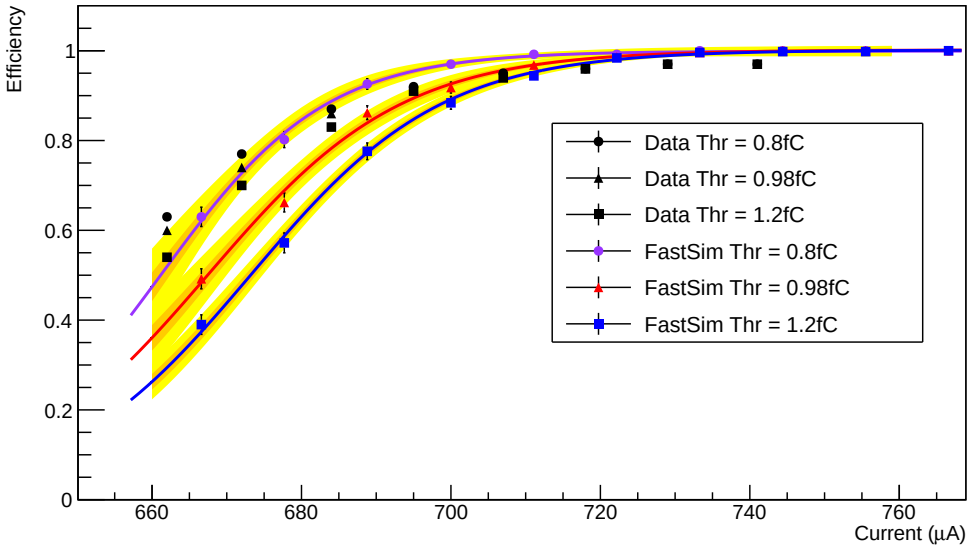

FIGURE 4.37: Efficiency curves as a function of the current from the Fermilab test beam the FastSim for three different thresholds.

to be the same.

The value of maximum efficiency found with the test beam results is equal to 97% against 100% for the FastSim. This is due to the fact that no effect (attachment and transparency) that can reduce the number of electrons inducing a signal is explicitly simulated. These effects are included in the effective gain. Therefore once the gain is high enough, each muon ionizing the gas will create a signal readable by the electronics. Although the agreement is not perfect, it is remarkable that the FastSim efficiency plateau occurs within ±20 μA from the experimental data. The disagreement in the influence of the threshold may also be due to the fact that the measurement have been done with the APV25 readout electronics emulating the VFAT binary readout.

Spatial Resolution We will now compare the spatial resolutions computed by the FastSim for the two reconstruction methods: the Binary read-out (Bin) and the Center-of-Gravity (CoG).

We have produced a sample of 500 events for a detector filled with the $Ar/CO_2/CF_4$ (45:15:40) gas mixture, a strip pitch of 0.817 mm, the current in the divider was set to 800 μA and the threshold put at 1 fC. The Figure 4.38 shows the residuals between the reconstructed hit and the simulated hit for both methods.

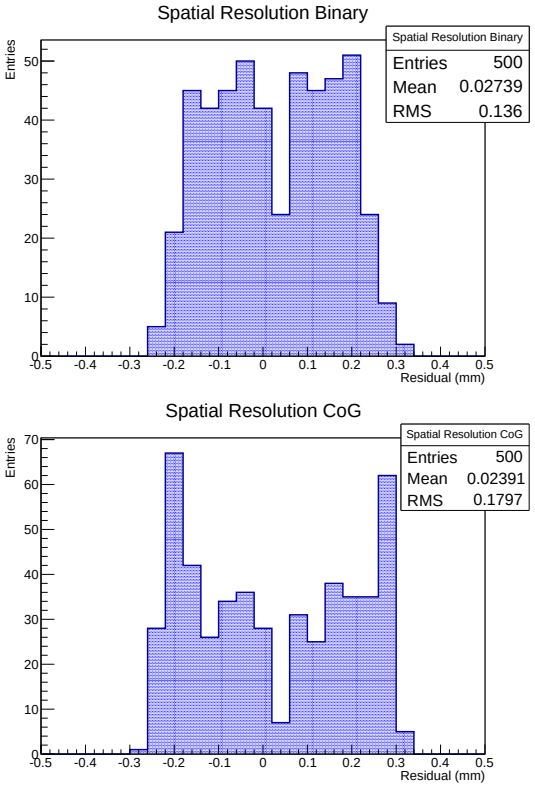

FIGURE 4.38: Residuals between the reconstructed hit and the simulated hit for both methods.

We can observe that for this set of parameters, the CoG method gives a RMS of $\sim$ 0.18 mm against $\sim$ 0.14 mm for the Bin method. This result seems to suggest that the binary readout could lead to a better spatial resolution than the analogue readout using a CoG method.

We will study in detail this unexpected result in the chapter 6.

4.4 Hybrid Simulation

The idea of the Hybrid simulation is to combine the FastSim with the GARFIELD simulation. This combination allows to keep the flexibility and speed of the FastSim

with a better computation of the induced signal produced by GARFIELD. Indeed, the induced signal will be computed on each strip for every electron instead of an infinite anode.
The primary goal of this simulation was to study the time resolution and understand the induction of the signal on several strips.

4.4.1 Implementation

The FastSim is used to create the muon track, compute the motion of the electrons and the amplifications. Then, the induction gap is completely simulated with GARFIELD.
The FastSim provides a collection of electrons to GARFIELD. Those electrons are the electrons entering the induction gap just after the third GEM foil ($e^- = (X_{GEM_3}, Y_i, t_i)$) and all the primary electrons released directly in the induction gap.
The detector simulated by GARFIELD is the induction gap with five strips and no amplification step.
Every electron will induce a signal on each of the five strips. The induction of the signal is computed by GARFIELD as presented in section 4.1.

4.4.2 Example of Signals

Figure 4.39 shows the raw signals induced on the five strips. The muon track was generated with $\phi = 0$ and Y_0 equal to the position between the strip 3 and 4 in the $Ar/CO_2/CF_4$ (45:15:40) gas mixture. The strip pitch is 0.6 mm.

The two main signals are shared in between the strips 3 and 4 while on the three other strips the signals induced are negligible. 500 signals have been produced in the same conditions and then convoluted with the VFAT3 transfer function. Figure 4.40 shows the distributions of the maximum amplitude of the 500 shaped signals on the five strips.

The distributions of maximum amplitudes confirm that the signal is mainly shared between the strips 3 and 4.

4.4.3 Time Resolution

To compare the results of the Hybrid simulation with the full GARFIELD simulation, the time resolution of the Hybrid simulation has been repeated with the CFD method (as explained in section 4.2.3).
The electric fields of the three first gaps simulated with the FastSim were 3/3/3 kV/cm,

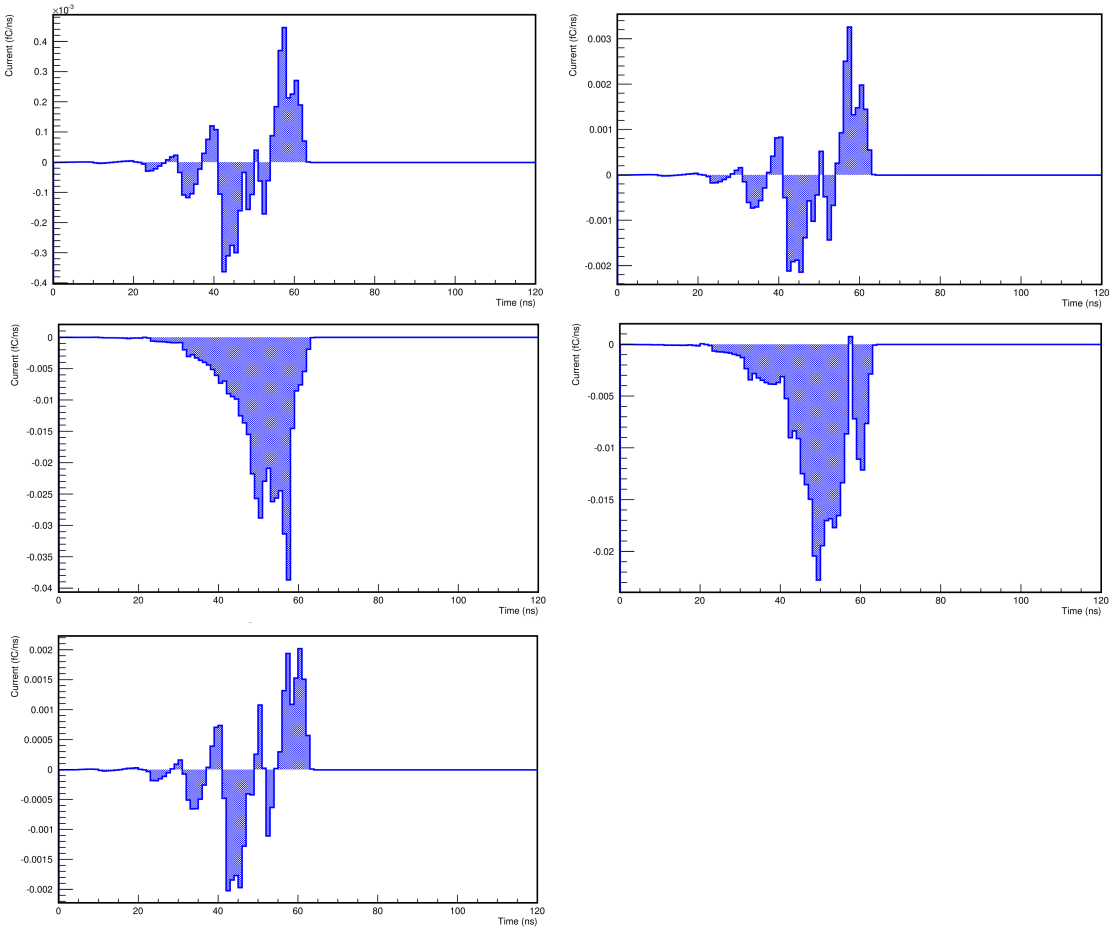

FIGURE 4.39: Raw signals induced on the five strips for perpendicular muon track passing between strip 3 and 4 in the $Ar/CO_2/CF_4$ (45:15:40) gas mixture.

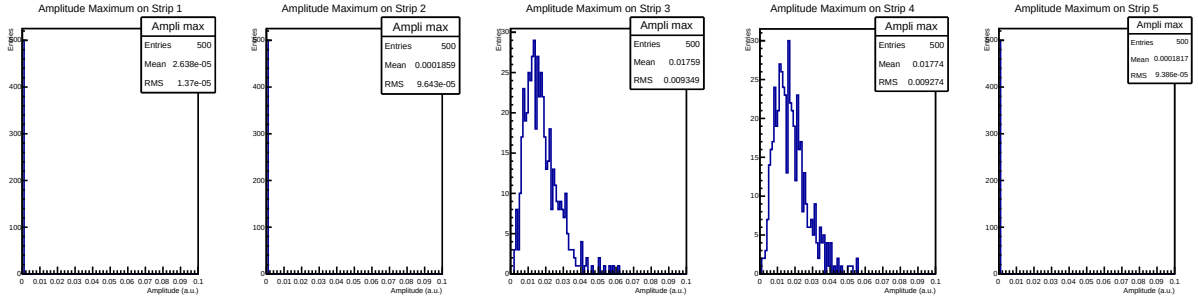

FIGURE 4.40: Distributions of the maximum amplitude of 500 shaped signals on the five strips for perpendicular muon track passing between strip 3 and 4 in the $Ar/CO_2/CF_4$ (45:15:40) gas mixture.

GARFIELD	Hybrid simulation strip 3	Hybrid simulation strip 4	FastSim
4.76 ± 0.16 ns	4.61 ± 0.17 ns	4.54 ± 0.18 ns	4.43 ± 0.16 ns

TABLE 4.5: Time resolutions computed with CFD method for a peaking time of 100 ns for the VFAT_ n3 for the three different simulations.

the voltage applied to the GEM foils 450/440/420 V, the transparency was activated and the energy of the muon was 1.5 GeV.
Figure 4.41 shows the residual distributions for both strip 3 and 4 and a peaking time of the VFAT electronics of 100 ns.

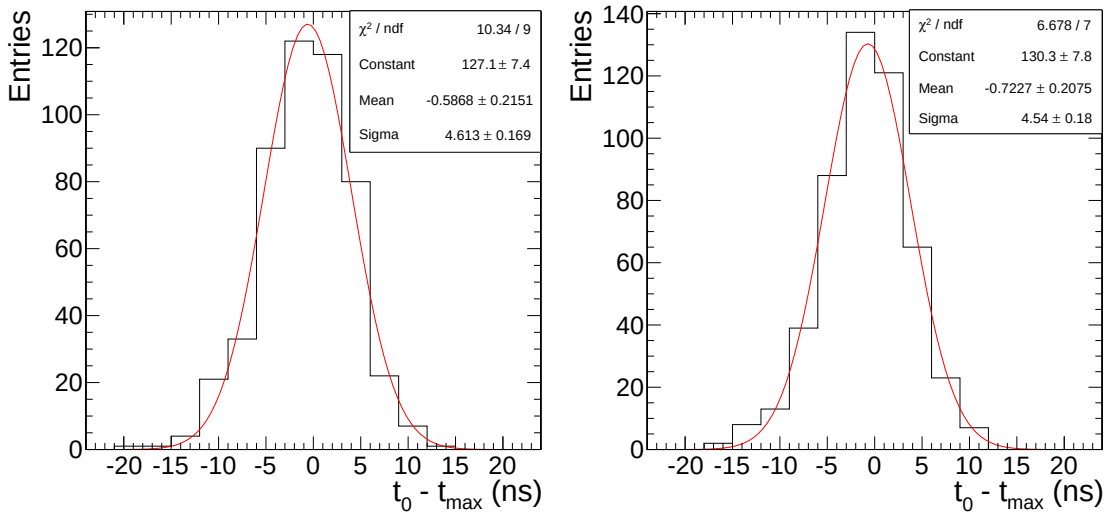

FIGURE 4.41: Time resolution distributions for strip 3 (Left) and strip 4 (Right) computed with the CFD method for a peaking time of 100 ns for the VFAT_ n3 obtain with the Hybrid simulation.

The time resolution found on both strips are similar within the error bars.
Those resolutions have to be compared with the resolutions found with the GARFIELD simulation and the FastSim.
Figure 4.42 shows the residual distribution for the FastSim with transparency. The residual distribution found with the signals simulated with GARFIELD was shown in Figure 4.12.

All the time resolutions are summarized in the table 4.5. The time resolution found with the Hybrid simulation, the full GARFIELD simulation and the FastSim are compatible within the error bars.

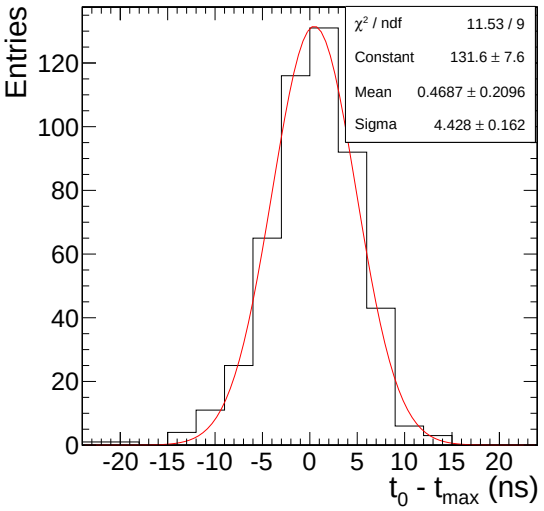

FIGURE 4.42: Time resolution distribution computed with the CFD method for a peaking time of 100 ns for the VFAT_ n3 obtain with FastSim with the transparency.

4.5 Conclusion

The detailed study of the time resolution which could be achieved with the CMS Triple-GEM detector read-out by the VFAT3 electronics has been presented in this chapter. The study has been performed using GARFIELD, state-of-the-art in gaseous detector simulations. The simulation has been used to compute the induced anode current which has been convoluted with the transfer function of the VFAT3 electronics.

The time resolution has been studied for two different methods, the TOT and CFD, and with several peaking times to reduce the effect of the time walk.

The GARFIELD study shows that the most efficient method, in terms of combined time resolution and latency, is the CFD method. The time resolution for this method is 4.98 ± 0.16 ns for a peaking time of 50 ns with a latency of 100 ± 5 ns.

It has also been showed that both VFAT3 designs, with a 2^{nd} and 3^{rd} order filter, give the same results in terms of the time resolution and the latency.

The different effects that can contribute to the time resolution of our detector have also been studied. It has been shown that the main contribution is due to the primary ionization clusters statistics. This effect accounts for ~ 3 ns for $Ar/CO_2/CF_4$ (45:15:40) gas mixture and ~ 4.5 ns for Ar/CO_2 (70:30) gas mixture.

In this chapter we also describe in details the FastSim, a fast parameterized simulation that has been developed during this thesis. This simulation framework has been designed to propose a fast alternative to GARFIELD to simulate Triple-GEM detector, where the geometry and the electric fields can easily be changed. To validate the FastSim, we have first computed the time resolution for the $Ar/CO_2/CF_4$ (45:15:40) gas mixture.

The resolution has been compared with the results obtained with GARFIELD. The results are comparable within two sigmas despite the simplification of the simulation with respect to GARFIELD. Then we have used the CFD method on signals produced with the FastSim for the Ar/CO_2 (70:30) gas mixture. The results show that the time resolution is better than 7 ns. This confirms that the CMS Triple-GEM detector fulfills the CMS upgrade requirement in terms of time resolution (presented in table 2.2) for both gas mixtures.

The FastSim performance has also been compared with real data. We have reproduced the efficiency of the CMS Triple-GEM detector found during the Fermilab beam tests. The agreement is not perfect but is well quantified.

Finally, a combination of the two simulations (FastSim and GARFIELD) called the Hybrid simulation has been presented. With the Hybrid simulation, we have computed the signal on multiple strips and performed a time resolution study. The time resolution found for the strips hit is fully compatible with the previous results where only one strip was simulated.

The FastSim has shown to be a very useful tool to study and understand the behavior of the Triple-GEM detectors. We will see in chapter 6 how its use can be extended to simulate other detector technologies.

Chapter 5

Triple-GEM Prototypes Performances

The effective gain of a GEM foil is a quite complex variable to simulate. Indeed the gain depends in a complicated way on several parameters like the geometry of the GEM holes, the electric fields, the gas mixture, etc. This is why the simulations like GARFIELD are not totally satisfying concerning the computation of the gain. To better understand the gain in the Triple-GEM detectors, we have decided to measure it on small prototypes. The goal of those measurements is to compute the effective gain of a single-GEM foil in order to use those results as an input for the FastSim instead of the effective gain computed by GARFIELD.
We have also participated in a test beam campaign that was intended to test several full size Triple-GEM detectors allowing us to compare different measurements to our FastSim.

In this chapter we will present the two types of Triple-GEM prototypes that we have studied. First in section 5.1, we will present the small 10x10 cm^2 prototypes, that we have built at CERN, together with the setup that the IIHE team has put in place in Brussels. Then we will focus on the measurement of the gain on those prototypes.
Afterwards, in section 5.2 we will present a test beam campaign that we joined. We will review the setup and also the full size Triple-GEM prototypes. Finally we will discuss different results obtained with the analysis of the data taken during the test beam and compared to our FastSim.

5.1 Gain Measurement with 10x10 cm^2 Prototypes

Small prototypes of a new detector type are useful to study and to understand the behavior of a specific new technology. For this purpose a small setup has been built at the IIHE lab to study the Triple-GEM detector and the new DAQ electronics being developed for the CMS upgrade.
In this section, the small prototypes will be described from their assembly to their installation on the test-bench. Afterward the experimental setup will be presented in details. Finally, we will discuss the gain measured with our prototypes.

5.1.1 The 10x10 cm^2 Detectors

The CERN PCB workshop [60] offers the possibility to buy 10x10 cm^2 "Triple-GEM build kit". The ULB group has bought and built two of those kits. Both detectors have been assembled by the IIHE team at CERN in a clean room (as shown in Figure 5.1).

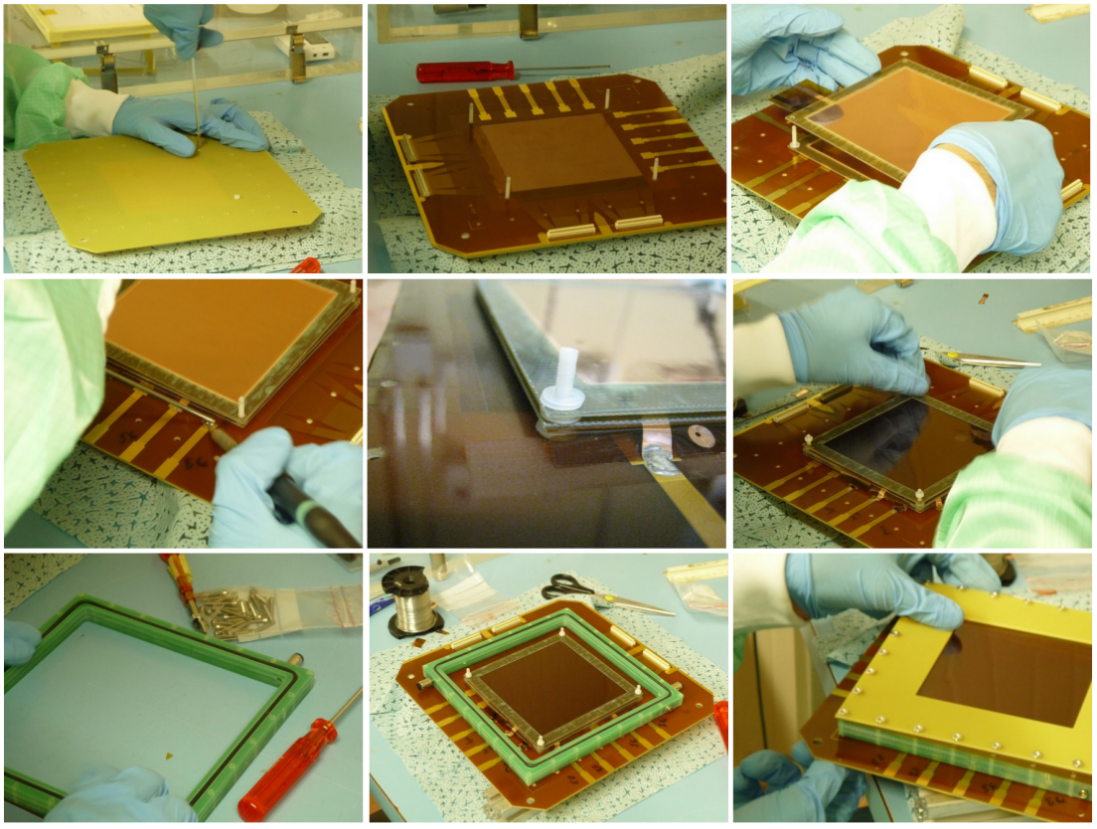

FIGURE 5.1: Assembly of one of the ULB 10x10 cm^2 Triple-GEM prototypes.

The base of the prototype detector is the readout board. On this board there are the copper strips, the *Panasonic* connectors and ten copper bands. The connectors are used

to connect the readout electronics to the strips and the copper bands are used to connect the GEM foils and the drift electrode to the high voltage.
The readout plane of the prototype is made of two sets of 256 strips. The two sets are perpendicular to each other and each set is divided into two groups of 128 channels. Each group is connected to a *Panasonic* connector. A schematic view of the readout plane is shown in Figure 5.2.

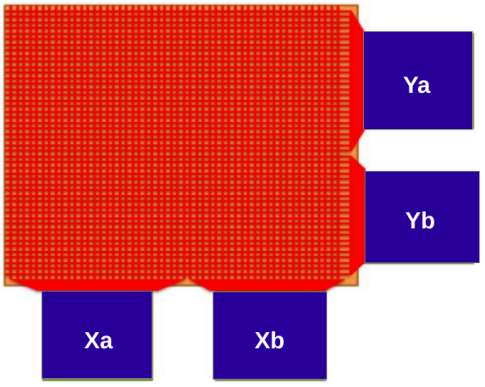

FIGURE 5.2: Schematic view of the Triple-GEM readout strips and the name we attributed to the four different connectors.

Four nylon screws are fixed at the four corners of the 10x10 cm^2 square formed by the strips. Those screws are the support of the GEM foils and the drift cathode.
Figure 5.3 shows a GEM foil used in the small prototype. The GEM foils are made of 50 μm kapton foil with 5 μm copper on both sides, the external diameter of the holes is 70 μm, the internal diameter is 50 μm and the pitch is equal to 140 μm. One can see on the top right of the foil two connector bands used to connect both top and bottom copper foils to the high voltage. This connection is done by soldering.

To separate the GEM foils and create the different gas gaps, plastic spacers of 0.5 mm are placed on the nylon screws. Finally, a bolt is used to keep the foils and spacers on the screw.
Figure 5.4 shows the three GEM foils on top of the readout board, the spacers in between the foils and the bolt that maintains the whole stack.

An outer frame is placed on the readout board. This frame contains the gas inlet/outlet. To assure the gas sealing, two O-rings are placed on the top and bottom of this frame. To close the gas volume, a kapton foil and a plastic frame are placed on the top of the outer frame.
To power the different electrodes of the detector, the voltage is distributed via a ceramic divider from a high voltage power supply. Figure 5.5 shows the HV connections to the

FIGURE 5.3: One GEM foil of the Triple-GEM build kit.

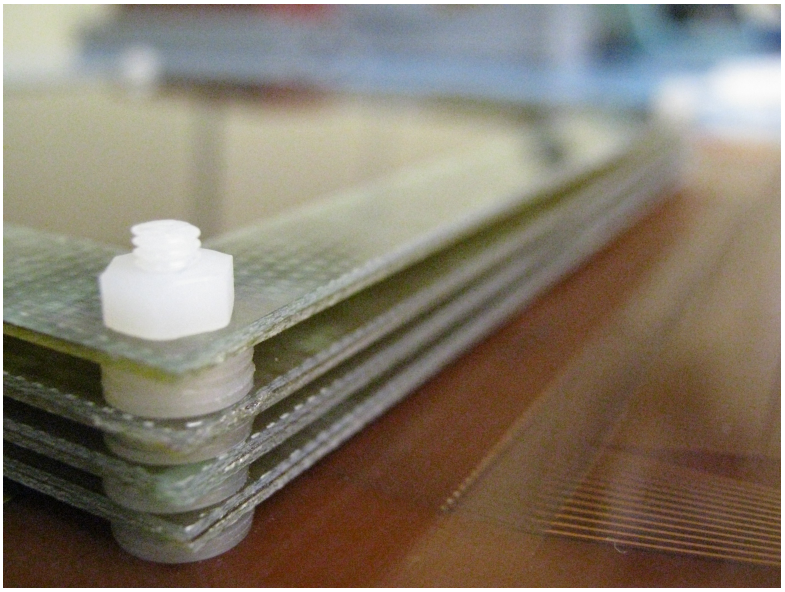

FIGURE 5.4: Triple-GEM foils spaced by plastic spacers on the nylon screw. The stack is ended by the bolt. At the bottom we can distinguish the readout board.

different GEM foils, the ceramic divider as well as the noise shielding (lower row of pictures). Figure 5.6 shows the full Triple-GEM test-bench.

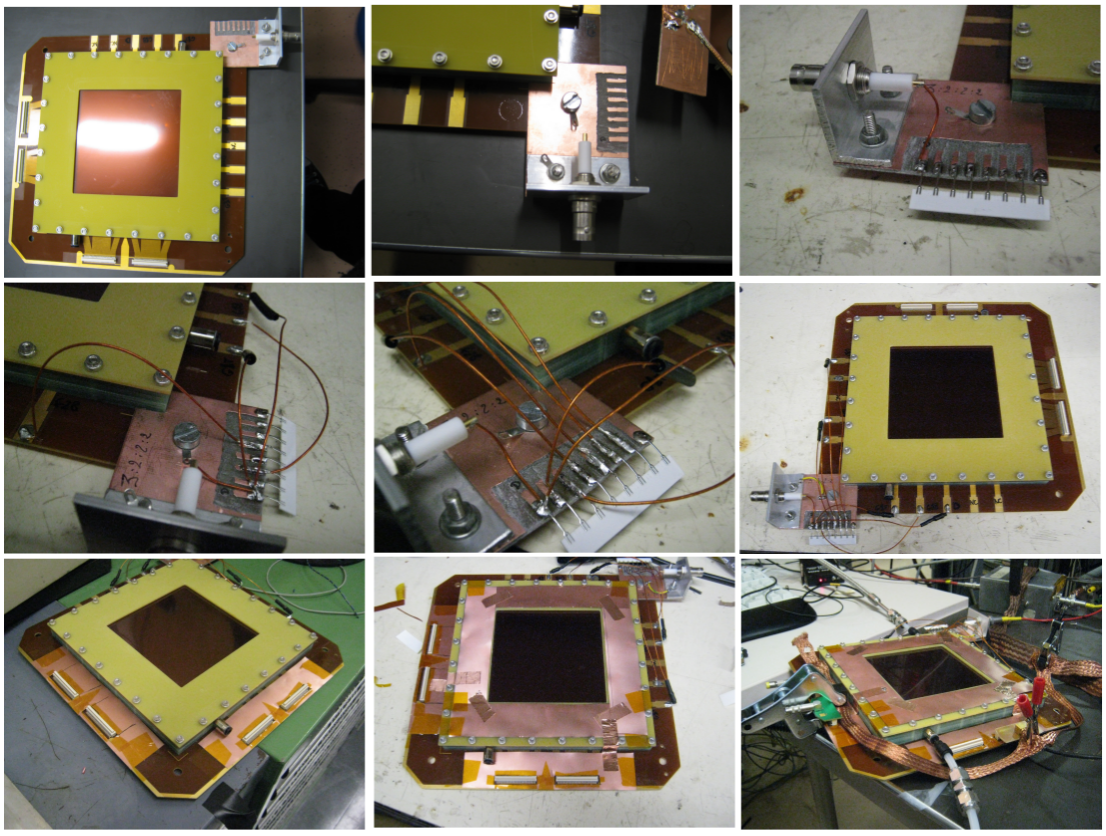

FIGURE 5.5: Assembly of the HV connection and of the ceramic voltage divider (upper row). Soldering of the HV connection between the divider and the detector electrodes (middle row). Addition of copper foils for shielding and grounding (lower row).

Later for the need of the gain measurements (see section 5.1.3), one of the two Triple-GEM prototypes has been transformed into a Double-GEM by removing one of the GEM foils. The geometry chosen for the Double-GEM is 3:2:1 mm.

In addition the powering scheme of this Double-GEM has been modified to enable a larger flexibility: each electrode is powered individually. In total five different power supplies are needed: one for the drift and four for the GEM electrodes (two per GEM foil). Figure 5.7 shows the five HV connections to the detector electrodes.

Since the two electrodes of a single GEM foil are powered separately, a mechanism has to be added in order to protect the GEM foil in the case of one of the power supply trips because of a discharge. Indeed, if one of the HV power supply trips, the voltage of the corresponding GEM electrode will go down to zero, increasing the potential difference across the GEM foil to the value of the electrode still powered, that is well beyond 500 V. This protection is provided by two Zener diodes facing each other and placed between the two GEM electrodes. The diodes have a breakdown voltage of -500 V. In case of

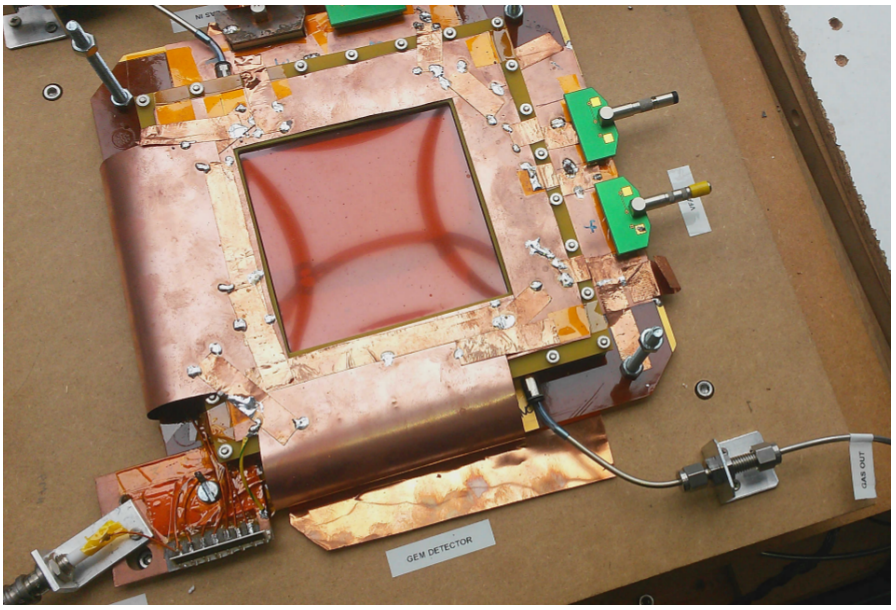

FIGURE 5.6: Triple-GEM prototype placed in the test-bench at the IIHE lab.

over-voltage the current will flow through the diode and bring the voltage across the foil to zero. Figure 5.7 shows also the four Zener diodes.

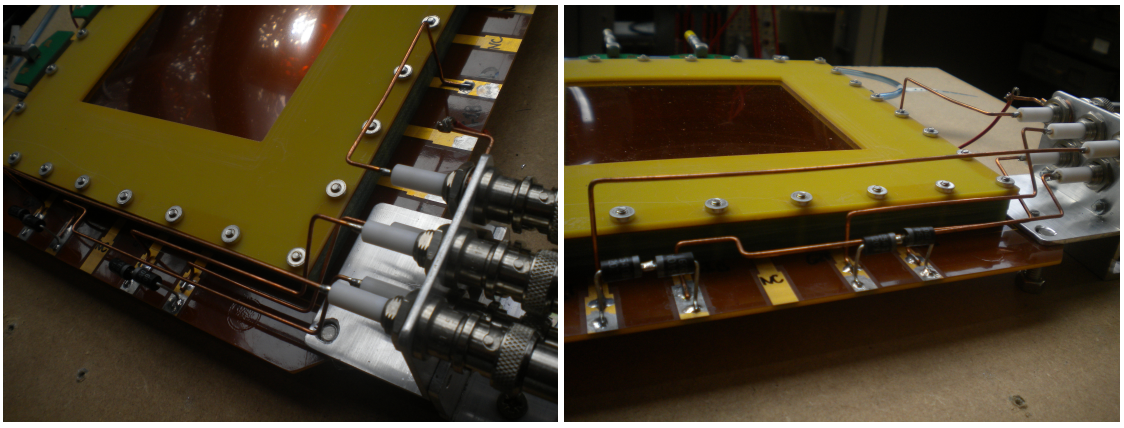

FIGURE 5.7: The five HV connector and the four Zener diodes of the Double-GEM prototype.

Figure 5.8 shows the Double-GEM prototype test-bench. On the top right, a pre-amplifier connected with a small Lemo cable to the *Panasonic* connector 'Yb' (see Figure 5.2) can be observed .

The voltage applied to the five electrodes of the Double-GEM foil for the different measurement points expressed in terms of equivalent current in the divider, the electric fields of the three gaps and the voltage applied to the foil of the Tripe-GEM are reported in Appendix B.

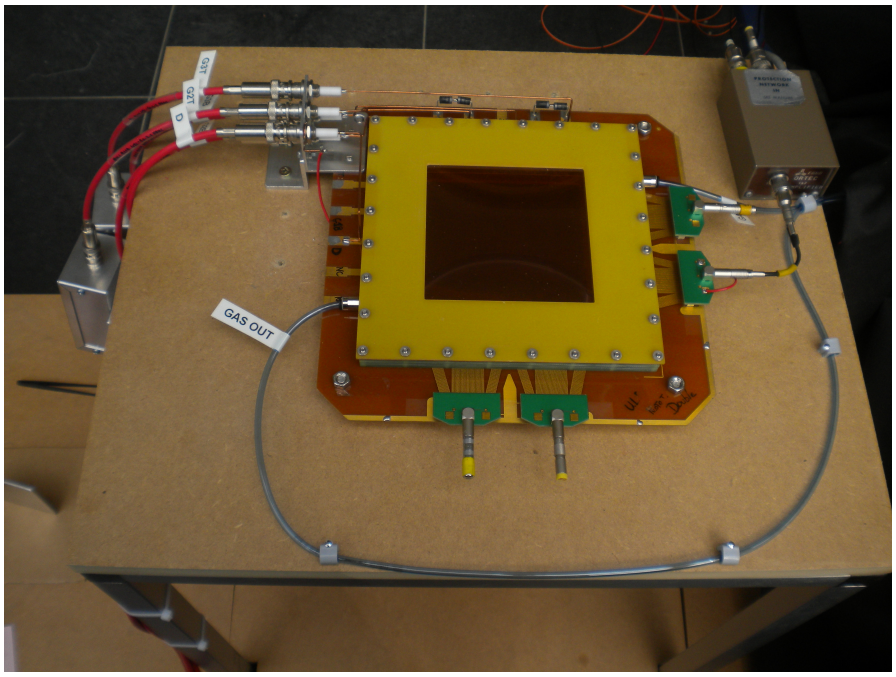

FIGURE 5.8: Double-GEM prototype placed in the test-bench at the IIHE lab.

5.1.2 Setup

The full experimental setup installed at the IIHE lab is composed of the detector, a gas system, a high voltage power supply and a readout system. Figure 5.9 shows a schematic view of the experimental setup.
Both the gas system and the high voltage power supply are controlled by a web interface through Ethernet.
The signal coming out of the detector is sent to a pre-amplifier and then an amplifier. Eventually, the signals are read with a scope or with NIM modules.

All the parts of the setup will be described in details in the following section.

DAQ Web Interface The DAQ web interface is made of three different entities: the user interface, the central node and the experimental side.
The user interface is a web application that provides the ability to control remotely different parameters of the experimental setup as the high voltage or the gas flow. The web application can be run on a simple web browser. It communicates with the central node.
The central node is a web server coupled to a database. The central node treats the communication between the user interface and the experimental side.
On the experimental side, a server with C and C++ software is located next to the

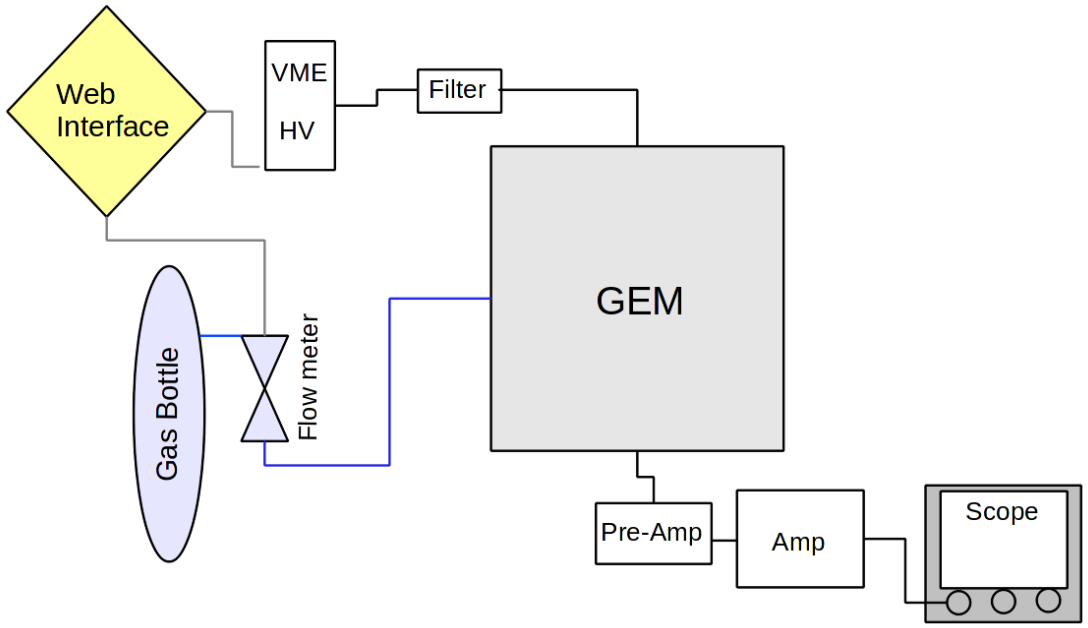

FIGURE 5.9: Schematic view of the experimental setup.

setup. The different softwares are used to communicate with the high voltage module and the gas system through Ethernet.

Gas System The gas mixture used for the different measurements is the Ar/CO_2 (70:30). The gas mixture is provided with a gas mixer and the flows are controlled by *HORIBA* flow meters [61].
Figure 5.10 shows the gas system used in the setup, with two gas bottles and the flow meters. The flow meters are connected to the experimental side server of the DAQ web interface.

High Voltage The high voltage is provided to the detector with a VME high voltage module. The module is able to power 6 channels independently up to 6 kV.
There is a filter installed between the HV module and the detector to reduce high frequency noise which could propagate to the readout. Figure 5.11 shows the voltage RC filter ($R = 300$ kΩ and $C = 2 \times 2.2$ nF).

Amplification Chain The signal coming out of the detector is amplified in two steps. The first amplification is done by an *ORTEC 142B* charge sensitive pre-amplifier [62]. Figure 5.12 shows a diagram of the *ORTEC 142B* circuit.

FIGURE 5.10: The two gas bottles and the *HORIBA* flow meters remotely monitored via Ethernet.

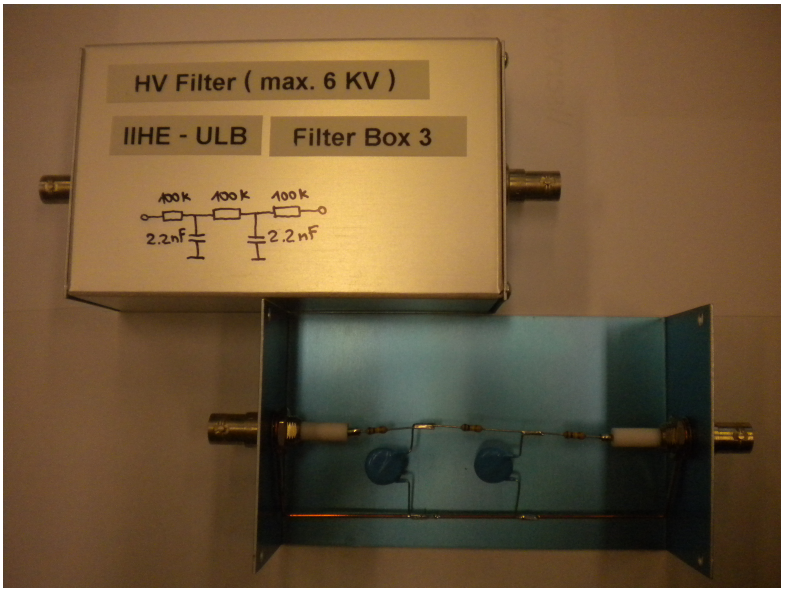

FIGURE 5.11: HV filter.

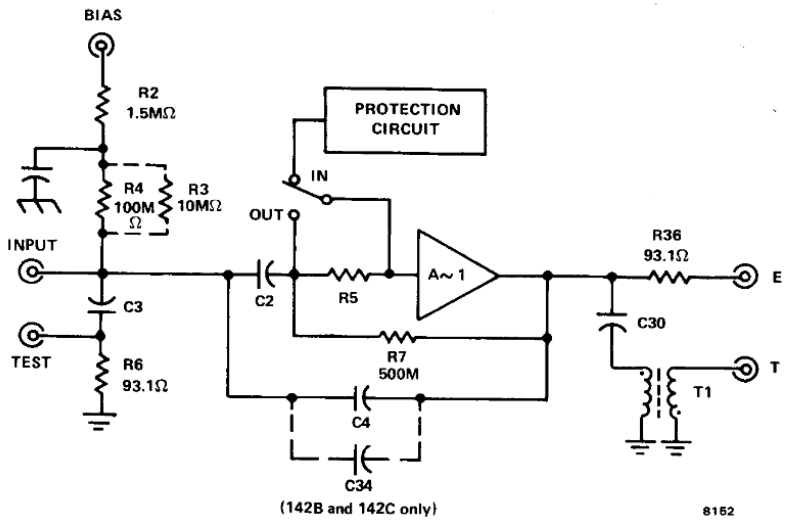

FIGURE 5.12: Diagram of the *ORTEC 142B* pre-amplifier circuit.

On the diagram a test input with a capacitor (C3) can be observed. C3 is a 2 pF capacitor that allows to do a calibration of the pre-amplifier. Indeed, by using a known square signal produced by external pulse generator sent to the test input, we can observe the output voltage with an oscilloscope.
To produce a semi-Gaussian shaped pulse and to improve the signal-to-noise ratio, the output signal of the pre-amplifier goes into a shaper. The shaper is the *ORTEC 575* amplifier [63].

Example of Signals Figure 5.13 shows the signals we observe with the oscilloscope for the Triple-GEM prototype after the full chain of amplification.

We can clearly see a noise level around 40 mV and the maximum amplitude of the signal have a mean value of 147 mV. The shape is asymmetric and the signal lasts for more than 1 μs.

5.1.3 Gain Measurements

As presented in section 3.7.3, only the effective gain can be measured. Since the effective gain is the ratio of the number of electrons inducing a signal to the anode plane (n_{eff}) and the number of primary electrons (n_0), to estimate the gain, n_{eff} must be measured and n_0 estimated.
n_0 is known since the gain measurement rely on a iron-55 (^{55}Fe) X-ray source.n_{eff} has been measured with two different methods: the measurement of maximum amplitude of

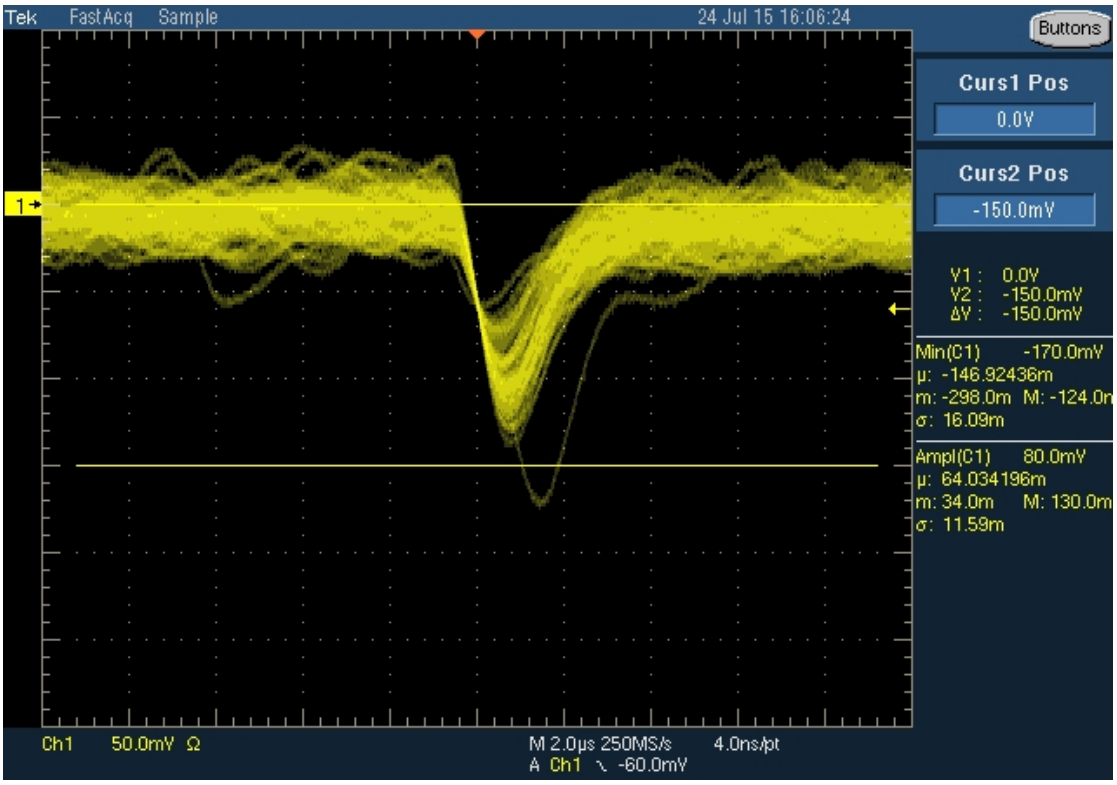

FIGURE 5.13: Output signals of the Triple-GEM prototype after the full chain of amplification observed with the oscilloscope.

the signal after the amplification chain and the measurement of the induced current on the anode plane.

^{55}Fe source The ^{55}Fe is a radioactive isotope of iron and therefore is an X-ray source with a well known energy spectrum. The main emission of the ^{55}Fe source is at 5.9 keV. Figure 5.14 shows the X-ray spectrum of the iron-55 source [64].

Two different peaks can be observed, the main peak is clearly visible at 5.9 keV and a second one is visible around 3 keV. The second peak is the escape peak of argon.
As explained in section 3.2.2, the mean energy loss (W) needed to create a ion-electron pair is defined by Eq. 3.2 and is experimentally determined. Since the gas mixture used for the measurements is Ar/CO_2 (70:30), the mean energy is given by:

$$W = \left(\frac{\%(Ar)}{W_{Ar}} + \frac{\%(CO_2)}{W_{CO_2}} \right)^{-1} = 27.8 \; eV$$

To compute the average number of ion-electron pairs produced by an X-ray photon of 5.9 keV, the Eq. 3.3 is used:

$$n_0 = 5.9 \; keV \cdot \frac{1}{W} = 212 \; e^-$$

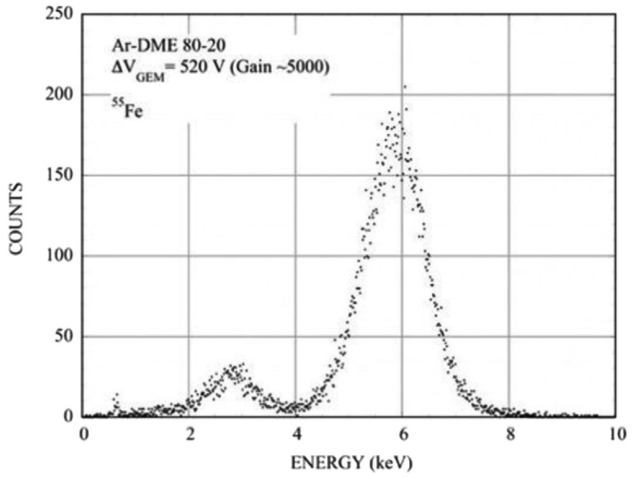

FIGURE 5.14: Energy spectrum of the ^{55}Fe source for a single GEM [64].

Measurements with the signal amplitude The first method used to estimate n_{eff} is by measuring the maximum amplitude of the ^{55}Fe signal after the amplification chain.

First a calibration of the full amplification chain is needed. The goal of this calibration is to determine the output amplitude for a given input charge. To control the input charge, a pulse generator is connected at the test pulse input of the pre-amplifier. By knowing the amplitude of a square pulse and since the capacitor of the test input is also known, the equivalent input charge can be computed.

Figure 5.15 shows the calibration curve measured for our setup, in other terms the input charge as a function of the amplitude of the output.

A linear function is fitted to the points and the slope ($p1$) is the coefficient between the measured amplitude and the input charge. The Y intercept of the fit ($p0$) is compatible with zero.

Therefore the effective gain (G) can be computed and is given by:

$$\begin{aligned} G &= \frac{p1}{n_0} \cdot A_{max} \\ &= \frac{7256}{212} \cdot A_{max}, \end{aligned}$$

where A_{max} is the maximum amplitude measured.

In the absence of an ADC adapted to our signals, we have determined the amplitude corresponding to the 5.9 keV peak (A_{max}) by using an oscilloscope. For each point a set of 50 signals was recorded and the mean of the 50 maximum amplitudes was used as the estimator of A_{max}.

Figure 5.16 shows the gain measured as a function of the HV on the Triple-GEM for two

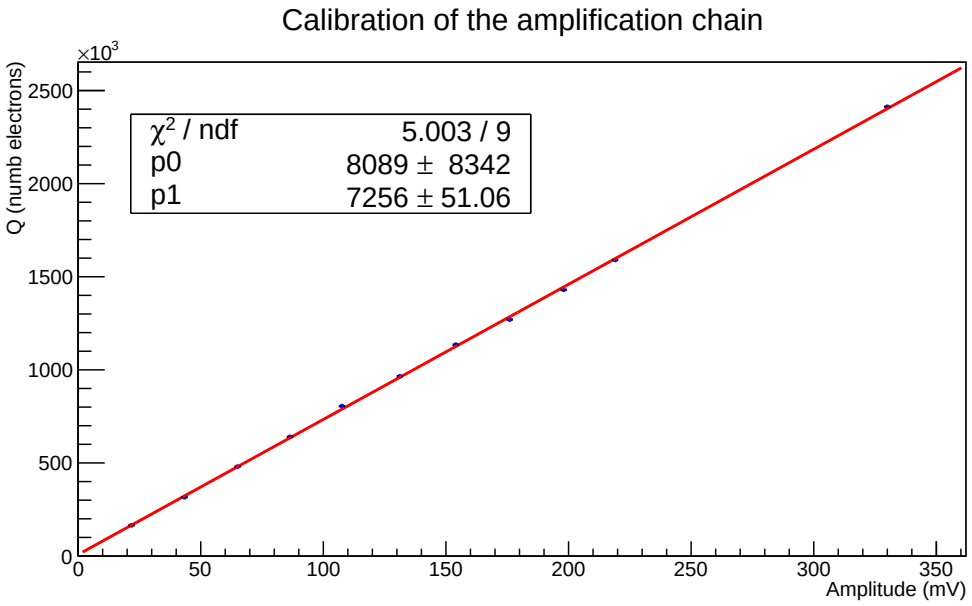

FIGURE 5.15: Calibration curve of the full amplification chain.

different positions of the source on the four connectors. The notation for the different positions is the following: the first two letters are the connector name (as defined in Figure 5.2) and then the last two letters indicates the position of the source along that connector. The error bars present on the graph are the statistical uncertainties.

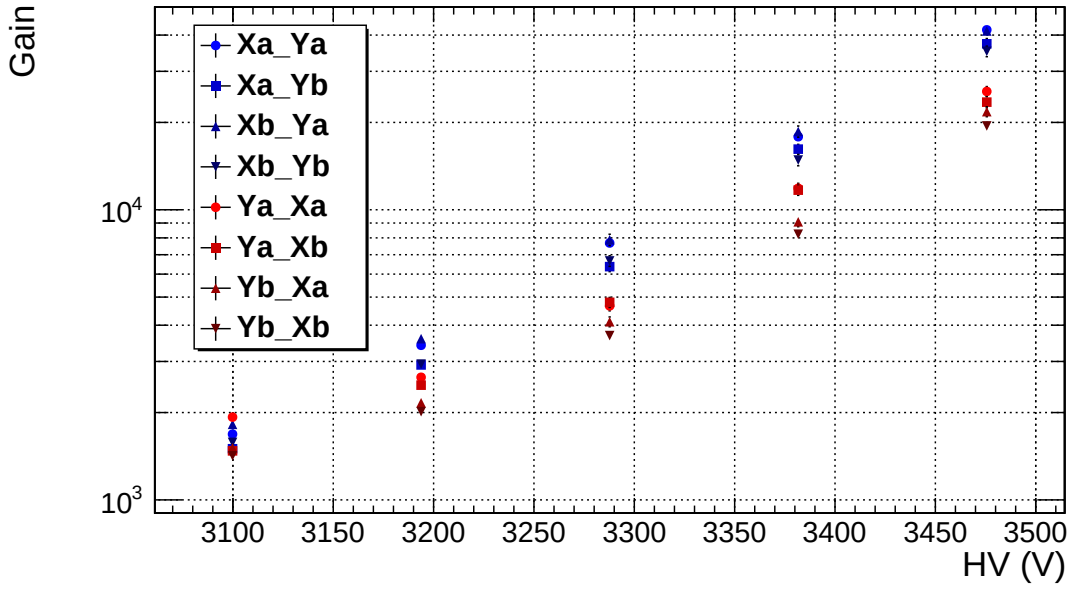

FIGURE 5.16: Measured gain as a function of the HV on the Triple-GEM for two different positions of the source on the four connectors.

The first thing to notice is that the gain can go up to $\sim$ 40000 for an high voltage of

$\sim$ 3460 V. But large discrepancies up to a factor of two can be observed between the eight sets of measurements.

First we can observe that the gain is systematically larger along the vertical strips read-out through connectors Xa and Xb. This discrepancy can reach 35 %. This can be easily understood, since the two sets of strips are perpendicular and the 'X' strips are on top of the 'Y' strips.

If we just look at the 'X' strips, a difference of 9 to 25 % can be observed for one connector and different positions of the source.
Between the two 'X' connectors we have up to 10 % difference in the measured gain.
All those variations are due to the way the prototype is built.
Indeed an important parameter of the geometry is the gap between the foils which affects the electric field and consequently the effective gain. In our prototypes the distance between the foils is maintained by the spacers and the bolts on the screws. The GEM foils are not stretched. This can lead to non-uniformities in the gap size and in the electric fields and therefore in the effective gain.

Measurements with the current To measure the effective gain G of a GEM detector using the recorded current on the read-out strips, the following formula is used [65]:

$$G = \frac{I_s}{e \cdot n_0 \cdot R} \tag{5.1}$$

Where e and n_0 are respectively the charge of the electron and the mean number of primary electrons produced, I_s the recorded current, and R the rate of the X-ray source times the efficiency of conversion.

Figure 5.17 shows the rate R measured as a function of the HV. We can see that beyond 3350 V the rate measured without veto (red inverted triangles) increases rapidly. This is due to the fact that with low electronics thresholds the large signals presenting a long tail of the order of the μs, can trigger multiple times the discriminator. To avoid this phenomena a veto is implemented. With a veto of 50 μs the measured rate reaches a plateau of 1.5 kHz. If we increase the veto length to 200 μs, the rate decreases to 1.1 kHz because several signals may occur during the veto time.

Once the X-ray rate has been measured, the current induced on the strips has been recorded with a *Keithley 6517* Electrometer/High Resistance Meter [66].
Figure 5.18 shows the comparison between the gain measured with the current and with the maximum amplitude. The measurements have been done at position 'Xa _ Ya'. One can see that both methods give an effective gain of the same order of magnitude but

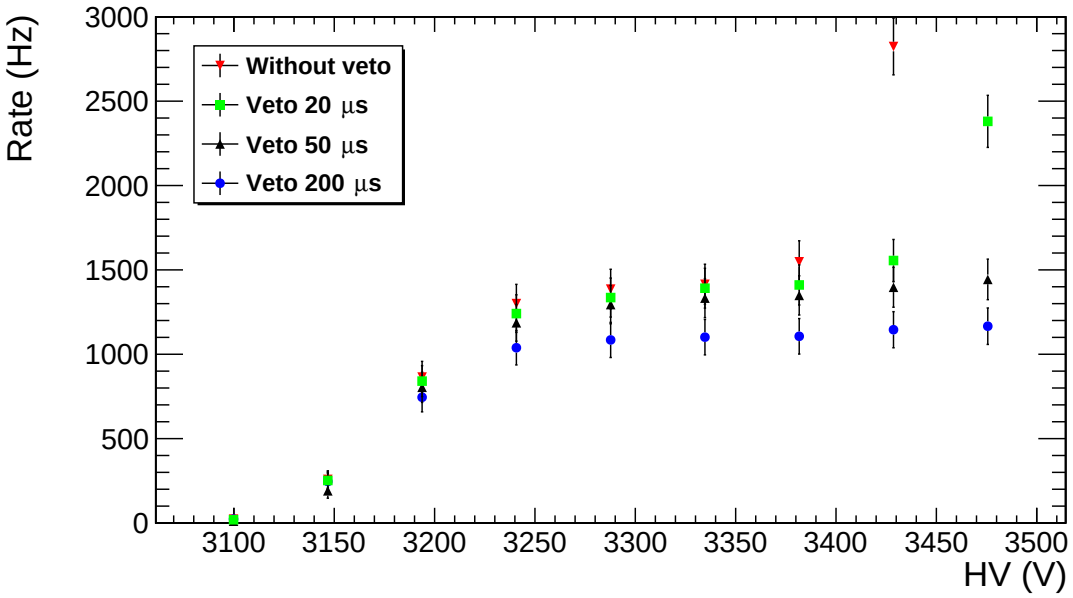

FIGURE 5.17: Measured rate of the ^{55}Fe source as a function of the HV of the Triple-GEM.

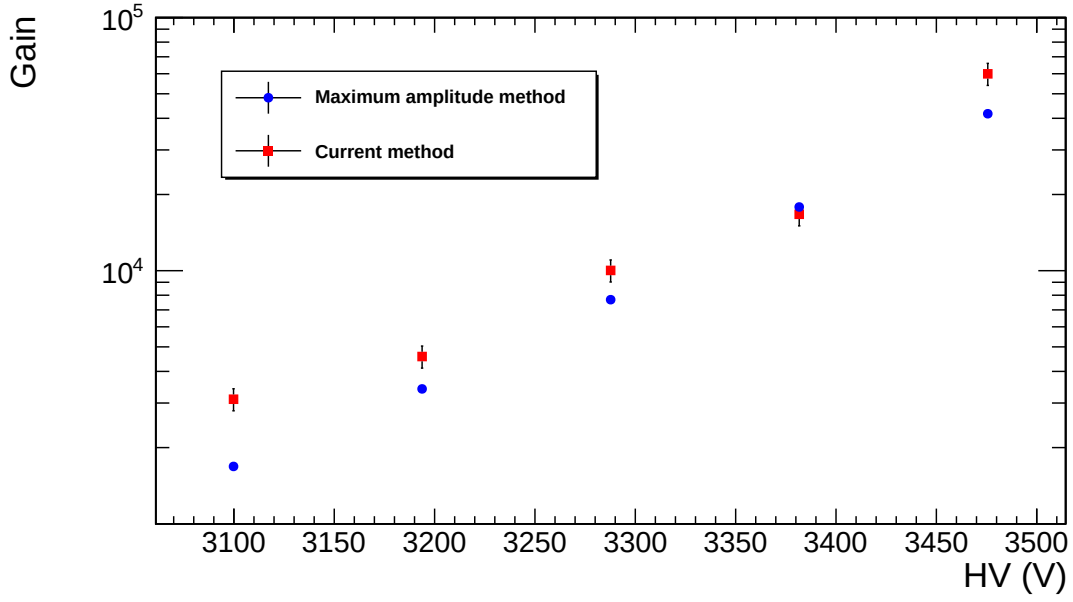

FIGURE 5.18: Measured gain of the Triple-GEM at the position 'Xa _ Ya' for both the current method and the maximum amplitude method.

are not compatible within the error bars. The measurement of the induced current has a precision of the order of a pico-ampere. The signal of our source is quite small (of the order of a hundred of pico-ampere) therefore the measure is very sensitive to external noise.
In view of the discrepancy in the results obtained for the effective gain with the maximum amplitude method, it is not surprising that both measurements do not agree much better. Note however that at high gain, when the currents are higher, the disagreements are within 55%.

Charging-up An effect that has also been observed and that can affect the effective gain is the charging-up. The charging-up causes an increase of the effective gain with time. This increase is due to an accumulation of electrons on the kapton of the GEM holes. Indeed, the electrons that enter a GEM hole (or are created there) have a certain probability to be captured on the kapton. The consequence is an accumulation of electrons on the kapton surface and therefore an increase of the electric field in the hole.
Figure 5.19 shows the measured gain of the Triple-GEM at the position 'Xa _ Ya' as a function of the time.

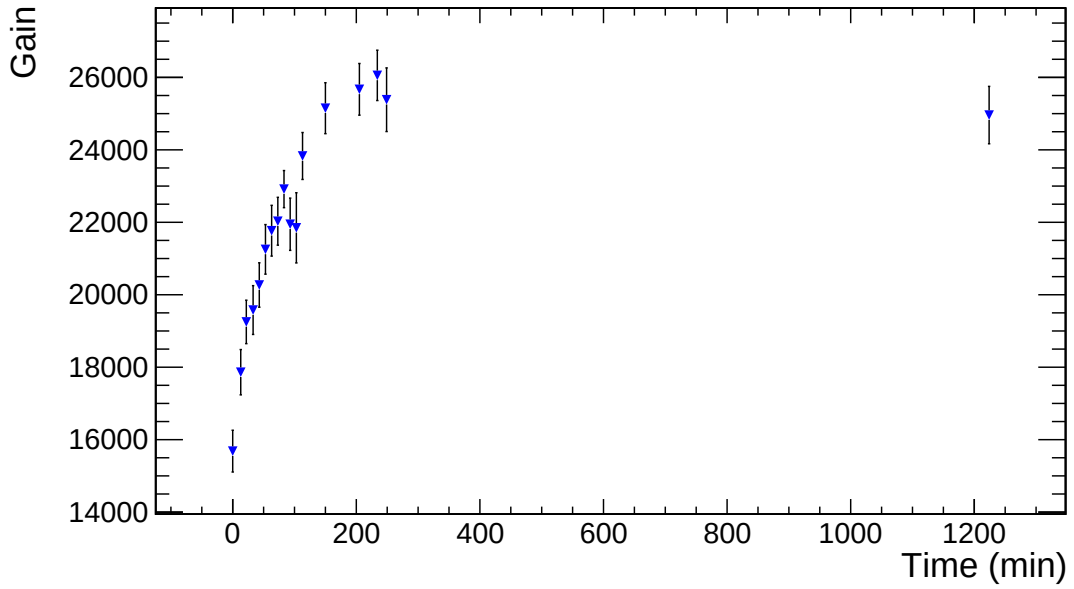

FIGURE 5.19: Measured gain of the Triple-GEM at the position 'Xa _ Ya' as a function of the time.

The measurement has been done during 1224 minutes. The gain increases clearly until it reaches a plateau that starts after around 200 minutes. The gain increases by $\sim 70\%$ between the first gain measurement and the plateau.

Gain of the single-GEM foil In this section we want to combine the gains measured with a Triple-GEM and with a Double-GEM to estimate the gain of a single-GEM foil. As explained in section 3.4, the gain of a gaseous detector follows an exponential. This means that we can express the effective gain of a single-GEM foil G as a function of the voltage applied to the GEM foil hv as:

$$G = \alpha \cdot \exp(\beta \cdot hv).$$

One can show that the effective gain of the Triple-GEM detector G_{triple} can be expressed as the product of the effective gain of the three single-GEM foils G_i.

$$G_{triple} = G_1 \cdot G_2 \cdot G_3.$$

So we can write:

$$G_{triple} = A \cdot \exp(\beta_1 \cdot hv_1 + \beta_2 \cdot hv_2 + \beta_3 \cdot hv_3),$$

where $A = \alpha_1 \cdot \alpha_2 \cdot \alpha_3$.
Since the voltage applied to each foil in our Triple-GEM is fixed via the ceramic high-voltage divider, we can write:

$$\begin{aligned} G_{triple} &= A \cdot \exp\left((\beta_1 \cdot R_1 + \beta_2 \cdot R_2 + \beta_3 \cdot R_3) \cdot I\right) \\ &= A \cdot \exp\left(B \cdot I\right) \end{aligned}$$

where I is the current applied to the high-voltage divider and R_i the resistance associated to the foil i.
In the same way, we can express the effective gain of a Double-GEM G_{double} as:

$$G_{double} = a \cdot \exp(b \cdot I),$$

where $a = \alpha_1 \cdot \alpha_2$, $b = \beta_1 \cdot R_1 + \beta_2 \cdot R_2$.
This means that we can write the effective gain of the single-GEM foil i as follow:

$$G_i = \alpha_i \cdot \exp(\beta_i \cdot I), \tag{5.2}$$

where $\alpha_i = \dfrac{A}{a}$ and $\beta_i = B - b$.
To measure the effective gain of the first GEM foil of the Triple-GEM detector, the configuration of the Double-GEM must be the complementary. It means that if the electric fields of the four gaps of the Triple-GEM are 3/3.5/3.5/5 kV/cm and the voltage applied to the three different GEM foils are 450/440/420 V and we want to estimate the gain of the first GEM foil, the electric fields of the three gaps of the Double-GEM

must be 3.5/3.5/5 kV/cm and the voltage applied to the two different GEM foils must be 440/420 V. The lists of complementary configurations of the Double-GEM equivalent to GEM1, 2 and 3 are given in Appendix C.

To estimate the effective gain of the three single-GEM foils of our Triple-GEM detector, we need to measure the gain of the Triple-GEM detector and the gain of the Double-GEM detector.

Gain of the Double-GEM We have performed the measurement of the effective gain of the Double-GEM with the maximum amplitude method.
Figure 5.20, 5.21 and 5.22 show the effective gain measured with the Double-GEM prototype for the configuration complementary to the Triple-GEM for the GEM1, 2 and 3 respectively.

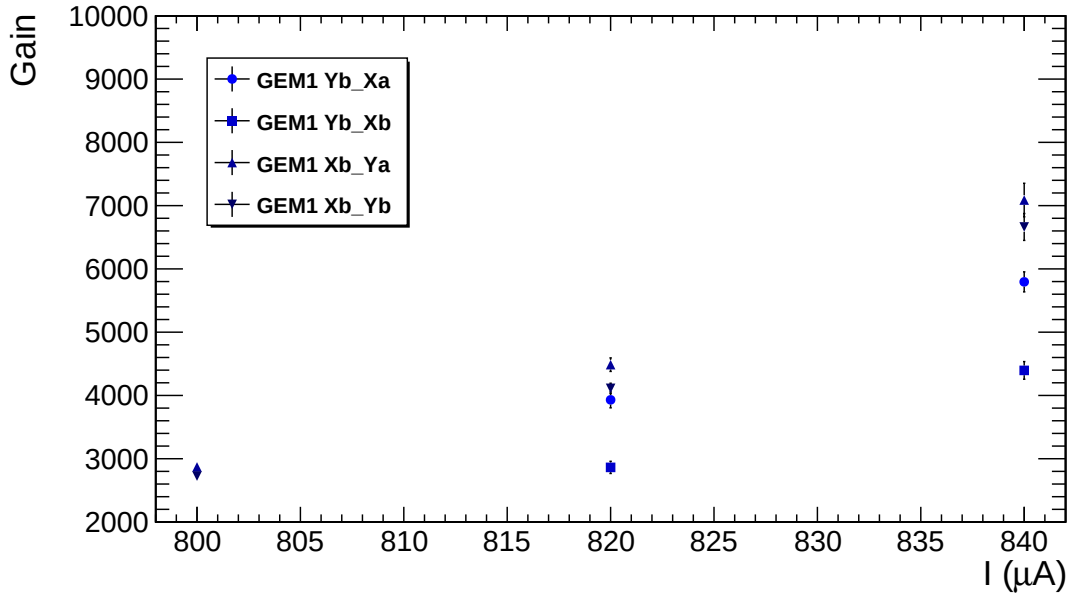

FIGURE 5.20: Effective gain of the Double-GEM for the configuration complementary to the GEM1 as a function of the current.

The measurements have been done on the connector 'Xb' and 'Yb' and two positions of the source.
The same sort of disagreement between the different sets of measurements than those observed with the Triple-GEM can be seen.

Combination Finally, the combination of the measurements of the Double- and Triple-GEM has to be done.

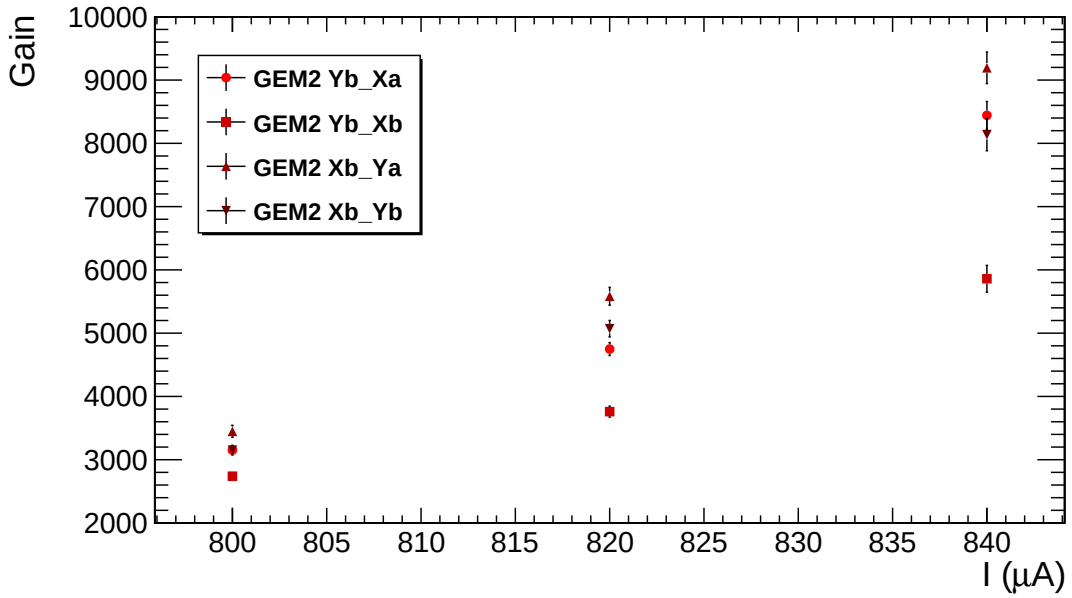

FIGURE 5.21: Effective gain of the Double-GEM for the configuration complementary to the GEM2 as a function of the current.

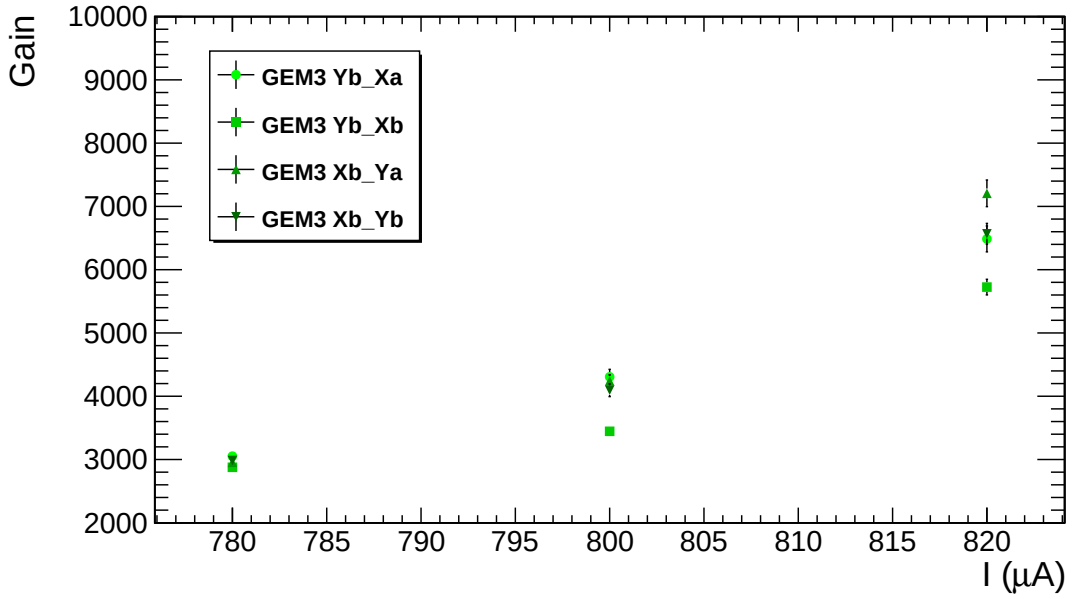

FIGURE 5.22: Effective gain of the Double-GEM for the configuration complementary to the GEM3 as a function of the current.

Figure 5.23 shows an exponential fit on the effective gain measured with the Triple-GEM at the position 'Xb _ Ya'.

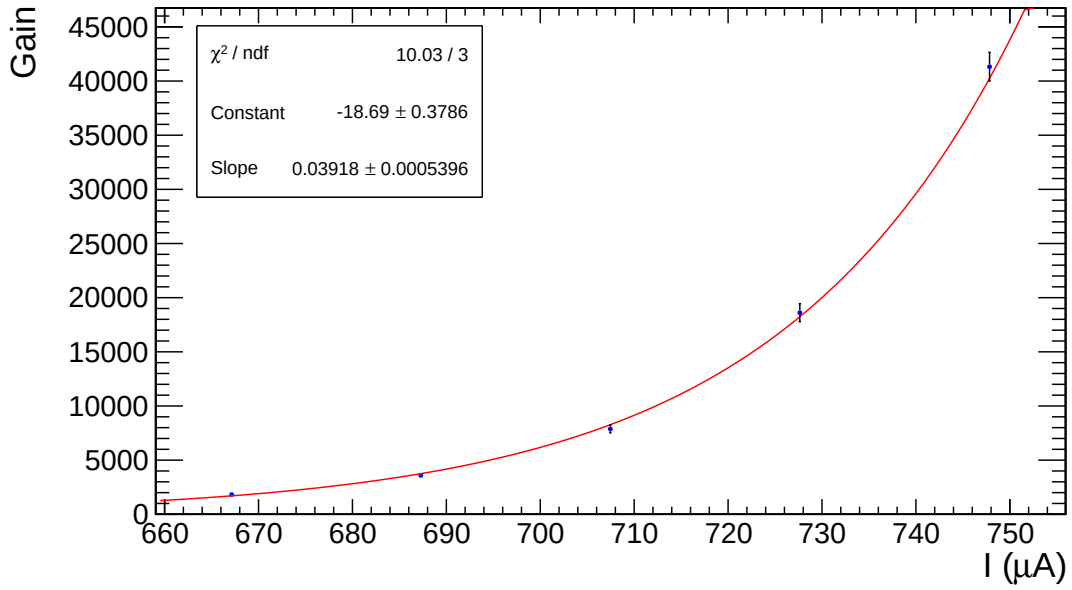

FIGURE 5.23: Measured gain as a function of the current for the Triple-GEM at the position 'Xb _ Ya' fitted with an exponential.

Figure 5.24 shows an exponential fit on the effective gain measured with the Double-GEM complementary to the GEM1 at the position 'Xb _ Ya'.

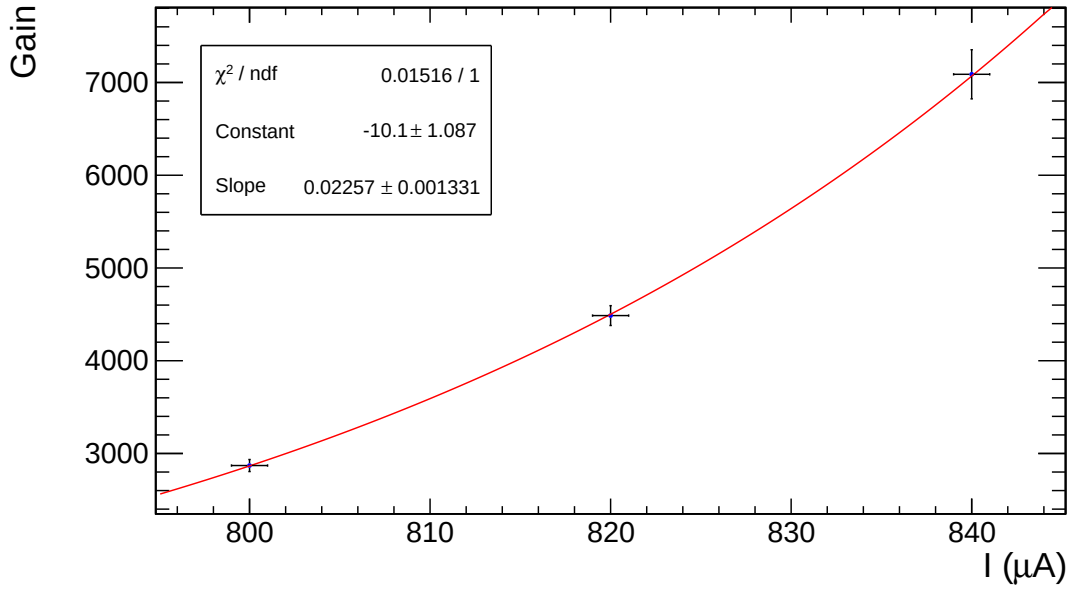

FIGURE 5.24: Measured gain as a function of the current for the Double-GEM at the position 'Xb _ Ya' fitted with an exponential.

With the fits to the Double- and Tripe-GEM measurements, we can use Eq. 5.2 to compute the effective gain of the three single-GEM foil respectively.
Figure 5.25 shows the gain of the three single-GEM foils as a function of the voltage applied to the foil.

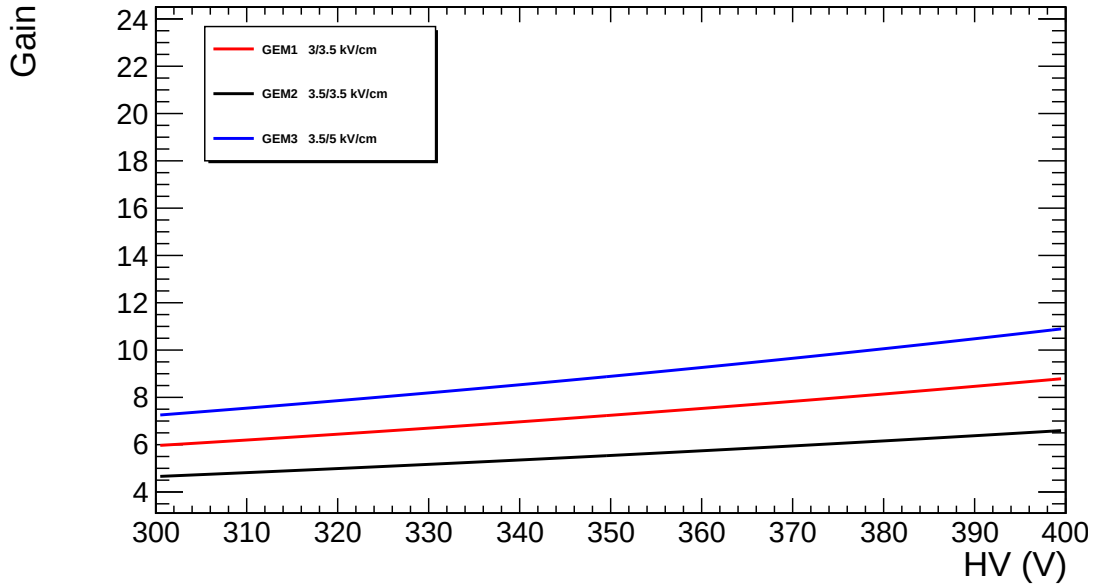

FIGURE 5.25: Effective gain of the three single-GEM foil as a function of the voltage applied to the foil.

In view of the disparity between the results of the different gain measurements on the two prototypes, we do not expect to obtain the exact gain. Nevertheless we can clearly see that the effective gain of the three foils is not equivalent. It is normal since the effective gain depends on both the fields above and below the GEM foil. This behavior is interesting to note that the effective gain of the third GEM foil is the highest and the second GEM foil have the lower gain.
Those results can be compared with the effective gain of a single-GEM foil predicted by GARFIELD. Figure 5.26 shows the effective gain of the three single-GEM foil as a function of the voltage applied to the foil for the three configurations of electric fields. We can observe that the effective gain computed with GARFIELD is higher than the effective gain computed from the measurements but the order is the same: for a fixed voltage applied to the foil, the effective gain of the third foil of a CMS Triple-GEM detector is the highest and the effective gain of the second foil is the lowest.

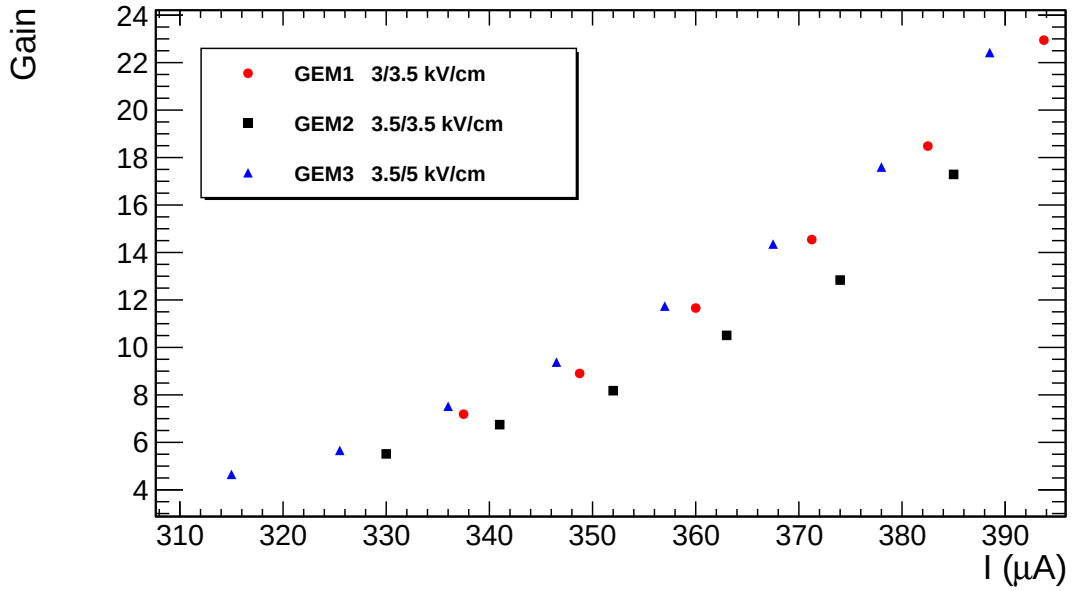

FIGURE 5.26: Effective gain of the three single-GEM foil as a function of the voltage applied to the foil simulated by GARFIELD.

5.2 Test Beam

In October 2014, three full size GE1/1 Triple-GEM detectors have been tested with beam. The tests were performed using a muon beam at the CERN SPS test beam facility [67]. To produce the beam, a proton beam is extracted from the SPS towards the North Area and goes to a primary target where a jet of pions is produced. The pion beam can be directly sent to the experimental hall or can pass through a secondary target. If the secondary target is introduced in the beam, only the muons coming from the pion decays will cross the target. Figure 5.27 shows the layout of the SPS and the three primary targets T2, T4, T6 of the North Area.

In this section we will present the setup used during the test beam together with the prototypes used during the test beam. Finally, we will show some results and compare them with the FastSim.

5.2.1 Setup

The test beam setup is made of three scintillators, a tracker and the GE1/1 Triple-GEM detectors. A schematic view of the setup is shown on Figure 5.28.

The scintillators are mounted with photo-multipliers tubes. The coincidence of the three scintillators provides the trigger to our setup.

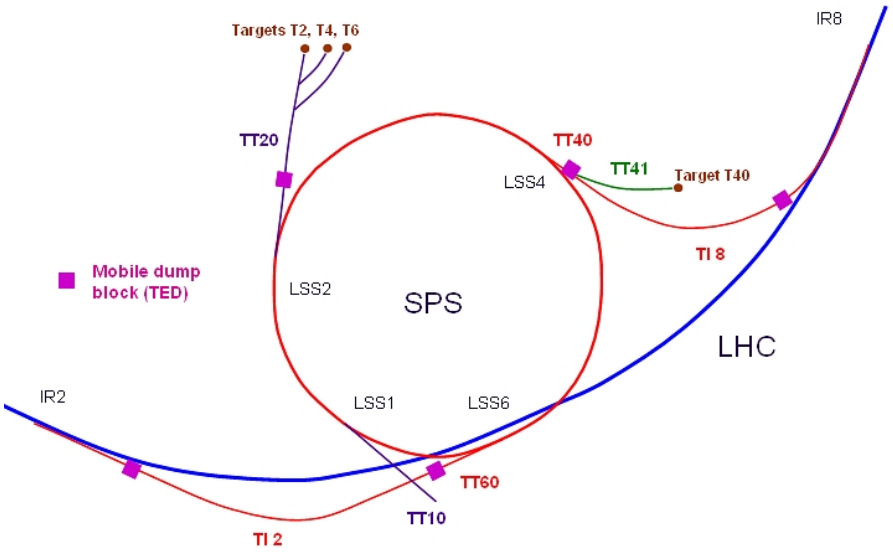

FIGURE 5.27: Layout of the SPS and its extraction areas.

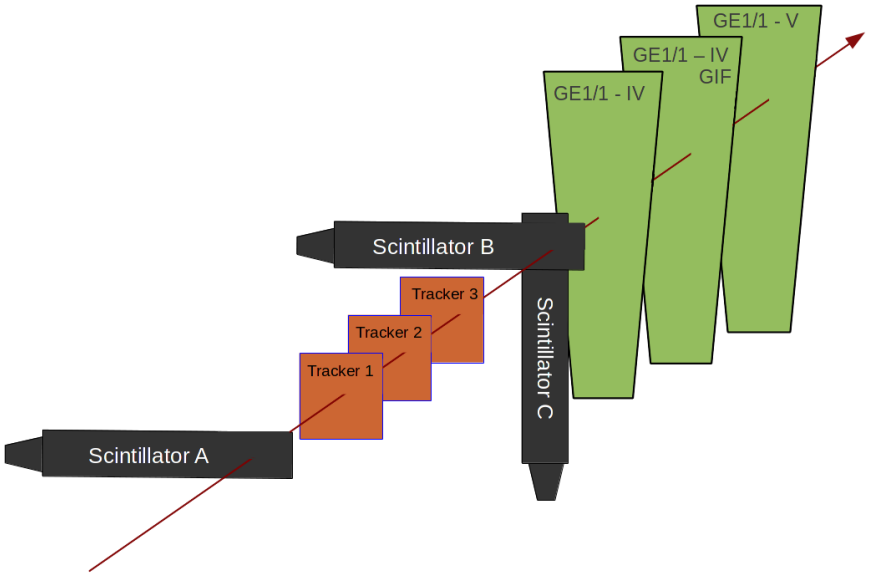

FIGURE 5.28: Schematic view of the test beam setup.

The tracker is made of three 10x10 cm^2 Triple-GEMs. Like the prototypes presented in the previous section, the three trackers detectors have 256 strips in both horizontal and vertical directions transverse to the beam and have a gap configuration of 3:2:2:2 mm. The tracker is used to reconstruct the muon tracks and the beam profile. Figure 5.29 shows the beam profile of the muon beam for the three tracker detectors.

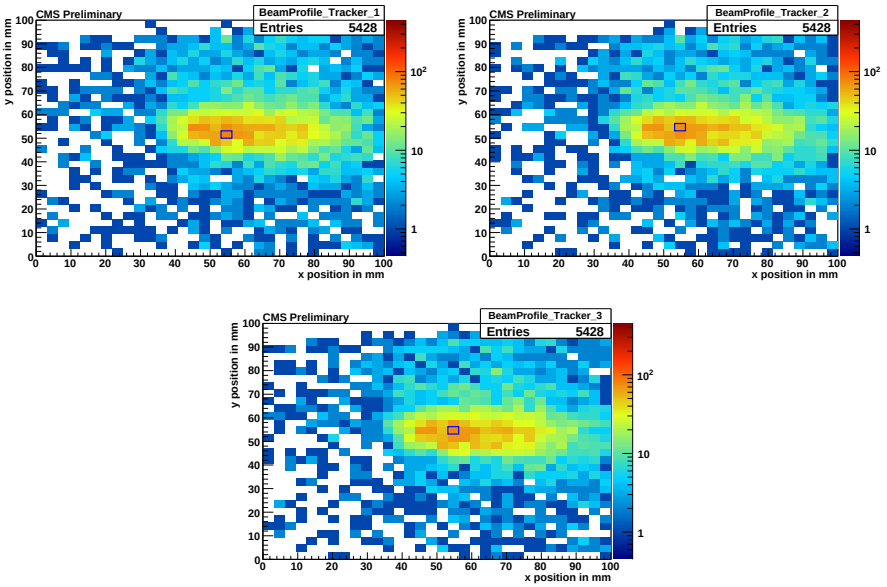

FIGURE 5.29: Muon beam profile of one run for the three trackers.

The three detectors tested are: a GE1/1-IV, a GE1/1-IV-GIF and a GE1/1-V. The detail of the different generations of prototypes has been presented in section 3.7.3. The GE1/1-IV-GIF is a generation IV prototype that has been irradiated for aging test at the GIF facility [68].

5.2.2 Results

Electronics The front-end electronics used during the test beam was the VFAT2 [69], precursor of the VFAT3 which has been described in section 4.2.2. It has a Signal-over-threshold digital readout. The VFAT2 chip has an internal clock of 40 MHz. The output pulse length is measured in integer number of clock cycles and is referred to as monostable pulse length (MSPL). For the different results presented in this section, the MSPL is always set at 4.

Like the VFAT3, the VFAT2 transmits 8 fast trigger signals (not used during this test beam) at 40 MHz and slow tracking data for all the 128 strips, when a trigger signal is received.

An important concept for the analysis is the VFAT2 latency. The VFAT2 latency is

the time, in clock cycles, between an external trigger input and a desired point in the memory where the tracking data is stored. This means that we have to measure the time between the trigger given by the three scintillators and the signal recorded by the GE1/1 prototype.
To measure the VFAT2 latency, we measure the ratio of signals recorded by the VFAT2 electronics to the number of triggers, for the different memory registers. This is called the latency scan. Figure 5.30 shows the latency scan for the GE1/1-V at 650 μA.

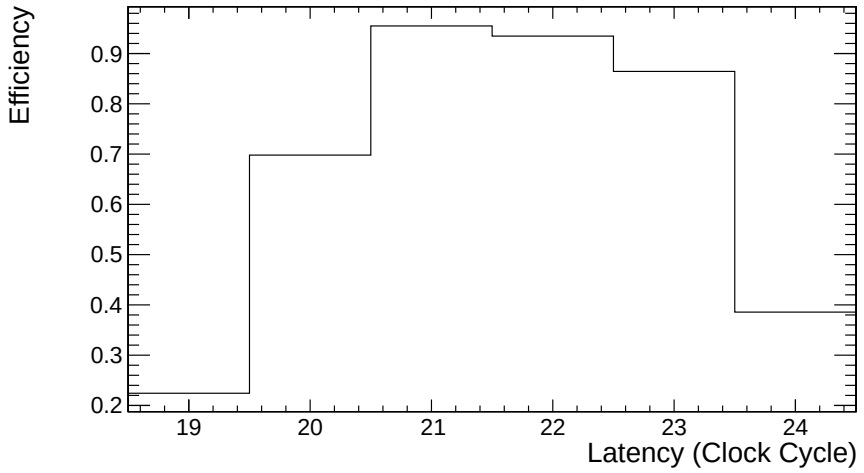

FIGURE 5.30: Latency scan of the GE1/1-V detector at 650 μA.

The latency can change with the current applied to the divider. Indeed, there is two effects that affect the time when the signal is recorded by the electronics. Firstly, as shown on Figure 4.5, the drift velocity of the electrons in the detector increases with the electric field and therefore with the current applied to the divider. Secondly, since the VFAT2 has a Signal-over-threshold readout, there is a time walk effect (as presented in section 4.2.3) which depends on the detector gain and therefore on the divider current. Figure 5.31 shows the evolution of the latency for the three detectors as a function of the current in the divider.

As expected, the latency increases with the current which means that the signal is recorded earlier in the electronics memory.

The back-end electronics is the TURBO. The TURBO can control up to 8 VFAT2 chips and has a clock frequency of 40 MHz.

Efficiency The efficiency of the detector (ε) is defined as follows:

$$\varepsilon = \frac{N_{GE1/1+trk}}{N_{trk}},$$

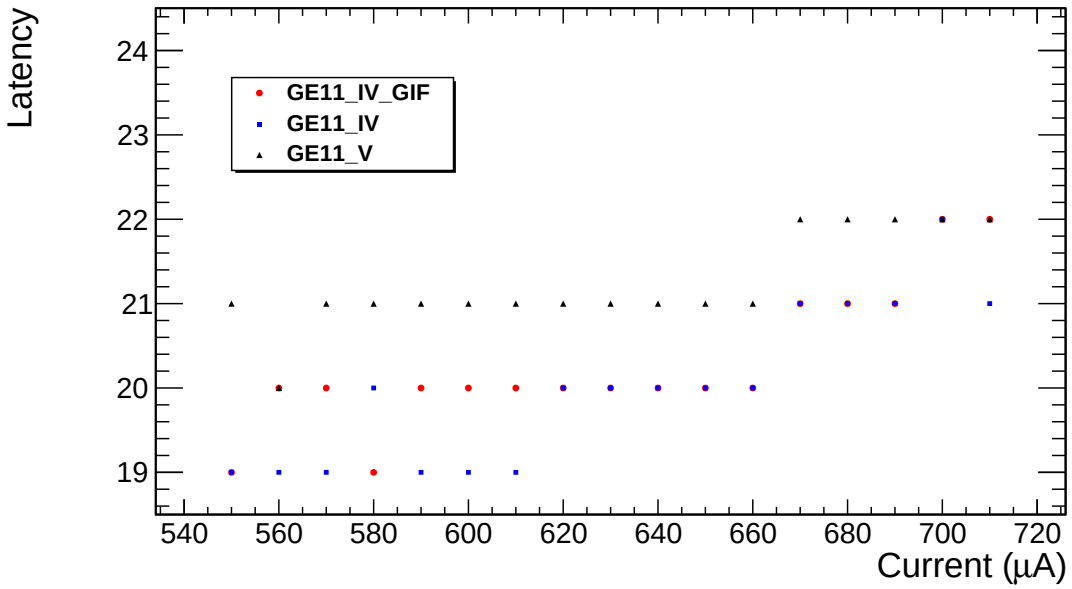

FIGURE 5.31: Evolution of the latency for the three GE1/1 prototypes as a function of the current in the divider.

where N_{trk} is the number of tracks reconstructed with the tracker and $N_{GE1/1+trk}$ is the number of events where a hit is found in the GE1/1 detector and with a reconstructed track.
The track is reconstructed by using a linear fit to the three tracker positions. The track is considered for the evaluation of the efficiency if the three trackers have a hit, and if the χ^2 of the linear fit is less than 5.
Figure 5.32 shows the efficiency for the GE1/1-V prototype for the six different latency values.

We can see that the efficiency curve is good for a latency of 21 or 22 as expected from the Figure 5.31. At the plateau, we achieved an efficiency of $\sim 98\%$.

Figure 5.33 shows the efficiency curve of the Triple-GEM GE1/1-V prototype for a latency of 22 and as a function of the current in the divider and the curve found with the FastSim.

As we already saw in section 4.3.7, the efficiency curve computed by the FastSim reaches the plateau within ± 20 μA with respect to the measured efficiency.

Cluster Size The last parameter that we have studied is the cluster size. The cluster size is the average number of strips hit per event. This parameter is crucial for the spatial resolution of a detector as we will see in the next chapter. Figure 5.34 shows the

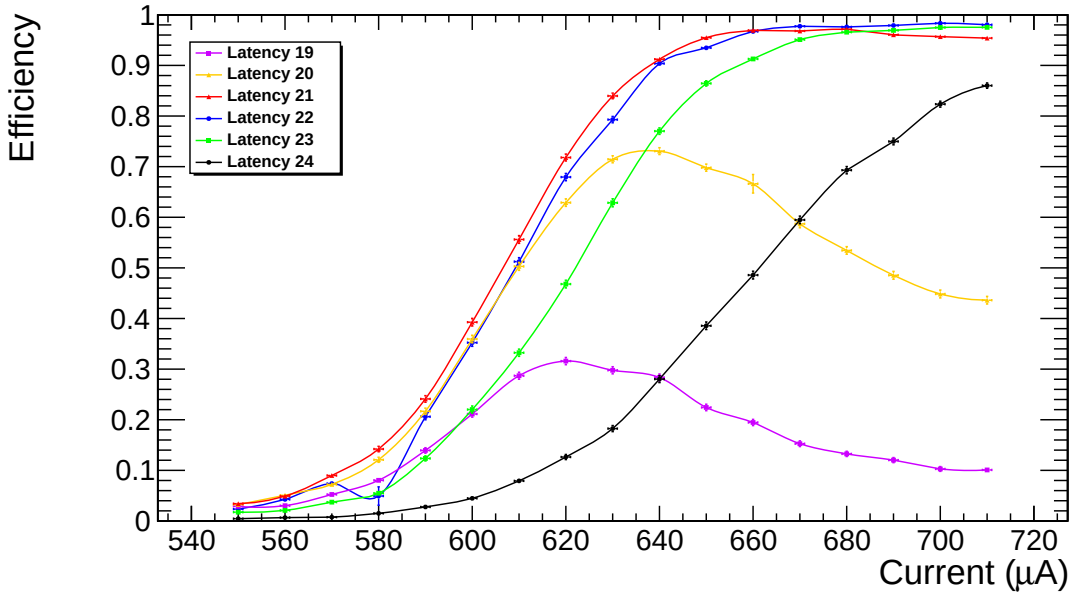

FIGURE 5.32: Efficiency curves for the GE1/1-V prototype as a function of the current in the divider for six different latency values.

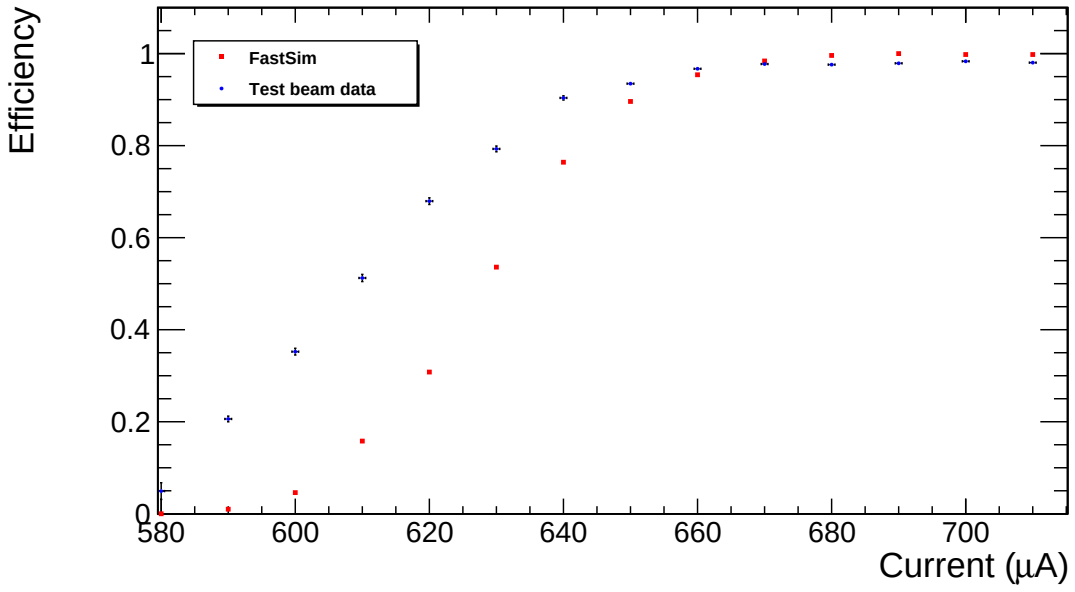

FIGURE 5.33: Efficiency curves as a function of the current in the divider for both the GE1/1-V prototype at a latency value of 22 and the FastSim.

evolution of the cluster size as a function of the current for both the FastSim and the GE1/1-V detector.

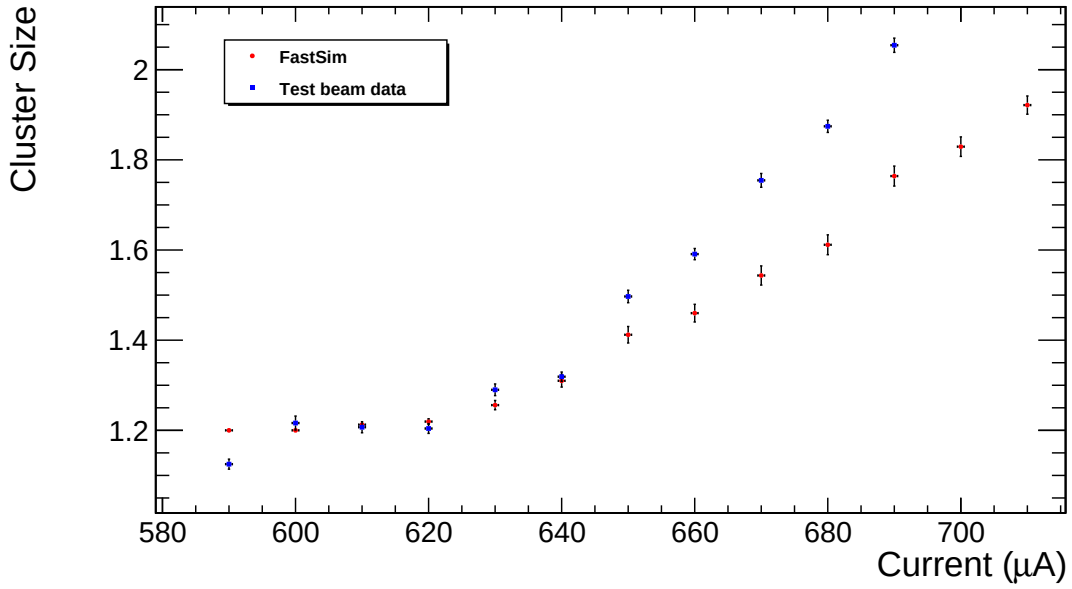

FIGURE 5.34: Evolution of the cluster size as a function of the current in the divider or both the GE1/1-V prototype and the FastSim.

We can see that the cluster size evolves with the current which is expected. Indeed, when the gain increases the tails of the Gaussian distribution of the electrons diffusion will be more populated and therefore the probability to induce a signal higher than the threshold on the adjacent strips increases.
The overall shape between the experimental points and the simulation points seems to be similar but the FastSim underestimates the cluster size for currents over 650 μA. This result is coherent with the discrepancy found in the efficiency curves and suggests that the effective gain used in the FastSim is underestimated.

5.3 Conclusions

The effective gain of the Triple-GEM detector is known to be very delicate to simulate even with the state-of-the-art simulation like GARFIELD. To properly reproduce by simulation Triple-GEM measurements like the detection efficiency, the spatial and time resolution, etc. it is important to rely on precise and well controlled experimental data. For this reason, we have performed ourselves a series of measurements with different Triple-GEM prototypes which allowed us to observe and better understand several processes that take place in our detectors.

The first step was to build two small 10x10 cm^2 prototypes together with the installation of a test-bench at the IIHE lab.
We have measured the gain of the Triple-GEM detector with two different methods that allowed us to confirm that high gains can be achieved for a reasonable voltage. We have also observed large disparities in terms of effective gain within one prototype (up to 25% as a function of the position of the X-ray source). This observation is not very surprising in view of the building process used for those small prototypes. Both methods still give an effective gain of the same order of magnitude even for the higher gains. We also have observed the charging-up effect which increases the gain measured in our GEM detectors.
After those measurements, we have developed a method to extract the effective gain of a single-GEM foil from the measurements of both a Triple- and a Double-GEM prototypes. Unfortunately in view of the discrepancy observed in the previous studies, the effective gain of the single-GEM foil can not be estimated accurately. Nevertheless those measurements have allowed us to better understand the gain in the Triple-GEM detectors.
In October 2014 we also had the opportunity to join a test beam campaign. We participated to the data taking as well as the data analysis. We focused on two important quantities: the efficiency and the cluster size. The results have shown that the CMS GEM detectors are able to reach a very high efficiency of $\sim 98\%$.
Finally we have compared both the efficiency and the cluster size measured during the test beam with the FastSim. Both comparisons are not perfect, however it is remarkable that our 'simple' FastSim reproduces the efficiency plateau within ± 20 μA on the current divider and that the cluster size is reproduced within $\pm 10\%$.
We will show in the next section how the FastSim can be a powerfull tool to understand the behavior of the spatial resolution in Micro-strip detectors.

Chapter 6

Spatial Resolution of Micro-Strip Detectors with Binary Readout

After studying the time resolution and efficiency of our Triple-GEM detectors, we will now focus on a third important parameter of a particle detector: the spatial resolution. As presented in Chapter 4, in the FastSim we reconstruct the position of an incident particle with two different methods (the center of gravity and binary reconstruction). We have observed that, in certain cases, the spatial resolution found with the binary reconstruction was better than the resolution found for the center of gravity method. This observation, a priori unexpected, has led us to study extensively the spatial resolution for the binary readout.

In large experiments such as CMS, comprising hundreds or thousands of detection elements, it is sometimes more advantageous to use a binary readout electronics than an analogue one. Indeed it is not always feasible to integrate an analog-to-digital converter (ADC) in each channel of the front-end ASIC; the constraints are typically associated with the total area of the integrated circuit and with the power consumption. With a binary readout the cost of an increased number of readout channels would then be balanced by a simpler readout circuitry. In addition the data volume is much smaller with a binary readout.

For many applications one can use the binary readout architecture. In this architecture each channel of the front-end electronics is equipped with an amplitude discriminator which generates 1-bit information in response to each signal above a given threshold. The information delivered by a strip detector is suppressed to the minimum already in the front-end circuit. Binary information can be easily stored in the integrated circuit separately for each channel, which allows one to cope with high rate of particles.

In this chapter, the spatial resolution will be estimated analytically and by Monte Carlo simulation for a binary readout for three types of detectors: silicon sensor, Micromegas and GEM-based detectors. The spatial resolution is studied as a function of several parameters: strip pitch, diffusion coefficients, detector volume, track incident angle, ionization statistics, etc. Our approach is rather generic which means that in the future these results could be used to optimize the geometry of new detectors.
The analytic model has been developed from the definition of the spatial resolution for a binary readout. From this definition, the formula is split into two terms: one term represents the geometrical effects and the second represents the diffusion effects. The geometrical effects result from wide strip pitches compared to a charge distribution that depends on the diffusion, the incident angle, and the threshold. The diffusion effect is almost independent of pitches and incident angles; it can be reduced by arranging a small diffusion coefficient or by increasing the number of ionization electrons.
The analytic calculation of the spatial resolution for a binary readout will be presented in details. The relative importance of both terms will be discussed for the 3 types of detectors. The results will also be compared with the simulations, for both a binary and analogue readout.

6.1 Detector Model

In this section, a simple model of detector will be presented to describe different types of detector technologies; semiconductor detectors, Micromegas, and GEM. The model can represent each technology by fixing some parameters.
The detector model consists of the drift region and the induction region, which are separated by an amplification step (Figure 6.1). The drift region is the sensitive part of the detector and the induction region is the volume where the signal is induced to the electronics. The drift region and the induction region have a parameterized size. The other end of the induction region is equipped with the electrode strips with the pitch p. The strips are to be connected to the readout electronics.

Those detectors are used to reconstruct the position of a 'charged particle track'. The position of a track is defined as the midpoint of the track segment in the drift region, and is referred to $\tilde{x}$ in this study. Note that $\tilde{x}$ can be always defined from the center of the nearest strip to the track position and thus $-p/2 \leq \tilde{x} \leq +p/2$.

The parameters used to compute the spatial resolution in this study are the number of primary electrons and the gap of drift region L, the gap of the induction region, the track incident angle ϕ from the vertical axis (z) to the strip plane, the transverse diffusion coefficient $C_d := \sigma_{\mathrm{d}}/\sqrt{z}$ with σ_{d} being the diffusion width of an electron cloud which

has drifted over a length z, namely C_d^{dr} for the drift region and C_d^{in} for the induction region, and an electronics threshold.

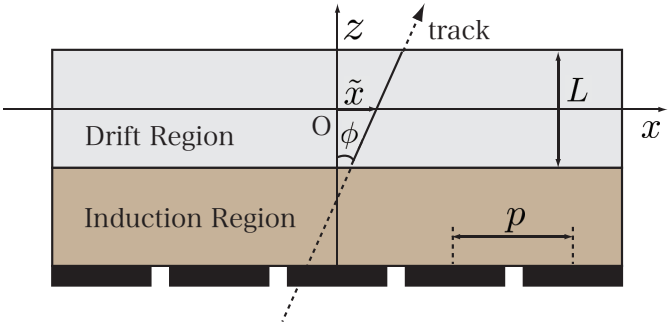

FIGURE 6.1: Detector Model.

6.1.1 Gaseous detectors

The two gaseous detectors considered for this study are the Micromegas [70] and the GEM detectors. Both technologies are classes of MPGD and were presented in section 3.7.

The model presented here describes a basic Single-GEM detector. In the Micromegas case, the difference is that the space between the grid and the anode plane defines the volume of amplification which coincides with the induction region.

6.1.2 Semiconductor detectors

The most important difference compared to the Micromegas and the GEM is that the detector uses a semiconductor material for its sensitive volumes instead of gas mixtures. Since the semiconductor has a factor 10 smaller ionization potential than gas, modern low-noise electronics can read out signals without amplification contrary to the gas-based detectors.

There is neither amplification nor induction region. The induction region coincides with the sensitive region also called the drift region (see our detector model above). Figure 6.2 shows a schematic drawing of a semiconductor detector.

6.2 Simulation

A simulation of the detector has been developed following the model described before. A simple geometry is fixed (the gap sizes, the pitch and diffusion coefficients, etc.), then a track is created. Electrons are created along the track in the drift region. Those

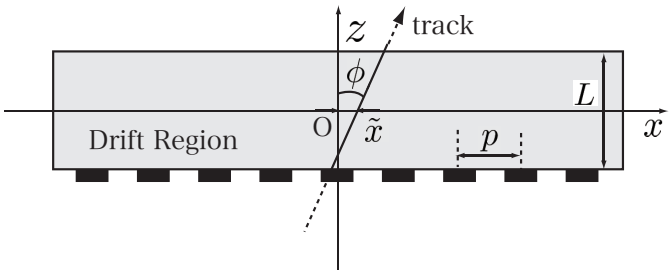

FIGURE 6.2: Schematic drawing of semiconductor detectors.

electrons drift and diffuse until the amplification region. Each electron arriving at the amplification region is multiplied by the gain g. After amplification, all electrons drift and diffuse until the strip plane.
This simulation is based on the FastSim described in chapter 4. Since the goal of this simulation is to obtain the reconstruction of a 'charged particle track', a lot of simplifications have been made in the different algorithms.
All the modifications made on the FastSim will now be described in details.

6.2.1 Charged particle track

It is well known that the detector medium affects the total number of ionized electrons, for instance, ∼100/cm for MIP in Ar gas, ∼1,000,000/cm for MIP in a silicon sensor. To take this fact into account in the simulation, the parameters for the gas-based and the semiconductor detectors are not the same.
For the gas-based detectors the number of clusters is taken randomly on a Poisson distribution with a fix mean value equal to 12, which is obtained from *Magboltz* [46] for a 3 mm argon based gas mixture. Then the number of electrons per cluster is taken randomly on the argon ionization cluster size distribution.
For the semiconductor case, the number of electrons per cluster is arbitrarily fixed to one, but the number of clusters is fixed to 20000, which is a typical value for 300 μm Si sensor.

6.2.2 Electrons motion and gain

The motion of each electron is defined by the following method. The distance L between the position of the electron and the position of the end of the drift region along the z axis is computed. Then the diffusion is computed with :

$$\sigma_d = C_d.\sqrt{L},$$

where C_d is the transverse diffusion coefficient. The new X position of the electron is randomly chosen on a Gaussian with a mean of $\tilde{x}$ and a sigma of σ_d.
Then, in the gas based detector, to simulate the gain $g-1$ electrons are created at that new position (X_{ampl}).
Each of those electrons is then moved to the readout plane and its X position is computed with the same diffusion formula (with L equal to the induction gap size).

6.2.3 Induction and threshold

To simulate the strips a histogram is created in the same way as the FastSim. The bin size is equal to the strip pitch, in this way, each bin represents a strip. For each electron, the bin corresponding to the final X position of this electron is filled. Then the electronics threshold is applied.
The computation of the induced current is not done in this simulation.

6.2.4 Reconstructed position

With the analog output, we reconstruct the X position with the center of gravity (CoG) method, and with the binary output, we use an average position of the hit strips. Both methods are described in section 4.3.6.
To obtain the spatial resolution we use the residual distribution. The residual is the distribution of the difference between the reconstructed position and the real position (in our case, the simulated position of the particle track). The mean of the residual distribution is, by definition, the bias of the reconstruction method and the RMS of the distribution is used as the spatial resolution of the method.

6.2.5 Spatial resolution

As a matter of fact, the reconstructed position from measured data is somehow displaced from the original track position because of stochastic processes in detectors and the finite strip pitch size. Therefore it is essential to take into account the spatial resolution to reconstruct the track position from measured data.
The spatial resolution σ_x can be defined with a probability $P(x_{reco}; x_{track})$ that a position x_{reco} is reconstructed for the track position x_{track}:

$$\sigma_x^2(x_{track}) = \int dx_{reco}\, P(x_{reco}; x_{track})\, (x_{reco} - x_{track})^2. \tag{6.1}$$

Experimentally, the RMS of the residual $(x_{reco} - x_{track})$ is often used to estimate σ_x. One can note that this definition is completely generic. It means that the time resolution or the energy resolution can be defined with the same expression by interpreting the meaning of x_{reco} and x_{track} as time or energy instead of position.

6.2.6 Effect of the Transverse Diffusion on the Spatial Resolution

Figure 6.3 shows an example of our simulation results in which spatial resolutions are plotted as a function of σ_d assuming typical semiconductor configurations and a track angle of $\phi = 0$. Note that each point represents a spatial resolution for a specific detector configuration that has a specific σ_d. The fact is that a σ_d represents several detector cases since σ_d depends on the drift region gap and the bias voltage. The evolution of the cluster size with respect to the σ_d is also plotted for the same configuration.

The spatial resolution with the analogue readout (CoG) improves as σ_d becomes larger, since the CoG method does not work well when the number of hit strips is less than three, which is described as the effects of finite size pads in ref.[71]. On the other hand, the spatial resolution with the binary readout has two characteristics:

1. a wavy structure, which makes roughly twice the difference at maximum,
2. the wavy structure becomes less visible as σ_d increases.

The understanding of these behaviors may open the possibility to improve the spatial resolution with the binary readout.

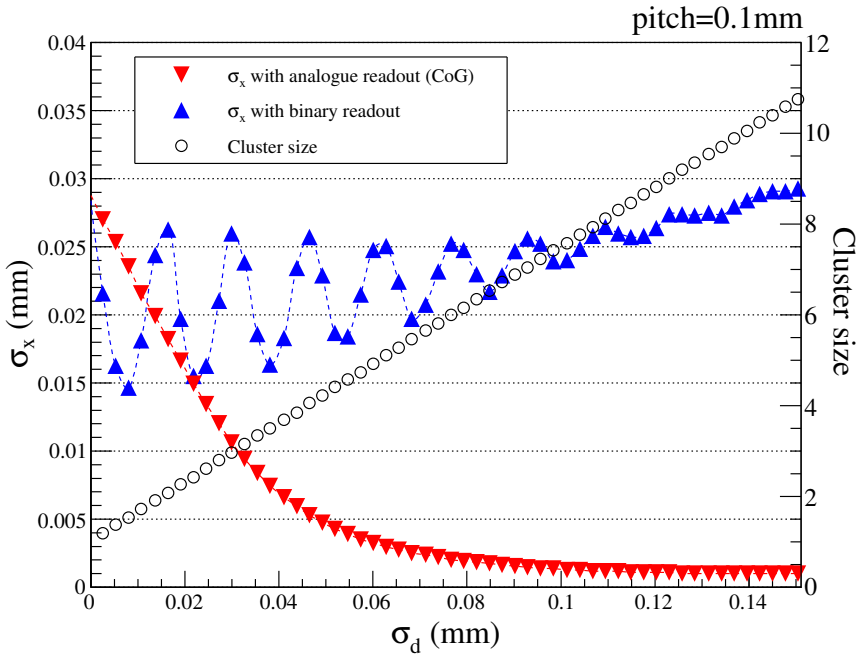

FIGURE 6.3: Spatial resolution σ_x as a function of σ_d for a typical semiconductor configuration, assuming the track angle $\phi = 0°$.

6.3 Analytic examination

In this section the focus will be on more analytic aspects in order to understand the behavior observed at the previous sections. A previous work [72] has shown that an analytic expression of the spatial resolution can be written for Time Projection Chambers (TPC). Here, a similar expression is formulated but considering the binary read-out and the different incident track angles to the readout plane.

6.3.1 Introduction

Accuracy term and Precision term The spatial resolution is defined at Eq.(6.1). However, the systematic error due to the finite strip pitch has to be taken into account and consequently the definition should be written as:

$$\begin{aligned} \sigma_x^2 &:= \frac{1}{p}\int_{-p/2}^{+p/2} dx_{track} \int dx_{reco}\, P(x_{reco}; x_{track})\,(x_{reco} - x_{track})^2 \\ &= \frac{1}{p}\int_{-p/2}^{+p/2} dx_{track}\, \left\langle (x_{reco} - x_{track})^2 \right\rangle , \end{aligned} \tag{6.2}$$

where we introduced the notation $\langle\,\rangle$ representing $\int dx_{reco} P(x_{reco}; x_{track})$. Eq.(6.2) is rewritten to split the formula into two terms as:

$$\begin{aligned} \sigma_x^2 &= \frac{1}{p}\int_{-p/2}^{+p/2} dx_{track}\,\left[\left\langle (x_{reco} - \langle x_{reco}\rangle)^2 \right\rangle + (\langle x_{reco}\rangle - x_{track})^2\right] \\ \left(\frac{\sigma_x}{p}\right)^2 &= \int_{-1/2}^{+1/2} d\left(\frac{x_{track}}{p}\right)\left[\left\langle \left(\frac{x_{reco}}{p} - \left\langle \frac{x_{reco}}{p}\right\rangle\right)^2 \right\rangle + \left(\left\langle \frac{x_{reco}}{p}\right\rangle - \frac{x_{track}}{p}\right)^2\right] \end{aligned} \tag{6.3}$$

In the last line, we divided both side of the equation by p^2 to be described by dimensionless parameters: σ_x/p, x_{track}/p, and x_{reco}/p. The first term is the variance of x_{reco}/p and the second term is the deviation of $\langle x_{reco}/p\rangle$ from the true position x_{track}/p, and thus these terms will be referred to as "precision term" and "accuracy term", respectively.

Each term is separately plotted, together with the simulation results in several conditions in Figure 6.4. The sum of the precision term and the accuracy term matches the corresponding simulation as expected. The precision term increases according to σ_d and thus this term can be taken as a contribution from the diffusion effect. On the other hand, the accuracy term has a periodic structure, and it is more clearly visible in smaller σ_d region, especially for semiconductor detector configuration in which a large number of ionized electrons are produced. GEM and Micromegas detector configurations give similar results except for small σ_d region because of the additional diffusion in the induction regions. The accuracy term will be revisited in section 6.3.2.

The track angle does not affect much the precision term, however it does affect the accuracy term. This behavior can be qualitatively understood as follows:

1. If the track angle is not 0°, the charge width at the readout plane depends not only on the diffusion σ_d but also on the projected length of a tilted track. This fact is schematically shown in Figure 6.5 with respect to different diffusion cases.

2. In small σ_d region, the projected length of a tilted track mimics the diffusion effect as shown at (T.1) in Figure 6.5. This means the behavior is similar to the 0° angle track case, but it must be shifted to left (to smaller σ_d) by the projected track length when one looks at the spatial resolution as a function of σ_d.

3. In large σ_d region, the charge spread evolves via (T.2) and (T.3) to (T.4) in Figure 6.5. In this case, the track angle effect is buried under the diffusion effect and thus the reconstructed position systematically displaced by $D\tan\phi/2$ at maximum.

Auxiliary parameter ΔW To investigate more concretely, let us introduce a new parameter representing an effective width of charge spread. In other words, the signal

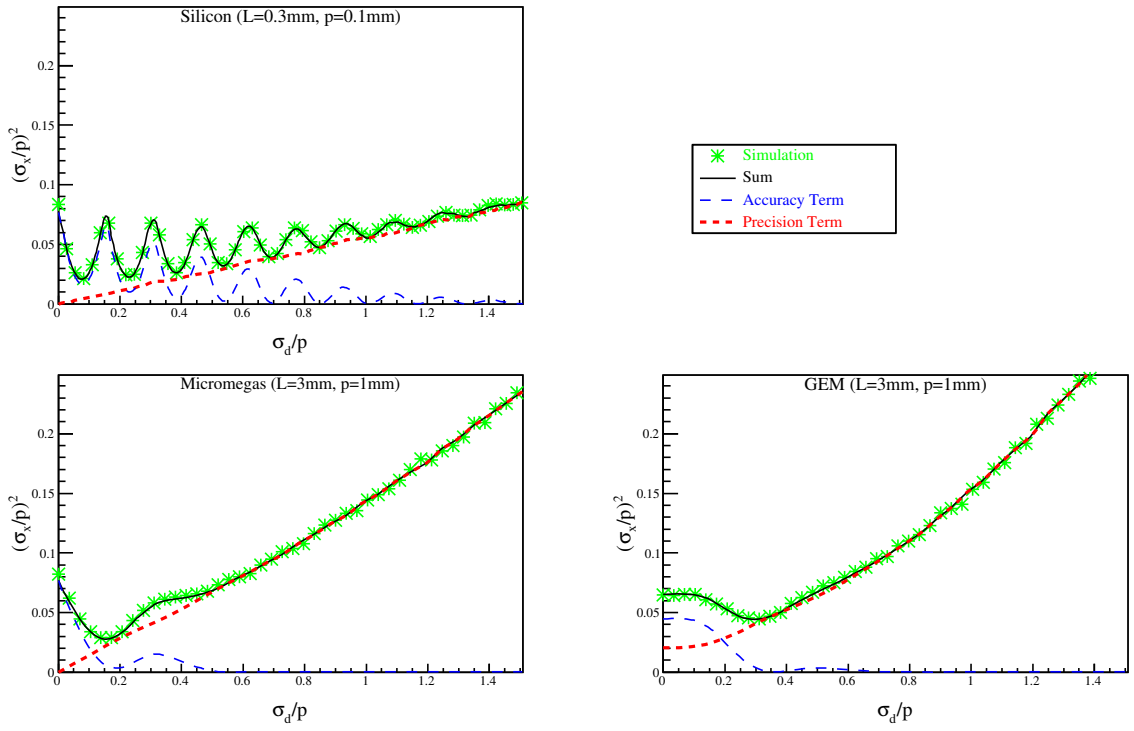

FIGURE 6.4: Comparison between our simulation (green, star) and the sum (black, solid line) of the precision term (red, dashed line) and the accuracy term (blue, dashed line) for three different detector models. The precision term and the accuracy term were numerically computed here.

is assumed to come from the strips within $x_{track} \pm \Delta W$ (as shown in Figure 6.6). ΔW is therefore the distance between the edge of the strip and the position of the incident particle from which the signal is detected by two strips. Note that this ΔW depends not only on the diffusion but also on the incident track angle as well as the electronic threshold. In reality this ΔW varies because of the stochastic processes such as the diffusion, the ionization, and the gas gain. However constant values for ΔW will be used as a first approximation, and this will be referred as "simplified model". Figure 6.7 shows a comparison of the cluster size as a function of the track position between the simulation and the simplified model.

As can be seen in Figure 6.7, the cluster size depends on the track position in a readout strip. To describe the boundary where the cluster size changes, let us define $\mu_{\pm n}$:

$$\mu_{\pm n} := \pm\left(n - \frac{1}{2} - \frac{\Delta W}{p}\right) := \pm\left(n - \frac{1}{2} - \Delta W_p\right), \tag{6.4}$$

where we defined ΔW_p as $\Delta W/p$. μ_{+n} is the value of x_{track}/p where the charge spread touches to the strip of $a = n$ from the lower side, and μ_{-n} is the value of x_{track}/p where the charge spread touches to the strip of $a = -n$ from the upper side. Figure 6.8 shows example cases of $n = 1$.

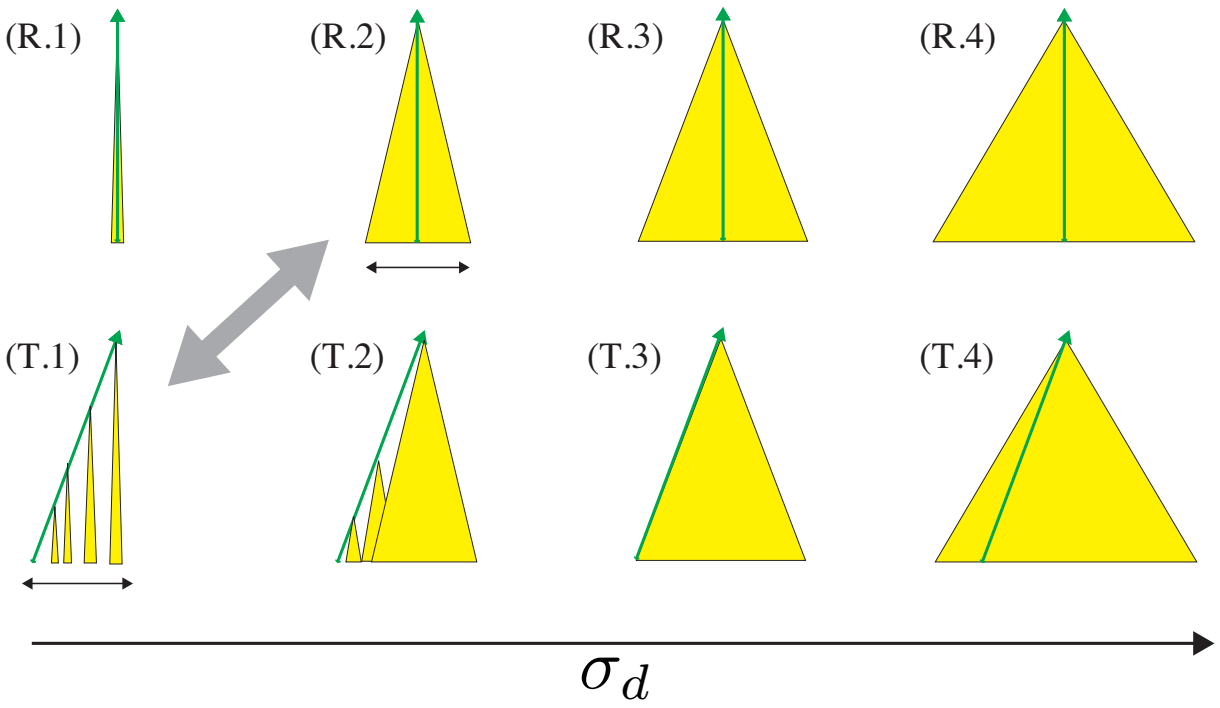

FIGURE 6.5: Evolving electron cloud (yellow) from a track (green) as a function of σ_d for the right angle tracks in the first row and for the tilted tracks in the second row. Comparing (R.2) and (T.1), they are similar in terms of signal width and thus (T.1) must give similar spatial resolution to (R.2), but with smaller σ_d. This results in a left-shift in the spatial resolution plots as a function of σ_d (Figure 6.4).

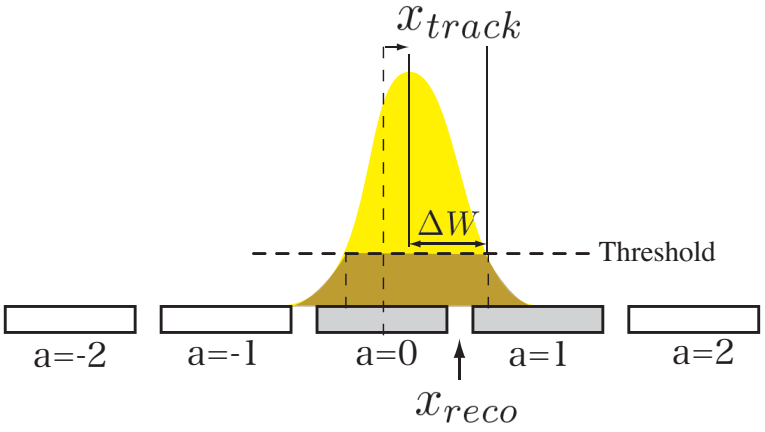

FIGURE 6.6: Graphical interpretation of ΔW. The yellow shape represents a charge spread and ΔW can be interpreted as an effective width of the charge spread. When the strips $a = 0$ and $a = 1$ collect a certain amount of electrons like in this figure, the reconstructed position (x_{reco}) is expected to be between $a = 0$ and $a = 1$. Note that the ΔW depends not only on the diffusion but also the threshold, the track angle and the diffusion in the amplification region e.g. GEM. Note that the threshold is applied on the integrated charge on the strips.

Note that

$$\frac{x_{reco}}{p} = \begin{cases} 0 & (\mu_{min} \leq x_{track}/p \leq \mu_{max}) \\ 1 & (\mu_{max} < x_{track}/p) \\ -1 & (\mu_{min} > x_{track}/p) \end{cases} \tag{6.5}$$

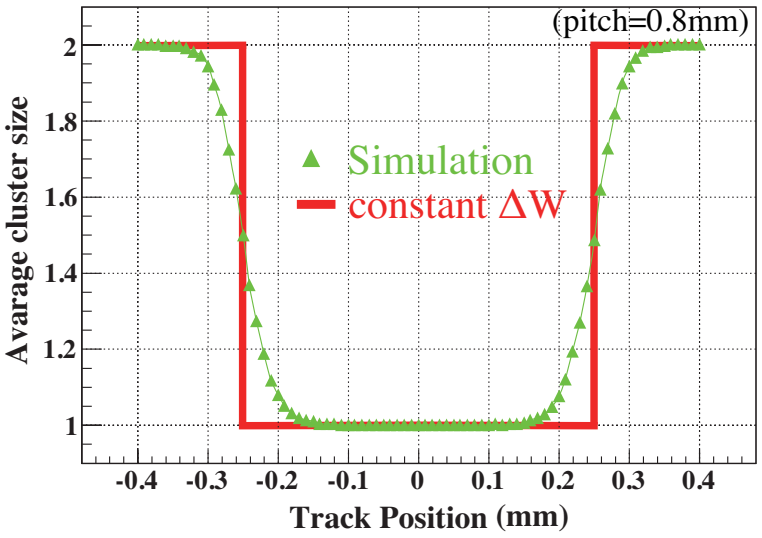

FIGURE 6.7: Schematic view to show difference between our simulation and simplified model in terms of the cluster size. The jump at $\pm \sim 0.25$ corresponds to $\mu_{\pm 1}$.

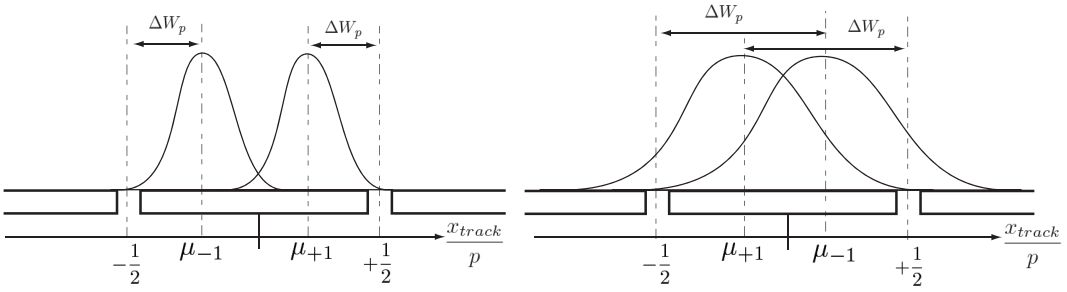

FIGURE 6.8: The charge spread touches the boundary of the strip $a = 1$ (-1) at $x_{track} = \mu_{+1}$ (μ_{-1}). On the left is a case of $\mu_{+1} > \mu_{-1}$. On the right is a case of $\mu_{-1} > \mu_{+1}$.

with μ_{max} being $\max(\mu_{+1}, \mu_{-1})$ and μ_{min} being $\min(\mu_{+1}, \mu_{-1})$.

6.3.2 One parameter model for the accuracy term

If we consider all the hit strips are in contact with their neighbor hit strips, the reconstructed position in an event is always discrete:

$$\frac{x_{reco}}{p} = 0, \pm 0.5, \pm 1.0, \pm 1.5 \cdots \tag{6.6}$$

This fact motivates us to rewrite the accuracy term in the following general expression:

$$\begin{aligned} \text{Accuracy Term} &= \int_{-1/2}^{+1/2} d\left(\frac{x_{track}}{p}\right) \left(\left\langle \frac{x_{reco}}{p} \right\rangle - \frac{x_{track}}{p} \right)^2 \\ &\equiv \int_{-1/2}^{+1/2} d\left(\frac{x_{track}}{p}\right) \left(\sum_{k=-\infty}^{+\infty} R_k(x_{track}) \frac{k}{2} - \frac{x_{track}}{p} \right)^2, \end{aligned} \tag{6.7}$$

where $R_k(x_{track})$ (k:integer) is the probability that the position is reconstructed at $k/2$. Note that a special condition $R_0 = 1$, $R_{k\neq 0} = 0$ gives a well known formula $(\sigma_x/p)^2 = 1/12$.

As a first step, let us develop Eq.(6.7) assuming a specific condition $\Delta W_p \leq 1$ in which Eq.(6.5) should be satisfied:

$$\begin{aligned}
\text{Accuracy Term} &= \int_{-1/2}^{+1/2} d\left(\frac{x_{track}}{p}\right)\left(\sum_{k=-\infty}^{+\infty} R_k(x_{track})\frac{k}{2} - \frac{x_{track}}{p}\right)^2 \\
&= \int_{-1/2}^{+1/2} d\left(\frac{x_{track}}{p}\right)\left(R_{+1}(x_{track})\cdot\left(\frac{1}{2}\right) + R_{-1}(x_{track})\cdot\left(\frac{-1}{2}\right) - \frac{x_{track}}{p}\right)^2 \\
&= \int_{-1/2}^{+1/2} d\left(\frac{x_{track}}{p}\right)\left(\frac{f_{+1}}{2} - \frac{f_{-1}}{2} - \frac{x_{track}}{p}\right)^2, \qquad (6.8)
\end{aligned}$$

where we defined "turn-on" functions of readout strip of $a = \pm 1$ as :

$$\begin{aligned}
f_{+1} &:= \begin{cases} 1 & \left(\frac{x_{track}}{p} \geq \mu_{+1}\right) \\ 0 & \left(\frac{x_{track}}{p} < \mu_{+1}\right) \end{cases} \\
f_{-1} &:= \begin{cases} 1 & \left(\frac{x_{track}}{p} \leq \mu_{-1}\right) \\ 0 & \left(\frac{x_{track}}{p} > \mu_{-1}\right). \end{cases} \qquad (6.9)
\end{aligned}$$

This model is only valid within $\Delta W_p \leq 1$ as assumed, but this can be easily generalized in a similar fashion:

$$\begin{aligned}
\text{Accuracy Term} &= \int_{-1/2}^{+1/2} d\left(\frac{x_{track}}{p}\right)\left(\sum_{k=-\infty}^{+\infty} R_k(x_{track})\frac{k}{2} - \frac{x_{track}}{p}\right)^2 \\
&= \int_{-1/2}^{+1/2} d\left(\frac{x_{track}}{p}\right)\left(\sum_{n=1}^{\infty}\left(\frac{f_{+n}}{2} - \frac{f_{-n}}{2}\right) - \frac{x_{track}}{p}\right)^2, \qquad (6.10)
\end{aligned}$$

with

$$\begin{aligned}
f_{+n} &:= \begin{cases} 1 & \left(\frac{x_{track}}{p} \geq \mu_{+n}\right) \\ 0 & \left(\frac{x_{track}}{p} < \mu_{+n}\right) \end{cases} \\
f_{-n} &:= \begin{cases} 1 & \left(\frac{x_{track}}{p} \leq \mu_{-n}\right) \\ 0 & \left(\frac{x_{track}}{p} > \mu_{-n}\right). \end{cases} \qquad (6.11)
\end{aligned}$$

Since the number of hit strips is likely less than 7 in most practical cases, f_{+n} and f_{-n} for $n > 3$ are expected to be 0. In such a case the sum in Eq.(6.10) is necessary only for $n \leq \sim 2$. A numerical computation of Eq.(6.10) is shown in Fig. 6.9 to see how the spatial resolution evolves with ΔW_p. This one-parameter model explains the wavy structure seen in the accuracy term.

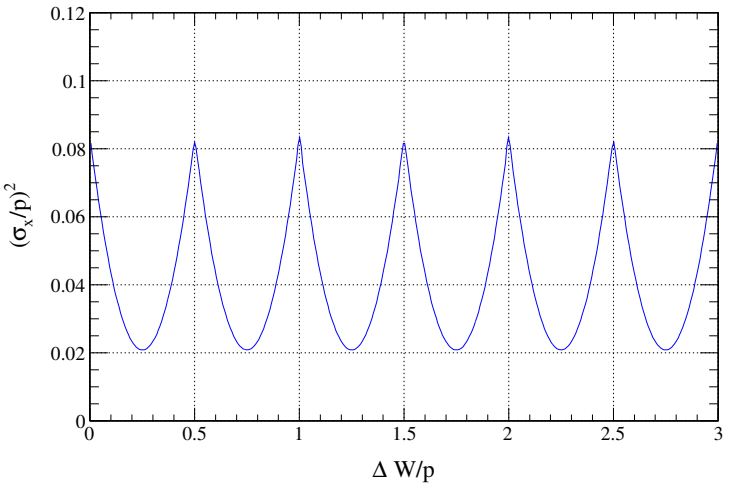

FIGURE 6.9: The accuracy term described with the one-parameter model (Eq.(6.10)). This model explains the wavy structure seen in the accuracy term.

Fig. 6.10 shows comparison between the accuracy term from the simulation and the one from the one-parameter model. The discrepancy getting larger according to σ_d/p is caused by the fact that the constant ΔW assumption becomes no longer valid due to large diffusion with limited ionization statistics.

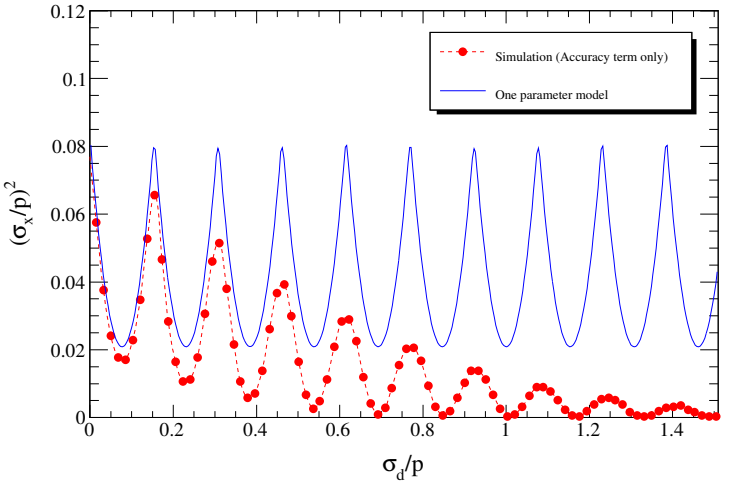

FIGURE 6.10: The one-parameter model compared to the simulation. In this example, we set $\Delta W = 3.25\sigma_d$ so that their periodic patterns are matched.

6.3.3 Two parameter model for the accuracy term

The diffusion causes fluctuations in ΔW, however this fact was not taken into account in the previous section. When ΔW fluctuates, the boundaries μ_n defined in Eq.(6.4) are no longer constant in each event. This fact was already observed in Figure 6.7, where the transition boundary between the cluster size of 1 and that of 2 can be defined as a

point (e.g. ± 0.25) in the model case (Red line) while it can be only defined as a range (e.g. from ± 0.18 to ± 0.32) in the realistic simulation (Green line). In order to take this effect into account, let's define transition regions with a width of 2δ as highlighted in yellow in Figure 6.11. The idea is to linearly weight $f_{\pm n}$ in the transition region. We

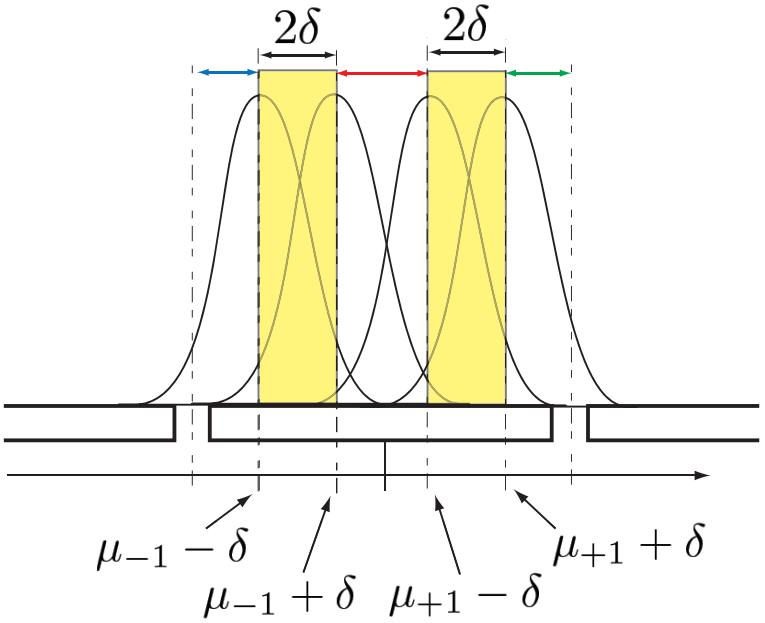

FIGURE 6.11: Transition region around $\mu_{\pm 1}$ with its width of 2δ in the two parameter model.

therefore constrain δ being proportional to ΔW_p as a first approximation. Eq.(6.11) can be modified as follows:

$$
\begin{aligned}
f_{+n} &= \begin{cases} 1 & \left(\frac{x_{track}}{p} > \mu_{+n} + \delta \right) \\ t_n & \left(\mu_{+n} - \delta \leq \frac{x_{track}}{p} \leq \mu_{+n} + \delta \right) \\ 0 & \left(\frac{x_{track}}{p} < \mu_{+n} - \delta \right) \end{cases}, \\
f_{-n} &= \begin{cases} 0 & \left(\frac{x_{track}}{p} > \mu_{-n} + \delta \right) \\ s_n & \left(\mu_{-n} - \delta \leq \frac{x_{track}}{p} < \mu_{-n} + \delta \right) \\ 1 & \left(\frac{x_{track}}{p} < \mu_{-n} - \delta \right) \end{cases}, \\
t_n &= \frac{1}{2\delta} \left(\frac{x_{track}}{p} - (\mu_{+n} - \delta) \right), \qquad (6.12) \\
s_n &= 1 - \frac{1}{2\delta} \left(\frac{x_{track}}{p} - (\mu_{-n} - \delta) \right). \qquad (6.13)
\end{aligned}
$$

Note that δ works as a second parameter to describe the fluctuations in ΔW. The main difference from the one-parameter model is, that $f_{\pm n}$ could shift simultaneously depending on the track position x_{track} within the transition region. This can recover the fluctuation effect on ΔW due to the diffusion in the drift region, which was missing in the one parameter model. This improvement can also be seen from the viewpoint of the cluster size (Figure 6.12).

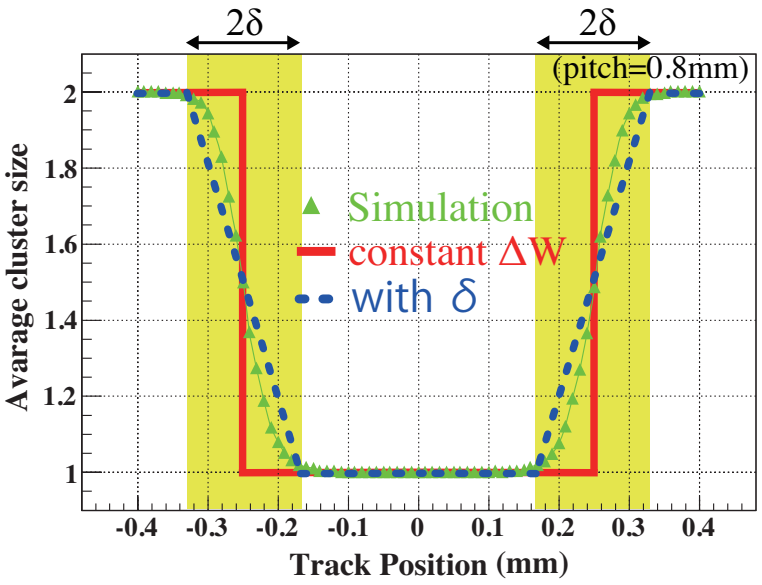

FIGURE 6.12: A comparable plot to Figure 6.7, but with including the transition regions. The blue dotted line corresponds to the new model introduced at section 6.3.3.

A numerical computation of Eq.(6.10) with Eq.(6.12) is shown in Figure 6.13 to see how the spatial resolution evolves with $\Delta W/p$. This two parameter model can describe the simulation result well with just two parameters; ΔW and δ.

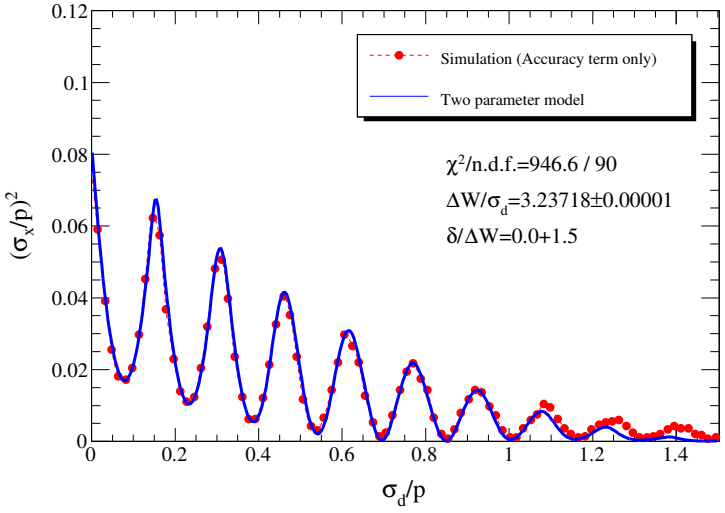

FIGURE 6.13: Two parameter model with fitted parameters of $\Delta W/\sigma_d = 3.23$ and $\delta/\Delta W = 0.99$ compared to the simulation. To compute χ^2, a fixed error of 0.0005 is assumed to each simulation point.

6.3.4 Sigmoid expression for two parameter model

Although the two-parameter model describes well the simulation result, it is difficult to generalize the integration over x_{track}/p due to the condition analysis (e.g. $f_{+n} = 1$ when

$x_{track}/p \leq \mu_{+n}$). To improve this situation we propose another formulation of $f_{\pm n}$ with the sigmoid functions:

$$\begin{aligned} f_{+n} &= \frac{1}{1+\exp[-\frac{x_{track}/p-\mu_{+n}}{2\delta}]}, \\ f_{-n} &= \frac{1}{1+\exp[\frac{x_{track}/p-\mu_{-n}}{2\delta}]}, \end{aligned} \tag{6.14}$$

where $\mu_{\pm n}$ are defined in Eq.(6.4). Noting Eq.(6.10) can be rewritten as:

$$\begin{aligned} \text{Accuracy Term} = \int_{-1/2}^{+1/2} d\left(\frac{x_{track}}{p}\right) \Bigg(& \frac{1}{4}\sum_{n=1}^{\infty}(f_{+n}-f_{-n})^2 + \frac{1}{2}\sum_{n<n'}(f_{+n}-f_{-n})\,(f_{+n'}-f_{-n'}) \\ & -\sum_{n=1}^{\infty}\frac{x_{track}}{p}\,(f_{+n}-f_{-n}) + \left(\frac{x_{track}}{p}\right)^2 \Bigg). \end{aligned} \tag{6.15}$$

Figure (6.14), (6.15) and (6.16) show fitting results with using the sigmoid expression model for a silicon detector case, a Micromegas detector case, and a GEM detector case. For the GEM detector case, an additional parameter $\Delta W_{\rm prf}/p$ is introduced to consider the diffusion in the induction region, and $\mu_{\pm n}$ in Eq.(6.4) is modified as:

$$\mu_{\pm n} := \pm\left(|n| - \frac{1}{2} - \sqrt{\left(\frac{\Delta W}{p}\right)^2 + \left(\frac{\Delta W_{prf}}{p}\right)^2}\right). \tag{6.16}$$

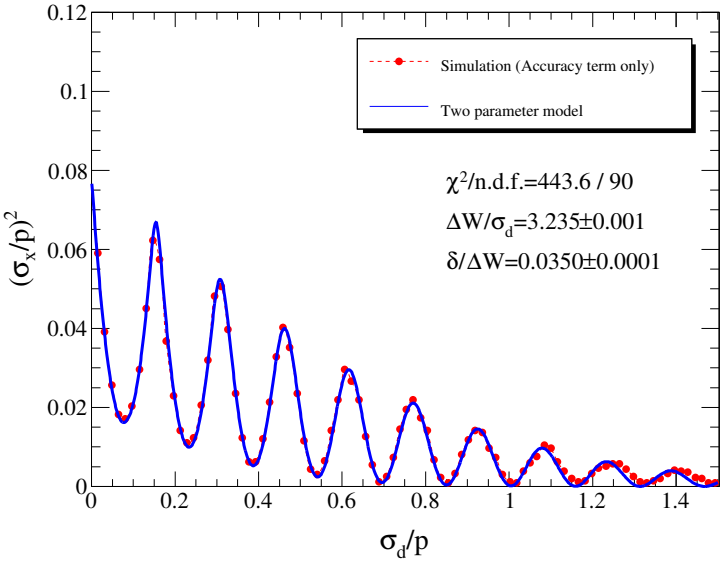

FIGURE 6.14: Two parameter model with sigmoid functions compared to the simulation for silicon detector configuration. To compute χ^2, a fixed error of 0.0005 is assumed to each simulation point.

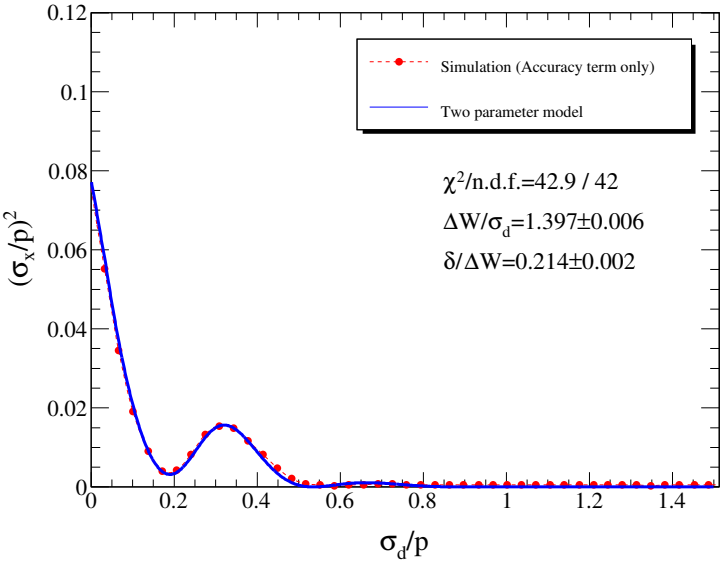

FIGURE 6.15: Two parameter model with sigmoid functions compared to the simulation for Micromegas detector configuration. To compute χ^2, a fixed error of 0.0005 is assumed to each simulation point.

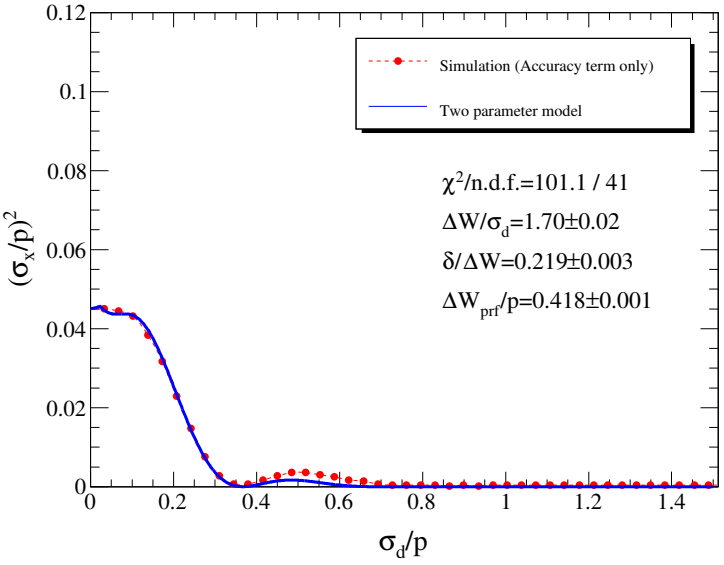

FIGURE 6.16: Two parameter model with sigmoid functions compared to the simulation for GEM detector configuration. To compute χ^2, a fixed error of 0.0005 is assumed to each simulation point.

6.4 Cluster size

The cluster size is defined as the average number of hit strips and is a measurable variable. Using $f_{\pm n}$ defined in the previous sections, the cluster size can be written

down as:

$$\text{Cluster Size} = 1 + \int_{-1/2}^{+1/2} d\left(\frac{x_{track}}{p}\right)\left\{\sum_{n=1}^{\infty}(f_{+n} + f_{-n})\right\}. \tag{6.17}$$

If adopting the sigmoid definition of Eq.(6.14), it can be rewritten as follows:

$$\text{Cluster Size} = 1 + \sum_{n=1}^{\infty}\left\{2 + 2\delta\left[\ln\left(\exp\left[-\frac{x_{track}/p - \mu_{+n}}{2\delta}\right] + 1\right)\right.\right. \\ \left.\left. - \ln\left(\exp\left[\frac{x_{track}/p - \mu_{-n}}{2\delta}\right] + 1\right)\right]_{-1/2}^{+1/2}\right\}. \tag{6.18}$$

An example plot is shown in Figure 6.17 together with the simulation result. The result shows that the two parameters can describe not only the spatial resolution but also the cluster size. This implies that, if the spatial resolution is dominated by the accuracy term, and once one measures the spatial resolution and the cluster size from an experiment, one can solve the Eq. of (6.15) and (6.18) and obtain the two model parameters: $\Delta W/\sigma_d$ and $\delta/\Delta W$. These two parameters will give a guiding principle how to optimize the spatial resolution for instance by changing electronics threshold, the electric field, gas mixture or readout pitch.

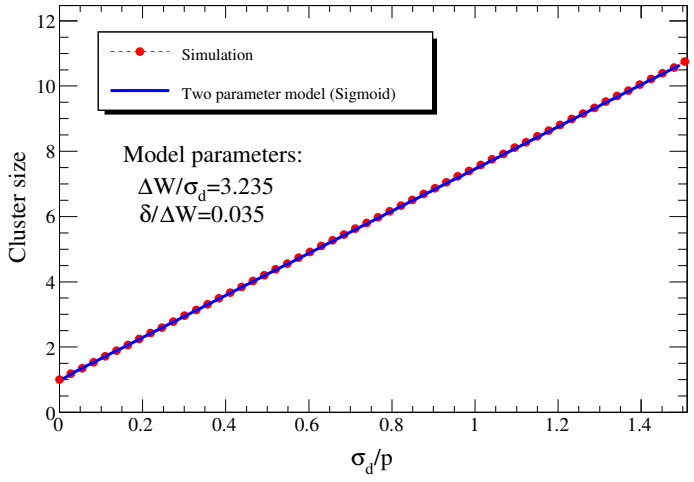

FIGURE 6.17: Cluster size compared with Two parameter model with sigmoid functions and the simulation for silicon detector configuration. The parameters for the model are same as the ones obtained by fitting the spatial resolution.

6.5 Conclusion

Studying the residuals between the reconstructed hit and the simulated hit with the FastSim software, we unexpectedly observed that in some cases the binary readout could lead to a better spatial resolution than the analogue readout when we use the center of gravity of the charge distribution.

This observation triggered a systematic study of the behavior of the spatial resolution with both readout types as a function of various parameters like the strip pitch, the diffusion coefficient, the primary ionization, etc.

The FastSim code, first developed for the CMS Triple-GEM simulation, has been extended to study various detector types including silicon detectors. A breakthrough of this work is also the development of the analytic formula describing the behavior of the spatial resolution, nicely confirmed by the simulations. The analytic formula is broken down into two terms the accuracy term and the precision term that can numerically be computed. The sum of them fits the corresponding simulation results.

We have also introduced a variable representing the effective width of the charge spread, ΔW, to explain the wavy structure of the accuracy term. Later we have improved our model by adding a second parameter named δ so that the fluctuations of ΔW due to the diffusion in the drift gap can be taken into account. The two parameter model is applicable for silicon detectors and Micromegas detectors. To model the GEM detectors a third parameter, $\Delta W_{\mathrm{prf}}/p$, taking into account the diffusion in the induction gap is added.

Once the two parameters for a silicon detector or a Micromegas detector are found by measuring the spatial resolution and the cluster size, the formula can be a guiding principle to improve the spatial resolution by optimizing such as the detector gap size, the strip pitch size, the electric field in the drift region, or the comparator threshold. For GEM detectors, an external measurement is necessary to determine the diffusion effect in the induction region.

This very promising analysis is now published in Nucl. Instr. and Meth. A [73].

In the future we would like to extend the study for tracks non-perpendicular to the strips. We also intend to find more experimental data in the literature against which our models can be confronted.

Chapter 7

Summary

This work is a contribution to the study of Triple-GEM detectors for the upgrade of the CMS muon spectrometer. This upgrade consists of the addition of a new layer of GEM detectors in the high-η region of CMS. It is within this framework that we have studied the three key parameters of the CMS Triple-GEM detectors: their time resolution, spatial resolution and efficiency. We had the opportunity to study those parameters both through different simulations and also by conducting several measurements on various prototypes.

For this upgrade a new front-end electronics, the VFAT3, is under design. We have therefore investigated by simulation the time resolution one can expect with a CMS Triple-GEM detector read-out with a VFAT3. The study has been performed using the GARFIELD simulation, the FastSim and the Hybrid simulation.
We have shown that the best method, in terms of combined time resolution and latency, is the CFD method which yields a time resolution of 4.98 ± 0.16 ns for a peaking time of 50 ns with a latency of 100 ± 5 ns.
The various effects that contribute to the time resolution of the Triple-GEM detector have been studied in detail. It has been shown that the main contribution is due to the primary ionization clusters statistics, accounting for ~ 3 ns for $Ar/CO_2/CF_4$ (45:15:40) gas mixture and ~ 4.5 ns for Ar/CO_2 (70:30) gas mixture.
The results of the FastSim for the $Ar/CO_2/CF_4$ (45:15:40) gas mixture are comparable with the results obtained with GARFIELD despite the simplification of the simulation. The main advantage of the FastSim compared to GARFIELD is the simulation time. GARFIELD simulations can take several hours against a few second for the FastSim to simulate one muon signal. Afterwards we have used the CFD method on signals produced with the FastSim for the Ar/CO_2 (70:30) gas mixture and we have shown that the time resolution is better than 7 ns which confirms that the CMS Triple-GEM

detector fulfill the upgrade requirement in terms of time resolution, with CF_4-free gas mixture.
With the Hybrid simulation, the induced anode current has been computed on multiple strips. The time resolution found for the strips hit is fully compatible with the results of the FastSim where only one strip was simulated.

So far all our simulations were based on GEM foil gains computed by GARFIELD simulations. To avoid this, we have performed a systematic measurement of the gain with several prototypes. Those measurements have allowed us to confirm that high gains can be achieved for a reasonable voltage even if large disparities in effective gain have been observed. We have also developed a method to extract the effective gain of a single-GEM foil from the measurements of both a Triple- and a Double-GEM prototypes. This method is promising, provided a better uniformity during the assembly.
In October 2014 we had the opportunity to join a test beam campaign. We participated to the data taking at CERN as well as the data analysis. The results of the data analysis have shown that the GE1/1 prototype can reach a get a very good detection efficiency of $\sim 98\%$.

Finally, after the different studies concerning the time resolution and efficiency of the Triple-GEM detectors, we focussed on the third important parameter of a particle detector: the spatial resolution. We have shown that in some cases the spatial resolution with the binary readout is better than the one with the analogue readout. This study has been done both by Monte Carlo simulation and analytically for a binary readout for three types of detectors: silicon sensor, Micromegas and GEM-based detectors.
The spatial resolution has been studied as a function of a series of parameters and we have shown that in the future these parameters could be used to optimize the geometry of new detectors.
A two parameter model of the spatial resolution with the binary readout has been studied and it has been shown that this model is applicable for silicon detectors and Micromegas detectors, and can be used for GEM detectors with the addition of one parameter.
Once the parameters for a silicon detector or a Micromegas detector (and for GEM detectors with an external measurement of the diffusion effect in the induction region) are found by measuring the spatial resolution and the cluster size, the formula can be a guiding principle to improve the spatial resolution by optimizing geometrical parameters of the detector. This is definitely an area where we will continue our investigations by comparing our models to existing experimental data.

To conclude, during this work we had the opportunity to study many aspects of the CMS Triple-GEM detectors. Our work confirms, by measurements and simulations, that this technology meets the CMS GE1/1 specification and is well suited for this upgrade. We

have also developed a fast simulation framework which, despite is level of simplification, permits to understand the behavior of the Triple-GEM detector as well as the spatial resolution of other micro-strip detectors including silicon sensors.

Appendices

Appendix A

Time Resolution Tables

Time resolution for VFAT_ n2 design found with GARFIELD

Peaking time (ns)	20	50	100	250	500
TOT (ns)	5.52 ± 0.22	5.17 ± 0.2	4.63 ± 0.18	4.52 ± 0.14	4.56 ± 0.24
CFD (ns)	6.88 ± 0.25	4.95 ± 0.16	4.59 ± 0.16	4.50 ± 0.15	4.58 ± 0.16

Time resolution for VFAT_ n3 design found with GARFIELD

Peaking time (ns)	25	50	75	100	200
TOT (ns)	5.19 ± 0.17	4.91 ± 0.15	4.81 ± 0.16	4.60 ± 0.14	4.65 ± 0.15
CFD (ns)	6.07 ± 0.18	4.98 ± 0.16	4.82 ± 0.16	4.76 ± 0.16	4.64 ± 0.16

Latency for VFAT_ n2 design found with GARFIELD

Peaking time (ns)	20	50	100	250	500
TOT (ns)	144 ± 12	272 ± 24	490 ± 46	1146 ± 112	2238 ± 222
CFD (ns)	72 ± 6	100 ± 5	149 ± 5	299 ± 5	548 ± 5

Latency for VFAT_ n3 design found with GARFIELD

Peaking time (ns)	25	50	75	100	200
TOT (ns)	153 ± 11	248 ± 20	343 ± 28	440 ± 37	825 ± 70
CFD (ns)	79 ± 6	105 ± 5	132 ± 5	159 ± 5	269 ± 5

Time resolution for VFAT_ n3 design found with the FastSim without transparency

Peaking time (ns)	25	50	75	100	200
'GARFIELD' parameter	5.66 ± 0.20	4.58 ± 0.15	4.24 ± 0.13	4.20 ± 0.13	4.39 ± 0.18
'standard' parameters	4.94 ± 0.17	4.21 ± 0.14	4.01 ± 0.11	3.80 ± 0.13	3.94 ± 0.14

Time resolution for VFAT_ n3 design found with the FastSim with transparency

Peaking time (ns)	25	50	75	100	200
'GARFIELD' parameter	5.43 ± 0.17	4.89 ± 0.18	4.51 ± 0.14	4.43 ± 0.16	4.44 ± 0.16
'standard' parameters	5.18 ± 0.28	4.18 ± 0.21	3.89 ± 0.21	3.83 ± 0.20	4.29 ± 0.24

Appendix B

Parameters of the CMS Triple-GEM

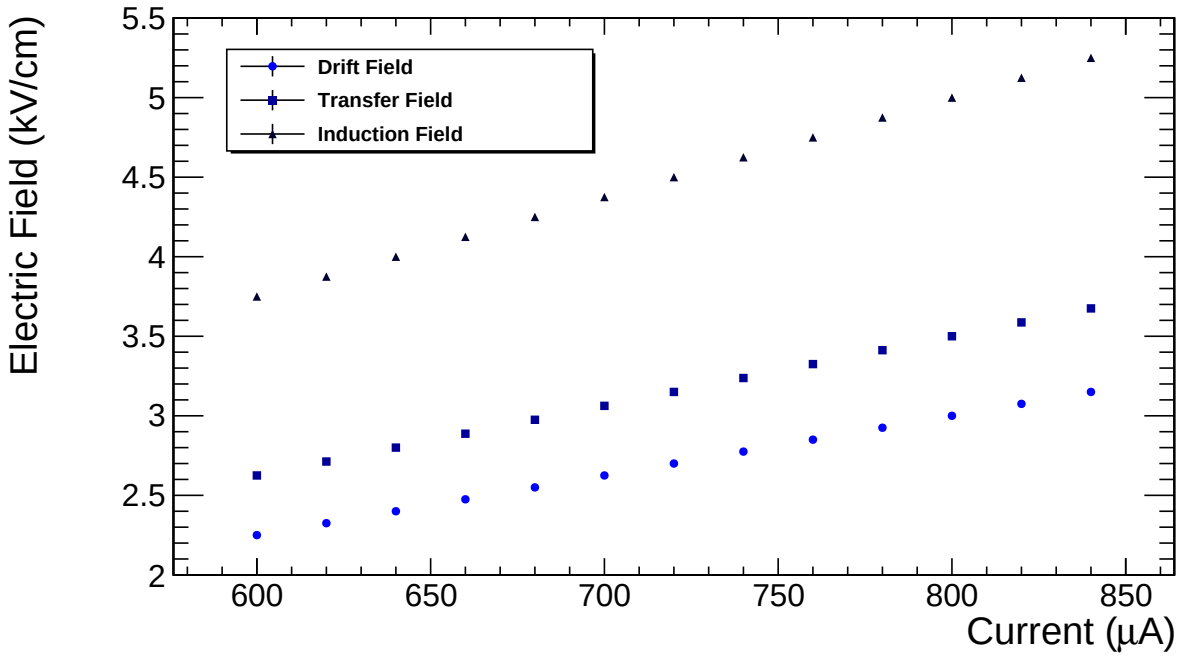

FIGURE B.1: Evolution of the electric fields in the different gap of the CMS Triple-GEM as a function of the current in the divider.

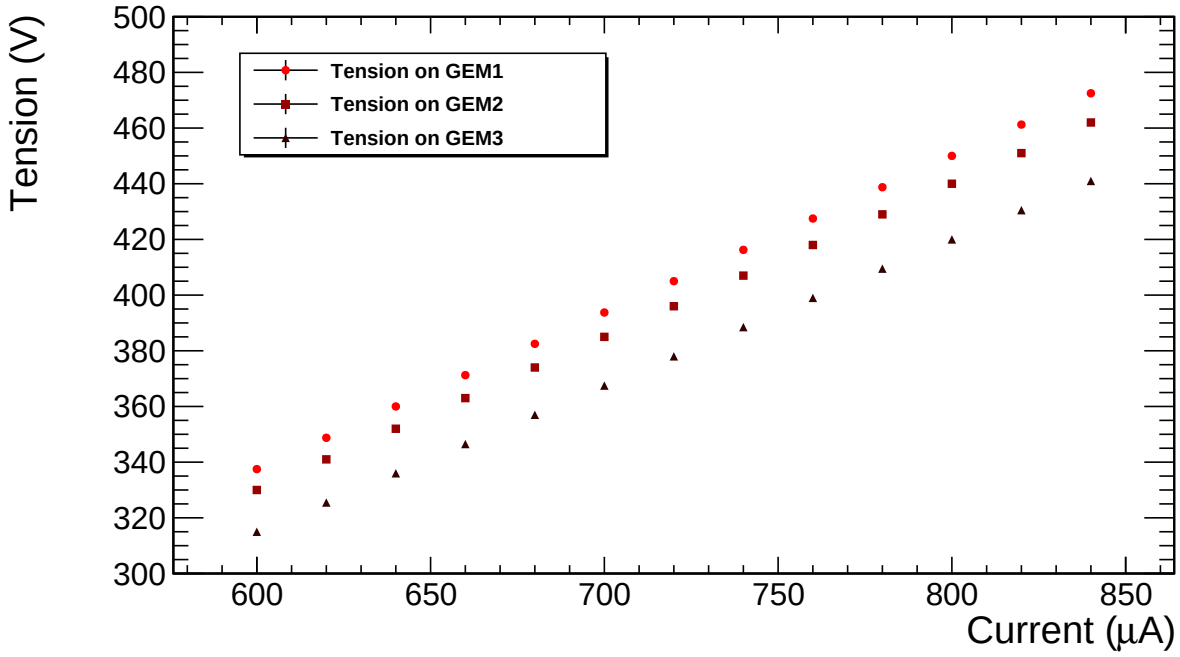

FIGURE B.2: Evolution of the electric tension applied to the different GEM foils of the CMS Triple-GEM as a function of the current in the divider.

Appendix C

Configurations of the Double-GEM

Tension applied to the Double-GEM equivalent to GEM1

Current (μA)	HV$_{G1bottom}$ (V)	HV$_{G1top}$ (V)	HV$_{G2bottom}$ (V)	HV$_{G2top}$ (V)	HV $_{drift}(V)$
600	375	690	1215	1545	2332.5
620	387.5	713	1255.5	1596.5	2410.25
640	400	736	1296	1648	2488
660	412.5	759	1336.5	1699.5	2565.75
680	425	782	1377	1751	2643.5
700	437.5	805	1417.5	1802.5	2721.25
720	450	828	1458	1854	2799
740	462.5	851	1498.5	1905.5	2876.75
760	475	874	1539	1957	2954.5
780	487.5	897	1579.5	2008.5	3032.25
800	500	920	1620	2060	3110
820	512.5	943	1660.5	2111.5	3187.75
840	525	966	1701	2163	3265.5

Tension applied to the Double-GEM equivalent to GEM2

Current (μA)	HV$_{G1bottom}$ (V)	HV$_{G1top}$ (V)	HV$_{G2bottom}$ (V)	HV$_{G2top}$ (V)	HV $_{drift}(V)$
600	375	690	1215	1552.5	2227.5
620	387.5	713	1255.5	1604.25	2301.75
640	400	736	1296	1656	2376
660	412.5	759	1336.5	1707.75	2450.25
680	425	782	1377	1759.5	2524.5
700	437.5	805	1417.5	1811.25	2598.75
720	450	828	1458	1863	2673
740	462.5	851	1498.5	1914.75	2747.25
760	475	874	1539	1966.5	2821.5
780	487.5	897	1579.5	2018.25	2895.75
800	500	920	1620	2070	2970
820	512.5	943	1660.5	2121.75	3044.25
840	525	966	1701	2173.5	3118.5

Tension applied to the Double-GEM equivalent to GEM3

Current (μA)	HV$_{G1bottom}$ (V)	HV$_{G1top}$ (V)	HV$_{G2bottom}$ (V)	HV$_{G2top}$ (V)	HV $_{drift}(V)$
600	262.5	592.5	1117.5	1455	2130
620	271.25	612.25	1154.75	1503.5	2201
640	280	632	1192	1552	2272
660	288.75	651.75	1229.25	1600.5	2343
680	297.5	671.5	1266.5	1649	2414
700	306.25	691.25	1303.75	1697.5	2485
720	315	711	1341	1746	2556
740	323.75	730.75	1378.25	1794.5	2627
760	332.5	750.5	1415.5	1843	2698
780	341.25	770.25	1452.75	1891.5	2769
800	350	790	1490	1940	2840
820	358.75	809.75	1527.25	1988.5	2911
840	367.5	829.5	1564.5	2037	2982

Bibliography

[1] F. Englert and R. Brout. Broken symmetry and the mass of gauge vector mesons. *Phys. Rev. Lett.*, 13:321–323, Aug 1964.

[2] Peter W. Higgs. Broken symmetries and the masses of gauge bosons. *Phys. Rev. Lett.*, 13:508–509, Oct 1964.

[3] G. S. Guralnik, C. R. Hagen, and T. W. B. Kibble. Global conservation laws and massless particles. *Phys. Rev. Lett.*, 13:585–587, Nov 1964.

[4] CMS Collaboration. Observation of a new boson at a mass of 125 GeV with the CMS experiment at the LHC. *Phys.Lett.*, B716:30–61, 2012.

[5] ATLAS Collaboration. Observation of a new particle in the search for the Standard Model Higgs boson with the ATLAS detector at the LHC. *Phys.Lett.*, B716:1–29, 2012.

[6] CERN Service graphique. Overall view of the LHC. Vue d'ensemble du LHC. Jun 2014. General Photo.

[7] Jean-Luc Caron. Accelerator complex of CERN: an overview of all accelerators of CERN. Vue d'ensemble de tous les accélérateurs du CERN. Jul 2001.

[8] K. Nakamura et al. (Particle Data Group). *Particle Physics Booklet.* IOP Publishing, 2010.

[9] Lyndon Evans and Philip Bryant. LHC Machine. *JINST*, 3:S08001, 2008.

[10] Tai Sakuma and Thomas McCauley. Detector and Event Visualization with SketchUp at the CMS Experiment. *J. Phys. Conf. Ser.*, 513:022032, 2014.

[11] S. Chatrchyan et al. The CMS experiment at the CERN LHC. *JINST*, 3:S08004, 2008.

[12] Serguei Chatrchyan et al. The performance of the CMS muon detector in proton-proton collisions at $\sqrt{s} = 7$ TeV at the LHC. *JINST*, 8:P11002, 2013.

[13] *The CMS muon project: Technical Design Report.* Technical Design Report CMS. CERN, Geneva, 1997.

[14] G Bauer, B Beccati, U Behrens, K Biery, O Bouffet, J Branson, S Bukowiec, E Cano, H Cheung, M Ciganek, S Cittolin, J A Coarasa, C Deldicque, A Dupont, S Erhan, D Gigi, F Glege, R Gomez-Reino, D Hatton, A Holzner, Y L Hwong, L Masetti, F Meijers, E Meschi, R K Mommsen, R Moser, V O'Dell, L Orsini, C Paus, A Petrucci, M Pieri, A Racz, O Raginel, H Sakulin, M Sani, P Schieferdecker, C Schwick, D Shpakov, M Simon, and K Sumorok. The data-acquisition system of the cms experiment at the lhc. *Journal of Physics: Conference Series*, 331(2):022021, 2011.

[15] CMS Collaboration. Technical proposal for the upgrade of the CMS detector through 2020. Technical Report CERN-LHCC-2011-006. LHCC-P-004, CERN, Geneva, Jun 2011.

[16] A Tapper and Darin Acosta. CMS Technical Design Report for the Level-1 Trigger Upgrade. Technical Report CERN-LHCC-2013-011. CMS-TDR-12, CERN, Geneva, Jun 2013.

[17] GEMs for CMS Collaboration. *Technical Proposal. A GEM Detector System for an Upgrade of the CMS Muon Endcaps.* CERN, CMS IN 2012/002.

[18] Florian Zenoni. *Study of Triple-GEM detectors for the CMS muon spectrometer upgrade at LHC and study of the forward-backward charge asymmetry for the search of extra neutral gauge bosons.* PhD thesis, Universite Libre de Bruxelles, 2016.

[19] William R Leo. *Techniques for nuclear and particle physics experiments: a how-to approach; 2nd ed.* Springer, Berlin, 1994.

[20] L. Rolandi W. Blum. *Particle Detection with Drift Chambers.* Springer-Verlag, 1993.

[21] Pascal VANLAER. *Contribution to the study of the central tracking system of the CMS detector at the future proton collider LHC.* PhD thesis, Universite Libre de Bruxelles, 1998.

[22] Gilles De Lentdecker. Etude d'un compteur a gaz a grille microscopique (micromegas) pour un traceur au lhc. Master's thesis, Universite Libre de Bruxelles, 1997-1998.

[23] Hansjörg Fischle, Joachim Heintze, and Bernhard Schmidt. Experimental determination of ionization cluster size distributions in counting gases. *Nuclear Instruments*

and Methods in Physics Research Section A: Accelerators, Spectrometers, Detectors and Associated Equipment, 301(2):202 – 214, 1991.

[24] Maximilien Alexandre Chefdeville. *Development of Micromegas-like gaseous detectors using a pixel readout chip as collecting anode.* PhD thesis, Universiteit van Amsterdam, 2009.

[25] P. Langevin. Sur la théorie de mouvement brownien. *C.R. Acad. Sci. Paris*, 146:530–533, 1908.

[26] G. CHARPAK et F. SAULI G. SCHULTZ. Mobilities of positive ions in some gas mixtures used in proportional and drift chambers. *Revue de Physique Appliquée*, 12:67–70, janvier 1977.

[27] F. Sauli. *Principles of operation of multiwire proportional and drift chambers.* CERN report, 1977.

[28] Ilc tpc wiki. http://www-hep.phys.saga-u.ac.jp/ILC-TPC/gas/index.html.

[29] H. Raether. *Electron avalanches and breakdown in gases.* Butterworth, 1964.

[30] John David Jackson. *Classical Electrodynamics Third Edition.* Wiley, 1998.

[31] Maxwell electromagnetic field simulation for high-performance electromechanical design. http://www.ansoft.com/products/em/maxwell/.

[32] A. Oed. Position-sensitive detector with microstrip anode for electron multiplication with gases. *NIM*, 263:351–359, January 1988.

[33] F. Angelini et al. *IEEE Trans. Nucl. Sci. NS*, 37, 1990.

[34] I. Giomataris et al. Micromegas: a high-granularity position-sensitive gaseous detector for high particle-flux environments. *Nucl. Instr. and Meth.*, A 376:29–35, january 1996.

[35] Joost Melai, Amos Breskin, Marco Cortesi, Yevgen Bilevych, Martin Fransen, Harry van der Graaf, Jan Visschers, Victor Blanco Carballo, Cora Salm, and Jurriaan Schmitz. A UV Sensitive Integrated Micromegas with Timepix Readout. *Nucl. Instrum. Meth.*, A628:133–137, 2011.

[36] J. Derré et al. Fast signals electron detection with micromegas photodetector. *NIM*, 499:314–321, 2000.

[37] F. Sauli. Gem: A new concept for electron amplification in gas detectors. *Nucl. Instr. and Meth.*, A 386:531–534, november 1997.

[38] S. Duarte Pinto, M. Villa, M. Alfonsi, I. Brock, G. Croci, E. David, R. de Oliveira, L. Ropelewski, and M. van Stenis. Progress on large area GEMs. *Journal of Instrumentation*, 4:12009, December 2009.

[39] A. Brensan et al. High rate behavior and discharge limits in micro-pattern detectors. *NIM*, 4 424:321–342, 1999.

[40] F. Sauli. Progress with the gas electron multiplier. *Nucl. Instrum. Meth.*, A522:93–98, 2004.

[41] K. A. Olive et al. Review of Particle Physics. *Chin. Phys.*, C38:090001, 2014.

[42] D. Abbaneo et al. Characterization of gem detectors for application in the cms muon detection system. In *IEEE Nucl. Sci. Symp. Conf. Rec. 1416-1422; RD51 Note 2010-005; arXiv:1012.3675v1*, 2010.

[43] Andrey Marinov. *Feasibility Study of a GEM Based Muon System for the CMS Detector at the Large Hadron Collider*. PhD thesis, Universiteit Gent, 2013.

[44] R. Veenhof. Garfield. garfield.web.cern.ch/garfield.

[45] Igor Smirnov. Heed. http://heed.web.cern.ch/heed/.

[46] S.F. Biagi. Monte carlo simulation of electron drift and diffusion in counting gases under the influence of electric and magnetic fields. *NIM*, A 421:234–240, 1999.

[47] Ansys. http://www.ansys.com/.

[48] Supratik Mukhopadhay and Nayana Majumdar. A nearly exact boundary element method. http://nebem.web.cern.ch/nebem/.

[49] S.F. Biagi. Monte carlo simulation of electron drift and diffusion in counting gases under the influence of electric and magnetic fields. *Nuclear Instruments and Methods in Physics Research Section A: Accelerators, Spectrometers, Detectors and Associated Equipment*, 421(1–2):234 – 240, 1999.

[50] S.L. Lin and J.N. Bardsley. The null-event method in computer simulation. *Computer Physics Communications*, 15(3):161 – 163, 1978.

[51] Stephen Biagi. Magboltz. http://rjd.web.cern.ch/rjd/cgi-bin/cross.

[52] P. Aspell. https://espace.cern.ch/cms-project-GEMElectronics/SitePages/Home.aspx.

[53] M. Dabrowski, P. Aspell, S. Bonacini, D. Ciaglia, G. De Lentdecker, G. De Robertis, K. Kloukinas, M. Kupiainen, P. Leroux, F. Tavernier, J. Talvitie, and T. Tuuva.

The vfat3-comm-port: a complete communication port for front-end asics intended for use within the high luminosity radiation environments of the lhc. *Journal of Instrumentation*, 10(03):C03019, 2015.

[54] Jan Antonio Aguilar Sánchez. *Analysis of the Optical Beacon system and search for point-like sources in the ANTARES neutrino telescope*. PhD thesis, Universitat de València, 2007.

[55] R. Brun and F. Rademakers. ROOT: An object oriented data analysis framework. *Nucl. Instrum. Meth.*, A389:81–86, 1997.

[56] A. Buzulutskov, Lev I. Shekhtman, A. Breskin, R. Chechik, G. Garty, and F. Sauli. The GEM photomultiplier operated with noble gas mixtures. *Nucl. Instrum. Meth.*, A443:164–180, 2000.

[57] F. Loddo and T. Maerschalk et al. Design of a constant fraction discriminator for the vfat3 front-end asic of the cms gem detector. *Journal of Instrumentation*, 11(01):C01023, 2016.

[58] D. Abbaneo et al. Performance of a Large-Area GEM Detector Prototype for the Upgrade of the CMS Muon Endcap System. In *2014 IEEE Nuclear Science Symposium and Medical Imaging Conference and 21st Symposium on Room-Temperature Semiconductor X-ray and Gamma-ray Detectors (NSS/MIC 2014 / RTSD 2014) Seattle, WA, USA, November 8-15, 2014*, 2014.

[59] M. Raymond, M. French, J. Fulcher, G. Hall, L. Jones, K. Kloukinas, L.-K. Lim, G. Marseguerra, P. Moreira, Q. Morrissey, A. Neviani, and E. Noah. The apv25 0.25 mu;m cmos readout chip for the cms tracker. In *Nuclear Science Symposium Conference Record, 2000 IEEE*, volume 2, pages 9/113–9/118 vol.2, 2000.

[60] E. van der Bij. http://ts-dep-dem.web.cern.ch/ts-dep-dem/overview/.

[61] HORIBA. http://www.horiba.com/semiconductor/products/product-lines/mass-flow-controller/mass-flow-meter/.

[62] ORTEC. Models 142a, 142b, and 142c preamplifiers operating and service manual. http://www.ortec-online.com/Products-Solutions/Modular-Electronic-Instruments-Preamplfiers.aspx.

[63] ORTEC. 575a amplifier manual. http://www.ortec-online.com/Products-Solutions/Modular-Electronic-Instruments-Amplifiers.aspx.

[64] Fabio Sauli. The gas electron multiplier (gem): Operating principles and applications. *Nuclear Instruments and Methods in Physics Research Section A: Accelerators, Spectrometers, Detectors and Associated Equipment*, 805:2 – 24, 2016. Special Issue in memory of Glenn F. Knoll.

[65] S. Bachmann, A. Bressan, L. Ropelewski, F. Sauli, A. Sharma, and D. Mörmann. Charge amplification and transfer processes in the gas electron multiplier. *Nuclear Instruments and Methods in Physics Research Section A: Accelerators, Spectrometers, Detectors and Associated Equipment*, 438(2–3):376 – 408, 1999.

[66] KEITHLEY. Model 6517a electrometer user's manual. http://www.keithley.nl/products/dcac/sensitive/highresistance/?mn=6517B.

[67] N Abgrall et al. Na61/shine facility at the cern sps: beams and detector system. *Journal of Instrumentation*, 9(06):P06005, 2014.

[68] Cern-gamma irradiation facility (gif). https://ep-dep-dt.web.cern.ch/irradiation-facilities/gif.

[69] Paul Aspell. VFAT2: A front-end system on chip providing fast trigger information, digitized data storage and formatting for the charge sensitive readout of multi-channel silicon and gas particle detectors. In *Electronics for particle physics. Proceedings, Topical Workshop, TWEPP-07, Prague, Czech Republic, September 3-7, 2007*, page 63, 2007.

[70] Voltaire. *Le Micromégas de M. de Voltaire*. Michel Lambert, Londres, 1752.

[71] D. C. Arogancia et al. Study in a beam test of the resolution of a Micromegas TPC with standard readout pads. *Nucl. Instrum. Meth.*, A602:403–414, 2009.

[72] R. Yonamine et al. Spatial resolutions of GEM TPC.A novel theoretical formula and its comparison to latest beam test data. *JINST*, 9:C03002, 2014.

[73] R. Yonamine, T. Maerschalk, and G. De Lentdecker. Study and optimization of the spatial resolution for detectors with binary readout. *Nuclear Instruments and Methods in Physics Research Section A: Accelerators, Spectrometers, Detectors and Associated Equipment*, 830:130 – 139, 2016.